Ultra-thin highly absorbing medium-based optical nanocavity for photonic and optoelectronic devices

by

Kyu-Tae Lee

A dissertation submitted in partial fulfillment
of the requirements for the degree of
Doctor of Philosophy
(Electrical Engineering)
in the University of Michigan
2015

Doctoral Committee:

Professor L. Jay Guo, Chair
Associate Professor Jinsang Kim
Professor Jamie D. Phillips
Associate Professor Zhaohui Zhong

2015

TO MY FAMILY AND DEAR MY WIFE

ACKNOWLEDGEMENTS

First and foremost, I would like to express my sincere appreciation to my PhD advisor, Prof. L. Jay Guo, for giving me a fantastic research opportunity with lots of great lab mates, offering invaluable advice, and supporting me throughout my whole PhD study. I have been truly fortunate to have such a wonderful advisor who has given me the freedom to explore various research topics, thus being able to intensify my capabilities in diverse areas and deepen the academic understanding. He has always encouraged me and has guided me to right path with his insightful suggestions and discussions when I had trouble. I have been motivated to address critical challenges and successfully able to achieve beyond my ability under his guidance. He also has helped me to build a successful career development and has instructed me on how to think and solve problems as an engineer. I have really enjoyed working with him and will definitely treasure all the experiences I have had throughout my PhD study in my life.

I would also like to express my deep gratitude to my doctoral committee members, Prof. Jinsang Kim, Prof. Jamie Phillips, and Prof. Zhaohui Zhong, for providing me with constructive advice and insightful discussions. I have been able to elucidate vague parts of my work after the discussion with them, thus remarkably improving the quality of my dissertation. Also, I am deeply indebted to my former advisor, Prof. Chang-Min Kim, for giving me valuable lessons in terms of both research and my life. Without his encouragement and support, my PhD journey at Umich would not have been possible.

I would like to thank Guo group members and precious friends at Umich. First of all, I am very grateful to Dr. Jae Yong Lee and Sungyong Seo for a lot of fruitful discussions and their great efforts to accomplish colored, semitransparent amorphous silicon photovoltaic cells and angle invariant structural color filters. I was truly lucky to have such great collaborators and I was able to experience what the really synergy is from the collaboration with you guys. I would also like to thank Dr. Masanori Fukuda for his endeavor to make perovskite photovoltaic devices, which would expand my knowledge. I should appreciate Prof. Hyoung Won Baac and Prof. Jong G. Ok for their great advice and assistance. Also, many thanks to former members, Prof. Hui Joon Park, Prof. Moon Kyu Kwak, Prof. Hongseok Youn, Dr. Young Jae Shin, Dr. Tao Ling, Dr. Yi-Kuei Wu, Dr. Alex Kaplan, and Andrew Hollowell. I am thankful to current team members, Chengang Ji, Taehwa Lee, Taehee Jang, Sangeon Lee, Dr. Jing Zhou, Chad Huard, Cheng Zhang, Ashwin Panday, Long Chen, Suneel Joglekar, Qiaochu Li, Xi Chen, and Qingyu Cui for sharing their experiences and time with me. Especially, special thanks to Chengang Ji. Despite many shortcomings as a mentor, he was always with me. I also appreciate Dr. Kyusang Lee, Hyunsoo Kim, and Byeongseop Song for their great help.

Most importantly, I would like to express my very profound appreciation and heartfelt gratitude to my dear wife, Junghye Baek, and my family, including dad, mom, grandma, two younger brothers, father-in-law, and mother-in-law for their constant encouragement, unconditional love, and unfailing support. I would never have been able to complete my PhD study without their patience and endless love. Especially, I am deeply thankful to my wife again for being brave when starting our journey together in US where everything could be strange. There are no words to describe how much I love you.

TABLE OF CONTENTS

LIST OF TABLES

LIST OF FIGURES

ABSTRACT

Optical cavities, which generally consist of an optically transparent medium with wavelength-scale thickness, have been widely used in various areas ranging from lasers and modulators to sensors and filters. A trivial optical absorption in the cavity allows incident light to constructively interfere with reflected light many times without serious loss, thus being able to create a resonance at a certain wavelength. However, a traditional optical cavity has faced challenges in achieving an angle-insensitive property, thereby dramatically limiting their applications in a wide variety of fields.

In this dissertation, we present several demonstrations, all based on optical nanocavities featuring strong resonance behaviors in highly absorbing media with the ultra-thin cavity thickness (< 30 nm) as compared to the wavelength of incident light, which is distinctly different from the conventional optical cavity systems. We firstly demonstrate angle invariant (up to 70°) transmissive and reflective structural color filters with high-color-purity exploiting a concept described above. We also present a new photovoltaic (PV) scheme incorporating novel optical design (ultra-thin cavity) and electrical design (dopant-free amorphous silicon) to create colored semitransparent PV cells, which could be harmoniously integrated with interiors and exteriors of the buildings, such as facades, windows, ceilings, and walls. This enables large surfaces of architectures to be efficiently utilized to generate the electric power. ~3 (2)% of power conversion efficiency with desired reflective (transmissive) colors that are insensitive to the

angle of incidence and the polarization state of incident light is achieved. To improve the power conversion efficiency of the colored PV cells, we propose and experimentally demonstrate a spectrum splitting method and microcavity-integrated PV scheme, both of which show ~4% of power conversion efficiency. Lastly, we describe how our strategy could be applied to other applications, such as perovskite PV cells, broadband visible absorbers, and low reflective wire grid polarizers. The presented approach could open door to numerous applications, such as energy-efficient ultra-thin colored display technologies and decorative building-integrated PV.

Chapter 1

Introduction

1.1 Fabry-Pérot Cavity

A Fabry-Pérot (F-P) optical cavity, which generally consists of wavelength-scale-thick transparent or low-absorbing medium sandwiched by two highly reflecting surfaces, has played an essential role in various fields ranging from lasers and spectroscopies to modulators and tunable filters [1-4]. Multiple reflections of the light in the cavity enable a certain wavelength (i.e., resonance) to form standing waves depending on both the thickness and optical property of the cavity medium. The incident light wave constructively interferes with multiple reflected waves without serious loss due to a negligible optical absorption in the cavity, thus leading to a long photon lifetime of the cavity. However, a critical challenge with the conventional F-P optical cavity still to be addressed is an angle dependent property. As shown in **Figure 1.1.1**, the resonance occurs when the sum of the propagation phase change and the two reflection phase changes (ϕ_{r12} and ϕ_{r23}) is equal to 2mπ. When the light is incident upon the structure at an oblique angle of incidence, the propagation phase change that is directly proportional to the incidence angle varies, thus resulting in a shifted resonance.

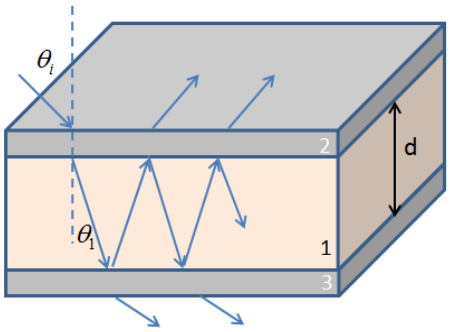

Resonance condition:

$$\phi_{r12} + \phi_{r23} + \phi_{propagation} = 2m\pi$$

$$\phi_{propagation} = \frac{2\pi n_1}{\lambda} 2d\cos(\theta_1)$$

Figure 1.1.1 A schematic diagram of the traditional F-P cavity comprising a transparent medium sandwiched by two high reflecting mirrors.

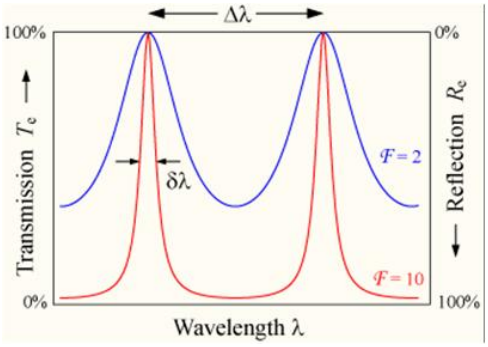

Figure 1.1.2 A transmission spectrum of the conventional F-P cavity depending on the finesse of the cavity.

Figure 1.1.2 exhibits a transmission of the traditional F-P optical cavity as a function of wavelength. $\Delta\lambda$ is the spacing in wavelength between two successive resonant cavity modes, defined as free spectral range (FSR). $\delta\lambda$ is the full width at half maximum (FWHM). The ratio of FSR to FWHM is finesse (***F***) expressed by the following **Equation 1.1.1**.

$$F = \frac{\Delta\lambda}{\delta\lambda} = \frac{\pi}{2\sin^{-1}(1/\sqrt{CF})} \tag{1.1.1}$$

where $CF = \frac{4R}{(1-R)^2}$ is the coefficient of finesse, and R is the reflectivity of the high reflecting mirrors. F is simply regarded as a photon lifetime (also related to Q-factor). When R is greater than 0.5, the finesse can be simplified by **Equation 1.1.2**.

$$F \approx \frac{\pi\sqrt{CF}}{2} = \frac{\pi\sqrt{R}}{(1-R)} \tag{1.1.2}$$

As can be seen in **Equation 1.1.2**, F increases as R increases, which mean that the photon can survive in the optical cavity system longer if the reflecting surfaces provide high reflections, leading to a sharp resonance that can be confirmed in the transmission spectrum as shown in **Figure 1.1.2**. The transmittance curve with F = 10 (red) shows much narrower resonance the transmittance curve with F = 2 (blue).

1.2 Thesis Outline

Chapter 2 introduces basic properties of highly absorbing media-based optical nanocavity. We will rigorously analyze how such lossy medium-based cavity is different from the conventional F-P optical cavity. We will explore which condition is necessary to create a resonance in an ultra-thin highly absorbing material and also study the phase cancellation required for attaining the angle-insensitive performance.

Chapter 3 describes structural color filters (both transmission and reflection type) with wide viewing angle that is highly desired property for a wide variety of applications, such as image

sensors, light emitting diodes, and liquid crystal display technologies. In this chapter, we will also study how the color purity of the devices can be improved by several strategies. As the last section of this chapter, we will introduce how to produce the reflective and transmissive colors via one-step fabrication, which is highly desired approach when patterning the individual colors by pixel units.

Chapter 4 presents subtractive color filters exploiting a plasmonic absorption property over a wide range of angles in a metal-insulator-metal (MIM) structure. We will exhibit that our proposed design has a very narrow bandwidth achieved by a near-perfect absorption at a resonance wavelength with the prominent suppression of off-resonance components, thus leading to high color purity. Moreover, a low sensitive directional performance whose resonance does not depend on an angle of incidence up to ±80° while preserving both the intensity and bandwidth is achieved, which is highly desired property, thus making them more attractive for numerous applications, including imaging sensors and liquid crystal display technologies.

Chapter 5 demonstrates wide-angle, polarization-independent structural reflective colors from both directions based on a one-dimensional photonic crystal. It will be presented that our device produces a distinct and saturated color with high angular tolerant performance till ±70° for any polarization state of incident light wave, which is highly desirable for a broad range of research areas. Moreover, the purity of the color and luminous intensity of the proposed device are improved as compared to conventional colorant based color filters and colloidal glasses. The

present approach can have the potential in replacing existing color filters and pigments and pave the way for various applications, including color displays and image sensor technologies.

Chapter 6 describes colored, semitransparent ultra-thin PV devices, which can be smoothly integrated with interiors and exteriors of the buildings, such as facades, windows, ceilings, and walls. This enables large surfaces of the architectures to be efficiently utilized to generate the electric power. In addition, the detailed investigations in terms of both optical and electrical performances of ultra-thin a-Si PV will be discussed. Lastly, we will present how the similar strategy could be applied to other material PV systems, such as perovskite semiconductor.

Chapter 7 reports colored, semitransparent PV cells by incorporating the microcavity with both the ultra-thin a-Si PV and perovskite PV. We will present how the color purity and the power conversion efficiency of the semitransparent a-Si PV can be improved as compared to what has been demonstrated in the chapter 6.

Chapter 8 describes a design principle of how to achieve flexible, ITO-free perovskite PV producing distinctive reflective colors. We will show several possible designs, their issues to be addressed, and then provide solutions.

Chapter 9 illustrates extraordinary optical absorption behaviors in ultra-thin a-Si PV devices. In this chapter, we will investigate the influence of the resonance depending on the thickness of the

photoactive layer on the electrical performance (short-circuit current density) of the PV cells. We will also examine angular dependences of the optical absorptions in the photoactive layer of the ultra-thin a-Si PV.

Chapter 10 demonstrates wide-angle, ultra-thin broadband visible absorbers based on multi-cavity resonances. We will present how the optical absorptions could be significantly boosted up by employing another cavity at different resonance wavelength, which could be useful for PV applications. We will also suggest the potential of tandem-mimicking ultra-thin a-Si PV device architectures utilizing such broadband visible absorber designs at the end of the chapter.

Chapter 11 presents possible designs of a transparent electrode for visible-blind ultra-violet (UV) photodetectors. We will investigate how the peaks in the transmission spectrum are related to the resonance of each cavity in the multilayer-based electrode design.

Chapter 12 suggests summary and possible future works exploiting strong interference effects in ultra-thin lossy media. At first, we will propose polarization-independent, angle-insensitive nearly perfect broadband absorbers, which could be useful for PV, bolometer, thermal emitter applications. And we will present how to design wire grid polarizers with low reflections employing strong resonance behaviors in ultra-thin semiconductor layers.

Chapter 2

Basic Properties of Lossy Medium-Based Optical Nanocavity

2.1 Introduction

In recent years, strong interference behaviors of light reflecting from an ultra-thin highly absorbing material on a metallic substrate in the visible wavelength ranges have been demonstrated [5-7]. The large absorption of highly absorbing material and non-trivial reflection phase shift (i.e., not 0 or π) at the interface between metal and semiconductor enable a strong absorption resonance to be formed in a nanometer thick highly absorbing medium. As a result, the cavity thickness can be significantly reduced using this strategy. The biggest advantage of such an ultra-thin cavity design over the conventional F-P cavity is that angular dependent property could be significantly improved due to the negligible phase shift accumulated during the propagation through the ultra-thin cavity medium that is much thinner than the wavelength of the incident light, which will be investigated in more detail later.

In this chapter, we will thoroughly analyze the lossy medium-based optical cavity and provide some insights and principles so that one could potentially utilize this strategy to create something useful in the future.

2.2 Analytical Models for Reflection Phase Shifts at Semiconductor-Metal Interface

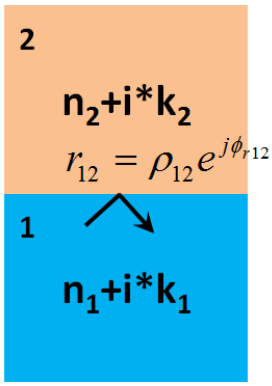

Figure 2.2.1 A phase shift (r_{12}) occurring upon the reflection at the interface between medium 1 and medium 2, both of which have complex refractive indices. The electromagnetic wave is coming from the medium 1 to medium 2.

Figure 2.2.1 presents a reflection phase shift (r_{12}) at the interface between medium 1 and medium 2. Both media have complex indices of refraction and the light is incident from the medium 1. To derive an explicit formula for the reflection coefficient in two media, we start from Fresnel reflection coefficient.

$$\frac{(n_1 + ik_1)\cos\theta_1 - (n_2 + ik_2)\cos\theta_2}{(n_1 + ik_1)\cos\theta_1 + (n_2 + ik_2)\cos\theta_2} \tag{2.2.1}$$

where θ_1 is the angle of incidence and θ_2 is the refracted angle that could be calculated by Snell's law ($n_1 \sin\theta_1 = n_2 \sin\theta_2$). It is convenient to set

$$\begin{aligned}(n_1 + ik_1)\cos\theta_1 &= u_1 + iv_1 \\ (n_2 + ik_2)\cos\theta_2 &= u_2 + iv_2\end{aligned} \tag{2.2.2}$$

After some algebra, the reflection phase shift at the interface between medium 1 and medium 2 is as follows.

$$\phi_{r12} = \tan^{-1}\left(\frac{\mathrm{Im}(r_{12})}{\mathrm{Re}(r_{12})}\right) = \tan^{-1}\left(\frac{2u_2v_1 - 2u_1v_2}{u_1^{\,2} - u_2^{\,2} + v_1^{\,2} - v_2^{\,2}}\right) \tag{2.2.3}$$

Considering $-\frac{\pi}{2} \le \tan^{-1}(x) \le \frac{\pi}{2}$, it is necessary to take into the four quadrants of the complex plane account since $-\pi < \phi_{r12} < \pi$. **Figure 2.2.2 (a)** exhibits the four quadrants of the complex plane and a plot of the inverse tangent of *x* is depicted in **Figure 2.2.2 (b)**.

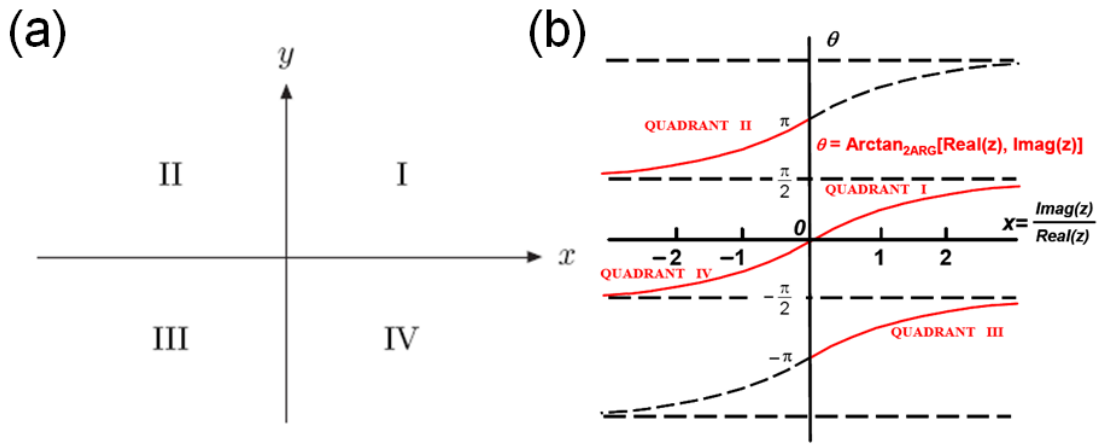

Figure 2.2.2 (a) Four quadrants of the complex plane. (b) Graph of inverse tangent of *x* depending on the four quadrants of the complex plane.

Table 2.2.1 Formulae for the phase of the complex number.

Quadrant	Sign of x and y	Phase
I	x > 0, y > 0	atan(y/x)
II	x < 0, y > 0	atan(y/x) + pi
III	x < 0, y < 0	atan(y/x) – pi
IV	x > 0, y < 0	atan(y/x)

Depending on the sign of real and imaginary part of the complex number, we need to plus (minus) additional π for the second (third) quadrant as described in **Table 2.2.1**.

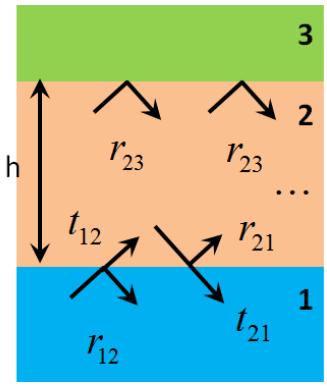

Figure 2.2.3 Three media with complex refractive indices. The media 1 and 3 are semi-infinite but the medium 2 has the thickness (*h*). The electromagnetic wave is coming from the bottom.

Now, we will investigate the total reflection phase shift from the three media, outer media of which are semi-infinite and the middle layer has a certain thickness (*h*). The net reflection phase shift is expressed as the following.

$$\begin{aligned} r &= r_{12} + t_{12}r_{23}t_{21}e^{2j\beta} + t_{12}r_{23}r_{21}r_{23}t_{21}e^{4j\beta} + \cdots \\ &= r_{12} + r_{23}t_{12}t_{21}e^{2j\beta}\left(1 + r_{21}r_{23}e^{2j\beta} + \cdots\right) \\ &= r_{12} + \frac{r_{23}t_{12}t_{21}e^{2j\beta}}{1 - r_{21}r_{23}e^{2j\beta}} = \frac{r_{12} + r_{23}e^{2j\beta}}{1 + r_{12}r_{23}e^{2j\beta}} \end{aligned} \tag{2.2.4}$$

where

$$r_{kl} = \frac{\tilde{n}_k \cos\theta_k - \tilde{n}_l \cos\theta_l}{\tilde{n}_k \cos\theta_k + \tilde{n}_l \cos\theta_l}$$

$$\beta = \frac{2\pi}{\lambda} n_2 h \cos\theta_2$$

After some algebra, we will obtain the explicit expression of the reflection phase shift as follows.

$$\phi_r = \tan^{-1}\left(\frac{\rho_{12}(1-\rho_{23}{}^2)\sin\phi_{r12} + \rho_{23}(1-\rho_{12}{}^2)\sin(\phi_{r23} + 2\beta)}{\rho_{12}(1+\rho_{23}{}^2)\cos\phi_{r12} + \rho_{23}(1+\rho_{12}{}^2)\cos(\phi_{r23} + 2\beta)} \right) \tag{2.2.5}$$

where ρ_{12} (ρ_{23}) is the magnitude of the reflection coefficient at the interface between medium 1 and medium 2 (medium 2 and medium 3).

To validate the accurateness of the explicit formula, we compare the phase shifts obtained from **Equation 2.2.5** with the results calculated by the transfer matrix method, showing great agreement as shown in **Figure 2.2.4**. In this example, the light from the germanium (Ge) layer is incident onto 10 nm of optically transparent silver (Ag) metallic layer and then to the air.

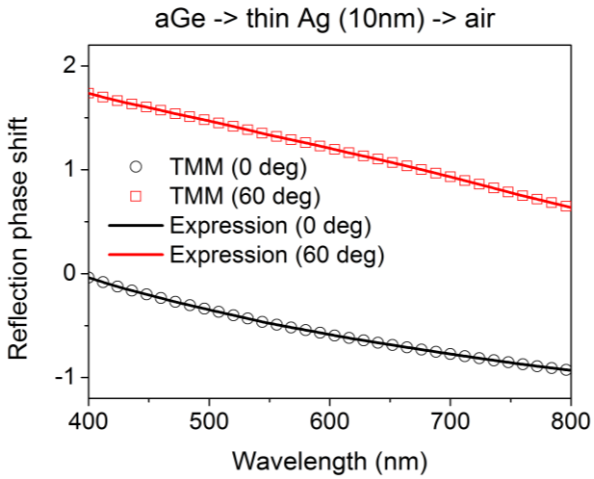

Figure 2.2.4 Calculated reflection phase shifts by the transfer matrix method in comparison to the results attained from the explicit expression of the reflection phase shift.

2.3 Resonance Behaviors in Ultra-thin Semiconductor Media

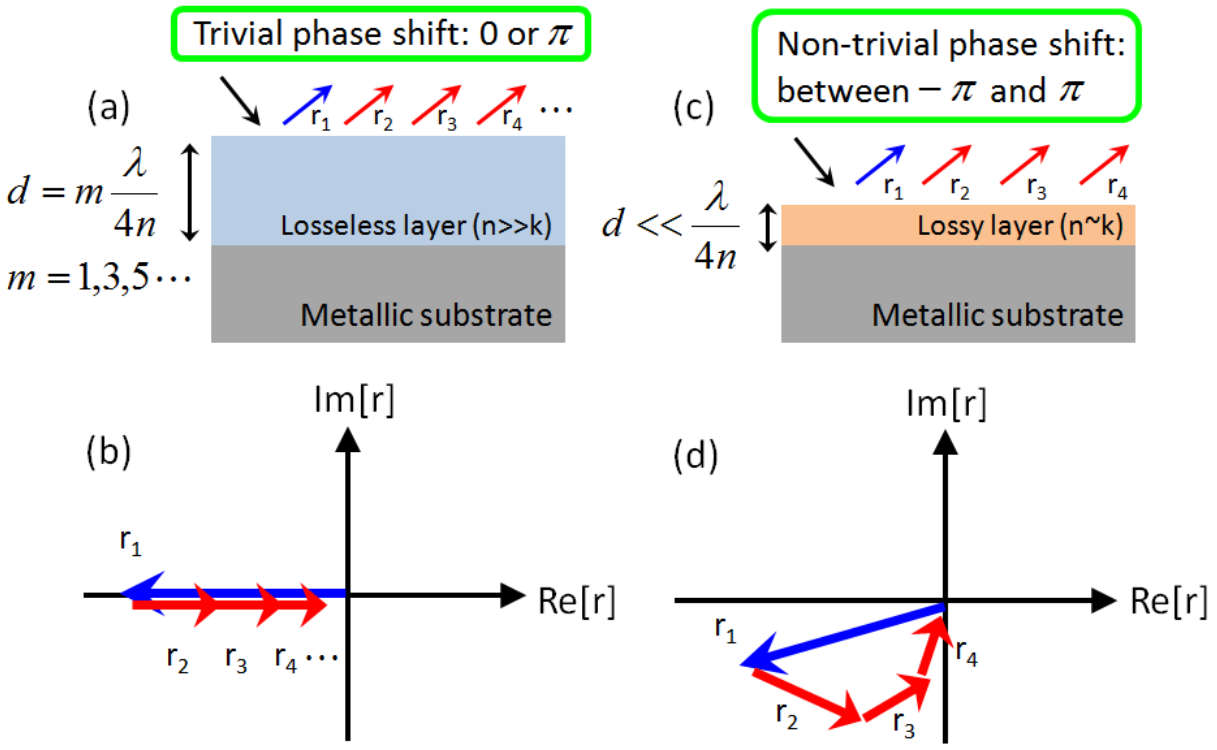

Figure 2.3.1 (a) A structure consisting of a lossless layer (i.e., real part of the refractive index (*n*) is much larger than the imaginary part of the refractive index (*k*)) on a metallic substrate. The phase shift occurring upon the reflection is trivial (i.e., 0 or π) in this case. (b) A phasor diagram of the structure described in (a). The first reflected light and the partial reflected light waves are represented by the blue and red colors, respectively. The phase of the first reflected light wave is π with respect to the incident wave, but the phase of the rest of all other partial reflected waves is 0. An infinite number of the partial reflected light waves cancel the first reflected light, thus creating complete absorption (i.e., resonance). A quarter wavelength-thick layer on the metallic substrate leads to a zero reflection due to the destructive interference. The phasor is along the horizontal axis in the complex plane. (c) A device structure that is composed of highly absorbing medium (i.e., *k* is now comparable to *n*) on the metallic substrate. In this case, the phase shift occurring upon the reflection is non-trivial (i.e., between -π or π). (d) A phasor diagram of the structure depicted in (c). The first reflected light and the partial reflected light waves are represented by the blue and red colors, respectively. The phase of the first reflection is greatly different from π (the phasor is not along the horizontal axis in the complex plane) and a few partial reflections is good enough to cancel the first reflection.

In **Figure 2.3.1 (a)**, a device structure that is composed of a lossless layer (i.e., real part of the refractive index (*n*) is much larger than the imaginary part of the refractive index (*k*)) on a metallic substrate is depicted. The first reflection and the remaining partial reflections are

denoted by the blue and red colored arrows, respectively. In this geometry, the reflection phase shift is trivial (i.e., 0 or π). **Figure 2.3.1 (b)** exhibits a phasor diagram of the schematic presented in **Figure 2.3.1 (a)**. The phase of the first reflected light is π with respect to the incident wave due to the index contrast, while the phase of all other partial reflected light waves is 0. When the cavity layer thickness is a multiple number of $m\lambda/4n \quad where \quad m = 1,3,5,\cdots$ (we assume that the metallic substrate is perfect electric conductor (PEC) and hence the reflection phase shift from the PEC is π), the first reflection will be cancelled out by the destructive interference with an infinite number of the rest of partial reflections, suggesting that the phasor trajectory ends at the origin. This gives rise to the resonance. In this case, the phasor is primarily along the horizontal axis in the complex plane. **Figure 2.3.1 (c)** illustrates the schematic diagram comprising highly absorbing medium (i.e., *k* is now comparable to *n*) on the metallic substrate. Unlike the previous case, the phase shift appearing on the reflection is non-trivial (i.e., between -π or π) at the highly absorbing medium-metal interface. In **Figure 2.3.1 (d),** the phasor diagram of the device structure studied in (c) is shown. The phase shift occurring on the first reflection (blue arrow) is considerably different from the trivial reflection phase shifts (i.e., between -π and π), meaning that the phasor is located anywhere in the complex plane depending on how large *k* the material has. A few partial reflections are sufficient to cancel the first reflection. Accordingly, the resonance in the optical absorption spectrum (i.e., absorption peak (reflection valley)) could appear in an optical cavity layer with a significantly reduced thickness as compared to the wavelength of incident light.

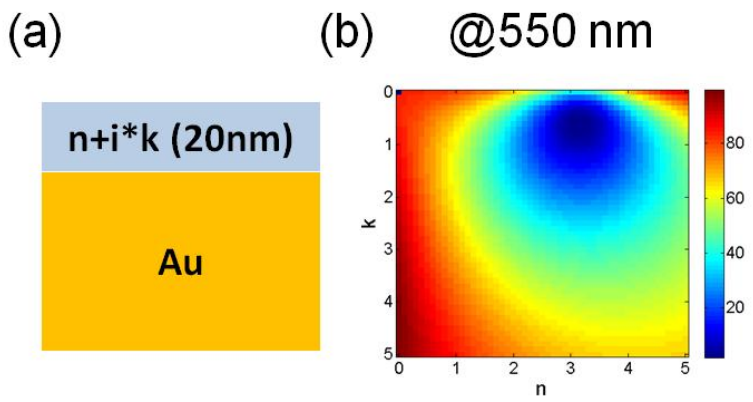

Figure 2.3.2 (a) A schematic view of the ultra-thin semiconductor layer on top of the Au metallic substrate. (b) A calculated contour plot of the reflection as a function of a complex index of refraction (real (*n*) and imaginary (*k*) parts) of the 20 nm of an arbitrary medium on the thick Au substrate at 550 nm. It is found that a very small reflection that corresponds to the optical absorption resonance at 550 nm is obtained when *n* and *k* are equivalent to 3.2 and 0.7. Color maps denote the intensity values of the reflected light.

In **Figure 2.3.2 (a)**, a schematic diagram of the lossy medium-based optical nanovavity comprising 20nm thickness of the ultra-thin semiconductor (arbitrary refractive index) on top of the thick Au substrate is shown. **Figure 2.3.2 (b)** illustrates the calculated contour plot of the reflection as a function of a complex refractive index of 20 nm thickness of the arbitrary medium on the Au substrate at 550 nm. The blue color implies the low reflection while the red color denotes the high reflection. It turns out that there is a region showing a fairly low reflection that corresponds to the absorption peak (i.e., resonance) at 550 nm when *n* and *k* are equivalent to 3.2 and 0.7, which is close to the amorphous silicon (a-Si) index ($n+ik = 4.4+i0.4$). This suggests that the resonance in the ultra-thin a-Si layer on top of the thick Au substrate could be created with slightly reduced cavity thickness due to the relatively large index of the a-Si material as compared to the optimized index of refraction. We will show another example of the structure consisting of 10 nm thickness of the arbitrary medium on top of the thick Ag substrate.

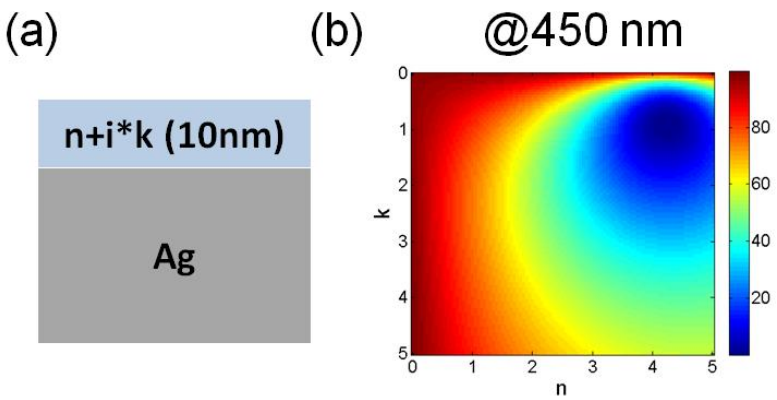

Figure 2.3.3 (a) A schematic diagram of 10 nm thickness of the arbitrary layer on top of the Ag metallic substrate. (b) A calculated contour plot of the reflection as a function of a complex index of refraction (real (*n*) and imaginary (*k*) parts) of the 10 nm of an arbitrary medium on the thick Ag substrate at 450 nm. It is obvious that a very lower reflection that corresponds to the optical absorption resonance at 450 nm is attained when *n* and *k* are equivalent to 4.25 and 0.9. Color maps indicate the intensity values of the reflected light.

A schematic view of the arbitrary medium with 10 nm thickness on top of the thick Au substrate is presented in **Figure 2.3.3 (a)**. In **Figure 2.3.3 (b)**, the calculated contour plot of the reflection as a function of a complex refractive index of 10 nm thickness of the arbitrary medium on the Ag substrate at 450 nm is depicted. It is clear to see that there is a region showing a fairly low reflection (i.e., blue color) that corresponds to the resonance behavior at 450 nm when *n* and *k* are equivalent to 4.25 and 0.9, which is quite close to the refractive index of the a-Si material (n+ik = 4.87+i1.08), thus implying that the resonance in the 10 nm thick a-Si layer on top of the thick Ag substrate could be attained.

2.4 Phase Cancellation Study For Angle-Insensitivity

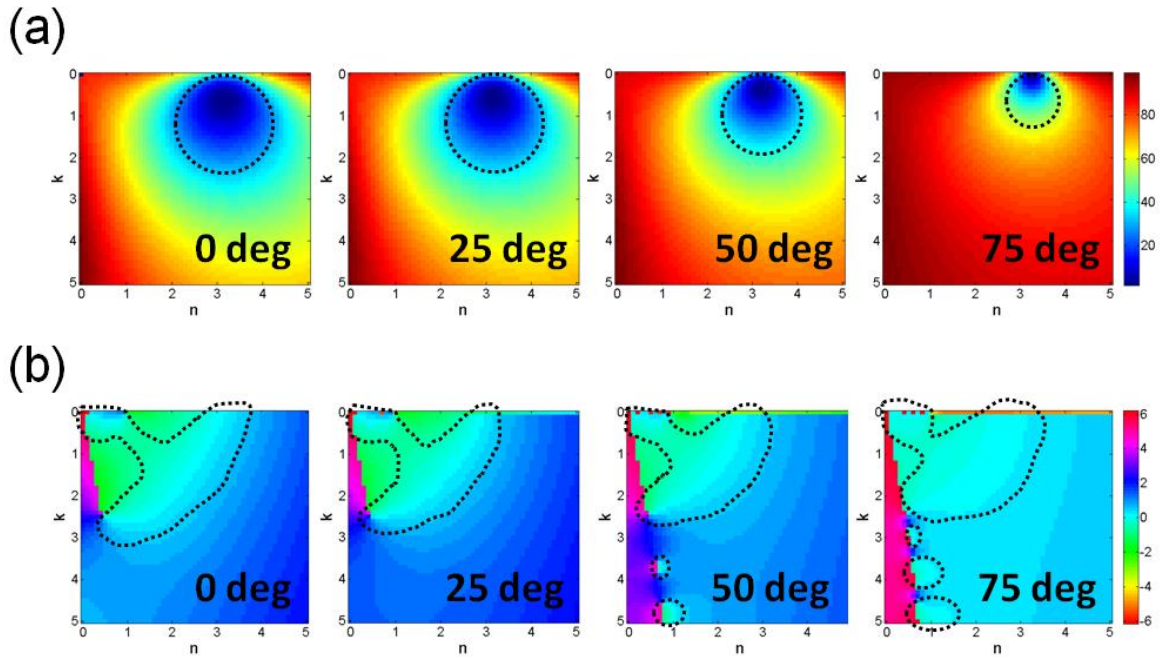

Figure 2.4.1 (a) Calculated contour plots of the reflection as a function of a complex refractive index (real (*n*) and imaginary (*k*) parts) of the 20 nm of an arbitrary medium on the thick Au substrate at 550 nm (the same device geometry described in Figure 2.3.2 (a)) at the angle of incidence ranging from normal (0 degree) to 75 degrees. The blue color denotes the low reflections whereas the red color signifies the high reflections in the colormap. (b) Calculated sum of the net phase shift, encompassing propagation phase shift as well as the two reflection phase shifts, of the same structure shown in Figure 2.3.2 (a) at the incident angles from normal (0 degree) to 75 degrees. The cyan color represents that the sum of the total phase shift is equal to the zero.

Figure 2.4.1 (a) describes the calculated contour plots of the reflection as a function of a complex refractive index (real (*n*) and imaginary (*k*) parts) of the 20 nm of an arbitrary medium on the thick Au substrate at 550 nm (the same device structure exhibited in **Figure 2.3.2 (a)**) at the angle of incidence ranging from normal (0 degree) to 75 degrees. The blue color denotes the low reflections whereas the red color signifies the high reflections in the colormap. The black dotted circle represents the region where the strong resonance behavior at 550 nm could be created with the material that has the refractive index roughly within the circle when the medium

thickness is 20 nm on top of the Au substrate. According to the calculation, it would be possible to have the material with the refractive index of $2.5 < n < 3.5$, $0 < k < 1$ on the Au substrate in order to create the resonance at 550 nm. **Figure 2.4.1 (b)** presents the calculated sum of the total phase shift, involving the propagation phase shift and the two reflection phase shifts, of the same structure shown in **Figure 2.3.2 (a)** at the incident angles from normal (0 degree) to 75 degrees. The cyan color represents that the sum of the total phase shift is equal to the zero, which is indicated by the black dotted lines. When these cyan colored regions (i.e., sum of the net phase shift is zero) at normal incidence are overlapped with those at the oblique angles of incidence, the change in the sum of the net phase shift with respect to the angle of incidence is almost negligible, thus suggesting the angle invariant performance. Hence, we will have the strong resonance behavior with the angle invariant characteristics at 550 nm when the 20 nm thick arbitrary medium has the refractive index that is within the common dotted regions shown in **Figure 2.4.1 (a)** and **Figure 2.4.1 (b)** on the Au substrate. We choose one possible index value (n+ik = 3.2+i0.5) within the overlapped dotted regions to confirm the existence of the resonance with angle robustness.

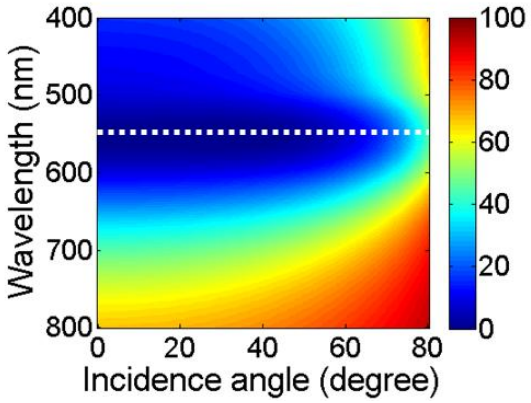

Figure 2.4.2 Calculated angle resolved reflection spectrum of the nanocavity that is composed of the 20 nm thick layer (n+ik = 3.2+i0.5) on top of the Au substrate.

The calculated angle resolved reflection spectrum of the optical cavity comprising 20 nm thickness of the material with the refractive index of 3.2+i0.5 on the Au substrate is depicted in **Figure 2.4.2**. It is clear that the resonance corresponding to blue color (i.e., optical absorption peak) is almost fixed with respect to the angle of incidence up to 80 degrees, thus proving the presence of the resonance with angle-insensitivity.

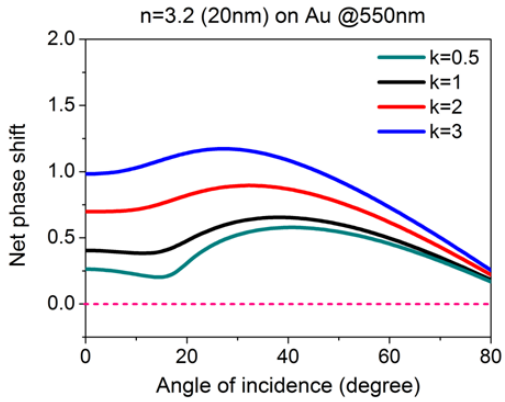

Figure 2.4.3 Calculated net phase shift, which involves the two reflection phase shift and the propagation phase shift, of the structure consisting of 20 nm thickness of 3.2+i*k* on the Au substrate at 550 nm.

In **Figure 2.4.3**, the calculated net phase shift of the device structure that consists of 20 nm thickness of 3.2+i*k* atop the Au substrate at 550 nm is demonstrated. As we already observed in **Figure 2.4.1**, the phase cancellation is better when the imaginary part of the arbitrary medium is less than 1, implying more improved angle insensitive performance. The similar study is done with the different device geometry comprising 20 nm thick arbitrary medium on top of the Al substrate at 550 nm.

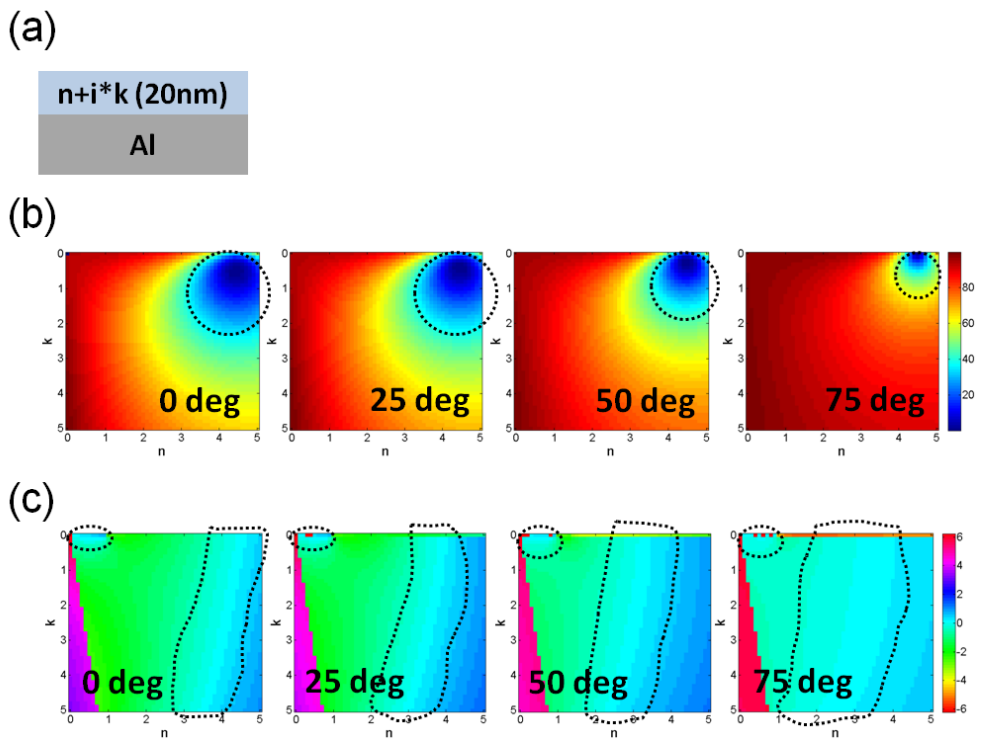

Figure 2.4.4 (a) A schematic representation of the 20 nm thick arbitrary layer atop the Al substrate. (b) Calculated contour plots of the reflection as a function of a complex refractive index (real (*n*) and imaginary (*k*) parts) of the 20 nm of an arbitrary medium on the thick Al substrate at 550 nm at the angle of incidence ranging from normal (0 degree) to 75 degrees. The blue color denotes the low reflections whereas the red color signifies the high reflections in the colormap. (c) Calculated sum of the net phase shift, including propagation phase shift and the two reflection phase shifts, of the structure shown in (a) at the incident angles from normal (0 degree) to 75 degrees. The cyan color denotes that the sum of the total phase shift is zero.

Figure 2.4.4 (a) depicts the schematic diagram of the 20 nm thick arbitrary medium on the Al substrate. The calculated contour plots of the reflection as a function of a complex refractive index (real (*n*) and imaginary (*k*) parts) of the 20 nm of an arbitrary medium on the thick Al substrate at 550 nm at the angle of incidence ranging from normal (0 degree) to 75 degrees are demonstrated in **Figure 2.4.4 (b)**. The blue color signifies the low reflections while the red color represents the high reflections in the colormap. The black dotted circle represents the area where the strong resonance behavior at 550 nm could be formed if we choose the material that has the

refractive index roughly within the circle when the arbitrary layer thickness is 20 nm on the Al substrate. According to the calculation, it would be possible to have the material with the refractive index of $3.5 < n < 4.5$, $0 < k < 2$ on the Al substrate to form the resonance at 550 nm. **Figure 2.4.4 (c)** describes the calculated sum of the net phase shift, which involves the propagation phase shift and the two reflection phase shifts, of the structure exhibited in **Figure 2.4.4 (a)** at the incident angles from normal (0 degree) to 75 degrees. The cyan color represents that the sum of the total phase shift is equal to the zero, which is marked by the black dotted lines. When these cyan colored areas (i.e., sum of the net phase shift is zero) at normal incidence have common regions to those at the oblique angles of incidence, the change in the sum of the net phase shift with respect to the angle of incidence is nearly insignificant, thus implying the angle robust property. Therefore, we will have the strong resonance behavior with the angle invariant characteristics at 550 nm when the 20 nm thick arbitrary medium has the refractive index that is within the common dotted regions shown in **Figure 2.4.4 (b)** and **Figure 2.4.4 (c)** on the Al substrate. We select one possible index value (n+ik = 4.5+i0.5) within the overlapped dotted areas to verify there appears the angle-insensitive resonance.

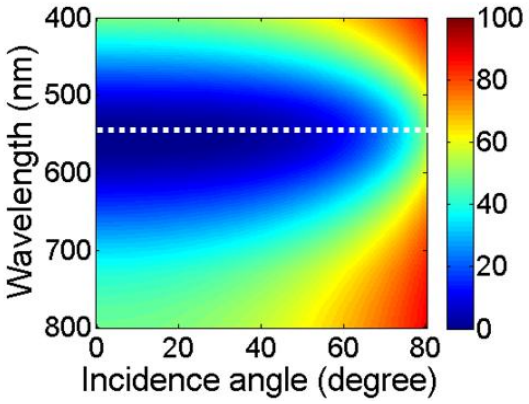

Figure 2.4.5 Calculated angle resolved reflection spectrum of the cavity comprising the 20 nm thick layer (n+ik = 4.5+i0.5) on the Al substrate.

The calculated angle resolved reflection spectrum of the nanocavity that consists of 20 nm thick layer with the refractive index of 4.5+i0.5 on the Al substrate is presented in **Figure 2.4.5**. It is apparent to see that the resonance corresponding to blue color (i.e., optical absorption peak) is nearly invariant with respect to the angle of incidence up to 80 degrees, therefore validating the existence of the angle robust resonance.

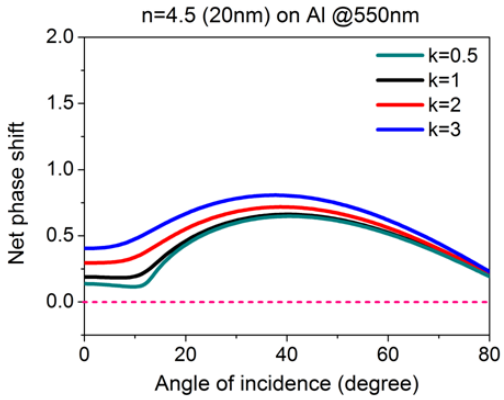

Figure 2.4.6 Calculated total phase shift, containing the two reflection phase shift and the propagation phase shift, of the structure consisting of 20 nm thickness of 4.5+i*k* on the Al substrate at 550 nm.

Figure 2.4.6 illustrates the calculated total phase shift of the device structure consisting of 20 nm thickness of 4.5+i*k* on the Al substrate at 550 nm. As we already studied in **Figure 2.4.4**, the phase cancellation could happen when the *k* value is less than 2.

Now, we will explore the phase cancellation effect in the three media saying that the cavity consists of the two Au layers are separated by the 20 nm thick arbitrary medium.

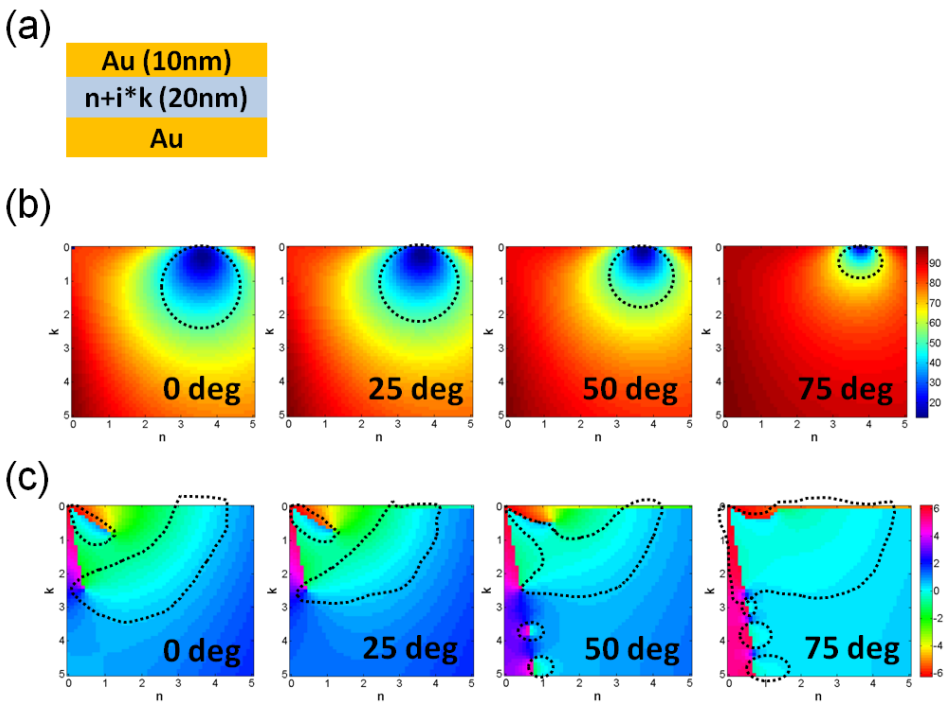

Figure 2.4.7 (a) A schematic representation of the 20 nm thick arbitrary layer sandwiched by the top thin (10 nm) and bottom thick Au film. (b) Calculated contour plots of the reflection as a function of a complex refractive index (real (*n*) and imaginary (*k*) parts) of the structure shown in (a) at 550 nm at the angle of incidence ranging from normal (0 degree) to 75 degrees. The blue color denotes the low reflections whereas the red color signifies the high reflections in the colormap. (c) Calculated sum of the total phase shift, encompassing propagation phase shift and the two reflection phase shifts, of the structure shown in (a) at the incident angles from normal (0 degree) to 75 degrees. The cyan color denotes that the sum of the total phase shift is zero.

Figure 2.4.7 (a) describes the schematic view of the 20 nm thick arbitrary medium sandwiched by the two Au layers. The top Au layer thickness is 10 nm so that the incident light can pass through the structure. The calculated contour plots of the reflection as a function of a complex refractive index (real (*n*) and imaginary (*k*) parts) of the 20 nm of an arbitrary medium sandwiched by the two Au layer at 550 nm at the angle of incidence ranging from normal (0 degree) to 75 degrees are shown in **Figure 2.4.7 (b)**. The black dotted circle represents the area where the resonance at 550 nm could be created if we select the material that has the refractive index within the circle when the arbitrary layer thickness is 20 nm between the two Au films.

According to the calculation, it would be possible to create the resonance at 550 nm when the two Au layers are separated by the material with the refractive index of $3 < n < 4$, $0 < k < 1.5$. **Figure 2.4.7 (c)** describes the calculated sum of the total phase shift, embracing the propagation phase shift and the two reflection phase shifts, of the structure presented in **Figure 2.4.7 (a)** at the incident angles from normal (0 degree) to 75 degrees. The cyan color indicates that the sum of the total phase shift is zero, which is denoted by the black dotted lines. When these cyan colored areas (i.e., sum of the net phase shift is zero) at normal incidence have common regions to those at the oblique angles of incidence, the change in the sum of the net phase shift with respect to the incident angle is nearly trivial. Thus, the strong resonance effect with high angular tolerant characteristics at 550 nm could be achieved when the 20 nm thick arbitrary medium has the refractive index that is within the common dotted regions shown in **Figure 2.4.7 (b)** and **Figure 2.4.7 (c)** between the two Au films.

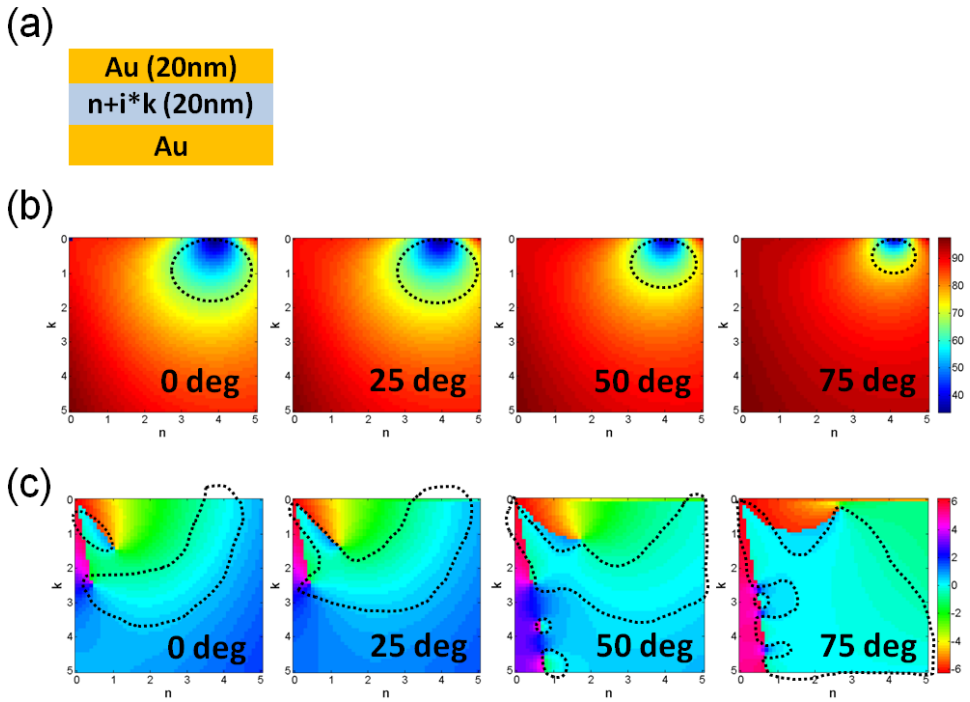

Figure 2.4.8 (a) A schematic representation of the 20 nm thick arbitrary layer sandwiched by the top thin (20 nm) and bottom thick Au film. (b) Calculated contour plots of the reflection as a

function of a complex refractive index (real (n) and imaginary (k) parts) of the structure shown in (a) at 550 nm at the angle of incidence ranging from normal (0 degree) to 75 degrees. The blue color denotes the low reflections whereas the red color signifies the high reflections in the colormap. (c) Calculated sum of the total phase shift, including propagation phase shift and the two reflection phase shifts, of the structure shown in (a) at the incident angles from normal (0 degree) to 75 degrees. The cyan color denotes that the sum of the total phase shift is zero.

The same study is done with 20 nm thickness of the top Au layer as shown in **Figure 2.4.8**. From the calculation, the resonance at 550 nm could be attained when the two Au layers are separated by the material with the refractive index of $3.5 < n < 4.5$, $0 < k < 2$.

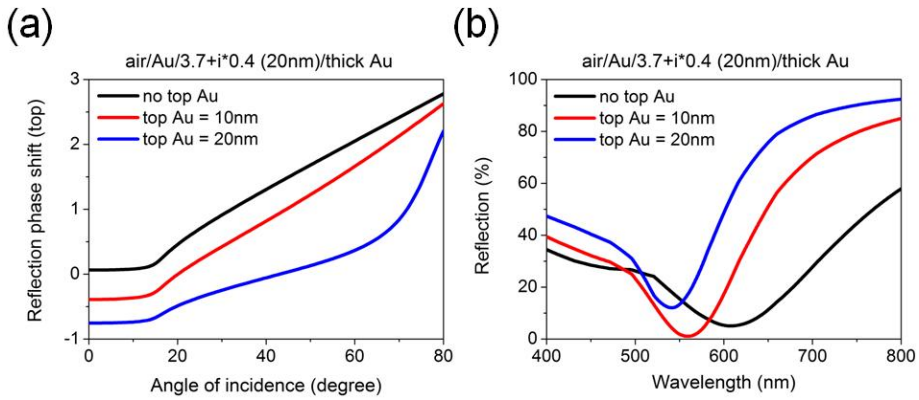

Figure 2.4.9 (a) Calculated reflection phase shifts at the top interface between the material with 3.7+i0.4 and air or optically thin Au layer. (b) Calculated spectral reflectance curves of the structure with (red: 10 nm, blue: 20 nm) and without (black) the top Au layer.

As the last section of this chapter, we investigate the influence of the top metallic layer on the phase cancellation of the cavity. **Figure 2.4.9 (a)** shows the calculated phase shift occurring upon the reflection at the interface between the material that has 3.7+i0.4 and air or thin Au top mirror. Increasing the thickness of the top Au layer leads to the lower reflection phase shift as compared to what has been attained without the top Au mirror. This reduced reflection phase shift allows the resonance wavelength to be shifted toward the shorter wavelength range as can be seen from **Figure 2.4.9 (b)**. We note that the spectrum gets sharp as the thickness of the top

Au mirror increases, which is attributed to the increased reflection at the top interface, thus improving the Q-factor of the cavity.

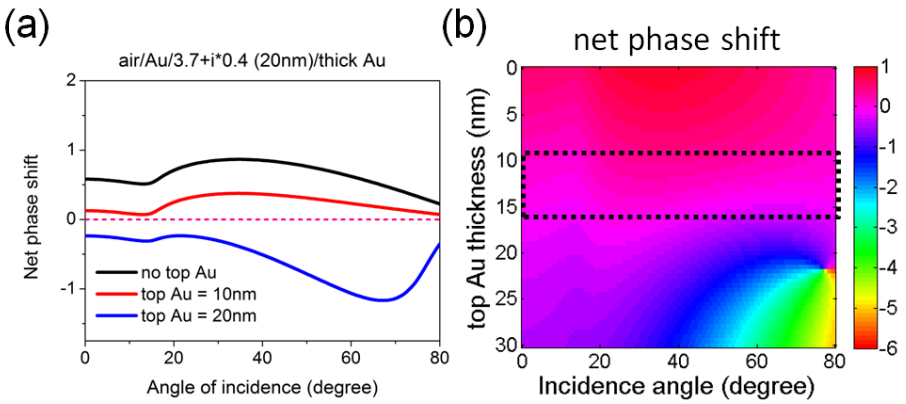

Figure 2.4.10 (a) Calculated sum of the net phase shift of the structure studied in Figure 2.4.9. (b) Calculated contour plot of the total phase shift as a function of the angle of incidence and the top Au thickness. The magenta color represents the zero total phase shift (i.e., phase cancellation).

Figure 2.4.10 (a) depicts the calculated sum of the net phase shift of the structure consisting of the 20 nm thickness medium with 3.7+i0.4 sandwiched by the two Au layers. As is seen from the figure, the structure with the 10 nm thick top Au mirror shows almost perfect phase cancellation as compared to others. With a proper thickness of the top metallic layer, we could enhance both the sharpness of the resonance and the phase cancellation required for achieving angle-insensitive property. It could be also observed in the dotted area in **Figure 2.4.10 (b).** From the calculation, it turns out that the thickness of the top Au layer would be from 10 nm to 15 nm in order to attain a great net phase cancellation, thus being able to accomplish high angular tolerant performance.

In the following chapters, we will propose and experimentally demonstrate photonic and photovoltaic devices exploiting what we have discussed so far.

Chapter 3

Ultra-Thin Highly Absorbing Medium-Based Angle Invariant Structural Color Filters

3.1 Introduction

Color filters have been regarded as crucial elements for a wide variety of applications such as complementary metal-oxide-semiconductor (CMOS) image sensors, light emitting devices, optical measurement systems, and liquid crystal display (LCD) technologies. Traditional color filters that are based on colorant pigments, however, are highly vulnerable to incessant ultraviolet light illuminations, heats, and moistures, thus causing degraded performance over time [8]. In order to address the aforementioned challenges, many researchers have put a lot of effort into developing structural color filters as attractive alternatives owing to their slim dimension, reliability, and better efficiency. Various approaches have been proposed by employing subwavelength grating-based photonic and plasmonic nanostructures [9-17]. However, the capability of filtering incident light wave for any direction is highly challenging to realize as the subwavelength gratings that provide the extra momentum is required in order to couple the incident light into a guided-mode resonance or surface plasmon resonance mode. Therefore, there is still a pressing need to improve the angle dependent property to be applied to practical applications.

In order to resolve this problem, metallic nanocavity-based angle-insensitive structural color filters have been proposed and experimentally demonstrated [18]. This work relies on funneling effects that lead the incident light wave to deep subwavelength grooves, giving rise to a strong absorption characteristic at a certain wavelength. However a series of complex fabrication processes such as patternings and etchings is needed, making it difficult to attain such structures over a large area for numerous applications. Hence, it is still necessary to make structural colors that have a simple geometry.

As introduced in a chapter 2, nanometer-thick optical coatings employing strong resonance effects in a highly absorbing medium on a metallic substrate have been demonstrated. The strong absorption property of the highly absorbing layer and the non-trivial reflection phase shift (i.e., not 0 or π) occurring at the highly absorbing material and metal interface are responsible for creating the resonance in such an ultra-thin cavity. In their report, germanium (Ge) and gold (Au) are used as the highly absorbing material and metal, respectively. Considering that there is the interband transition of Au at 470 nm and strong absorption of Ge (band gap: 0.66 eV) across entire visible wavelengths that can give rise to poor Q-factor resonance, these material selections particularly for color generations are not desired [19,20]. This is because a spectral response of devices has too broad profile, suggesting low color purity that needs to be addressed.

In this chapter, we will propose and experimentally demonstrate structural color filters producing either distinctive reflective or transmissive colors with high angular tolerance based on strong resonance effects in highly absorbing medium-based optical nanocavity [21-24].

3.2 Structural Colors for Reflective Color Generation

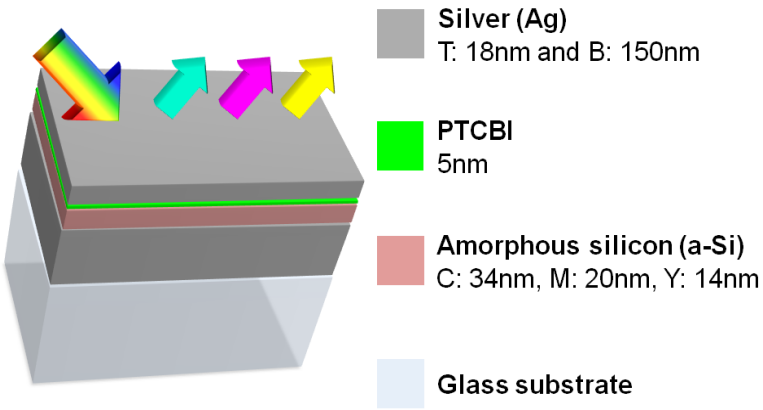

Figure 3.2.1 A schematic diagram of proposed angle invariant CMY color filters

A schematic representation of the proposed structure, which is composed of a lossy medium sandwiched by two metal layers on a glass substrate, is shown in **Figure 3.2.1**. Since an optical absorption of the material, which is expressed by **Equation 3.2.1**, is directly proportional to both real and imaginary parts of the refractive index of the material, amorphous silicon (a-Si) that has lower complex refractive index than Ge is selected as the highly absorbing medium as depicted in **Figure 3.2.2** [25].

$$\text{Absorption} = \frac{2\pi c \varepsilon_0 nk}{\lambda} \left| E(x,\lambda) \right|^2 \tag{3.2.1}$$

where c: speed of light, ε_0 : permittivity of free space, n: real part of the refractive index, $k = \frac{\lambda\alpha}{4\pi}$: extinction coefficient, α : absorption coefficient.

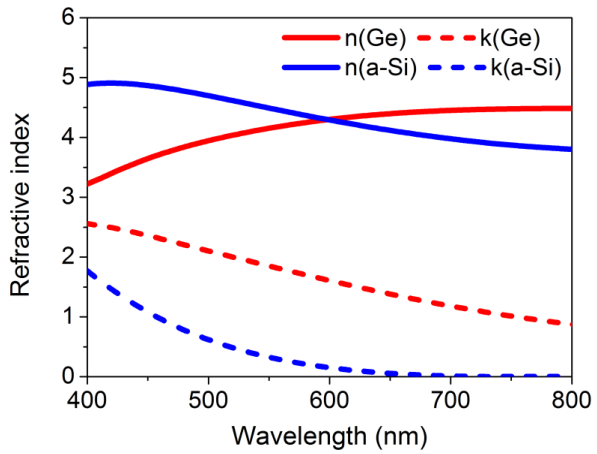

Figure 3.2.2 Complex refractive indices of Ge (red) and a-Si (blue) materials measured by a spectroscopic ellipsometer (M-2000, J. A. Woollam).

This relatively low material absorption loss leads to enhanced Q-factor resonance and keep the strong resonance behaviors in the ultra-thin cavity thickness regime at the same time. For both top and bottom metallic films, silver (Ag) is used because it has the lowest absorption and highest reflection at visible frequencies. It should be noted that an optically thin Ag layer (~18 nm) is added atop the whole structure to increase the reflection at the top interface between a-Si and Ag. This increased reflection enables the resonance to be sharp so that the color purity can be enhanced further. The optically thin top Ag layer enables the incident light wave to go through the whole structure while the optically thick bottom Ag film (~150 nm) is utilized in order to block the transmitted light. We also note that there is a trade-off between the spectral bandwidth and the reflection efficiency. The bandwidth of the resonance gets narrow that can result in enhanced chromaticity with the lower reflection efficiency as the top Ag mirror thickness increases. A-Si was deposited by plasma-enhanced chemical vapor deposition (PECVD) and the thermal evaporation was used to deposit Ag.

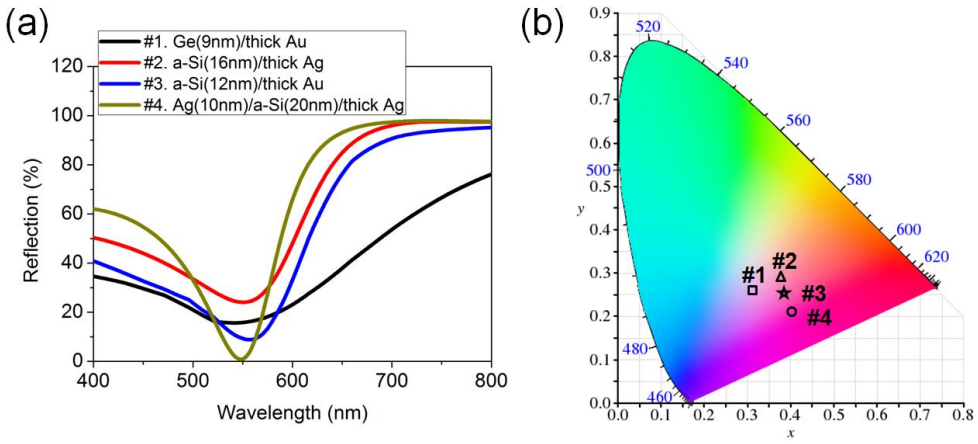

Figure 3.2.3 (a) Simulated reflection spectra of four cavities with different combination of the lossy medium on the metallic substrate for the magenta color. (b) The representation of the color coordinates described on the CIE 1931 chromaticity diagram.

In order to explore how the color purity gets improved by the two strategies described above (i.e., 1. selecting low absorbing medium & 2. putting additional thin metal layer), a numerical simulation is carried out on the structure comprising different lossy medium (i.e., either Ge or a-Si) on different metallic substrates (i.e., either Au or Ag) to calculated each spectral reflectance as exhibited in **Figure 3.2.3 (a)**. As explained earlier, the reflection spectrum of #1 device consisting of Ge (9 nm) on top of the Au substrate has the most broad reflection profile, which is primarily attributed to Ge's strong absorption at visible frequencies. When Ge on Au is replaced by a-Si on Ag (#2), a narrow bandwidth of the reflection spectrum is attained and the corresponding color coordinates move toward the magenta region. The chromaticity of the magenta color generated by a-Si on Au (#3) is fairly similar to that of previous structure (#2) as 550 nm (i.e. reflection valley) is distant from the interband transition of Au that leads to much reduced optical absorption of Au at the resonance. Placing additional thin Ag film on top of the structure (#4) allows the color to be more distinctive, which can be confirmed by the fact that the color coordinates go to the border of the diagram indicating remarkably improved chromaticity as compared to the case of #1. The corresponding investigations for both the yellow and cyan

colors, which show a similar trend with what has been observed in the magenta color study, are described in **Figure 3.2.4**. A full width at half maximum (FWHM) and the corresponding Q-factor of each colored samples are summarized in **Table 3.2.1**. It is clear that the Ag/a-Si/Ag cavity system shows much narrower FWHM and therefore higher Q-factor than Ge/Au geometry for all CMY colors, thus validating enhanced color purity.

Table 3.2.1 Summary of the FWHM and Q-factor of the CMY color filter devices.

Geometry	Yellow	Magenta	Cyan
	FWHM (Q-factor)	FWHM (Q-factor)	FWHM (Q-factor)
Ge/Au	262nm (1.79)	259nm (2.12)	308nm (1.98)
Ag/a-Si/Ag	153nm (3.07)	102nm (5.39)	64nm (9.53)

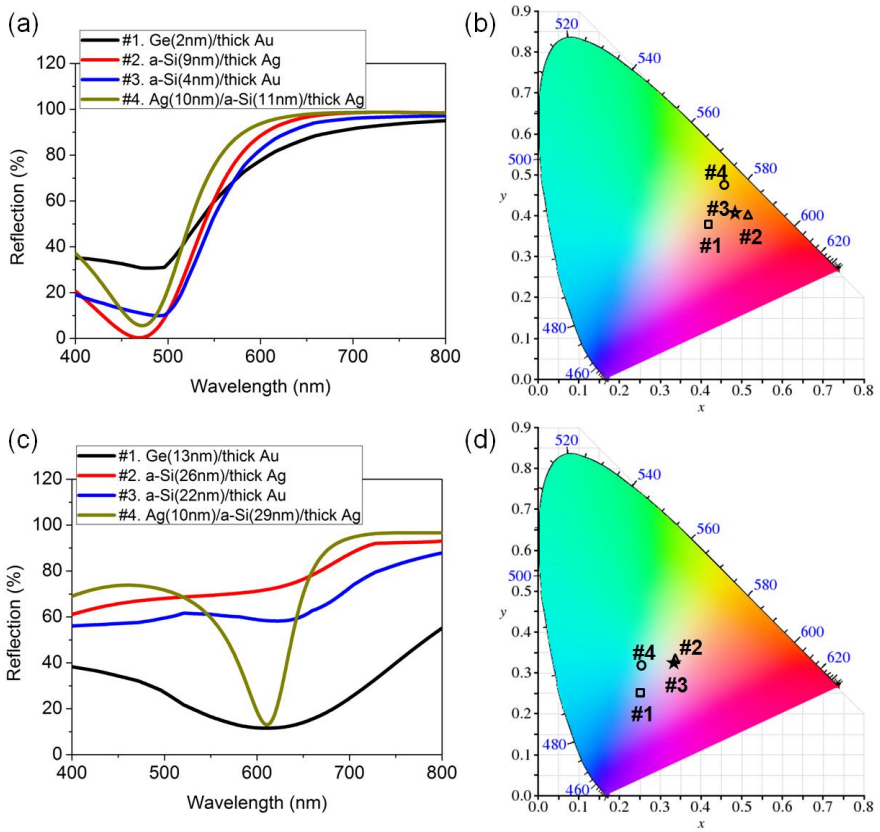

Figure 3.2.4 (a) & (c) Simulated reflection spectra of four cavities with different combination of the lossy medium on the metallic substrate for the yellow and cyan colors, respectively. (b) & (d) The color coordinate representations corresponding to (a) and (c), respectively.

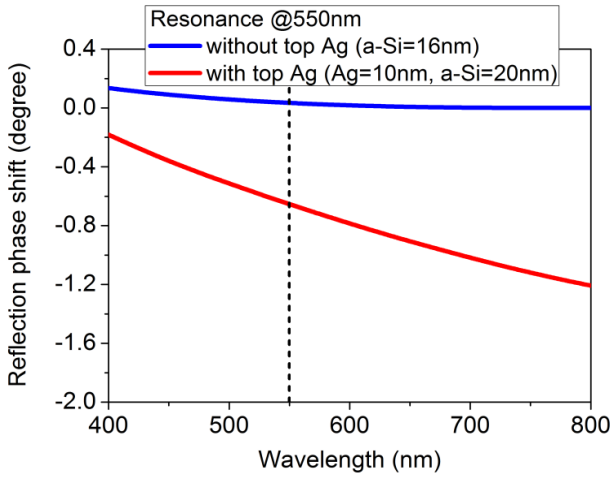

Figure 3.2.5 Calculated phase shifts occurring upon the reflection from the top interface without top Ag (i.e., air/a-Si) and with top Ag layer (i.e., Ag/a-Si).

The resonance exists when the sum of the two reflection phase shifts and propagation phase shift equals to $2m\pi$. It is noted that the different a-Si thickness is used for #2 (16 nm) and #4 (20 nm) to create the resonance at the same position in **Figure 3.2.3 (a)**, which is due to the fact that the reflection phase shift at the air/a-Si interface is greater than that of Ag/a-Si interface as shown in the **Figure 3.2.5**. This implies that it is necessary for the structure with the top Ag mirror to have the thicker a-Si layer to obtain the same resonance (i.e., 550 nm).

Next, we discuss the function of an organic material underneath the top Ag mirror before showing optical property results of the CMY color filters. Regarding an optical characteristic, the light scattering can be induced by the rough surface, which gives rise to a broad spectral response of transmittance and reflectance. Such broad profile is not desired in particular for color filter applications. In addition, for an electrical performance, the non-even metal surface leads to the high sheet resistance (i.e., poor electrical conductivity) so that it is hard to be used as an electrode. It is thus important to characterize a surface morphology of the thin Ag layer. It was

reported that a fairly smooth surface of the thin Ag film is achieved when depositing Ag on top of the Ge nucleation layer, which is because the surface diffusion and mass transportation of Ag can be diminished by the Ge wettability. Since the Ge material is highly transparent in infrared (IR) wavelengths beyond > 2 μm, it has been widely utilized for various IR applications, including metamaterials with the combination of Ag and Ge. But, due to the band gap of Ge (0.66 eV corresponding to 2 μm), the optical absorption of the Ge material is pretty significant throughout whole visible frequencies. Hence, there is a crucial necessity to provide smooth surface of the thin Ag layer without a significant material absorption loss.

As is seen in the schematic diagram of the proposed angle invariant structural color filters (See **Figure 3.2.1**), we employ perylenetetracarboxylic bis-benzimidazole (PTCBI), which is typically used as a hole blocking layer in organic solar cells, to make the surface of the thin Ag film smooth, thus minimizing the light scattering. In order to prove an effect of the PTCBI on the surface morphology of the thin Ag film, atomic force microscope (AFM) measurements on the surface of the thin Ag film (~10 nm) deposited on PTCBI, Ge, and silicon substrates are performed. As shown in **Figure 3.2.6**, it is apparent that the surface roughness of the thin Ag film on both Ge and PTCBI substrates is almost negligible as compared to the Ag film surface on the silicon substrate. 10 nm Ag on the silicon substrate shows 8.40 nm of an average root-mean-square (RMS) value. On the contrary, the thin Ag layers on 2 nm PTCBI and 2 nm Ge exhibit 0.213 nm and 0.235 nm of RMS values, respectively, suggesting that the light scattering loss is markedly reduced.

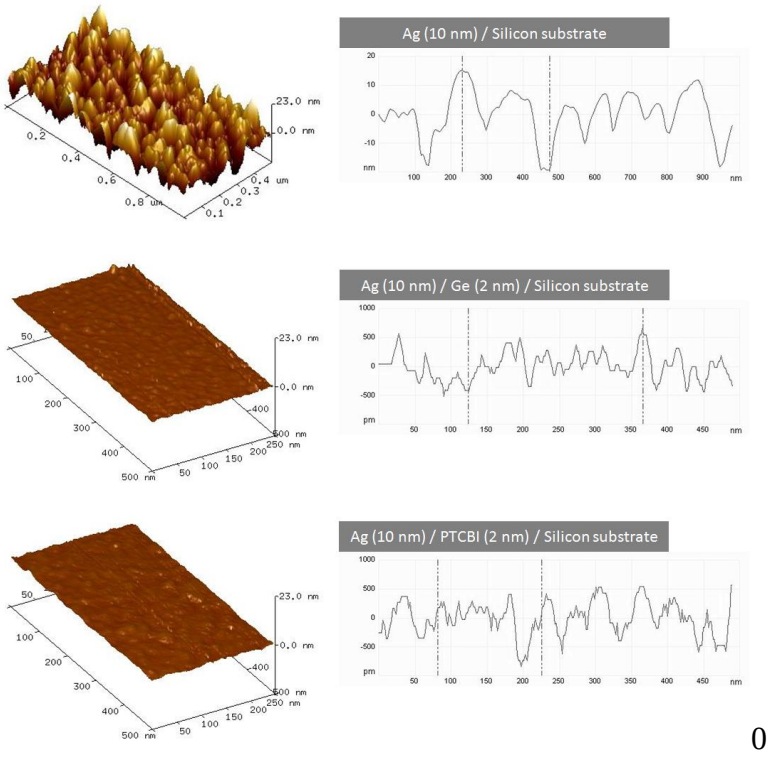

0

Figure 3.2.6 Atomic force microscope (AFM) images of 10 nm of Ag layer on Si, Ge, and PTCBI substrates.

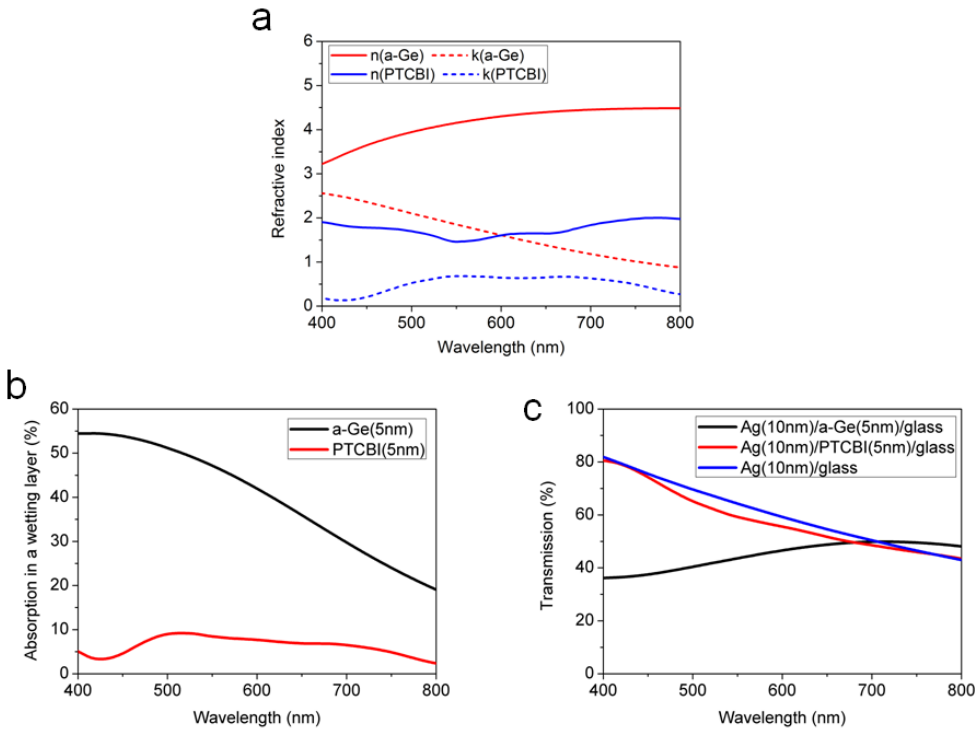

Figure 3.2.7 (a) Refractive indices of PTCBI and a-Ge measured by a spectroscopic ellipsometer (M-2000, J. A. Woollam). (b) Simulated absorption spectrum in wetting layers with the same thickness. (c) Simulated transmission spectrum of 10 nm Ag film on wetting layers.

Another important property of the PTCBI wetting layer is much lower visible absorption than the optical absorption of Ge material. As discussed in a previous section (See **Equation 3.2.1**), the optical light absorption is directly proportional to the real (*n*) and imaginary parts (*k*) of refractive index of the material, implying that the high refractive index material experiences the large optical absorption loss. The refractive indices of PTCBI and Ge are measured by a spectroscopic ellipsometer (M-2000, J. A. Woollam) as depicted in **Figure 3.2.7 (a)**. As can be seen from the figure, the *n* and *k* values of PTCBI layer are much smaller than those of Ge, which indicates much lower optical light absorption of PTCBI. The calculated light absorption spectra of 5 nm Ge and PTCBI are plotted in **Figure 3.2.7 (b)**, demonstrating that Ge material shows much higher optical absorption than PTCBI across whole visible wavelengths. Moreover, **Figure 3.2.7 (c)** describes the transmission spectra of 10 nm Ag on 5 nm Ge and PTCBI on glass substrates, showing that Ag/PTCBI has higher transmittances between 400 and 700 nm. From this study, it is found that the PTCBI has a great potential for producing very smooth surface of the thin Ag film at visible frequencies.

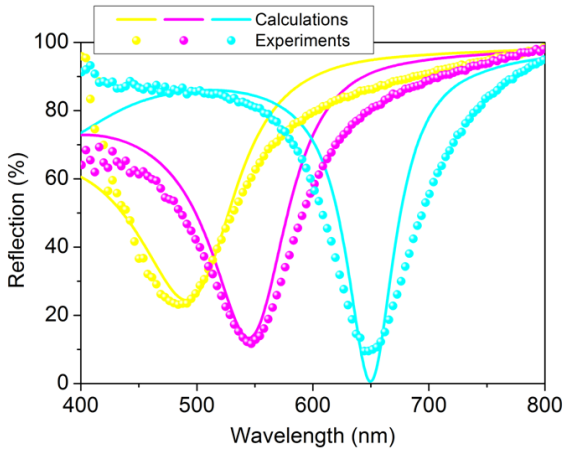

Figure 3.2.8 Simulated and measured spectral reflectance curves at normal incidence.

The thicknesses of the a-Si layer for producing CMY colors are found to be 34, 20, and 14 nm and the corresponding resonances (i.e. reflection dip or absorption peak) are 650, 545, and 490 nm, respectively. The simulated reflection spectra (solid lines) at normal incidence calculated by a transfer matrix method are depicted in **Figure 3.2.8** that matches well with the experimental results (solid symbols) measured using a spectrometer (HR4000CG, Ocean Optics). There is a slight difference between the measured and calculated results, which is attributed to the non-even surface of each layer. This results in a scattering loss and hence produces broader profiles. It is obvious that the reflection spectrum of the cyan color shows the narrowest bandwidth among the three colors, exhibiting 74 nm (the corresponding FWHM from the simulation: 58 nm) of FWHM. As there is no transmitted light due to an optically thick metallic substrate, the complementary spectrum of the reflection profile is the absorption spectrum, both of which exhibit the narrowest FWHM from the cyan device. This is because the imaginary part of the refractive index of the a-Si reduces as the wavelength increases, yielding increased Q-factor. On the contrary, the yellow device shows the broadest FWHM that is attributed to the large absorption of a-Si material at shorter wavelengths. Note that the FWHMs of the yellow and magenta colored devices obtained from the experiment (simulation) are 136 nm (122 nm) and 114 nm (98 nm), respectively.

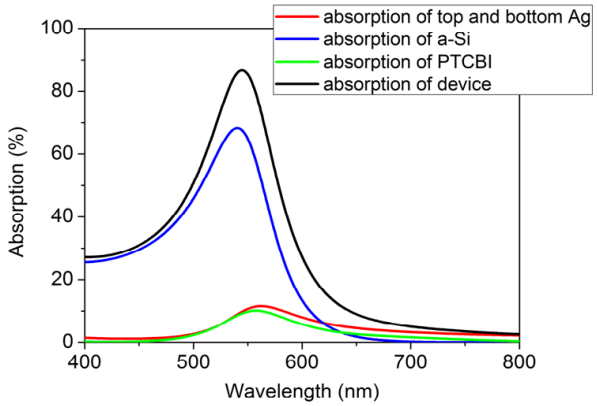

Figure 3.2.9 Simulated optical absorption spectra of a whole device and individual layers.

Figure 3.2.9 shows the calculated optical absorption spectrum of an entire device plotted together with the optical absorption spectra of other rest layers. As is seen from the figure, the large complex refractive index of the a-Si layer leads to the strong optical light absorption as compared to that of the remaining layers. We note that there are the optical absorption peaks for all the layers near the resonance because the incident light can pass through every layer more times than the off-resonance condition, hence leading to higher absorption.

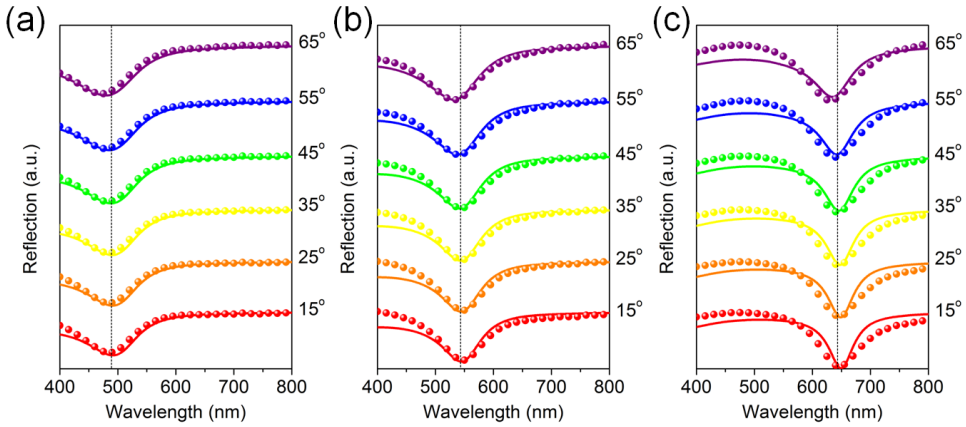

Figure 3.2.10 Simulated and measured angle resolved reflection spectra at an angle of incidence from 15° to 65° for TM polarization for yellow (a), magenta (b), and cyan (c) colors.

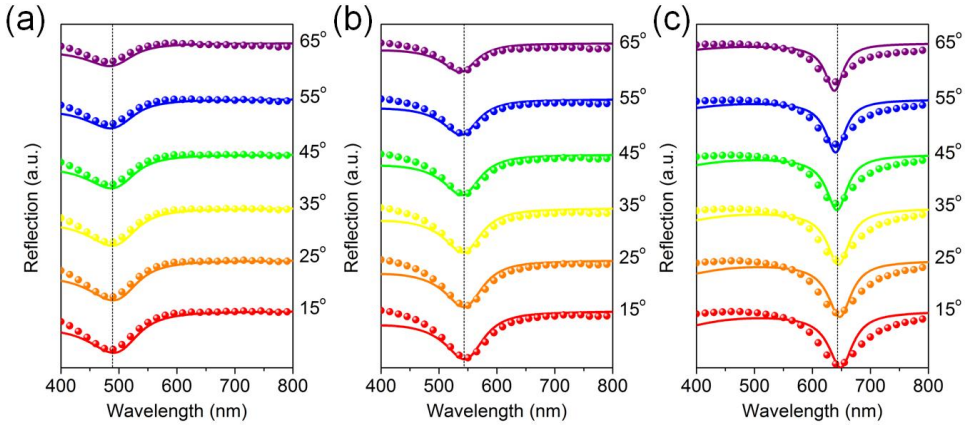

Figure 3.2.11 Simulated and measured angle resolved reflection spectra at an angle of incidence from 15° to 65° for TE polarization for yellow (a), magenta (b), and cyan (c) colors.

To explore the incident angle dependence of such spectrum filters, angle resolved reflection spectra for transverse magnetic (TM) and transverse electric (TE) polarization are simulated by the transfer matrix method (solid lines) and the corresponding measured profiles (solid symbols) are obtained by a variable angle spectroscopic ellipsometer (V-VASE, J. A. Woollam) for incident angles of 15° to 65° as exhibited in **Figure 3.2.10 (a) - (c)** and **Figure 3.2.11 (a) - (c)**, respectively. Calculation results show good agreement with the experiment data. The resonance wavelength remains invariance over a wide range of incident angles for all three colors for both polarizations. It is noted that the position of the resonance is still maintained while the intensity gets reduced at larger angles than 65°.

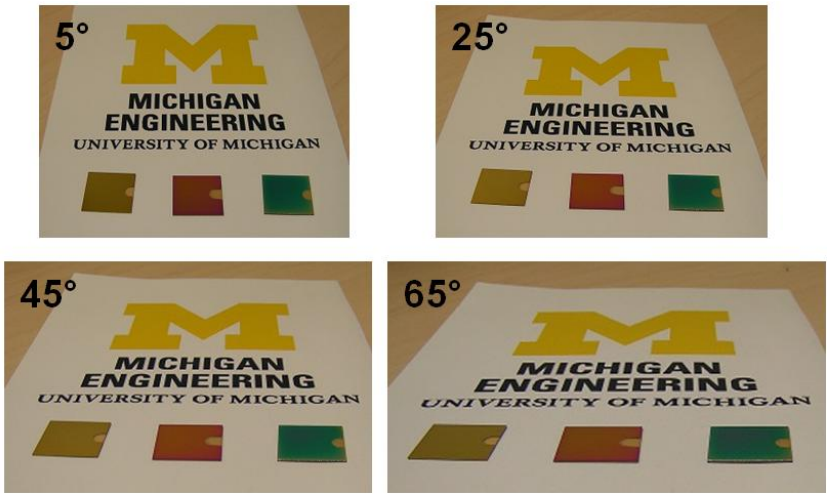

Figure 3.2.12 Photographs of the fabricated color filter devices taken from 5° to 65°. It is obvious that an original color can preserve even at very large angle (65°), confirming the angle invariant characteristic of the proposed filters.

Optical images in **Figure 3.2.12** were taken with an indoor ambient light at four different angles showing no color change. The size of the fabricated spectrum filters is 2 cm x 2 cm. The capability of such angle insensitivity could be potentially useful in light emitting devices, image sensors, and display applications.

Such angle-invariant resonance behavior is in stark contrast to that in a normal F-P resonator, e.g. by sandwiching a transparent medium between two reflecting metal films. Previous studies of structures containing ultra-thin absorbing material on top of a metal have attributed the angle-insensitive behavior to the negligible propagation phase in the ultra-thin dielectric layer. However as is shown by the detailed calculation, even though the propagation phase in an ultra-thin absorbing material is small than of a normal transparent medium, it is non-trivial and show the same angle-dependent behavior. Therefore the ultra-thin absorbing material alone cannot explain the peculiar angle-independence effect.

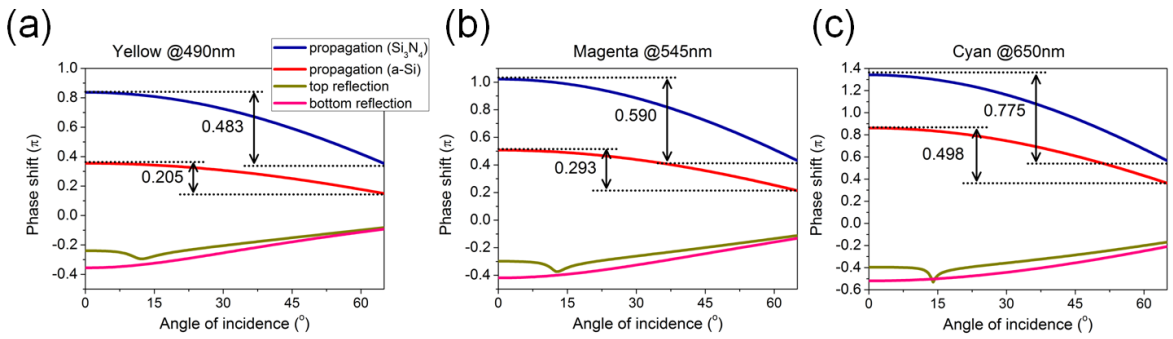

Figure 3.2.13 (a) - (c) Calculated non-trivial reflection phase shifts at both the top and bottom semiconductor and metal interfaces and the accumulated phase shift during the propagation as a function of the angle of incidence for (a) Yellow corresponding to 490 nm. (b) Magenta corresponding to 545 nm. (c) Cyan corresponding to 650 nm. The propagation phase shift attained from an optically transparent cavity (Si_3N_4) is included as a reference.

Figure 3.2.13 (a) - (c) display the angle dependent propagation phase and the phase shift when light reflects from the two metal surfaces. These results are obtained by using the transfer matrix method. As seen in the figures, the phase due to the light propagation in the ultra-thin highly absorbing material is about half of that in an optically transparent material (e.g. Si_3N_4, [n=2 and k=0 at visible frequency]), and decreases with increasing angle. Note that the same metal

thicknesses as in the fabricated structures are used for the reference structure (Ag/ Si_3N_4/Ag) in order to establish the same resonance wavelength, and the thickness of the Si_3N_4 layer is chosen as 109, 83, and 68 nm respectively to create the CMY colors. Note that the thickness of Si_3N_4 is thicker than that of a-Si to obtain the same resonance position. As we explained previously, the strong resonance in the ultra-thin thickness of a-Si layer is enabled by the non-trivial reflection phase shifts. In the case of reference structure where a transparent medium sandwiched by two metal films, the phase shift of light reflecting from the metal surface is close to and with weak angle-dependence. Therefore the F-P cavity containing transparent medium will show the typical angle-dependent resonance shift. In the case of a highly absorbing medium, the phase shift of light reflecting from the metal surface is very different from but non-trivial, and varies with the angle of incidence. But interestingly, the phase change due to propagation in the lossy medium and those due to the reflections from the metal mostly cancels out at all angles, leading to a close-to-zero phase in the resonator!

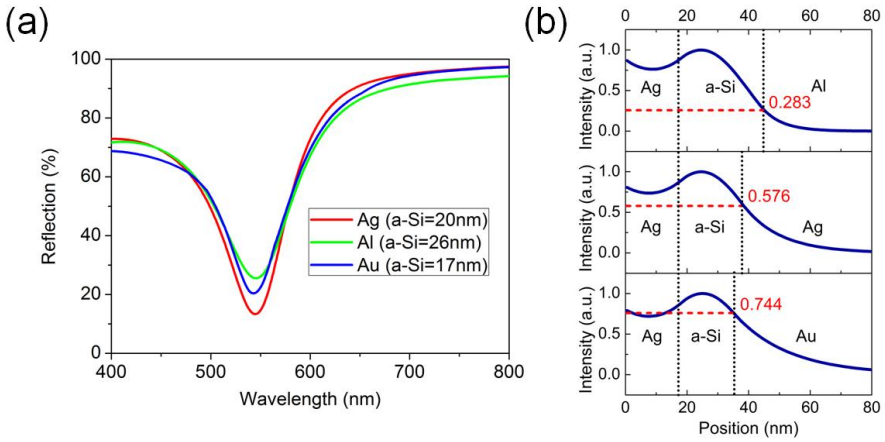

Figure 3.2.14 (a) Simulated reflection spectra at normal incidence obtained from different metallic substrates. (b) The normalized intensity distributions of the electric field at 550 nm for different metallic substrates, showing different penetration depth of the metals.

From physics point of view, the phase shift of light reflecting from a metal is related to the light penetration into the metal at the visible band. In **Figure 3.2.14 (a)**, the calculated reflection spectra from three metallic substrates (Ag, Al, and Au) are displayed. To create a resonance at the same wavelength of 550 nm, it is found that different thickness of a-Si layer is required. This is due to the different skin depth (δ) of these metals. For example, δ for Al and Au are about 13 nm and 31 nm at 620 nm, respectively [26]. δ of Ag has an intermediate value of ~22 nm, between that of Al and Au [27]. Since light can penetrate deeper into Au at this wavelength than those of Al and Ag, the thickness of a-Si layer needed to establish the same resonance condition is correspondingly smaller (17 nm) that that in the case of Al substrate (26 nm). This phenomenon can also be seen by examining the normalized electric field distributions at the resonance (550 nm) for the different metallic substrates as shown in **Figure 3.2.14 (b)**: the amplitude of the electric field entering into the Au is much larger than the Ag and Al, which is due to the longer penetration depth of the Au.

3.3 Structural Colors Creating Transmissive Colors

The previous section of the chapter 3 describes the ultra-thin lossy medium-based angle invariant structural colors generating distinctive reflective CMY colors. However, creating the resonance in transmittance (i.e., RGB transmission colors) is much more desired than producing the optical absorption resonance (i.e., CMY reflection colors) for numerous practical applications. In this section, we will present the RGB transmission color filters utilizing the same principle.

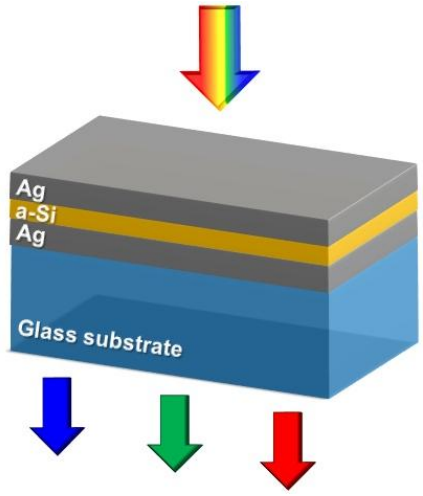

Figure 3.3.1 A representation of the proposed angle invariant transmission visible wavelength filters, comprising a semiconductor layer sandwiched by two thin metal layers on a glass substrate. The transmission color can be altered by varying the thickness of a-Si layer under the white light illumination. To create RGB colors the required a-Si thicknesses are 28, 15, and 9 nm, respectively.

A schematic geometry of the proposed visible wavelength filters is depicted in **Figure 3.3.1**. The structure has simply three layers consisting of a semiconductor material between two optically thin metal layers deposited on a glass substrate. Many semiconductor materials (e.g. a-Si or Ge) absorb the visible wavelength ranges because of the presence of the band gap and hence they can be utilized as a lossy layer for the cavity. The thickness of cavity can be smaller by using Ge as compared to that using a-Si due to the higher optical constant of Ge. However, the cavity with Ge will experience a larger absorption loss that leads to a resonance with low efficiency and broad bandwidth. This is because the absorption loss is proportional to the optical constant of the material as described in **Equation 3.2.1**. As a result, we choose a-Si that can provide a sharper resonance in ultrathin cavity thickness ranges. For the metal, Ag is chosen due to its high reflection and low absorption at visible frequencies. It should be noted that PTCBI is deposited before the Ag film deposition to make the surface of thin Ag layer smooth. This could significantly reduce the light scattering loss induced by the rough surface.

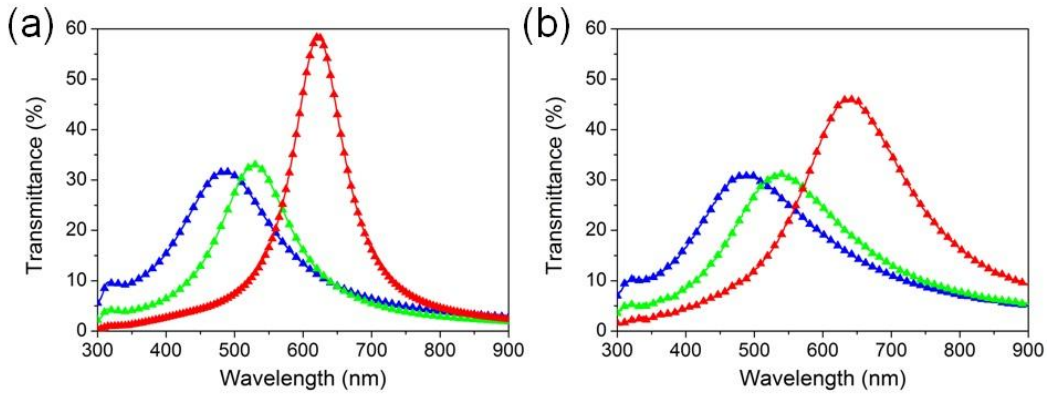

Figure 3.3.2 Simulated and measured transmittances at normal incidence in (a) and (b), respectively.

In **Figure 3.3.2 (a) - (b)**, the simulated and measured transmittances of the proposed visible wavelength filters at normal incident angle from 300 nm to 900 nm are shown, respectively. The simulated transmittance profiles are attained by using a Fourier Modal Method (FMM), which is based on the spatial frequency domain where Maxwell's equations are transformed into the algebraic eigenvalue equations and the electromagnetic field distributions are described by a Bloch eigenmode expansion which is a pseudo-Fourier series. A complete set of eigenmodes for an optical structure spans all possible optical fields within the finite dimensional numerical framework. The material parameters of permittivity and permeability are denoted by a tensor form to be used in FMM simulation [28]. The measured spectra are obtained by a spectrometer (HR4000CG, Ocean Optics). Generally, measured profiles are in fair agreement with the simulation results, but with relatively lower efficiency and broader bandwidth, which are attributed to surface roughness of the actual films. Increasing the thickness of a-Si layer enables the resonance wavelength to occur at the longer wavelength (i.e. red shift) creating red colors. According to this simple design principle, we chose a-Si thickness of 28, 15, and 9 nm to create RGB transmission colors, respectively. The thickness of top and bottom Ag layers is found to be

~18 nm. Note that there is a trade-off between the bandwidth and the transmission efficiency depending on the thickness of the metal layer. A-Si was deposited using PECVD, and Ag and PTCBI were thermally evaporated. The green and blue filters have broader peaks than that of red due to the higher absorption of a-Si at shorter wavelengths that result in lower Q-factors.

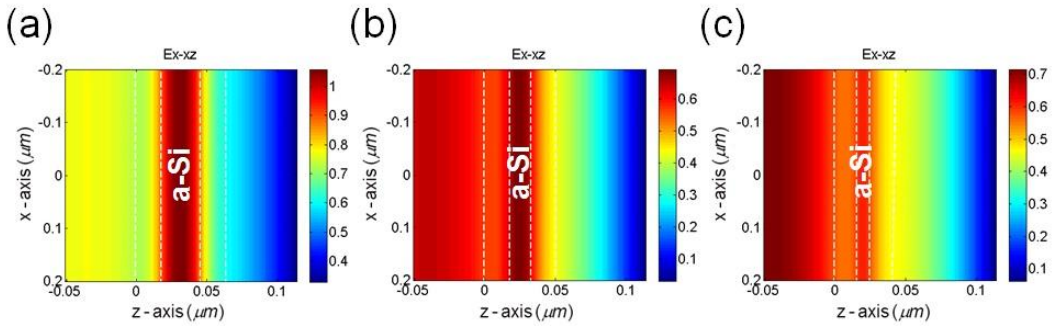

Figure 3.3.3 Electric field distributions at a transmission peak for (a) red (@ 622 nm), (b) green (@ 530 nm), and (c) blue (@485 nm). It is obvious to observe that the electric field intensity in a-Si layer is stronger than that in other layers, indicating the F-P cavity effect in the ultrathin semiconductor layer.

We perform the FMM simulation to examine the resonance effect in the ultrathin cavity layer by plotting the electric field distribution at a resonance for individual RGB colors as illustrated in **Figure 3.3.3 (a) - (c)**. Due to the high optical constant of a-Si material, it is found that the optical field is primarily concentrated in the a-Si layer, exhibiting a strong resonance effect in the ultrathin cavity. As introduced earlier, the resulting strong resonance in the ultrathin cavity is attributed to the large absorption coefficient of the a-Si material and the non-trivial phase change (i.e. not 0 or π) from the reflection at the interface between metal and a-Si. The related phase shifts will be discussed in more detail in the following section.

Figure 3.3.4 Optical photographs of fabricated visible wavelength filter devices on 2 cm x 2 cm glass.

To visually show the RGB colors of our proposed devices, optical photographs of the fabricated RGB samples on 2 cm x 2 cm glass substrate are displayed in **Figure 3.3.4**. It is clear that the background image can be seen through the fabricated filters with distinct colors.

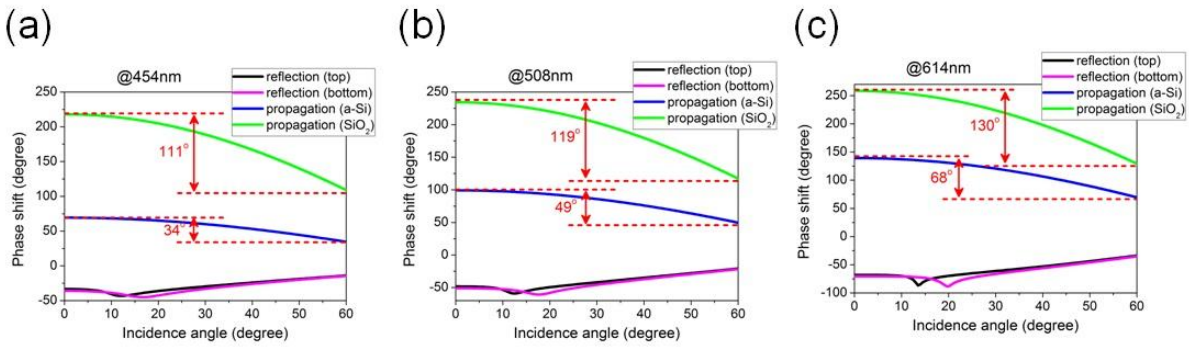

Figure 3.3.5 (a) - (c) The simulated propagation phase change and the non-trivial reflection phase changes at both the top and bottom a-Si and Ag interfaces as a function of the incident angle at the resonance. For the comparison, the propagation phase change obtained from the transparent cavity layer (SiO_2) is described as well.

Next, we investigate the angular dependence of these designed filters. When the light is incident on to the structure at an oblique angle in conventional F-P resonator systems containing low loss or transparent medium (i.e. the real part of the optical constant is much larger than its imaginary part), the optical path length is decreased that results in the blue shift of the resonance. In **Figure 3.3.5 (a) – (c)**, the calculated reflection phase shifts at both the top and bottom a-Si-Ag interfaces

and propagation phase shift in ultrathin a-Si as a function of the angle of incidence at the resonance are shown. The propagation phase change through a transparent medium (in this case, SiO_2 [n=1.45]) is also depicted as a reference. For the geometry of the reference, the thickness of top and bottom Ag layers is 18 nm, and the thicknesses of the SiO_2 to create the same resonance are 152, 114, and 95 nm for RGB, respectively. The corresponding resonances are 614, 508, and 454 nm, respectively. As can be seen in the figure, by using ultrathin absorbing material in our cavity design, the accumulated phase shift during the propagation (blue solid line) is much smaller as compared to the propagation phase change in a traditional F-P cavity using a transparent medium (green solid line). Moreover, there is interesting compensation of propagation phase shift in a-Si and the reflection phase shift from the metal layers with increased incident angle. These two effects combined are responsible for the angle-insensitive transmission colors.

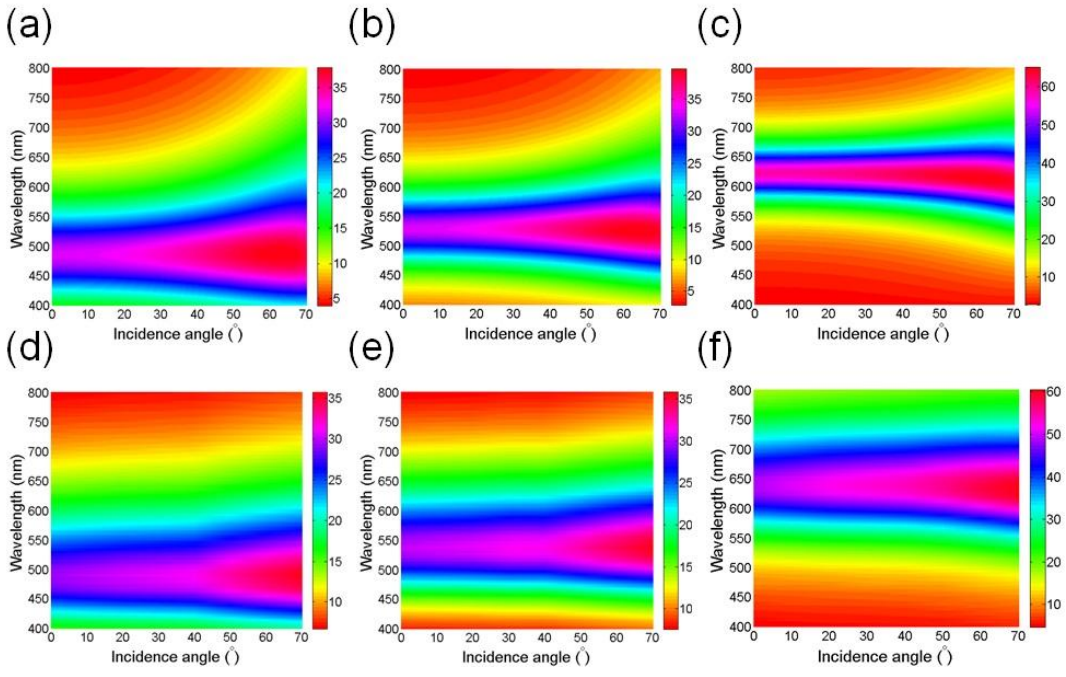

Figure 3.3.6 (a) - (c) The simulated angle resolved transmission spectra of the proposed visible wavelength filters. The incident angle is varying from 0° to 70° under the TM-polarized light illumination. (d) - (f) The measured results corresponding to those in (a) - (c).

In order to prove the angle robustness of our designed filters, the numerical simulation is carried out using a transfer matrix method based on refractive index data for a-Si and Ag obtained by a spectroscopic ellipsometer (M-2000, J. A. Woollam). The measured refractive indices can be found in the supplementary material. **Figure 3.3.6 (a) - (c)** plot the calculated angle resolved transmission spectra for TM polarized incident light. The corresponding experimental angle resolved transmission spectra [**Figure 3.3.6 (d) - (f)**] are measured by the spectrometer from 0° to 70°, showing a close match with the simulation results. From both the simulation and experiment, it is evident that the position of the transmission peak does not change with respect to the incident angle. In addition to this angle insensitive feature that is important for many applications, it is worthwhile to mention that only material deposition process is required to create the RGB colors. This is much simpler than those reported in previous works that rely on either subwavelength nano-grooves or gratings involving more sophisticated fabrication techniques such as nanoscale patterning and etching, thus opening up the possibility of practical applications over large areas.

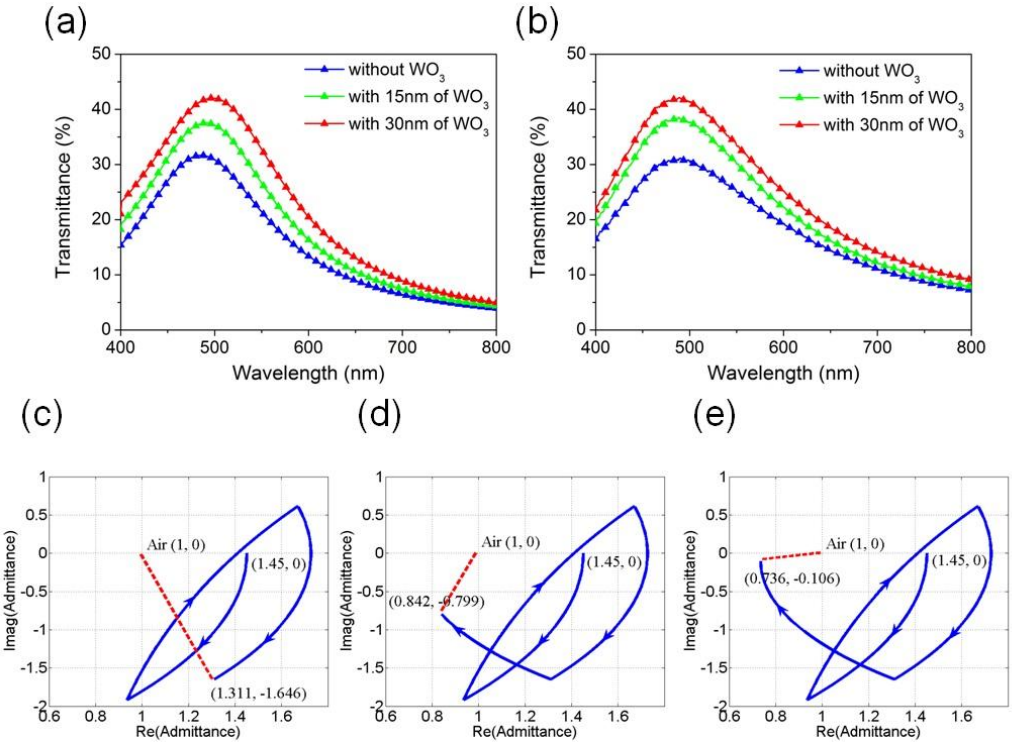

Figure 3.3.7 The simulated and measured optical transmittance spectra of the filter creating the blue color with (green: 15 nm and red: 30 nm) and without (blue) WO_3 layer in (a) and (b), respectively. The admittance diagrams (c) without a top WO_3, (d) with 15 nm of WO_3, and (e) with 30 nm of WO_3 layer. The starting point of all the cases is the same (1.45, 0), whereas the ending point of the device with 30 nm top WO_3 is quite close to the point of air (1, 0), implying that the reflection is highly suppressed by anti-reflection coating.

As a final part of this study, we explore the benefit of adding a transparent anti-reflection coating to increase the transmission efficiency of the filters. Tungsten trioxide (WO_3) with 15 and 30 nm thicknesses is used as the dielectric coating. The devices with 15 and 30 nm WO_3 show the higher optical transmittance than the device without WO_3 layer in both simulation and measurement [**Figure 3.3.7 (a) and (b)**]. This can be attributed to the reduced reflection at the air-WO_3 interface arising from the small contrast between the optical constants of air and WO_3 as compared to the contrast between air and Ag. This can be further confirmed by using an admittance diagram (i.e. the inverse of impedance) as described in **Figure 3.3.7 (c) - (e)** [29]. The admittance of the entire structure starts from the glass substrate (1.45, 0) and its trajectory is

rotated depending on the both the thickness and the optical constant of the material. Minimizing the difference between the overall admittance (i.e. termination point of the stack) and that of the air (1, 0) where light is incident from allows the reflection to be suppressed. From the device without a top WO_3 layer, the admittance terminates at the point of (1.311, -1.646) that is quite far from the point of air, leading to a fairly strong reflection (~35%). The reflectivity can be calculated using the following expression.

$$R = \left(\frac{1-(x+iy)}{1+(x+iy)} \right)^2 \tag{3.3.1}$$

where x and y are the real and imaginary parts of the final admittance. The admittance obtained from the device with 15 nm of WO_3 layer terminates at (0.842, -0.799) that is closer to the (1, 0) than previous case but still produces the high reflection (~17%). In contrast to these, the ending point of the admittance from the device with 30 nm top WO_3 layer is (0.736, -0.106) that is much closer to the air (1, 0) than previous two cases, resulting in the suppressed reflection (~2%). By this analysis we note that the total transmission efficiency can be further improved by introducing another appropriate dielectric layer on the substrate before the Ag layer deposition.

3.4 Patterned Structural Colors Via One-Step Fabrication

Even though a highly desired angle insensitive performance is achieved, the thickness of the semiconductor layer needs to be varied in order to tune the colors. This is not a good approach when patterning individual CMY or RGB colors by pixel unit since it requires three separate lithographic processes. To address this challenge, here we will present wide-angle subwavelength grating patterned CMY and RGB color filters. Altering the width of the

subwavelength grating enables the resonance to be shifted (i.e., color can be tuned) so that all the individual CMY or RGB color pixels can be made by one patterning process [30].

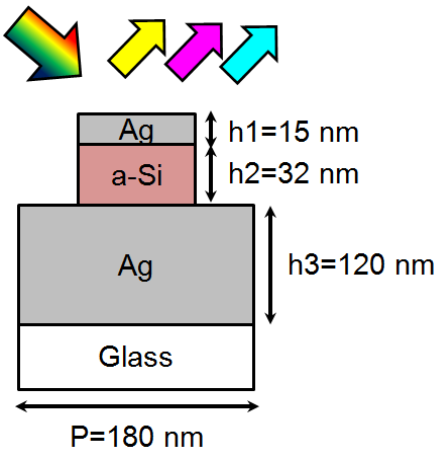

Figure 3.4.1 A schematic view of the proposed wide-angle subwavelength grating patterned CMY color filters. Unlike the designs discussed in the previous sections, the color is tuned by varying the width of the subwavelength gratings.

A schematic representation of the proposed high angular tolerant subwavelength grating-based CMY color filters is described in **Figure 3.4.1**. The working principle is the same with what we have discussed in the previous sections (i.e., strong interference phenomena in ultra-thin semiconductor layers). But the semiconductor and top metallic layer are 1D patterned so that the structure would respond to only one polarization state of the incident light. For TM polarization (electric field of the incident light wave is perpendicular to the gratings), a large proportion of the incident light will be reflected with experiencing small loss. On the contrary, TE-polarized light whose electric field of the incident light wave is parallel to the gratings will respond to the subwavelength grating structure, resulting in the F-P cavity resonance in the reflection spectrum (i.e., reflection valley) that creates the reflective CMY colors. The bottom Ag mirror thickness is 150 nm to block the transmitted light. The thicknesses of the top Ag and a-Si layers are 15 and 32 nm, respectively, and the period is 180 nm. We note that the spectral response of this design

is insensitive to the period so we can easily use a larger period. It should also be noted that this structure can be made over a large area by using the nanoimprint lithography.

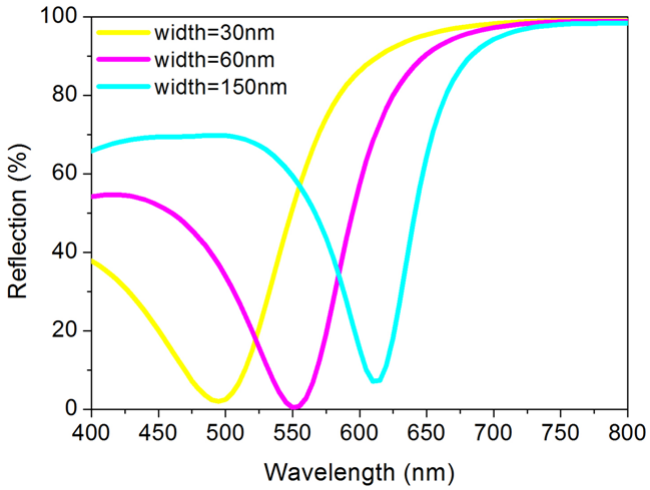

Figure 3.4.2 Simulated spectral reflectance curves with increasing the width of the subwavelength gratings. As the width of the gratings increases, the red-shift resonance occurs (i.e., the color varies from yellow to cyan).

Figure 3.4.2 presents simulated reflection spectra at normal incidence for TE polarization. The reflective colors can be tuned by changing the width of the subwavelength gratings. To produce the CMY colors, 150, 60, and 30 nm of the grating widths are utilized, respectively. Owing to the increased reflection from the top surface by putting additional top Ag mirror, the reflection spectra have pretty narrow bandwidths as is seen from the figure. We note that the individual CMY color pixels can be achieved by one patterning step, which is highly desired when making the color pixels.

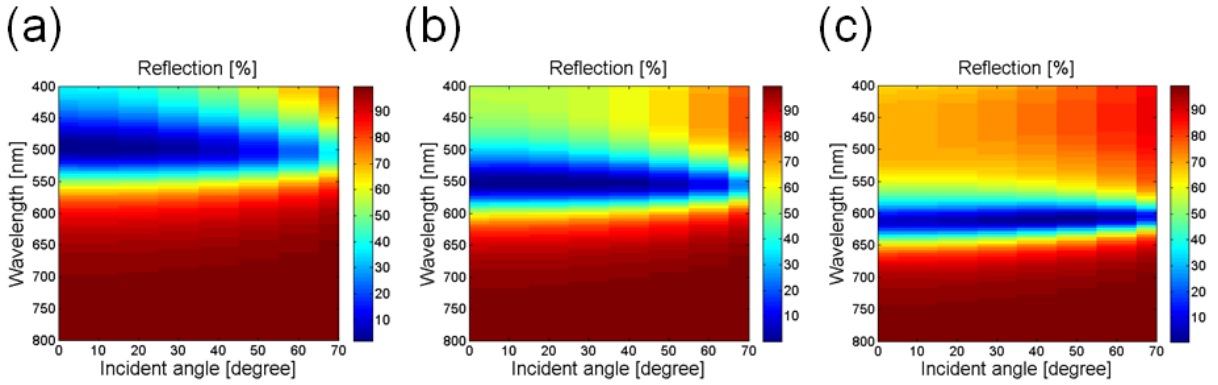

Figure 3.4.3 Simulated angle resolved reflection spectra for the individual reflection colors showing that the angle robust characteristic can preserve up to ±70°.

As we discussed in the previous sections, the proposed designs, which rely on the strong interference effects in the ultra-thin highly absorbing material, show an angle-insensitive performance. In this study, since the same strategy is exploited it is thus anticipated that our designs also exhibit the angle invariant characteristics. In **Figure 3.4.3 (a) – (c)**, calculated angle resolved reflection spectra of the yellow, magenta, and cyan color filters are depicted. It is clear that the resonance (i.e., reflection valley [blue color]) is nearly fixed with respect to the angle of incidence up to ±70° for all the colored devices, demonstrating the flat dispersion curves. This approach is the first demonstration that can provide angle-insensitive, polarization-independent, and one pattering process to create the individual CMY colors with great color purity. This device could be fabricated by the following procedures. The first thing we need to do is to deposit the thick Ag on glass substrate, followed by the deposition of a-Si and thin Ag layer atop. We note that if removing the top thin Ag film is difficult, we don't need to deposit Ag since the index contrast between air and a-Si is fairly large that leads to strong reflection. And a thermal imprint resist (e.g., MRI) could be patterned by the nanoimprint lithography and then the residual layer could be etched by the RIE etching. After shadow evaporating the Cr as a mask of the resist,

the top Ag mirror and the a-Si could be etched. Finally, the imprint resist could be removed by the lift-off process.

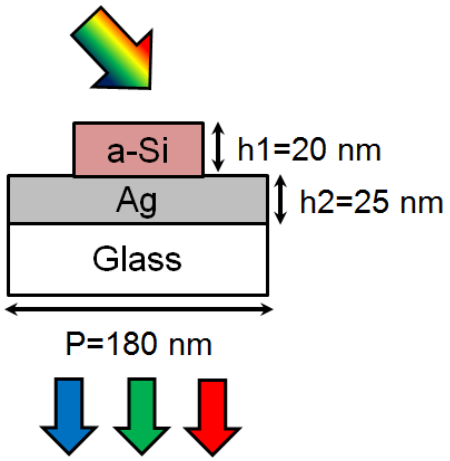

Figure 3.4.4 A schematic diagram of the proposed high angular tolerant subwavelength grating patterned RGB color filters. Producing the transmission colors at a certain resonance wavelength is enabled by making a bottom metallic layer optically thin.

As we described before, being able to generate the transmissive RGB colors is highly desired particularly for the colored display technologies. Making the bottom Ag layer optically thin (~ 25 nm) allows the incident light wave to be transmitted that leads to the trnsmissive RGB colors as depicted in **Figure 3.4.4**. The thickness of the a-Si layer is 20 nm and the RGB colors can be tuned by varying the width of the subwavelength grating patterns.

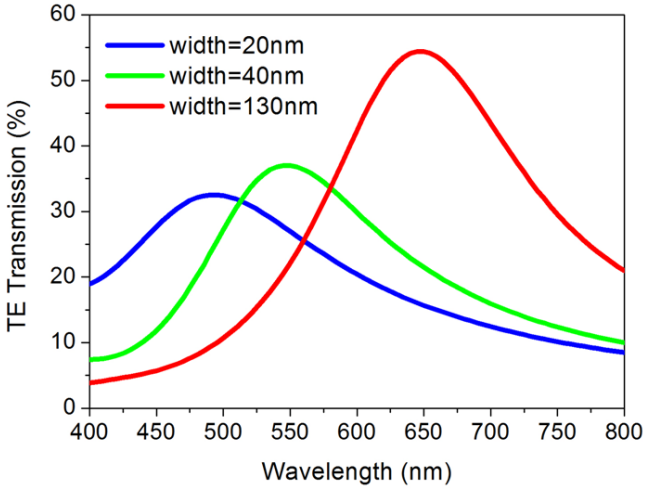

Figure 3.4.5 Simulated transmittances for TE polarization with increasing the width of the subwavelength gratings.

Figure 3.4.5 presents simulated transmission spectra at normal incidence for TE polarization. 130, 40, and 20 nm of the grating widths are used for producing the RGB transmission colors. From the simulation, it turns out that putting additional top Ag layer is not helpful to improve the color purity so we didn't put top Ag mirror in this design.

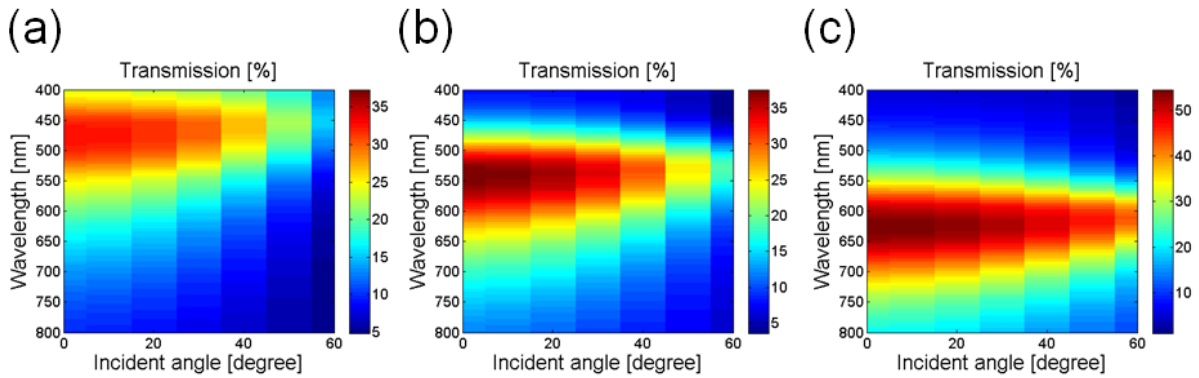

Figure 3.4.6 Simulated angle resolved transmission spectra for the individual transmission colors.

In **Figure 3.4.6**, simulated angle resolved transmission spectra of the RGB structural colors for TE polarization are shown. As we observed in the previous reflection designs, the resonance (i.e., transmission peak corresponding to a red color in the color map) is almost insensitive with

respect to the incident angle up to ±60° for all the RGB structural colors. One thing that needs to be addressed in the future study would be to improve the color purity of this structural color filter designs.

3.5 Conclusion

In Chapter 3, we have presented angle robust reflective/transmissive spectrum filters with high-color-purity exploiting strong resonance effects in a F-P optical cavity containing lossy media. Significantly enhanced color purity is attained by choosing the absorbing material that possesses the lower complex dielectric constant and by inserting additional top thin Ag layer. The reflection spectrum with narrow bandwidth (～74 nm) is achieved from the fabricated spectrum filter, which shows good agreement with the simulated profiles. Due to the negligible propagation phase shift in the ultra-thin a-Si layer, the devices exhibit excellent angle invariant characteristic up to ±70° that can address a crucial challenge in current plasmonic and photonic based spectrum filters, potentially opening the door to various applications such as light emitting devices, display technologies, and image sensors. We have also studied that adding an anti-reflection layer can improve the overall transmission efficiency. Furthermore, the proposed devices can be made by much simpler fabrication that only involves deposition process to produce the transmission colors, thereby making the approach suitable for large area applications. Lastly, we have proposed nanostructured subwavelength grating-based structural color filters that could be made via one-step fabrication, thus enabling the individual CMY and RGB colors to be patterned by pixel unit.

Chapter 4

High-Color-Purity Subtractive Color Filters with a Wide Viewing Angle Based on Plasmonic Perfect Absorbers

4.1 Introduction

It has long been believed that color filters received a substantial amount of attention as a vital element for diverse applications, such as image sensors, liquid crystal displays, light emitting diodes, and optical measurement systems. Traditional color filters, however, make use of colorant organic dyes that are highly sensitive to long-term heat exposure, strong intensity of ultraviolet irradiation, and moisture, which results in performance deterioration over time [8]. In recent years, a great effort has been made to develop structural color filters that provide distinct advantages over existing color filters. Various schemes have been suggested based on plasmonic nanoresonators, perforated metal films, metal-dielectric multilayer systems, photonic crystals, nanovolcano arrays, nanorod arrays, and nanowires [9-17, 31-41]. Even though these approaches show a performance enhancement in terms of the efficiency, durability, and dimension, there still have been great difficulties in achieving an angle insensitive behavior that is of critical importance in a wide variety of fields. In addition, a spectral response of the structural color filters based on above concepts has a relatively broad profile whose full width at half maximum (FWHM) is in general broader than 100 nm and also encompasses a large amount of off-resonance wavelength components, thereby greatly reducing the purity of the color. These

drawbacks significantly limit the practical applications and therefore it is indeed necessary to develop a platform that offers not only incident angle independent performance but also narrow FWHM with highly suppressed off-resonance wavelengths.

In this chapter, we demonstrate subtractive structural color filters with enhanced color purity employing a nearly perfect plasmonic absorption behavior in the metal-insulator-metal (MIM) configuration for addressing aforementioned challenges simultaneously. The proposed devices exhibit almost perfect absorption property (~97%) at a resonance wavelength and thus its complementary spectrum is reflected, being able to produce reflective colors. Such sharp resonance or color characteristic is retained over a large angle of incidence up to ±80° without sacrificing the intensity and bandwidth. The FWHM of the fabricated samples is only 36 nm with highly suppressed off-resonance wavelengths, thus accomplishing improved purity of the color.

4.2 Design Principle and Results

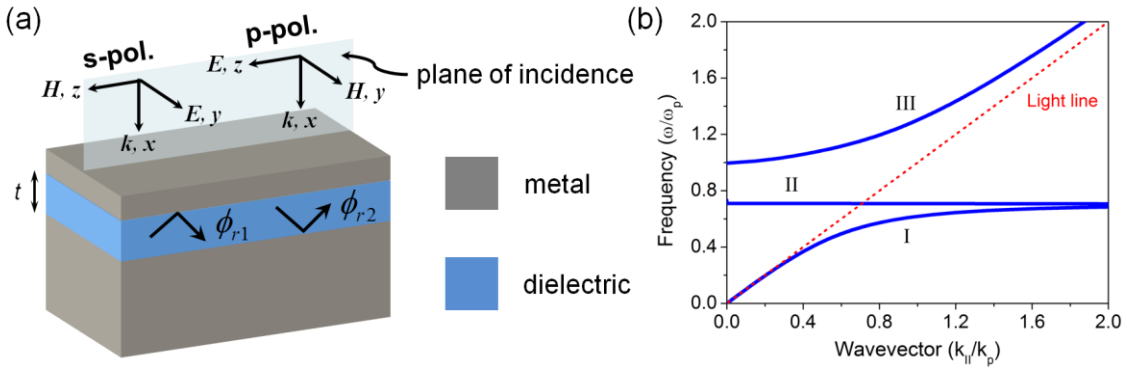

Figure 4.2.1 (a) A schematic representation of the proposed angle insensitive color filters exploiting a perfect absorption property in a microcavity, composed of metal-insulator-metal (MIM). For producing the reflective yellow (420 nm) and cyan (627 nm) colors, TiO_2 and a-Si are used as insulator layers. Ag is chosen as a metal mirror due to its lower absorption at visible frequency. (b) Dispersion curve of a MIM structure comprising two Ag mirrors separated by an air with the thickness of $\lambda_{sp}/4$.

A device structure under investigation, as shown in **Figure 4.2.1 (a)**, is composed of the MIM resonator on a silicon substrate. We select silver (Ag) for a metallic layer since it has lower optical absorption loss at visible frequencies. The dispersion curve of the MIM structure consisting of two semi-infinite Ag metallic mirrors separated by $\lambda_{sp}/4$-thick air medium is exhibited in **Figure 4.2.1 (b)**. The wave vector and frequency are normalized with respect to $k_p(=\omega_p/c)$ and ω_p, where ω_p is plasma frequency and *c* is the speed of light in free space. As is seen from the figure, there are three discrete modes: I. Propagating surface plasmon polariton (SPP) mode, II. Quasi-bound mode, III. Radiative mode. The SPP and radiative modes correspond to the antisymmetric solution and quasi-bound mode to the symmetric one in the MIM structure. The SPP mode has real k_z and imaginary k_x, thus propagating along the metal-insulator interface (i.e., *z*-direction) while the quasi-bound mode has real k_x and imaginary k_z, thus radiating into the forward direction (i.e., *x*-direction). The radiative mode has real k_z and real k_x. The analytical dispersion characteristics of these modes are derived in the reference of 42 and more detailed investigations can be given in the references of 43-45. Here we will mainly focus on the mode II that can be easily coupled without any external mechanism since its dispersion curve lies above the air light line. When the parallel component of the wave vector (k_{II}) goes to the infinity, the mode II's dispersion frequency ($\omega_{II}(k_{II})$) moves toward the SPP frequency in free space ($\omega_{sp} = \frac{\omega_p}{\sqrt{2}}$) occurring at the interface between air and metal. From the SPP dispersion expression ($k_{II} = \frac{\omega}{c}\left(\frac{\varepsilon_{metal}\varepsilon_{insulator}}{\varepsilon_{metal}+\varepsilon_{insulator}}\right)^{1/2}$), it is obvious that the permittivity of the metallic layer should be the same to the permittivity of the insulator with opposite sign at the SPP frequency

(i.e., $\varepsilon_{metal} = -\varepsilon_{insulator}$). When the thickness ($t$) of the insulating layer is equal to $\frac{\pi c}{2\omega_{sp}\sqrt{\varepsilon_{insulator}}}$, the dispersion frequency at $k_{II} = 0$ ($\omega_{II}(k_{II} = 0)$) will correspond to the SPP frequency. Simultaneously satisfying above two conditions enables the high angular tolerant resonance to appear at the SPP frequency, thus showing a flat dispersion band in the MIM configuration.[42, 46] Such a flat dispersion characteristics at visible frequency will be exploited in order to create reflective colors with wide viewing angle.

Real parts of the permittivity of Ag, titanium dioxide (TiO_2), and amorphous silicon (a-Si) materials as a function of wavelength measured by a spectroscopic ellipsometer (M-2000, J. A. Woollam) are depicted in **Figure 4.2.2**. For easy comparison the permittivity of Ag with opposite sign is plotted by a dotted line. As shown in the inset of the figure, absolute values of the permittivity of Ag are found to be 5.302 and 17.580 that demonstrate excellent match with the permittivity of TiO_2 (5.325) and a-Si (17.585) at 420 nm and 627 nm, respectively. It is thus expected that the resonance behaviors with a low sensitivity to the angle of incidence appear with the proper thickness of the middle insulating layer (either TiO_2 or a-Si). An adequate thickness of the insulator is calculated exhibiting that 46 nm of TiO_2 and 35 nm of a-Si layers are needed in order to create the resonance at the SPP frequency.

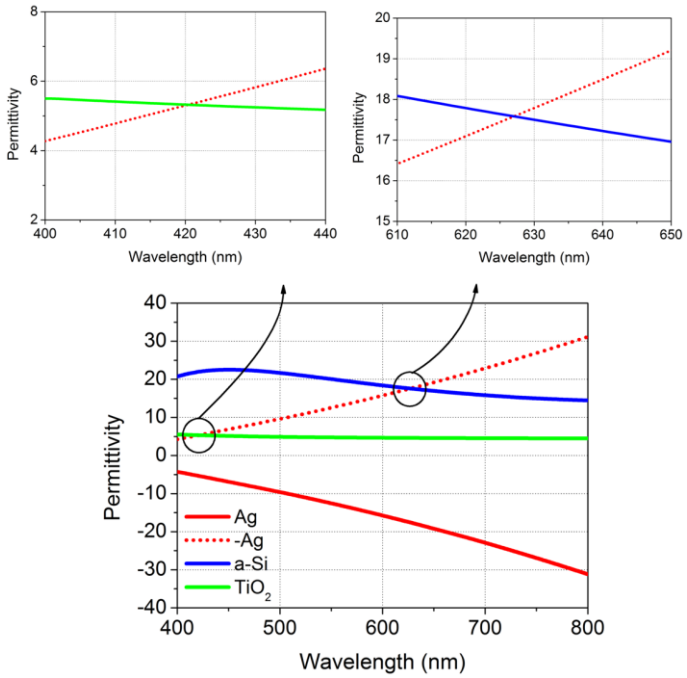

Figure 4.2.2 Real parts of the dielectric constant of Ag, TiO_2, and a-Si as a function of wavelength measured by a spectroscopic ellipsometer (M-2000, J. A. Woollam). The inset shows an enlarged view of the dielectric constant in the vicinity of each surface plasmon resonance wavelength.

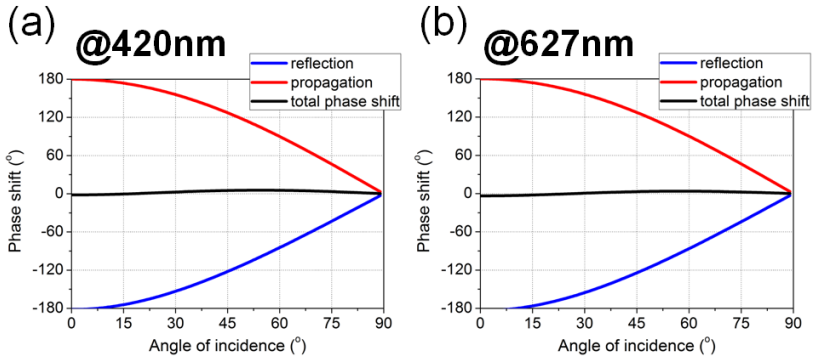

Figure 4.2.3 The net phase shift (black solid line), including the reflection phase shift (blue solid line) and the propagation phase shift (red solid line) obtained from the round-trip in the MIM resonator as a function of the angle of incidence at (a) 420 nm and (b) 627 nm that correspond to the surface plasmon resonance wavelength of each resonator.

In **Figure 4.2.3**, the calculated total round-trip phase shift, encompassing the reflection and propagation phase shifts, exhibited at the SPP frequency as a function of the incidence angle.

The reflection phase shift is computed from the reflection coefficient for p-polarization that is $r = \frac{r_{12} + r_{23}e^{2jk}}{1 + r_{12}r_{23}e^{2jk}}$ where $r_{pq} = \frac{n_p \cos(\theta_q) - n_q \cos(\theta_p)}{n_p \cos(\theta_q) + n_q \cos(\theta_p)}$ and $k = \left(\frac{2\pi}{\lambda}\right) n_2 t_2 \cos(\theta_2)$. Medium 1, 2, and 3 correspond to the top thin Ag, insulator, and bottom thick Ag layer, respectively. And the propagation phase shift through the insulator medium is calculated by $\left(\frac{2\pi}{\lambda}\right)\sqrt{\varepsilon_{insulator}}\, 2t_{insulator}\cos\theta$.

When satisfying the second condition, the accumulation of the phase shift during the light propagation through the insulating layer approximately cancels out the phase shift obtained from the reflection at the interface between metal and insulator. From the calculation, the sum of the two reflection phase shifts (ϕ_{r1} and ϕ_{r2}) increases with increasing the angle of incidence (i.e., from -180° to 0°), whereas the phase shift associated with the round-trip propagation decreases with increasing the incidence angle (i.e., 180° to 0°), showing that the sum of the reflection and propagation phase shifts leads to the zero (i.e., $2m\pi$ (m is an integer)) for all angles of incidence. This signifies that the resonance stays at the SPP wavelength over a large angular range under the appropriate condition.

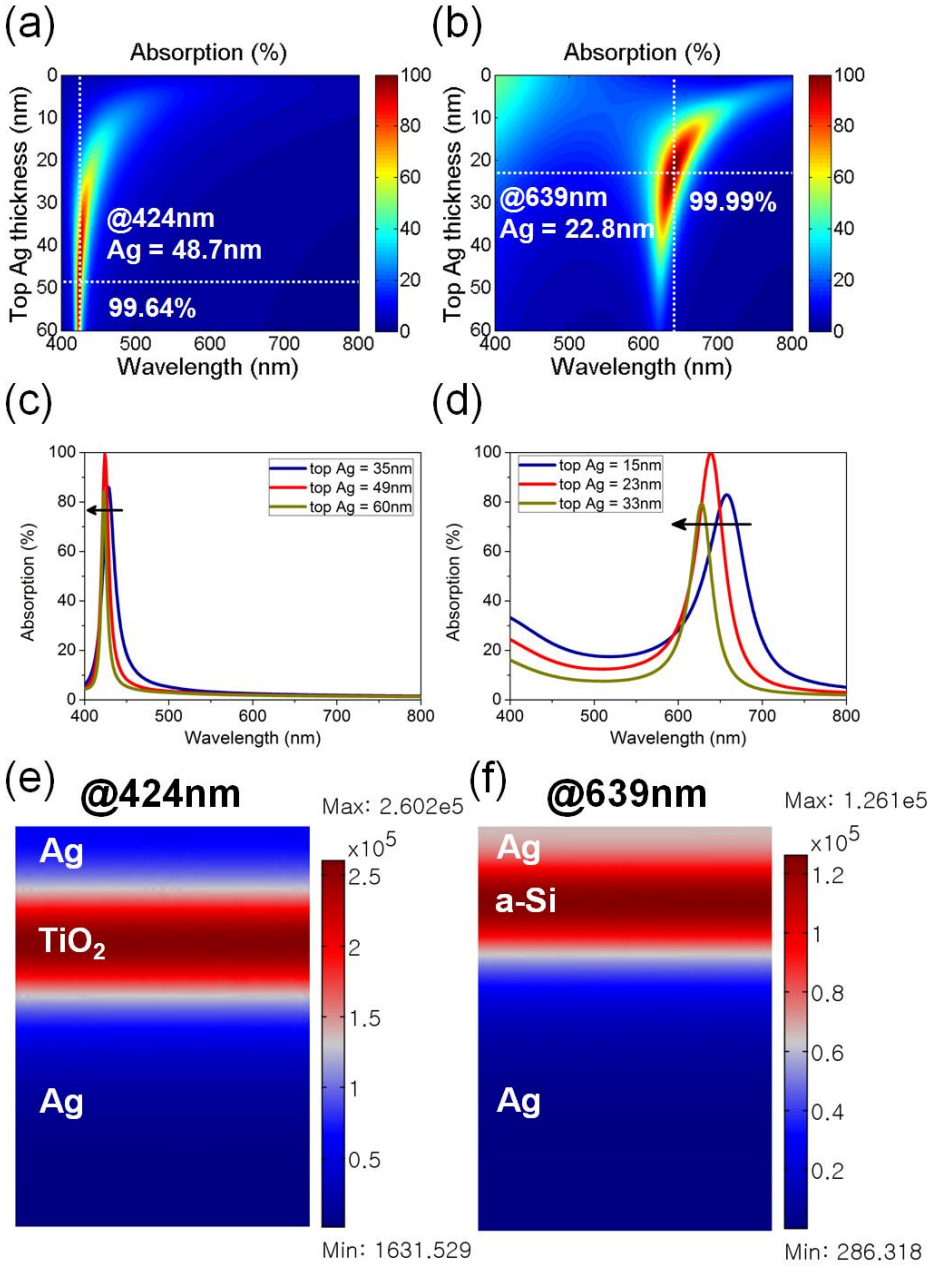

Figure 4.2.4 The calculated contour plots of the absorption for (a) yellow (420 nm) and (b) cyan (627 nm) as a function of wavelength and the thickness of top Ag layer. Almost perfect absorption is observed under the critical coupling condition for both cases. The calculated absorption spectra corresponding to the under (blue), critical (red), and over (dark yellow) coupling conditions for (c) yellow (420 nm) and (d) cyan (627 nm). The electric field profiles at (e) 424 nm and (f) 639 nm showing a highly concentrated field in the insulator layer with symmetric distribution in the MIM resonator under the critical coupling condition.

Next, we investigate an optical absorption characteristic in the MIM resonator system near the condition of a critical coupling. When the internal loss rate (γ_{int}) is equal to the radiation coupling rate (γ_{rad}), the 100% optical absorption can be achieved that is attributed to the perfect destructive interference between the incident light wave and the reflected light wave yielding the total absorption at the critical condition.[47-50] **Figure 4.2.4 (a) – (b)** show simulated contour plots of the absorption as a function of wavelength and the thickness of a top Ag film. Nearly perfect absorptions are attained with 48.7 nm and 22.8 nm of the top Ag layer for the yellow (420 nm) and cyan (627 nm), respectively. In **Figure 4.2.4 (c) – (d)**, simulated absorption spectra for three different cases of over coupling (dark yellow solid line, $\gamma_{\text{int}} < \gamma_{rad}$), critical coupling (red solid line, $\gamma_{\text{int}} = \gamma_{rad}$), and under coupling (blue solid line, $\gamma_{\text{int}} > \gamma_{rad}$) are illustrated. As can be seen from the figure, a nearly total absorption performance is obtained at the critical coupling condition, while the absorption efficiency starts decreasing in the over and under coupling regimes. Also, as the thickness of the top Ag layer increases the resonance is slightly shifted toward the shorter wavelength range due to the varied reflection phase shift at the top metal-insulator interface depending on the metal thickness. The resonance also gets sharper with increasing the thickness of the metal, which is attributed to the enhanced reflectivity of the metal surface (i.e., high Q-factor). Normalized electric field profiles at the resonance wavelength are shown in **Figure 4.2.4 (e) – (f)** exhibiting a symmetric distribution of the field in the MIM resonator.

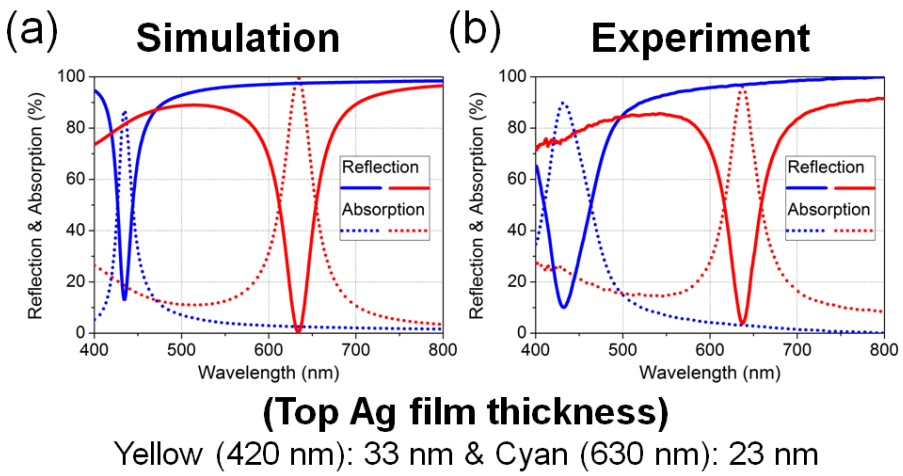

Figure 4.2.5 (a) The calculated reflection (solid lines) and absorption (dotted lines) spectra of the proposed color filters at normal incidence. The thicknesses of the TiO_2 and a-Si layers necessary for creating the yellow (420 nm) and cyan (627 nm) reflective colors are 46 nm and 35 nm, respectively. The thicknesses of the top Ag film for creating yellow (420 nm) and cyan (627 nm) are 33 and 23 nm, respectively. (b) The measured spectra corresponding to the profiles in (a) exhibiting slightly broader profiles due to the scattering loss induced by the non-smooth surfaces.

Figure 4.2.5 (a) describes simulation profiles of the reflectance (solid lines) and the absorption (dotted lines) of the designed structure. As there is no transmittance due to an optically thick bottom metallic substrate, the complementary spectrum of the absorption is the reflectance according to the well-known relation (1 = R + A). It is noteworthy to mention that the top metal has to be somewhat thin that allows incident light wave to traverse an entire structure and simultaneously provides a sufficient reflection phase change to achieve the wide angle plasmonic resonance effect. From the study in a previous section, we found that the top Ag layer for the yellow color (420 nm) needs to be 48.7 nm that is too thick for incident light to pass through the whole resonator system. Although we lose the absorption efficiency to some extent, the thickness of the top Ag layer for creating the yellow color (420 nm) is designed to be 33 nm (i.e., over coupling regime). The thickness of the top Ag layer for the cyan (627 nm) color is 23 nm that enables the resonator to operate at the critical coupling. Varying the insulator material yields the

change in the SPP frequency and as a result the reflective color can be tuned. We note that the magenta color can also be made by using zinc telluride (ZnTe) whose permittivity is fairly similar to the permittivity of Ag at ~525 nm. A silicon substrate was piranha cleaned (mixture of H_2SO_4 and H_2O_2 with 1:1 volume ratio) for 25 min. Ag and TiO_2 were deposited by the e-beam evaporation at a rate of 5 $\mathring{A}s^{-1}$ with a high vacuum ($1x10^{-6}$ mbar) and a-Si was deposited by using the plasma-enhanced chemical vapor deposition (PECVD) at a rate of 1 $\mathring{A}s^{-1}$ (SiH_4 gas with 13.56 MHz RF power). The experimental spectra of the reflectance are measured by using a film thickness measurement instrument (F20, Filmetrics) integrated with a spectrometer and white light source unit, and the optical absorption profiles are attained from 1 – R relation as shown in **Figure 4.2.5 (b)** that shows fair agreement with the calculated profiles. A non-smooth surface of each layer results in the scattering light loss, making the bandwidth of the measured data slightly wider. It is clear that the discrepancy between calculated and measured spectra is large for the yellow (420 nm), implying that the scattering loss of the yellow-colored device (420 nm) is more significant than that of the cyan sample (627 nm). This is in accordance with the Rayleigh scattering cross-section ($\sigma_s = \frac{2\pi^5}{3}\frac{d^6}{\lambda^4}\left(\frac{n^2-1}{n^2+2}\right)^2$) that is inversely proportional to fourth power of wavelength. *d* is the size of the particle and the *n* represents the index of refraction. We note that such undesired scattering loss can be reduced by depositing perylenetetracarboxylic bis-benzimidazole (PTCBI) before the thin Ag film deposition or ultra-smooth Al-Ag alloying film.[51-53] It is also important to note that the FWHM of the reflectance is only 36 nm with highly suppressed off-resonance wavelength components from experimental results, thereby yielding improved color purity.

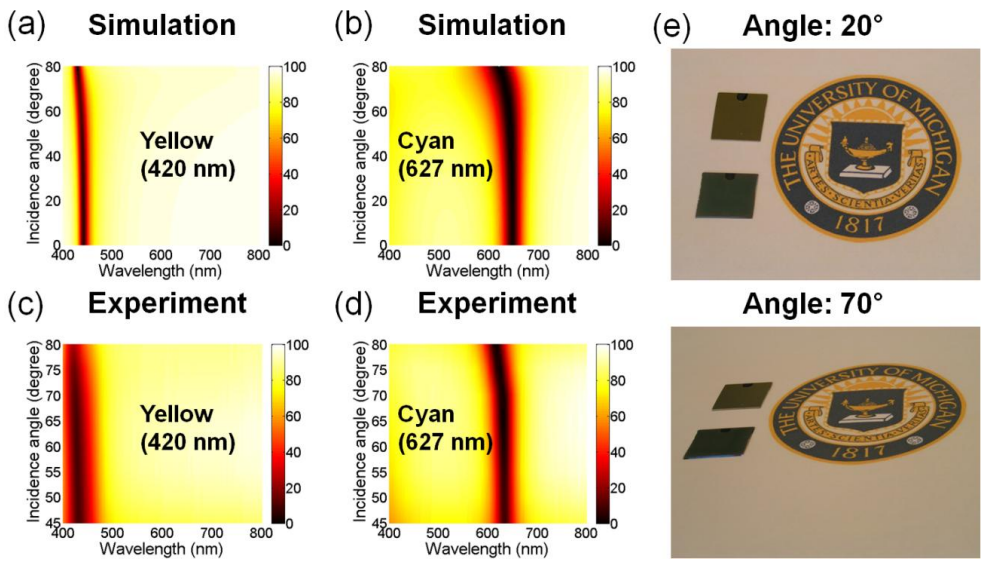

Figure 4.2.6. The calculated dispersion curves of (a) yellow (420 nm) and (b) cyan (627 nm) show that the surface plasmon resonance wavelengths stay approximately constant over a wide incident angular range, thus validating the angle insensitive characteristic in the MIM resonator. (c) - (d) The measured dispersion curves corresponding to the those in (a) - (b). The angle resolved reflection spectra are measured by a spectroscopic ellipsometer (M-2000, J. A. Woollam) at the incidence angle from 45° to 80° for p-polarization. (e) The optical images of the fabricated devices illuminated by the indoor light at two different oblique angles of incidence displaying no color change.

Lastly, we study the angular behavior of the proposed color filters. As described earlier, we utilize the mode that has the flat dispersion characteristic in the MIM configuration arising from the fact that the phase change acquired by the light propagating through the cavity approximately compensates the reflection phase changes, suggesting that our devices show the directional independent performance. Such phase compensation related to non-trivial reflection phase shifts obtained at the metal-semiconductor interface to form a resonance in an ultra-thin semiconductor medium as compared to the wavelength of incident light was recently investigated.[21-24] To validate such angle insensitive performance of our designs, the transfer matrix method-based simulation is carried out. As expected, the simulated dispersion curves exhibit that the resonance remains at the surface plasmon resonance wavelength over a large incident angular range for p-

polarization as exhibited in **Figure 4.2.6 (a) - (b)**. From the simulation, the FWHMs of the yellow (420 nm) and cyan (627 nm) devices are 20 nm and 31 nm, respectively, and its high efficient properties are retained up to ±80° from the simulation. The dispersion properties of the fabricated devices are measured by the spectroscopic ellipsometer (M-2000, J. A. Woollam) from 45° to 80° and illustrated in **Figure 4.2.6 (c) - (d)**, which agree well with the calculated results. The measured data show 51 nm and 36 nm of the FWHM for the yellow (420 nm) and cyan (627 nm) filters, displaying relatively broader FWHM than the simulated profile that is because of the light scattering loss. It is obvious that the measured spectra have low background noise level that primarily determines the purity of the color. It should be noted that the resulting spectrum of the fabricated samples keeps its intensity and the bandwidth over a wide incident angular range. The photographs of the fabricated samples at oblique angles of incidence are shown in **Figure 4.2.6 (e)**. The original reflective colors remain the same even at a large angle, therefore confirming the angle robust performance of the proposed designs. The color creation with wide viewing angle is highly desired in a variety of areas, such as color displays and light emitting diodes.

4.3 Conclusion

To sum up, we have demonstrated the subtractive color filters capable of producing the reflective colors with narrow bandwidth based on the plasmonic perfect absorption characteristic over a broad incident angular range in the MIM structure. There is no change in the reflected color with improved purity of the color even at a very large angle of incidence, ±80°. Presented strategy can

pave the way for many applications such as color display devices, optical measurements, light modulators, and image sensors.

Chapter 5

High Angular-Tolerant, Polarization-Independent, and High-Purity Reflective Structural Colors Based on 1D Photonic Crystals

5.1 Introduction

In recent years, renewed attention has been drawn to structural colors for their great promise in a wide variety of fields such as optical measurement systems, light modulators, light emissive diodes, imaging sensors, colored display devices, and high chroma pigments [54–58]. These structural colors have significant advantages over the traditional colorant based, typically an organic dye or chemical pigment, color filtering technologies in terms of high efficiency, slim dimension, long-term stability, free from photobleaching, but most importantly for its unique metallic and iridescent appearance.

Over the last decade, many research groups have proposed various plasmonic nanostructures, including nanorod, nanowire, and naoncavity [9-17, 31-41]. In addition to the plasmonic structures, numerous subwavelength grating-based photonic designs have been utilized to achieve the filtering capability in the visible wavelength ranges. However, a suppression of an angular dependence remained challenging. This is due to the fact that a light coupling scheme, for example prism and grating coupling, is required to couple incident light wave to the surface plasmon or guided mode resonant modes. Although great efforts are being

made to generate the structural colors with the angle-independent characteristic, the scalability of these proposed designs still remains questionable [56-59]. Besides, most of previously reported works utilize the one-dimensional (1D) grating structure that works for only one polarization. Furthermore, the most widely used geometries are metal-dielectric-metal (MDM) designs that involve optically thick bottom metal layer, thus resulting in a color only from the illumination direction. Unless such bottlenecks are addressed, it is extremely difficult to be used as an alternative to the conventional color filters.

In this Chapter, we present a new scheme that provides a distinct color that is insensitive to wide range of viewing angles and irrespective of the polarization states of incident light. By adopting a 1D photonic crystal (PC) configuration, the proposed device shows angular robust reflective color up to ±70° for both transverse electric (TE) and transverse magnetic (TM) polarized light. In addition, a symmetric structure design enables the same reflection color from both the top and bottom sides, which allows these films to be used as pigment flakes in paint [60]. Furthermore, the spectral profile of our structural color has almost negligible off-resonance wavelengths, leading to great color purity with high luminous intensity, which has not been observed by using a colloidal nanoparticle array approach. The strategy described in this study can open a new path to the extensive use of the structural colors for various applications that are difficult with conventional techniques.

5.2 Design Principle and Results

A schematic diagram of a proposed wide-angle, polarization-independent reflection structural color is shown in **Figure 5.2.1 (a)**, where the structure is composed of alternating layers of Si_3N_4

and a-Si. Even though our strategy can be used to produce various colors, we are targeting a high-color-purity angle-insensitive red color that was proved difficult to achieve [61]. In the case of the structural colors, creating a resonance at longer wavelengths (i.e., red color) requires a thicker layer, thus causing a sensitivity with respect to the angle of incidence due to the longer thickness as compared to other colors. Such an angle sensitive attribute could be addressed by employing high index materials. However, it requires a large number of periodic units with a low optical contrast [62]. In addition, a higher-order resonance appears at a shorter wavelength range, which degrades the color purity. We design our PC structure to have the band edge located around 600 nm in order to reflect strong red colors. The center wavelength (λ_c) of a photonic stopband (i.e., high reflection window) is designed to be 800 nm.

The thickness of each layer required to achieve strong constructive interferences of the reflected light at λ_c is a quarter wavelength ($d_{1,2} = \frac{\lambda_c}{4n_{1,2}}$), which leads to 100 and 50 nm of thickness for Si_3N_4 (n_1=2) and a-Si (n_2=4) layer, respectively. The bandwidth ($\Delta\lambda_c = \frac{4\lambda_c}{\pi}\sin^{-1}\left(\frac{n_2 - n_1}{n_2 + n_1}\right)$) of the photonic stopband of our designed structure is 350 nm, so that it generates strong reflection at wavelengths beyond ~600 nm. **Figure 5.2.1 (b)** depicts a band structure for the quarter-wave stack proposed in this paper with n_1=2 (Si_3N_4 at λ_c=800 nm) and n_2=4 (a-Si at λ_c=800 nm).

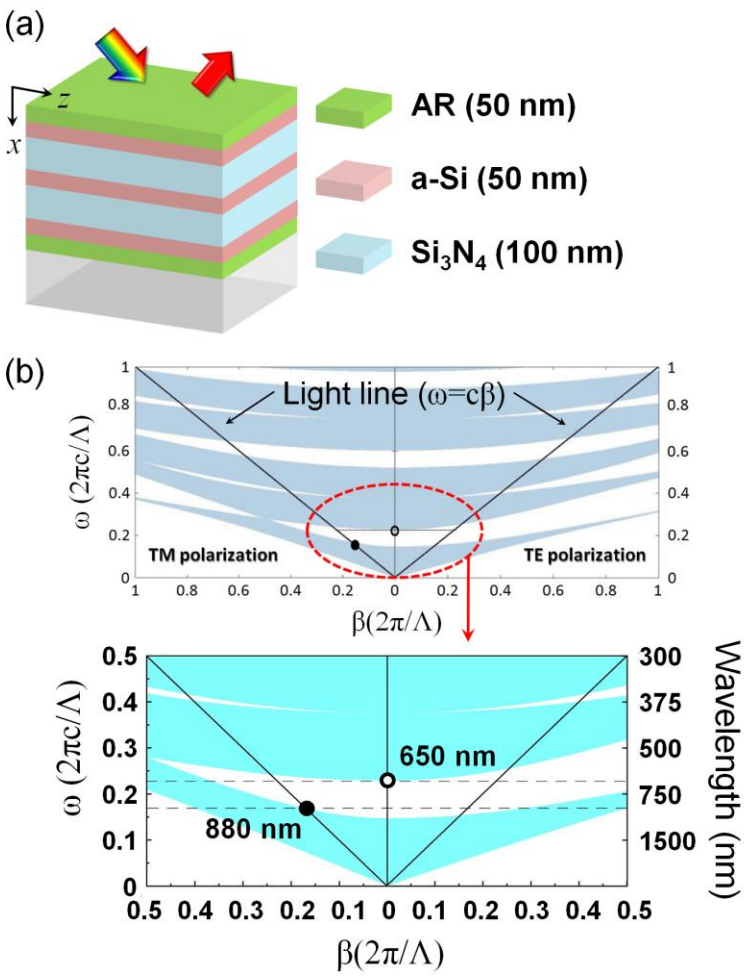

Figure 5.2.1 (a) A schematic diagram of a proposed polarization independent structural color with wide viewing angles based on a 1D photonic crystal (PC). (b) A projected band structure for our proposed multilayer system without the anti-reflection (AR) layers, which is periodic in x direction with n_1=2 and n_2=4. The electromagnetic modes for TM and TE polarizations are described to the left and right of the origin. An enlarged view of the red dotted region is shown below.

Generally, for a 1D periodically stratified medium with a refractive index that is periodic in *x* direction and wave propagating in the *x*-*z* plane, the wave vectors k_x in *x* and β in *z* represent the electromagnetic modes. The projected band structure is obtained by utilizing the dispersion relationship $K(\beta,\omega)=(1/\Lambda)\cos^{-1}[1/2(A+D)]$ for the Bloch wave function based on Floquet theorem, where *K* is the Bloch wave number, ω is the mode frequency and *A* and *D* are the

transfer matrix elements for the periodic structure [63]. There exist electromagnetic modes in the shaded regions while the white regions represent the photonic stopband. Moreover, the electromagnetic modes in the surrounding medium obey $\omega = c\sqrt{k_x^2 + \beta^2}$, where *c* is the speed of light in air and k_x is wave vector in *x* direction, and those modes can be represented by the whole area above $\omega > c\beta$ as shown in the figure. In **Figure 5.2.1 (b)**, the forbidden band for TM modes shrinks to zero when $\beta = (\omega / c) n_2 \sin\theta_B$ with the Brewster's angle $\theta_B = \tan^{-1}(n_1 / n_2)$, where the Fresnel reflection on the multilayer interfaces vanishes. The criterion for omnidirectional reflection behavior is that no incident light can be coupled into the structure from air, which means there exists a frequency zone where the band structure of the stack does not overlap with $\omega > c\beta$. In the visible wavelength, this frequency range is found as $0.17 < \omega\Lambda / 2\pi c < 0.23$, indicated as the filled and open circles in **Figure 5.2.1 (b)**, and the corresponding wavelength range is between 650 nm and 880 nm. Such an omnidirectional reflection characteristic of our proposed structure is attributed to the existence of a complete photonic band gap [64, 65], and the relative flat band structure with respect to β , which will be investigated in the last section of the paper.

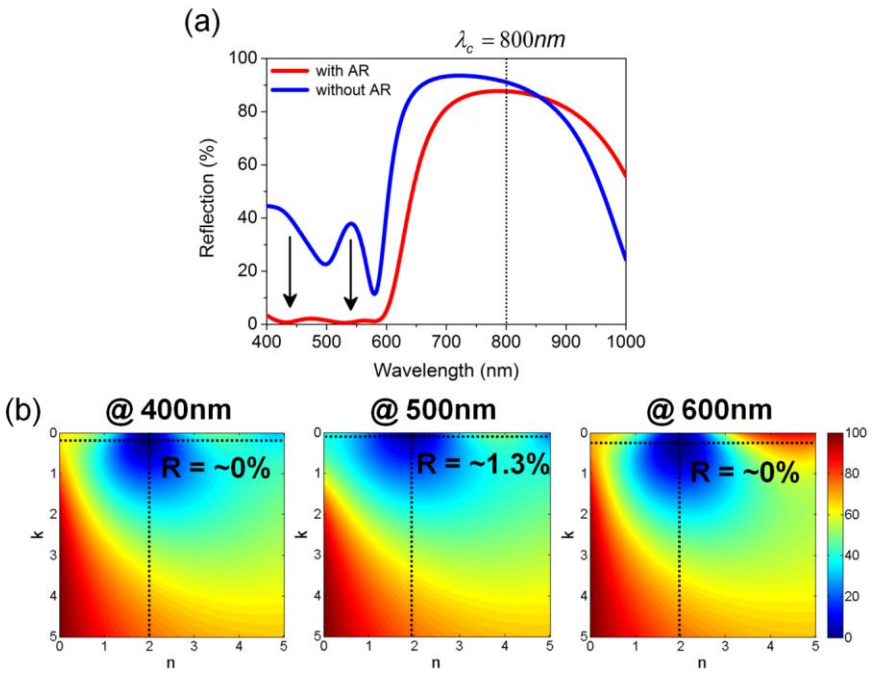

Figure 5.2.2 (a) Calculated spectral reflectance curves with (red solid line) and without (blue solid line) an AR coating showing that the reflections from 400 nm to 600 nm are greatly suppressed by adding the AR layer. (b) Calculated contour plots of the reflection as a function of a complex index of refraction (real (n) and imaginary (k) parts) of the 50 nm thick AR layer at 400, 500, and 600 nm, respectively. It is found that nearly insignificant reflections smaller than ~1.3% in the wavelength regimes between 400 nm and 600 nm when n and k are equivalent to 1.98 and 0.14, respectively. Color maps denote the intensity values of the reflected light.

Based on this design the reflections from 400 nm to 600 nm are ~33% due to a high index contrast between air and a-Si as shown in **Figure 5.2.2 (a)** (blue solid line). To address this problem, we add an AR layer, and simulation is carried out to mitigate the reflections in this wavelength range. **Figure 5.2.2 (b)** shows calculated reflections as functions of real (*n*) and imaginary (*k*) parts of the refractive index of the AR layer with a given thickness (50 nm) at 400, 500, and 600 nm. It is apparent that the reflection value is almost negligible (less than ~1.3%) in the wavelength regions from 400 nm to 600 nm when *n* and *k* are equal to 1.98 and 0.14, respectively. We note that the decreased (or increased) thickness of the AR layer could be used with the increased (or decreased) *n* value of the AR film. Experimentally, we choose Si_3N_4 as the

AR coating material because its refractive index is fairly close to the optimized index needed for the AR effect (i.e., n=2). Note that other dielectric materials with the index close to 2, such as WO_3, MoO_3, and Ta_2O_5, can be used for the AR layer as well.

We also investigate the AR coating by utilizing an optical admittance diagram to further validate its effect [66,67]. The optical admittance ($Y = \sqrt{\varepsilon/\mu}$) is the inverse of the impedance and widely used at optical frequencies to describe the characteristic of the thin-film multilayer structure due to negligible magnetic effects, which lead to its numeric value equal to the complex refractive index of a material although their physical meanings are different. At normal incidence, the amplitude of the reflection coefficient of a surface is expressed by the following equation:

$$r = \frac{Y_0 - Y}{Y_0 + Y} \tag{5.2.1}$$

where Y_0 is the incident medium's optical admittance and Y is the optical admittance of the surface, respectively. After substituting $r = |r|e^{i\varphi} = \alpha + i\beta$ where $\varphi = \frac{2\pi n}{\lambda} d\cos(\theta_{inc}), d = \text{thickness}, \text{and } \theta_{inc} = \text{incidence angle}$ and $Y = x + iy$ into the **Equation 5.2.1**, then

$$|r|e^{i\varphi} = \frac{Y_0 - x - iy}{Y_0 + x + iy} \tag{5.2.2}$$

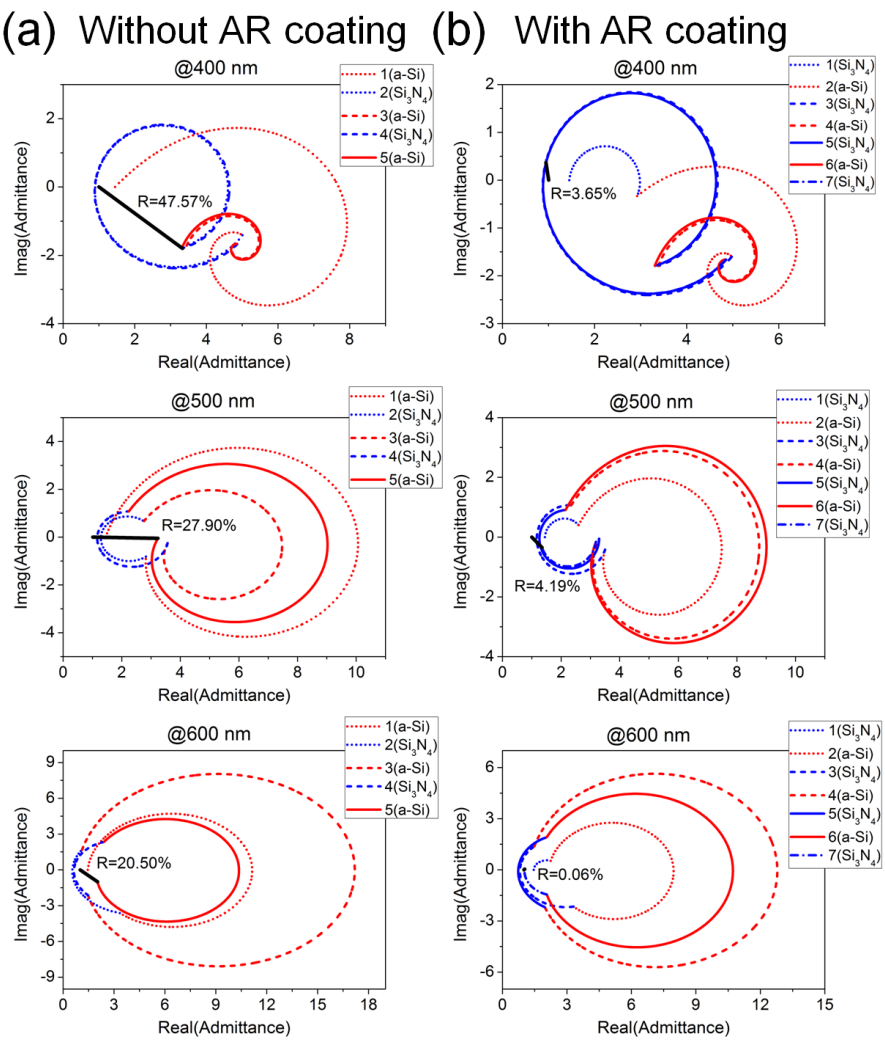

Figure 5.2.3 Optical admittance diagrams of the proposed PC-based multilayer structure (a) without and (b) with AR coating layers (50 nm Si_3N_4) at 400, 500, and 600 nm. An initial admittance point is the glass substrate and the following locus is determined by the thickness and refractive index of the medium. It is clear that the distance from the final admittance point to the air is considerably decreased after adding the AR layers, achieving greatly reduced reflections in a short wavelength range from 400 nm to 600 nm and thus excellent color purity.

Multiplying each side of **Equation 5.2.2** and its complex conjugate together leads to

$$x^2 + y^2 - 2Y_0\left(\frac{1+r^2}{1-r^2}\right)x + Y_0^{\,2} = 0 \qquad (5.2.3)$$

Equation 5.2.3 describes the optical admittance of the surface and the resulting admittance is the equation of a circle on the real axis in the case of transparent dielectric media or perfect electric conductors. In absorbing medium cases such as semiconductors or real metals, however, the extinction coefficient of the material renders the admittance locus somewhat distorted, thus yielding spirals [68]. The optical admittance of the structure begins with the point of the substrate (n_{sub}, 0). As the thickness of the dielectric medium is increased, the admittance rotates on the circle. A zero-reflection is achieved by perfectly matching the admittance of the system with that of the air (i.e., the admittance terminates at the air (1, 0)). This also suggests that the reflection can be suppressed depending on how close the air and the last admittance points are. In **Figure 5.2.3 (a) and (b)**, the optical admittance diagrams of the proposed PC-based structural colors without and with the AR coating at 400, 500, and 600 nm are presented. Paths of the optical admittance traced out by the a-Si and Si_3N_4 layers are represented by a red and blue colored line, respectively. The black solid line indicates the distance from the termination point to the air along with the expected reflection that can be computed by the following equation ($R = \left(\frac{Y_0 - Y_1}{Y_0 + Y_1}\right)\left(\frac{Y_0 - Y_1}{Y_0 + Y_1}\right)^*$ where Y_0 and Y_1 are the optical admittance of the starting incident medium and ending point). Calculated coordinates of the final admittance obtained without the AR coating are (4.85, -1.66), (3.24, -0.05), and (2.03, -1.02) for 400, 500, and 600 nm wavelength, respectively. These admittance points are fairly far from that of the air, which gives rise to a strong reflection at that wavelength as can be seen from the calculated reflection values. On the contrary, the distance between the air and termination point is highly reduced by adding the AR layer and the corresponding coordinates are (0.95, 0.38), (1.35, -0.34), and (1.03, 0.04), all of which exhibit significantly suppressed reflections of less than 5%. We study the influence of the thickness of the AR coating medium on the reflection, which is found in **Figure 5.2.4 (a)**

and (b). Both Si_3N_4 and a-Si materials are deposited by the PECVD. The refractive indices of deposited Si_3N_4 and a-Si are measured by a spectroscopic ellipsometer (M-2000, J. A. Woollam Co.) and given in **Figure 5.2.5**.

After applying the AR coating to our design, the resulting spectral response shows significantly suppressed reflections between 400 and 600 nm as represented by red solid line in the **Figure 5.2.2 (a)**, which will be confirmed by the experiment in the following section.

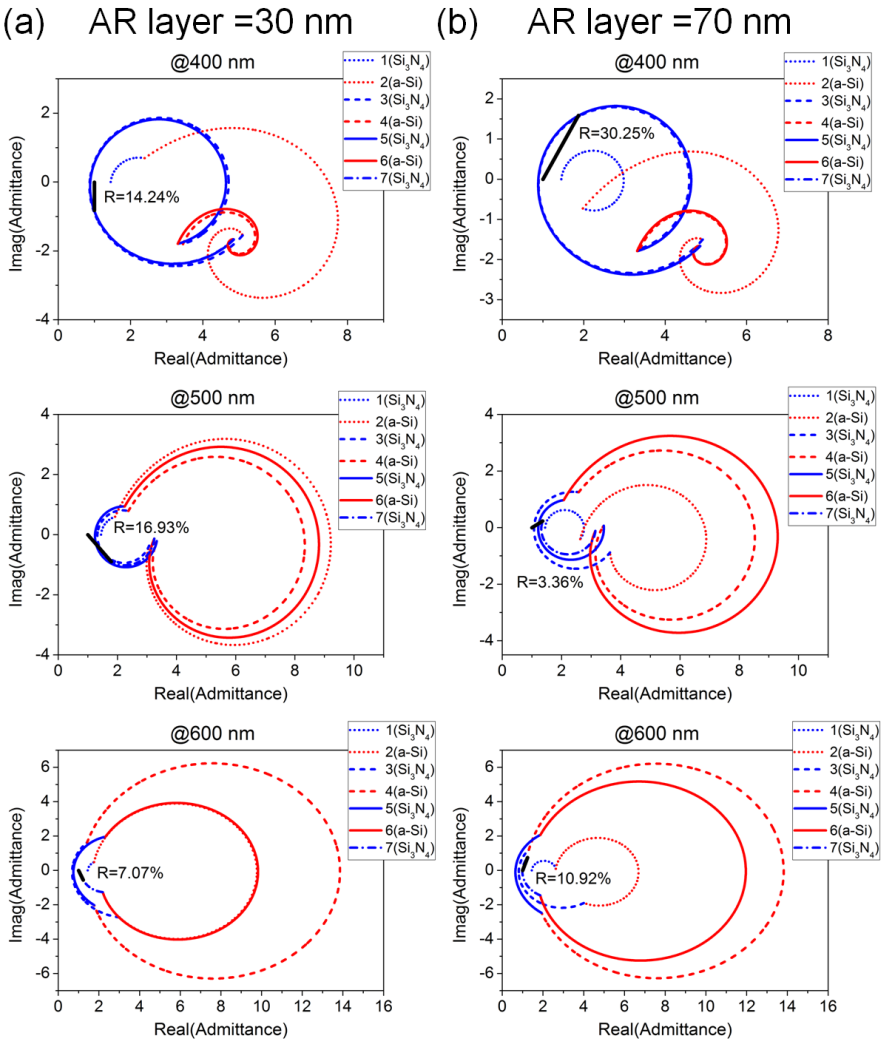

Figure 5.2.4 Optical admittance diagrams of the PC-based multilayer structure with (a) 30 nm and (b) 70 nm of the AR coating layers at 400, 500, and 600 nm. With increased and decreased thicknesses of the AR media, the reflections between 400 and 600 nm are higher than those obtained from the structure with 50 nm of the AR coating layers as shown in Figure 5.2.3.

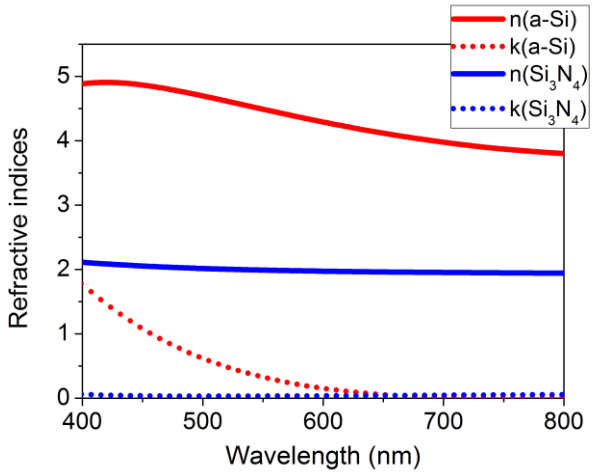

Figure 5.2.5 Wavelength-dependent complex refractive indices of Si_3N_4 and a-Si measured by using the spectroscopic ellipsometer (M-2000, J. A. Woollam).

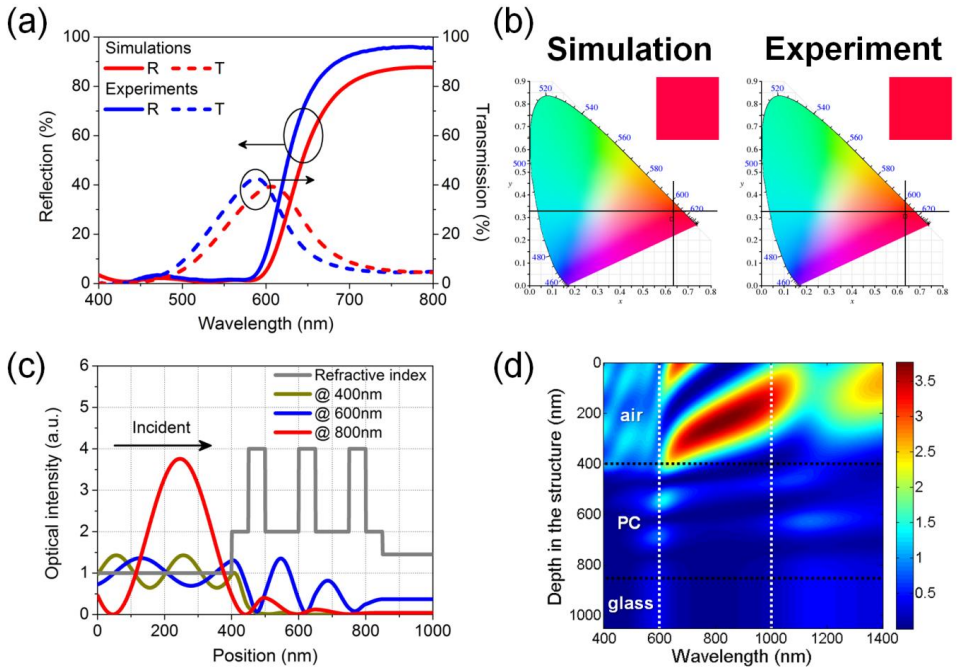

Figure 5.2.6 (a) Calculated and measured spectral reflectance (solid lines) and transmittance (dotted lines) curves at normal incidence, both of which are in great agreement. (b) An illustration of the color coordinate from both the simulation and experiment depicted on the CIE 1931 chromaticity diagram. The crossing point of the two black solid lines signifies a standard red color coordinate (0.64, 0.33) for the liquid crystal display devices. (c) Optical intensity distributions of the electric field at 400 (dark yellow), 600 (blue), and 800 nm (red) together with

the refractive index profile (gray), incident from the left-hand side. The interference of the counterpropagating light waves leads to the oscillating intensity outside the PC structure (i.e., air from 0 to 400 nm in position). The strong absorption of the a-Si medium at 400 nm results in little field penetration while the light of 800 nm can get fully reflected from the PC structure. (d) A field penetration into our designed PC multilayer structure as a function of wavelength. The color map denotes the optical intensity inside the structure.

In **Figure 5.2.6 (a)**, the calculated and measured reflection (solid curves) and transmission (dotted curves) spectra at normal incidence angle are depicted. A transfer matrix method based on the measured refractive indices of Si_3N_4 and a-Si is used to plot the calculated spectra and the spectral profiles of the fabricated sample is measured by using a thin-film measurement system (F20, Filmetrics) incorporated with the light source and spectrometer. Excellent agreement is obtained between the simulation and experimental data. We note that the measured spectral responses show blue-shifted profiles with relatively higher intensitiy as compared to the calculated spectra, which could be attributed to the fact that the refractive indices of both Si_3N_4 and a-Si materials for the fabricated samples are slightly lower than those used in the simulation. It is also clear that the measured reflection spectrum has a sharper slope at 650 nm than the simulated profile, which is attributed to the lower optical absorption loss (Absorption = $\frac{2\pi c\varepsilon_0 nk}{\lambda}|E(x,\lambda)|^2$, where c: speed of light, ε_0: permittivity of free space, n: real part of the refractive index, $k=\frac{\lambda\alpha}{4\pi}$: extinction coefficient, α: absorption coefficient) resulting from the lower refractive indices (i.e., high Q-factor) [25]. In particular, strong reflections from 600 nm to 800 nm are achieved while the reflections at shorter wavelength regions (i.e., 400 - 600 nm) are greatly reduced, thereby creating red reflective color with high color purity. The luminous intensity of our targeted color (~96%) obtained from the experiment is much improved as compared with that of the traditional organic dye based red color (~70%). In order to evaluate the

purity of the produced red color, the color coordinates (*x*,*y*) are calculated from the calculated and measured reflection spectra, and described on the CIE 1931 chromaticity diagram as presented in **Figure 5.2.6 (b)**. It is noted that the crossing point of the two black solid lines indicates a standard red coordinate (0.64, 0.33) for the liquid crystal display (LCD) devices. The color coordinates (*x*,*y*) for the simulation and experiment are (0.655, 0.294) and (0.656, 0.321), respectively, both of which are quite close to the standard red point (0.64, 0.33), indicating that the red color of our design shows great color purity. We note that the approach described here could be expanded to create blue and green colors as well by reducing the thickness of each medium with appropicate thickness of the AR coating layer while sacrificing the luminous intensity to some extent due to the absorption loss of the semiconductor layer at shorter wavelengths. Optical intensity distributions of the electric field at different wavelengths are shown in **Figure 5.2.6 (c)**. The light is incident from the left-hand side where the incident medium is the air (0 – 400 nm in position) and passes through the PC structure (400 – 850 nm in position) on the glass substrate (850 – 1000 nm in position). The gray solid line represents the profile of refractive indices of air, Si_3N_4, a-Si, and SiO_2 corresponding to 1, 2, 4, and 1.45, respectively. The field inside the PC at 400 nm (dark yellow) is almost 0 that is due to the strong absorption of the a-Si layer whereas the light of 600 nm (blue) can get through the whole PC structure and thus be partially transmitted. It can also be seen that the field intensity in the incident medium at 800 nm (i.e., λ_c) is much stronger than that at either 400 or 600 nm, implying that a significant portion of the light for 800 nm is reflected from the PC. To clearly see how the optical field penetrates into the PC structure for the whole visible wavelength ranges, **Figure 5.2.6 (d)** describes the field distribution as functions of wavelength and depth in the

structure. As can be seen from the figure, there is trivial field penetration in the PC but strong field in the air within the photonic stopband (i.e., 600 and 1000 nm).

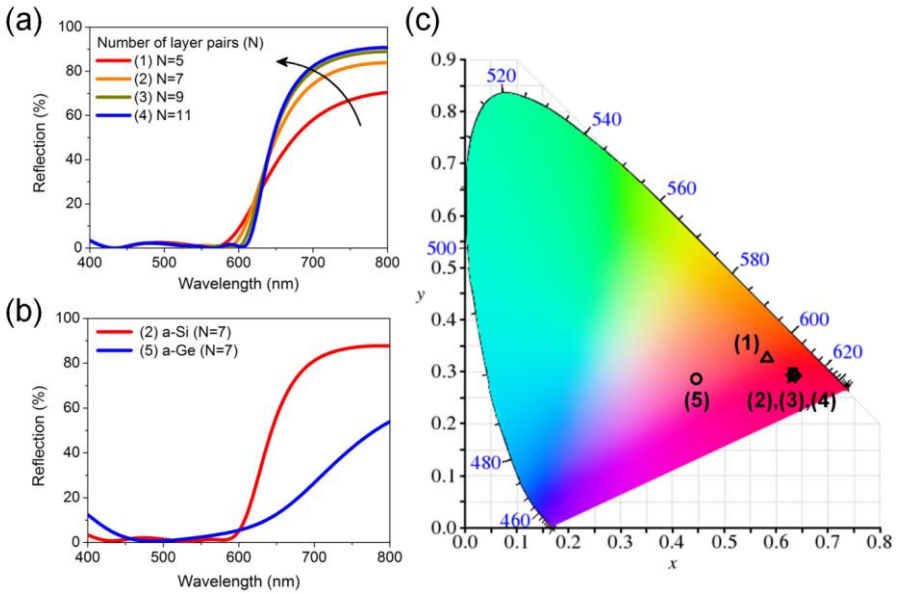

Figure 5.2.7 (a) Calculated reflection responses with different number of layer pairs from 5 to 11. (b) Calculated spectral reflectance curves of the PC that is composed of 7 layer stacks made of a-Si/Si_3N_4 and a-Ge/Si_3N_4 pairs. (c) A representation of the color coordinate from the reflection spectra studied in (a) and (b) described on the CIE 1931 chromaticity diagram.

Next, we examine the influence of the number of pairs and the selection of the semiconductor material on the color purity. **Figure 5.2.7 (a)** depicts the calculated reflection spectra depending on how many layer pairs the PC structure has. It is expected that increasing the number of pairs (i.e., combination of a-Si and Si_3N_4) enables a steeper photonic stopband and thus stronger reflection, because more constructive interferences occur with increasing the number of layer pairs. Next we compare the contribution of different semiconductor layers. In **Figure 5.2.7 (b)**, the calculated reflection spectra of the PC structure comprising either 7 layer pairs of a-Si/Si_3N_4 (red solid line) or amorphous germanium (a-Ge)/Si_3N_4 (blue solid line) are shown. As is seen in the figure, the spectral reflectance of the PC involving a-Si/Si_3N_4 combination has much sharper

profile than that of the a-Ge/Si_3N_4 case. The broad spectrum for the latter case is attributed to a large absorption of the a-Ge material across the entire visible wavelength spectrum, which results in poor quality factor (Q-factor) of the PC. To estimate how the color purity varies depending on the number of stacks of layers and the choice of the semiconductor, the color coordinates (*x*,*y*) of the reflection spectra discussed in **Figure 5.2.7 (a) and (b)** are calculated and represented on the CIE 1931 chromaticity diagram as shown in **Figure 5.2.7 (c)**. When the number of layer pairs is 5, the photonic stopband is not sharp enough to achieve the pure red color, because it contains a small portion of the yellow light, thus the calculated color coordinate lies midway between the yellow and red (i.e., orange color). When the number of stacks is greater than 7, it is evident that the purity of the red color is improved due to the increased number of the constructive interferences. Since the color purity of the PC that contains 7 pairs is fairly comparable to that of the PC consisting of 9 and 11 layer stacks, we choose the PC device with 7 layer pairs as a demonstration. The spectral reflectance of the PC made of 7 layer pairs of a-Ge and Si_3N_4 has some portions of the blue wavelengths, which lead to the color coordinate shifting toward the bluish region (i.e., magenta color).

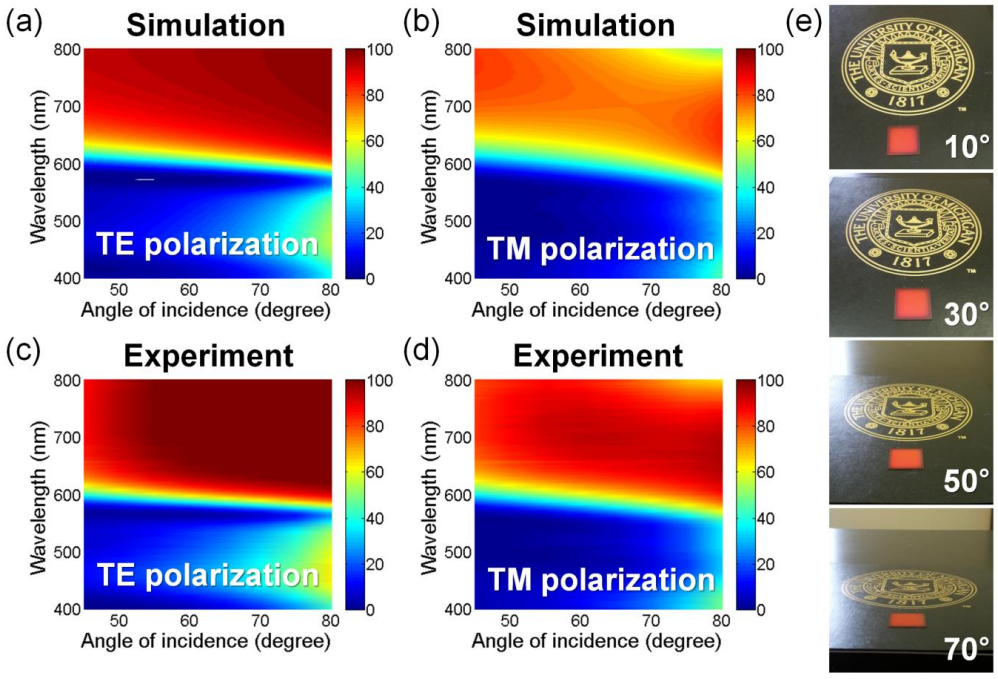

Figure 5.2.8 (a) – (b) Calculated angular dependences of the designed device for TE and TM polarizations. (c) – (d) Measured angular dependences corresponding to those in (a) – (b). (e) Optical images of the fabricated device on a black paper at the four oblique angles of incidence are taken with the indoor light, displaying that the red color can be maintained over a wide angular range. Note that the black paper is used to prevent the reflected light from interfering with the transmitted light.

Lastly, we explore the dependence of our proposed structure on the angle and polarization states of the incident light. The calculated and measured angle resolved reflection spectra for both TE and TM polarizations are presented in **Figure 5.2.8 (a) – (d)**. The simulation data are obtained from a transfer matrix method and the angular behavior of the fabricated device is measured by using spectroscopic ellipsometer (M-2000, J. A. Woollam Co.) from 45° to 80°, showing great match with the simulation. As can be seen from both the simulation and experiment, the strong reflections from 600 nm to 800 nm with highly suppressed reflections below 600 nm are achieved over a large angle of incidence for both polarizations, which was expected from the band structure as shown in **Figure 5.2.1 (b)**. Within the frequency zone (white region) in the projected band structure, there will be a total reflection from any incident angle for both

polarizations with a finite number of films, which is consistent with both the simulated and measured angle resolved reflection spectra presented in **Figure 5.2.8 (a) – (d)**. For the waves below 650 nm, the reflection is much lower because most lights transmit due to the coupling between incident wave and the modes in the structure, and then are absorbed by the a-Si layer and partially transmitted. Optical photographs of the fabricated sample on a black paper at several oblique angles of incidence under the ambient light illumination (i.e., unpolarized light) are shown in **Figure 5.2.8 (e)**. It is clear that the reflective red color can be viewed from various angles with the unpolarized light, thus validating our design that color characteristics insensitive to the incidence angle and polarization. It should be noted that the sample is placed on the black paper to absorb the transmitted light that could be interfered with the reflection color. We also note that the red color can be observed from the opposite side since the proposed structure is symmetric and not opaque. Such bi-directionality with the angle invariant and polarization independent properties is highly desirable for certain applications. Moreover, the structures could be made into pigment form and applied as a coating layer to an object to produce the desired colors.

5.3 Conclusion

In conclusion, we proposed and experimentally demonstrated a polarization independent structural color with improved viewing angles employing a 1D PC structure. The proposed device exhibits a distinct reflective color with high purity and luminance over a wide angular range up to ±70° regardless of the incident polarization from both directions. The approach

discussed here can be potentially useful for diverse applications, including colored displays and image sensors.

Chapter 6

Colored Photovoltaic (PV) Cells Based on Strong Resonance Effects in Ultra-Thin Lossy Media

6.1 Introduction

It is a dream of many to utilize solar energy to solve the world energy crisis and to curb climate change. Every minute, the earth receives sufficient energy from the Sun to satisfy the world's total energy requirements for the entire year. PV are promising platforms for the harvesting of this inexhaustible solar energy, and new device concepts with improved efficiency are constantly emerging in this field. The currently widespread inorganic thin-film PVs are dull and black in color and are not visually appealing. Therefore, they are normally installed on rooftops. Thus, there is a strong need to develop multifunctional PVs that can offer attractive design features, e.g., with desired colors and patterns, to allow them to be easily integrated with both interior and exterior architectural features, such as facades, skylights, windows, and offices.

The black color of the traditional PV panel is caused by the use of a thick semiconductor layer to absorb most incident light. To create colored PV panels, thinner semiconductor layers must be used. To produce colors, one may potentially exploit the concepts and designs studied in the field of structural colors [9-17, 31-41]. For instance, the integration of organic semiconductors into specially designed reflective color filters has previously been demonstrated

to permit the generation of electric power through the simultaneous harvesting of the absorbed light [16]. However, organic PVs are known to suffer from oxygen and moisture sensitivity and have short lifetimes [69]. The nanostructures used in this previous demonstration are also difficult to scale to practical large areas. It is also desired that the color appearance should not change with viewing angle, but the previous approach cannot satisfy this requirement because it uses gratings to couple the incident light. Clearly, a general and simpler design principle is needed to naturally integrate the semiconductor materials into the structure while addressing both the optical and electrical requirements.

The simplest approach to obtaining a dual-function colored PV device is to use a metal-semiconductor-metal (MSM) structure. Because of partial reflection from the metals, a F-P resonator can be formed to produce the desired reflected colors, which are determined by the thickness of the semiconductor. The two metal layers also simultaneously function as electrodes to extract the photocurrent produced by the light absorbed by the semiconductor layer. However, typical F-P resonances are known to exhibit strong angle dependence, which will need to be addressed for our application. A-Si is chosen because it is a mature semiconductor technology that is already used in the production of a-Si PVs and because its deposition is also compatible with the proposed MSM structure. Moreover, it can suppress the angle dependence of the resonance, as will be explained later. However, a quick calculation indicates that one would need an a-Si layer of 10 - 30 nm to produce reflected colors in the visible range. This is challenging because it is known that the doped layers alone in traditional a-Si PV already constitute a thickness of 40 - 50 nm [70]. Evidently, a new device structure is needed to comply with both the optical and electrical characteristics required of dual-function solar cells.

In this chapter, we introduce an approach to addressing these challenges by introducing an a-Si/organic hybrid solar cell structure, which allows for the use of an ultra-thin undoped a-Si layer and can produce desirable colors. Furthermore, the colors are not sensitive to the angle of incidence for angles of up to 60° nor to the polarization state of the incident light. We borrow the underlying concept from organic PVs and use very thin inorganic and organic charge transport layers to sandwich the undoped intrinsic (i-) a-Si active layer at the anode and cathode interfaces. Because the thickness of the ultra-thin photoactive layer ranges from 10 nm to 27 nm (an order of magnitude smaller than that of the typical p-i-n a-Si) [71] and because of the elimination of the doped n and p regions, which are known to cause significant charge recombination, [72] the measured external quantum efficiency (EQE) of the devices closely matches the calculated optical absorption of the thin a-Si layer. As a result, the colored hybrid cells can produce a power conversion efficiency close to 3 %, despite the use of an a-Si layer ten times thinner than that of traditional a-Si PVs. This achievement would have not been possible without the optical resonance effect and the suppression of charge recombination. By combining differently colored PV cells, arbitrary patterns or images can be obtained. Furthermore, a cascaded PV scheme based on tunable spectrum splitting can be employed to increase power efficiency by absorbing a broader band of light energy. This study pioneers a new approach to architecturally compatible and decorative thin-film PV [51,52, 73-77].

6.2 Amorphous Silicon (a-Si) PV Creating Reflection Colors

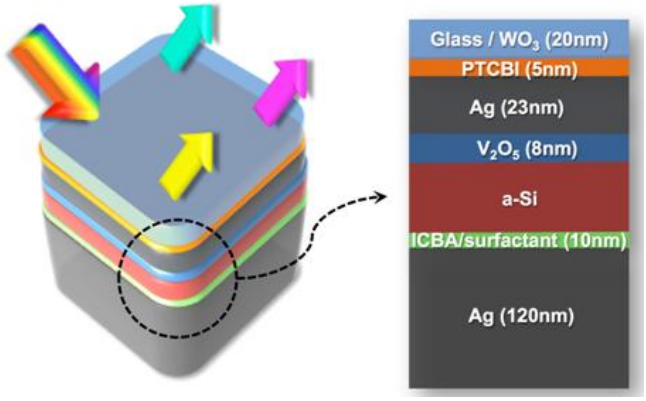

Figure 6.2.1 The device structure for the proposed dual-function hybrid cells. The cathode comprises a thick Ag layer and an organic layer, and a dielectric-metal structure is used for the anode. Between the two electrodes is an ultra-thin a-Si layer.

The dual-function a-Si/organic hybrid solar cells are constructed on transparent fused silica substrates. The main components of the hybrid cells are an anode, an ultra-thin a-Si layer, and a cathode with a thick Ag layer, as shown in **Figure 6.2.1**. For the anode, a dielectric-metal structure (i.e., WO_3-Ag) is used to produce relatively high transmission. Following the anode, a high work function vanadium oxide (V_2O_5) [78] serves as a hole-transporting layer for the undoped a-Si and simultaneously blocks electrons.

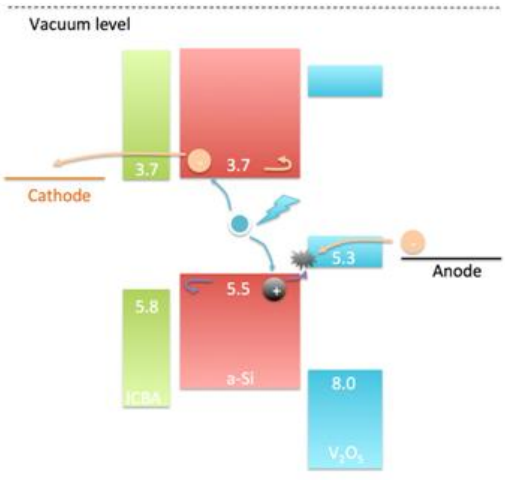

Figure 6.2.2 The band diagram of an a-Si photoactive layer interfaced with ICBA and V_2O_5.

Following the deposition of the a-Si layer, a thin organic layer of indene-C_{60} bisadduct (ICBA) is deposited to serve as an electron-transporting layer for the a-Si because its lowest unoccupied molecular orbital (LUMO) is well aligned with the a-Si conduction energy band, as shown in **Figure 6.2.2**. Another organic material of bis-adduct fullerene surfactant (C_{60} surfactant) is spin cast on top of the ICBA to lower the Ag work function, thus forming an ohmic contact between the ICBA and the thick Ag cathode. All anode and cathode materials, except the ICBA, were thermally evaporated with the same thicknesses, regardless of the device type, without breaking the vacuum below $1x10^{-6}$ mbar. The ICBA was spin cast. The undoped a-Si layers were deposited using a PECVD tool for colored PV devices. An anode of WO_3/Ag was thermally deposited onto a fused silica substrate, producing a sheet resistance below 6 ohm/sq. In the same chamber, without breaking the high vacuum (10^{-6} mbar), V_2O_5 was deposited at a rate of 0.2 Å s^{-1} to form a hole-transport layer. An undoped a-Si photoactive layer was deposited at 240 ℃ using SiH_4 gas in a PECVD apparatus with 13.56 MHz RF power. To create electron-transporting and Ag work function tuning layers, ICBA/chlorobenzene solution and C_{60} surfactant were then spin cast onto the a-Si layer. Finally, thick Ag was thermally evaporated on top of the previous layers as a cathode electrode and a strong reflector.

In the anode structure, a thin Ag layer (23 nm) forms a semi-transparent anode and also provides sufficient reflectivity to form the F-P resonance with the thick Ag cathode reflector. Additionally, the thickness of the Ag determines the conductivity of the anode, of which the sheet resistance is below 6 ohm/sq. A wetting layer, PTCBI, is utilized for the formation of a continuous Ag film, which can reduce the scattering loss significantly. Although the band gap of PTCBI is 2.2 eV, it is found that the absorption loss of a few-nanometer PTCBI layer is trivial. We should note that

the behavior is quite different if the PTCBI is replaced by Ge, a commonly used seed layer for thin Ag films, as Ge causes much more significant absorption in the visible range.

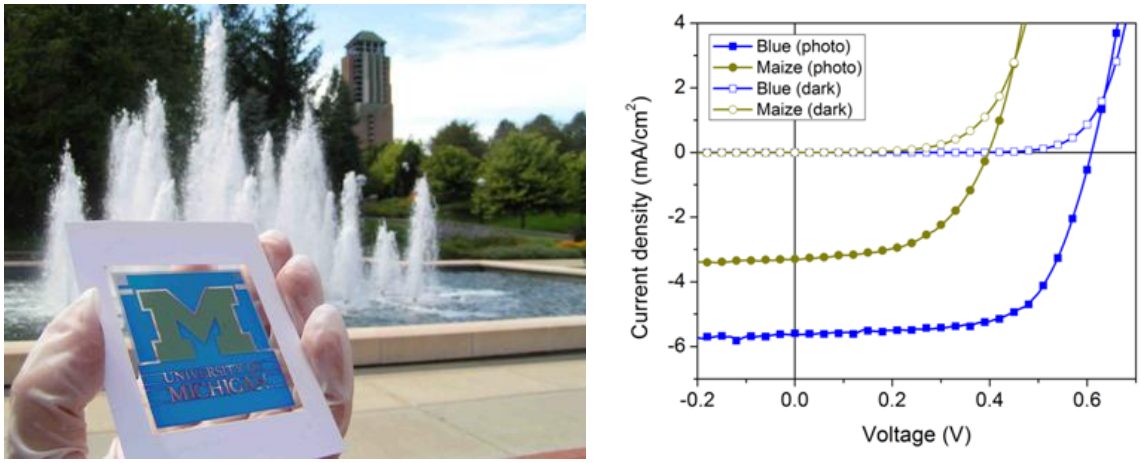

Figure 6.2.3 (a) The University of Michigan logo, consisting of maize and blue colors, is successfully realized with the generation of electric power. (b) Current density vs. voltage (J-V) characteristics of the maize-and-blue-colored, 1 mm diameter devices under AM1.5 illumination.

As a demonstration (**Figure 6.2.3 (a)**), we fabricated an electric-power-generating University of Michigan logo (3 inches by 2.3 inches). The vivid maize and blue colors are evident in the image. The J-V performances of the 1 mm diameter devices are depicted in **Figure 6.2.3 (b)**. In principle, any colored image can be designed using shadow masks and colored PVs.

Figure 6.2.4 Images of the fabricated devices displaying vivid cyan, magenta, and yellow (CMY) colors. The colored cells clearly demonstrate angle-insensitive performance at large angles of incidence (15°, 30°, and 60°).

In a typical F-P resonator based on a transparent medium, the resonance wavelength blue-shifts when the incidence angle increases because of the increase in the propagation phase in the dielectric medium. This angle-dependent color appearance is not desirable for colored PV panels. However, our PV cells display strong, angle-independent colors. Photographs of the fabricated colored PVs at various angles of incidence (15°, 30°, and 60°) are provided in **Figure 6.2.4**, and the CMY colors exhibit high contrast and do not change their color appearance even at high viewing angles. The reason for the strong, angle-independent resonance that is observed is as follows. For a highly absorbing material (e.g., a-Si, for which the imaginary part of the refractive index is comparable to the real part at visible frequencies), the phase change upon the reflection at the interface between an optically lossy medium and a metal varies from 0 to π because of the complex refractive index of the metal in the visible range and the large absorption of the lossy medium, which is markedly different from the case of a transparent medium. These non-trivial reflection phase changes enable the desired resonance to be created in an ultra-thin cavity where the thickness of the absorbing material is much smaller than the wavelength of the incident light. Our PV cell exploits this property to produce an angle-insensitive color appearance because the propagation phase through the ultra-thin Si layer is reduced and can be partially cancelled out by the reflection phase shifts at the interface between the a-Si and the metal.

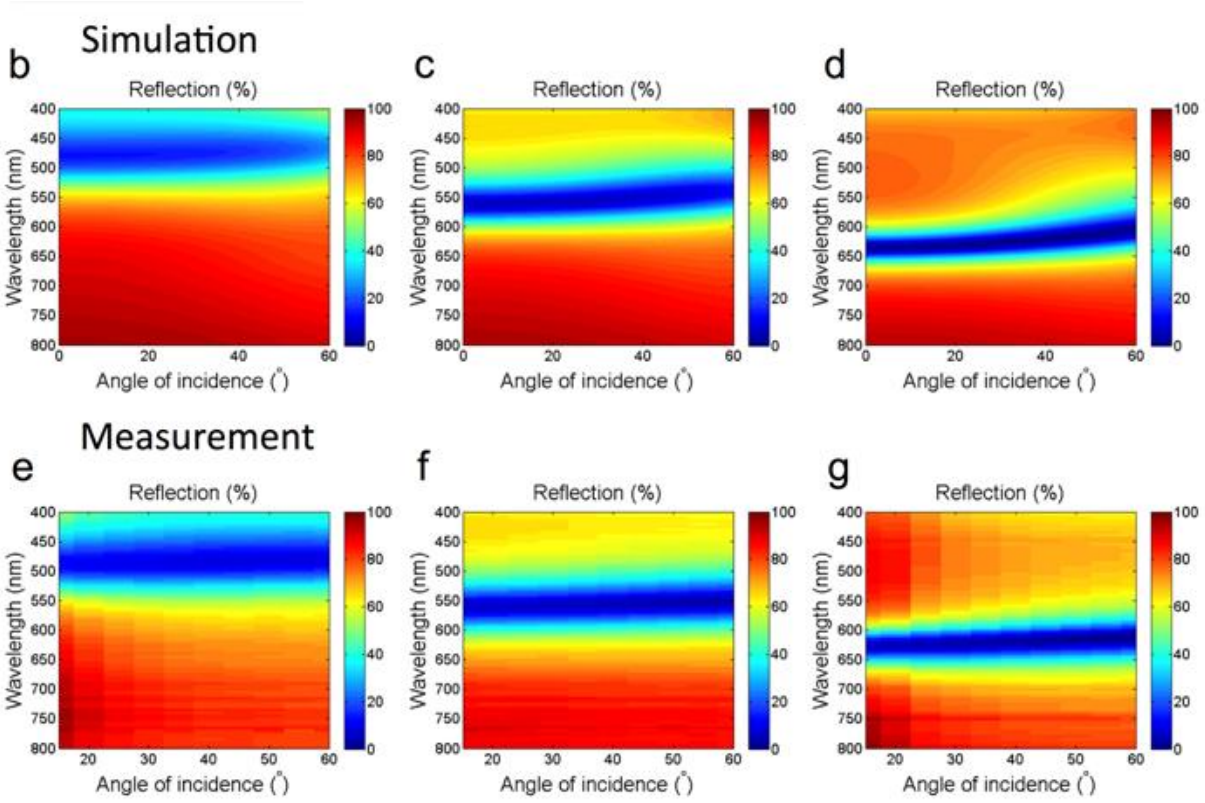

Figure 6.2.5 (b) – (d) Dispersion curves (for TM-polarized light) obtained through simulation (transfer matrix method) for yellow (10 nm), magenta (18 nm), and cyan (27 nm), respectively. The flat dispersion curves indicate that the devices have low sensitivity to angles of incidence ranging from 0° to 60°. The color maps represent the intensity values for the reflected light. (e) – (g) Experimental dispersion curves measured using an ellipsometer and corresponding to those in (b) – (d).

A numerical analysis of the reflected spectra at various angles was performed using a transfer matrix method, and the results are presented in **Figure 6.2.5 (b) – (d)**. The resonance (reflection dip) of each color is invariant with respect to the angle of incidence for angles of up to 60°, as indicated by the flat dispersion curve. Experimentally, these angular behaviors were measured and confirmed using a variable-angle spectroscopic ellipsometer (VASE, J. A. Woollam Co.) for angles of 15° to 60° under TM-polarized light illumination, as illustrated in **Figure 6.2.5 (e) – (g)**. The measured reflected responses at the various angles agree well with the results of the simulation.

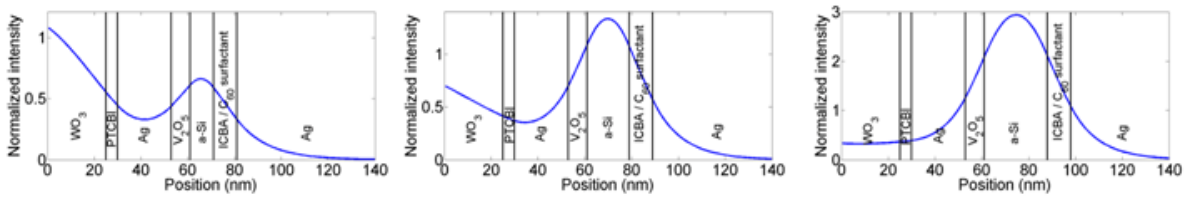

Figure 6.2.6 The normalized intensity distribution of the electric field inside the a-Si layer at the resonance for each individual color.

In addition, the light absorption is strongly confined within the thin a-Si layer at the resonance wavelength (**Figure 6.2.6**), facilitated by the higher *n* and *k* values of a-Si compared with the other layers. The high concentration of the field within the a-Si film contributes to the photocurrent generation.

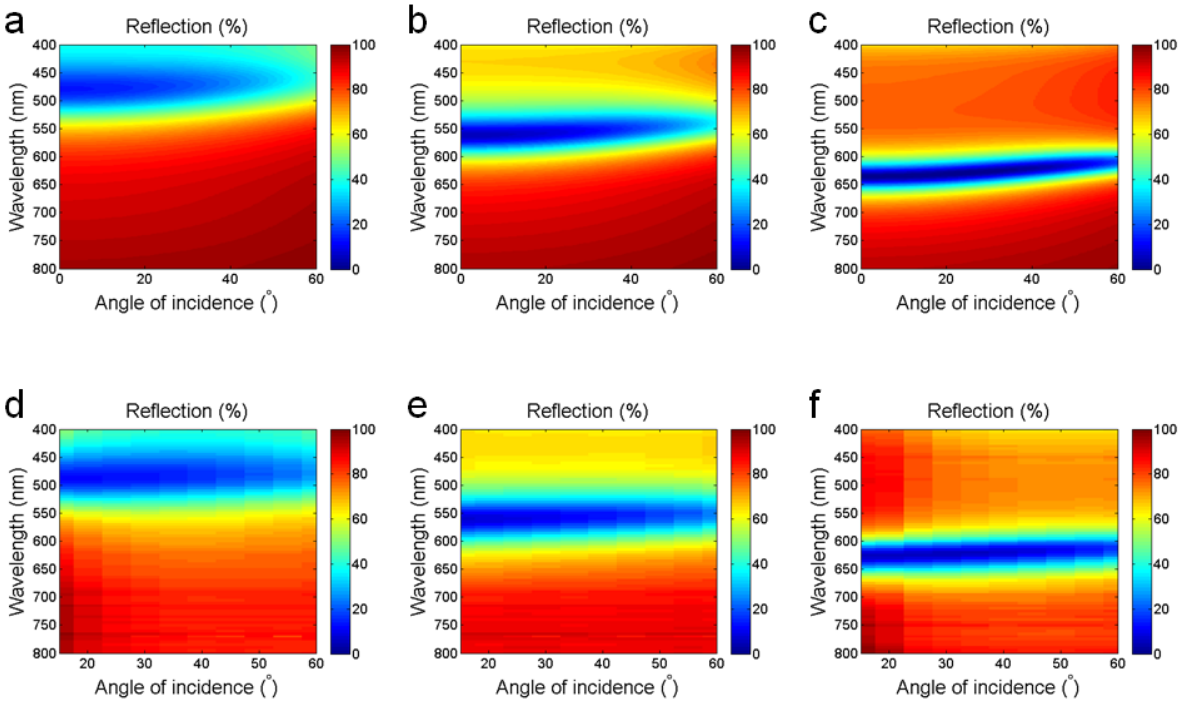

Figure 6.2.7 Simulated ((a) – (c)) and measured ((d) – (f)) angular dependences for TE polarization.

Another key feature of our designed colored cells is their low sensitivity to the polarization state of the incident light, which means that light of any polarization can be fully absorbed by the a-Si active layer and thus contribute to the photocurrent generation, which is a highly desirable feature, as sunlight and ambient light are mostly unpolarized. In **Figure 6.2.7**, the angular dependence for TE-polarized light is also presented.

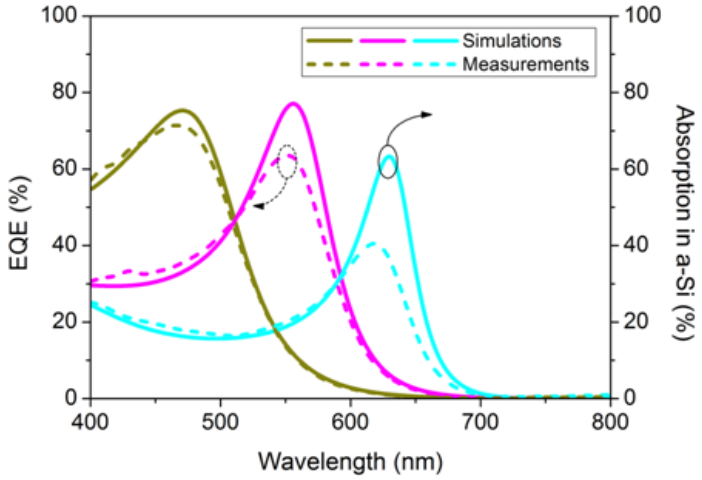

Figure 6.2.8 Measured external quantum efficiency (EQE) spectra and simulated absorption profiles of the a-Si layers for three individual colors: CMY.

Next, we discuss the benefit of the hybrid cell structure without doped p and n layers in the a-Si cell. The thin organic and metal-oxide interfacial layers have much lower refractive indices than do doped a-Si layers and therefore do not significantly affect the optical resonance. Moreover, they also facilitate the extraction of the photogenerated charge to the electrodes with significantly reduced recombination. In **Figure 6.2.8**, the simulated absorption spectra of the a-Si active layers for the CMY colored cells are compared with the measured EQE values for these devices. On the whole, the two spectra match remarkably well. This finding indicates that most of the absorbed photons are harvested and contribute to the photocurrent with negligible electron-hole recombination. This high efficiency arises because the thickness of the active layer

is much smaller than the typical charge-diffusion length in a-Si, and therefore, most photogenerated charges are efficiently extracted to the electrodes via the organic/inorganic (electron/hole) transporting layers. For the magenta and cyan devices, the EQE spectra exhibit slightly lower profiles than the simulated absorption profiles for a-Si. This discrepancy is attributed to fabrication imperfections, such as physical defects and surface roughness, which affect the resonance behavior. In particular, the cyan color has the strongest resonance because of the lower absorption by a-Si at longer wavelengths; it is evident that a scenario with stronger interference (i.e., more round trips of light reflected by the two electrodes) can be more strongly affected by defects and imperfections.

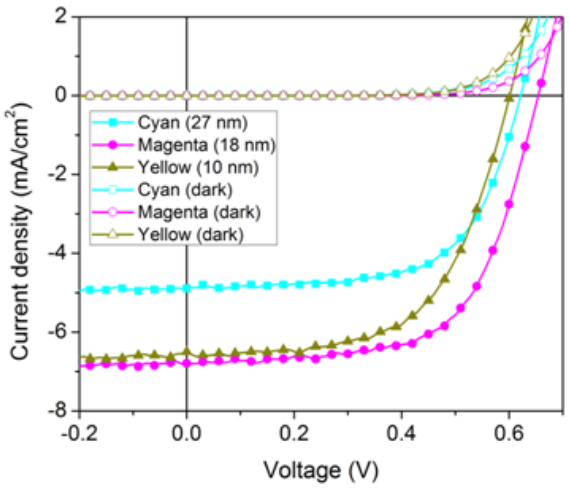

Figure 6.2.9 Measured J-V characteristics of individual colored cells under both AM1.5 illumination and dark conditions.

Considering the EQE characteristics of the hybrid cells shown in **Figure 6.2.8**, we expect fairly similar electric-current performance from the yellow cell (10 nm) and the magenta cell (18 nm), even though their thicknesses differ by nearly a factor of two. This expectation is supported by the electrical characterization, which is presented in **Figure 6.2.9**.

The J-V curves displayed in **Figure 6.2.9** represent the average efficiency performance measured for multiple devices of each color type (CMY). For all devices, the measured short-circuit currents presented in **Figure 6.2.9** agree with the integrated EQE results presented in **Figure 6.2.8**. The yellow device has a very similar current density (6.50 mA cm^{-2}) to the magenta one (6.79 mA cm^{-2}), with a comparable fill factor of above 60 %. This result is consistent with the similar integrated EQEs seen in **Figure 6.2.8** for the yellow cell (10 nm) and the magenta cell (18 nm) despite their difference in thickness. Importantly, the magenta device generates a power efficiency of nearly 3 % with an undoped a-Si active layer of only 18 nm in thickness. This is a remarkable result when compared with the record 10 % efficiency obtained for a single-junction cell using a 250 nm intrinsic a-Si layer, which is over 10 times thicker than our device. This result demonstrates that the efficient photon management achieved through the establishment of optical resonance and the reduced charge recombination in ultra-thin a-Si plays a crucial role in our dual-function cells. More detailed information concerning the power efficiencies of the three types of devices is summarized in **Table 6.2.1**. Notably, all three types of devices, regardless of their thickness (10 - 27 nm), operated well, with fill factors over 60 %. The electrical performance of our colored PVs was characterized through J-V measurements. Circular-shaped devices of 1 mm in diameter were tested under illumination with AM1.5 simulated sunlight (100 mW cm^{-2}). The intensity of the light was uniformly distributed throughout the cell area by the optical setup. A Keithley 2400 instrument was used for the data acquisition of the current and voltage values during J-V characterization. The power conversion efficiency of each colored cell was determined from the average values of Jsc, Voc, and FF of multiple cells on the same substrate.

Table 6.2.1 Summary of power conversion efficiency of colored CMY cells.

	Efficiency (%)	Jsc (mA/cm^2)	Voc (V)	FF (%)
Cyan device	**1.92**±0.01	**4.89**±0.11	**0.62**±0.02	**63**±0.89
Magenta device	**2.80**±0.22	**6.79**±0.19	**0.65**±0.02	**64**±1.98
Yellow device	**2.36**±0.12	**6.50**±0.24	**0.60**±0.01	**61**±3.13

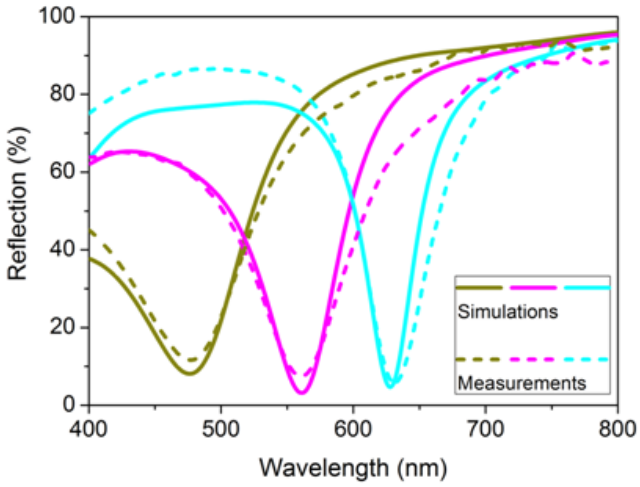

Figure 6.2.10 Simulated (solid lines) and measured (dotted lines) reflection spectra of the CMY devices at normal incidence. The thicknesses of the a-Si layer for the CMY colors are 27, 18, and 10 nm, respectively, given fixed thicknesses of all the other layers as shown in Figure 3.3.1.

Now, we discuss the optical design principle. In the ultra-thin hybrid structures described above, because of the strong F-P resonance formed between the reflecting electrodes, the device produces high absorption of a certain wavelength component while reflecting the complementary spectrum. By simply varying the thickness of the a-Si layer inside the F-P resonator, different colors can be obtained. For example, to create the CMY colors, a-Si layers of 27, 18, and 10 nm in thickness were used, respectively, and the corresponding resonances (reflection dips) are observed at 630, 560, and 480 nm. **Figure 6.2.10** presents the measured and simulated reflection spectra at normal incidence, which exhibit excellent agreement. It is worth noting that the

imaginary part of a-Si becomes insignificant at longer wavelengths, which results in lessened propagation loss through the a-Si film and a correspondingly narrower bandwidth. Therefore, the cyan-colored device has the sharpest resonance among the three colors represented in **Figure 6.2.10**. For optical performance characterization, the reflection spectra of the colored PV cells at normal incidence were measured using a spectrometer (HR4000CG, Ocean Optics). A halogen lamp was used as a white light source.

Simulations of the electric field profiles, the reflection, the absorption in the a-Si layer, and the angular dependent spectra were performed using a transfer matrix method. Broadband white light from 400 nm to 800 nm was used as the input illumination. The complex wavelength-dependent optical constants of all materials were measured using a spectroscopic ellipsometer (M-2000, J. A.) with a B-spline fitting function and were then used in the simulations.

Figure 6.2.11 A photograph of the devices reflecting CMY colors.

The photographs displayed in **Figure 6.2.11** show the CMY colors reflected by our devices against a background of a tower on the university campus. The devices for the evaluation of both optical and electrical performance were all fabricated using the same process.

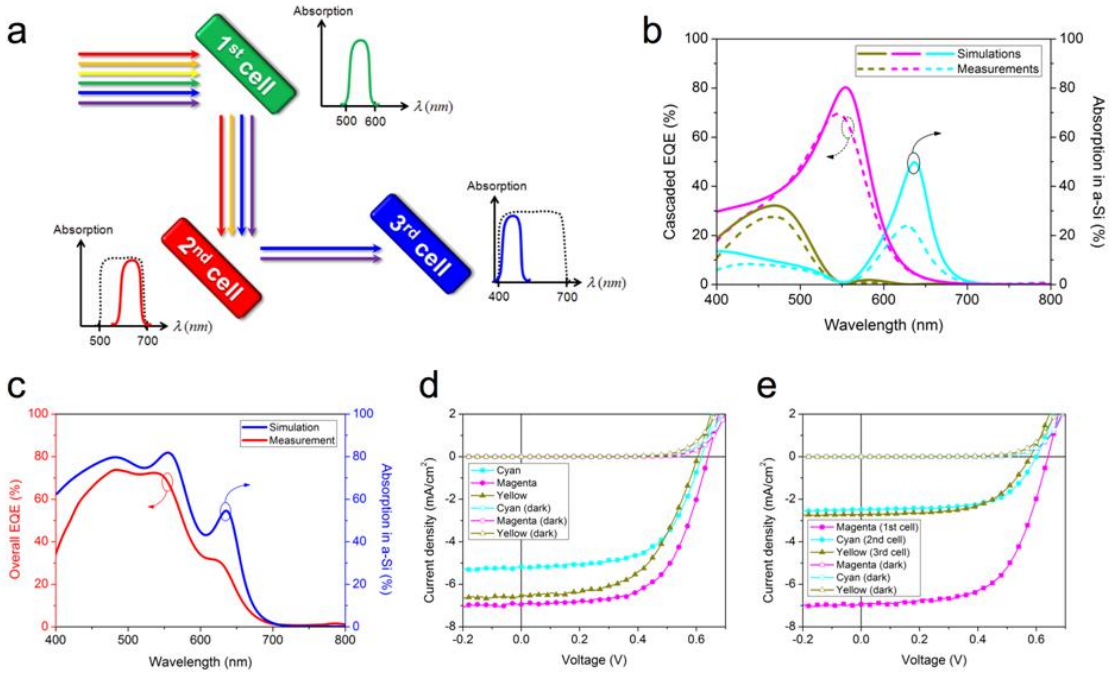

Figure 6.2.12 (a) A schematic illustration of the arrangement of each cell. The light is reflected by the first cell, which predominantly absorbs the green portion of the spectrum (thus reflecting a magenta color that encompasses the blue and red spectral regions), and passes into the second cell, which has a resonance that corresponds to an absorption peak in the red region and harvests longer-wavelength components. By adding a third cell that reflects with a yellow color (has an absorption peak in the blue region), the remaining incident light, which still contains a strong blue spectral component, can be recycled. (b) After the application of the cascaded platform, the experimentally achieved EQE data and the corresponding numerical absorption spectra in ultra-thin a-Si layer are illustrated. (c) The overall EQE profile obtained by summing the three individual EQE spectra and, for comparison, the corresponding simulated result for the total absorption in the three a-Si layers. (d) J-V characteristics of the individual CMY cells under AM1.5 illumination. (e) J-V performance of the three cells as measured in the cascaded platform, depicting photon recycling for the generation of electric current in consecutive cells.

Finally, we suggest another innovative use of our colored reflection-type PVs. Recently, increasing interest has arisen in the use of the spectrum-splitting approach to spread the solar spectrum into multiple bands and use semiconductor PVs with the appropriate band gap for each band. This approach has the potential to yield record high efficiency without the need of engineering sophisticated vertical tandem cell structures for broadband absorption. However, spectrum-splitting approaches always require a specifically designed external element to spread

the spectrum, such as a filter [79], grating [80], prism [81], or beam splitter [82]. Such an external element is not required for our proposed cascaded configuration, as shown in **Figure 6.2.12 (a)**: because of its strong resonance behavior, our colored PV device can absorb a certain spectral band of solar light and naturally reflect its complementary spectrum, which can be harvested by another cell with a different resonance wavelength. Simply altering the thickness of the a-Si layer in the PV cell enables the resonance to be shifted in a controllable manner. The angle-insensitive behavior of these devices is also advantageous for cascading multiple stages of PV cells. As a demonstration, we constructed a cascaded solar cell platform based on spectrum splitting, as illustrated in **Figure 6.2.12 (a)**, to span a wide range of wavelengths. We designed and fabricated three cells with different thicknesses of a-Si such that they exhibit different resonances. The light is incident at an oblique angle on the first cell, which absorbs the green band and hence reflects its complementary colors. The longer wavelengths in the unabsorbed spectrum are re-utilized by the second cell, whose resonance is at 630 nm. Finally, the third cell harvests the remaining photons in the blue region. Note that the color of each cell in **Figure 6.2.12 (a)** represents its primary absorption region. The accumulated absorption spectra are represented by dotted curves.

To study the optical and electrical characteristics of the cascaded system, we calculated the absorption spectra in the a-Si and measured the EQEs of the three cells, which are compared in **Figure 6.2.12 (b)**. In general, the calculated spectra are quite consistent with the experimental EQE data, with some discrepancy at longer wavelengths, as explained above (see the discussion related to **Figure 6.2.12 (a)**). From the overall EQE and a-Si absorption spectra depicted in **Figure 6.2.12 (c)** (sum of three profiles), it is evident that a broad range of incident light from 400 to 700 nm can be harvested to generate electric power, thereby validating the cascaded-cell

concept. We also investigated the J-V characteristics of the individual cells (**Figure 6.2.12 (d)**) and the cascaded system (**Figure 6.2.12 (e)**), the latter of which clearly demonstrate that the short-circuit current densities of the second and third cells become further reduced as each consecutive cell receives a lesser amount of light for a-Si absorption compared with the first cell. We should note that even longer wavelength ranges can be harvested by employing lower band gap semiconductor materials in subsequent cells.

6.3 A-Si PV Generating Transmission Colors

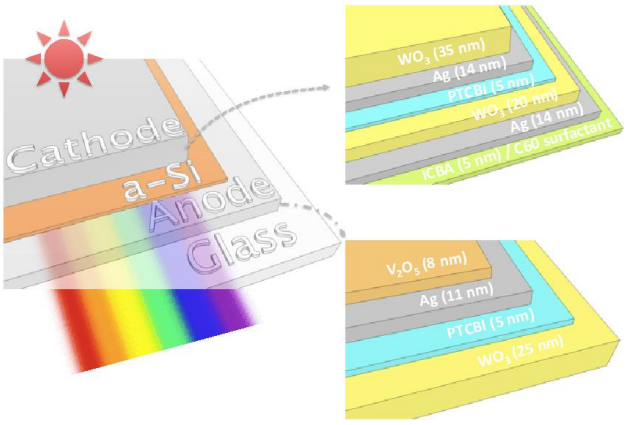

Figure 6.3.1 A schematic diagram of the proposed structure consisting of cathode, anode, and ultra-thin undoped a-Si layer. The cathode is composed of dielectric-metal-dielectric (DMD) and organic layers, and only DMD structure for the anode. The ultra-thin a-Si layer thickness is 6, 11, and 31 nm for blue, green, and red, respectively.

The ultra-thin a-Si/organic hybrid solar cells are built on fused silica substrates, comprising an anode, an ultra-thin a-Si layer, and a cathode as shown in **Figure 6.3.1**. The anode structure is designed to transmit a wide range of wavelengths. The electrodes are derived from the dielectric-metal-dielectric (DMD) structures that were developed as ITO-free transparent electrodes [83, 84]. For the anode, the metal and dielectrics are Ag, WO_3 and vanadium pentoxide (V_2O_5). In

particular V_2O_5 is interfaced with a-Si and utilized as a transporting layer for the photogenerated holes due to its high work function. A thin Ag (11 nm) is sandwiched between the two dielectric layers in the anode; here the Ag thickness determines the conductivity of the electrode, of which a sheet resistance below 10 ohm/□ is obtained. PTCBI is used as a wetting layer underneath the Ag in order to form a smooth and continuous Ag thin film. We did not use Ge as the wetting layer for Ag due to its strong absorption in the visible range [85].

The cathode begins with a thin organic layer, indene-C_{60} bisadduct (ICBA) [86], which operates as a very efficient photogenerated electron transport layer as its lowest unoccupied molecular orbital (LUMO) level well aligned with a-Si conduction energy band. The ICBA is followed by another organic material of bis-adduct fullerene surfactant (C_{60} surfactant) [87], which effectively lowers the Ag work function and forms ohmic contact for the electrons. The cathode is completed with the combination of Ag and WO_3 with different thicknesses according to our theoretical calculation (**Figure 6.3.1**). All the anode and cathode materials, except ICBA and C_{60} surfactant, were thermally evaporated consecutively without breaking the vacuum (base pressure 1×10^{-6} mbar). The ICBA and C_{60} surfactant were spin casted all in the same conditions as well. The undoped a-Si layers were deposited by using a PECVD tool. To produce the blue, green and red colors, 6, 11, and 31 nm of a-Si were deposited, respectively.

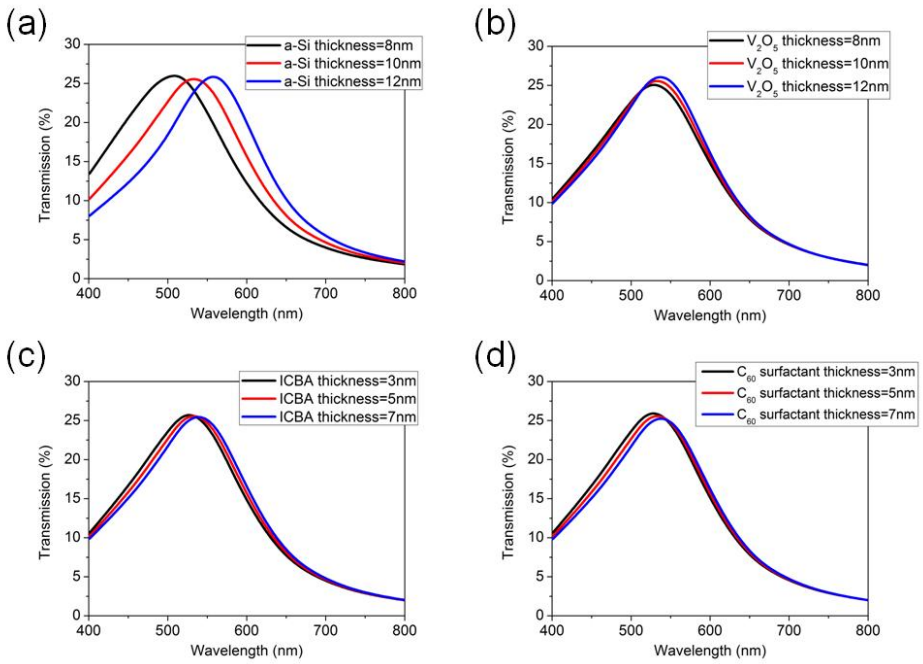

Figure 6.3.2 Simulated transmission spectra for different thickness of (a) a-Si layer (b) V_2O_5 layer (c) ICBA layer (d) C_{60} surfactant.

In our design, a thin Ag layer is added to increase the reflection at the interface between Ag and V_2O_5 and consequently a Q-factor yielding a narrow resonance bandwidth. Ag is selected for both top and bottom electrode since Ag has the highest reflectivity and the lowest absorption at visible frequencies. A strong resonance behavior arises from the cavity comprising a highly lossy material, a-Si, sandwiched by the two electrodes. Though ICBA, C_{60} surfactant, and V_2O_5 layers can contribute to the resonance, we found that the resonance is primarily determined by the a-Si layer due to the high refractive index of a-Si as exhibited in **Figure 6.3.2**.

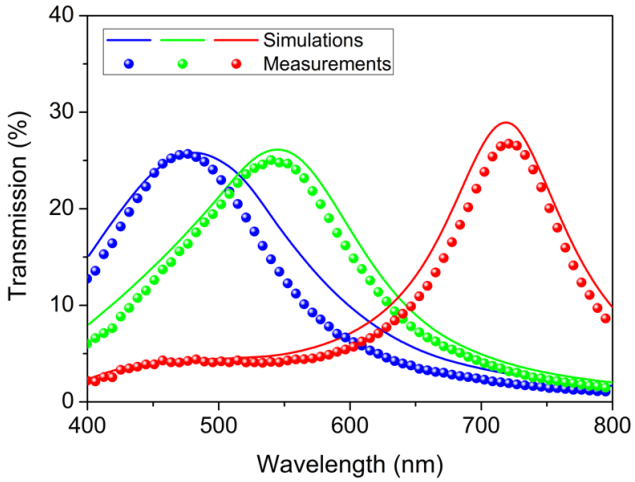

Figure 6.3.3 Simulated and measured transmission spectra of individual colors (blue, green, and red) at normal incidence.

The calculated (solid line) and the measured (dotted line) transmission spectra of individual colors of devices with varied a-Si thickness at the normal incidence are depicted in **Figure 6.3.3**. We performed all the optical simulation by using a transfer matrix method based on the measured indices of refraction of each material. The experimental spectra show an excellent agreement with the simulated profiles. The a-Si thicknesses of 6 nm, 11 nm, and 31 nm determine the transmission peaks located at 478 nm (blue), 542 nm (green), and 720 nm (red), respectively, while the thicknesses of all other layers remain the same for all devices.

Figure 6.3.4 Photographs of distinct blue, green, and red colors by the fabricated devices.

The photograph images of fabricated samples are shown in **Figure 6.3.4**. It is obvious to see the water fountain and buildings through our devices with distinct colors. It is noteworthy to mention that there is no change in color even with oblique angles of incidence, which will be discussed more in detail in the following section. This simplicity of the fabrication process involving only film deposition can be easily scaled to large area substrate for industry level production.

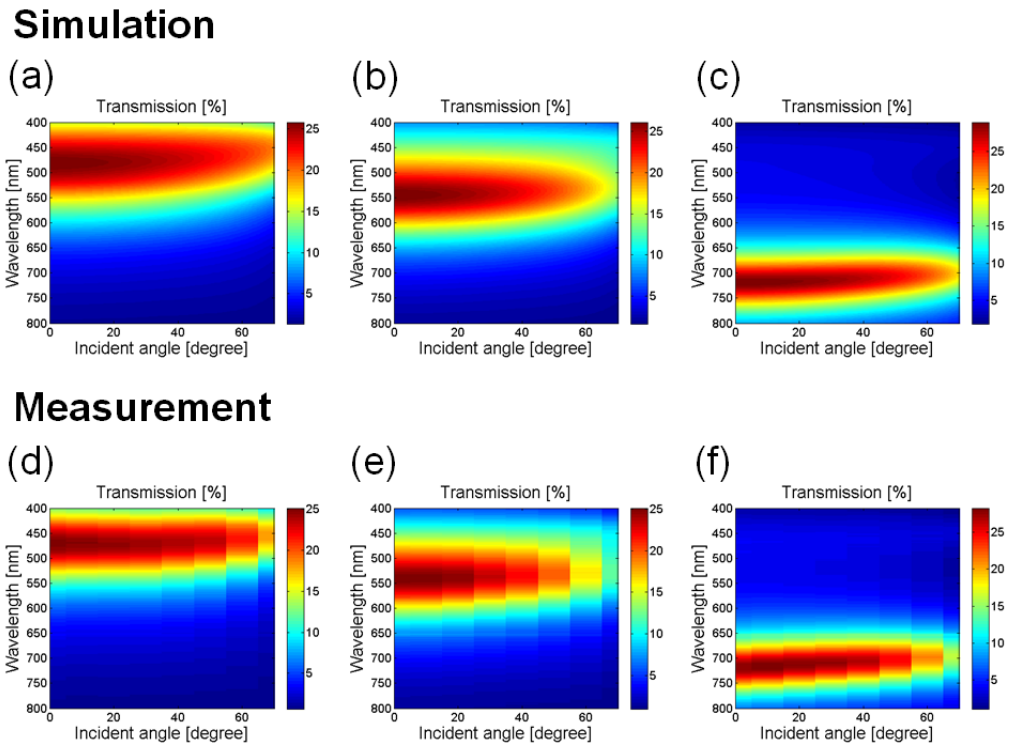

Figure 6.3.5 Simulated and measured angular dependence under unpolarized light illumination. (a) - (c) Calculated angular behaviors of blue (6 nm), green (11 nm), and red (31 nm) devices, respectively, showing that the resonance corresponding to the peak (red in the color map) in the transmission spectra remains at fairly same level over a relatively wide range of incidence angle up to 70°. The color bars denote how much the light is transmitted through the whole device. (d) - (f) Measured incidence angle dependence corresponding to those in (a) - (c).

To investigate the angular dependence of our decorative panels, we performed a simulation: the calculated dispersion curves are illustrated in **Figure 6.3.5 (a) – (c)**. The flat dispersion curves indicate that the resonance wavelengths of the blue, green, and red colored devices are retained

up to ±70°. This angle insensitivity is experimentally verified by the measured transmittance of the devices for incident angle varying from 0 to 70° under unpolarized light illumination (**Figure 6.3.5 (d) – (f)**), which showed excellent agreement with the calculated profiles. As noted earlier the resonant wavelength in conventional F-P cavity is inherently related to the angle of incidence. The angle robustness of our devices are due to the use of ultra-thin a-Si, which results in relatively insignificant phase change accumulated as light propagates through the a-Si layer as compared to the phase shift upon reflection at the interface. Thus the resonance can remain fairly unvaried as the angle of incidence increases. The angle robustness and wide angle acceptance is also beneficial for the solar panel deployment in which no external sun tracking systems are needed. Another important feature of our device is the polarization independence. As all common light sources, including the sun, fluorescent, and ambient light, produce unpolarized light, our proposed devices can utilize all sources of light to generate electricity efficiently. The angular dependences for both TE and TM polarizations were explored as well and can be found in **Figure 6.3.6 and 6.3.7**, respectively.

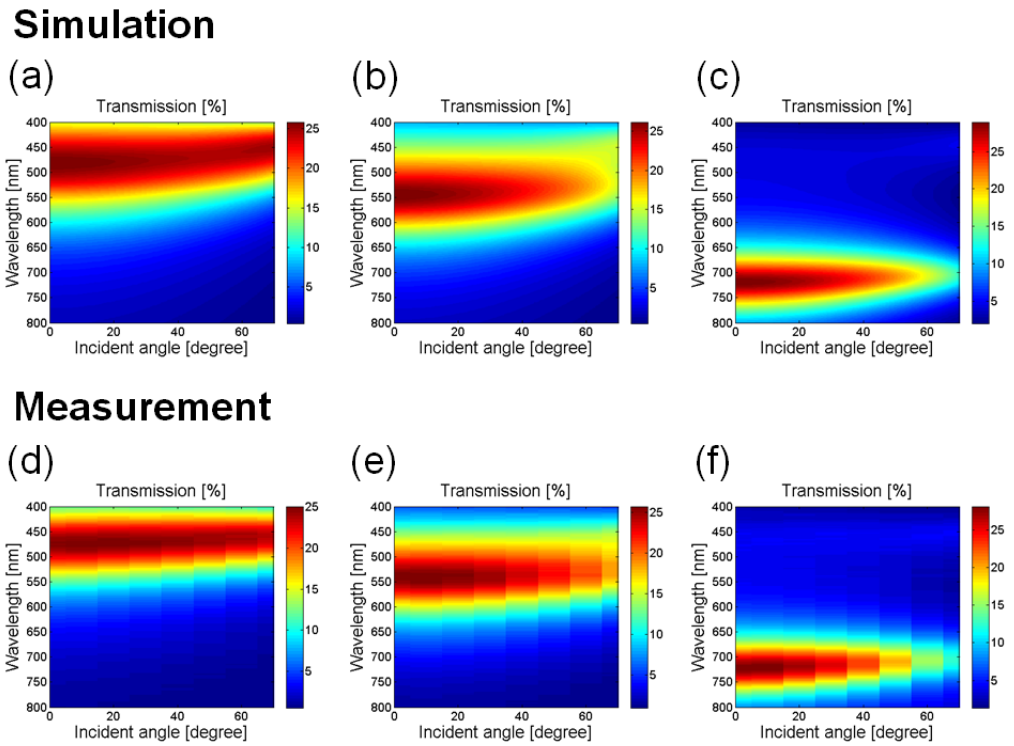

Figure 6.3.6 Simulated (a-c) and measured (d-f) angle resolved transmission spectra for TE polarization.

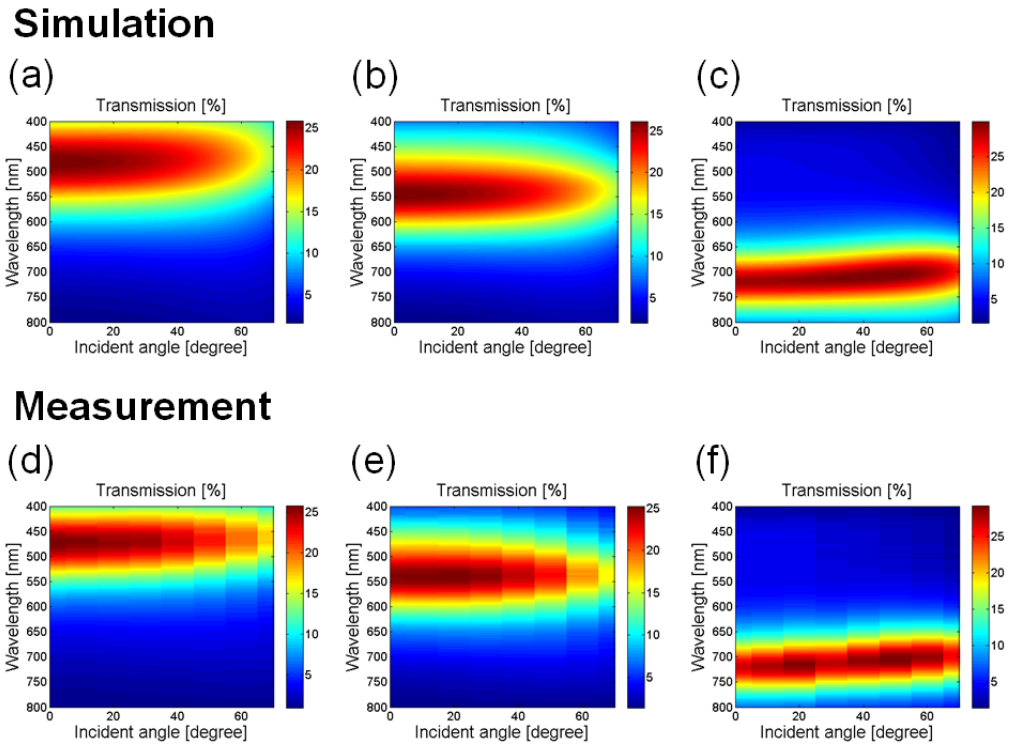

Figure 6.3.7 Simulated (a-c) and measured (d-f) angle resolved transmission spectra for TM polarization.

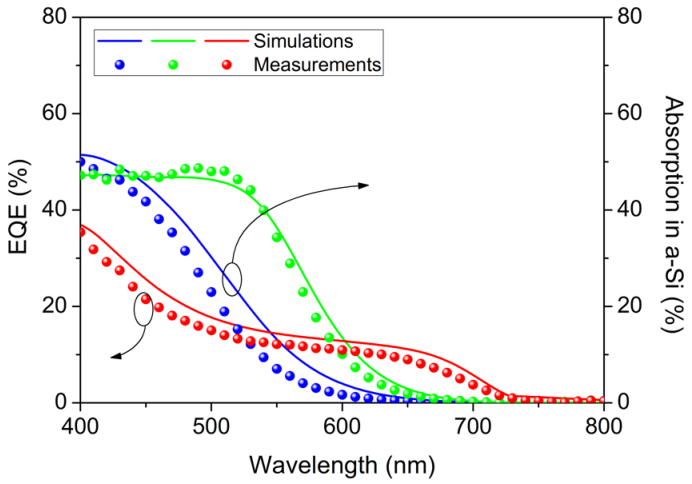

Figure 6.3.8 Comparison of calculated incident light absorption profiles by ultra-thin a-Si layer and measured external quantum efficiency (EQE) spectra for three different types of devices (blue, green, and red)

For the blue, green, and red device types, absorption spectra of a-Si active layers versus wavelength were calculated as shown in **Figure 6.3.8**. Remarkably, the electrically measured external quantum efficiency (EQE) profiles are well matched with the calculated absorption spectra. The EQE spectrum represents actual incident photon-to-charge conversion efficiency and is determined by the light absorption by the active layer and the internal quantum efficiency of the photoactive/transporting layers. The close match between the calculated a-Si absorption and the measured EQE curves implies that the internal quantum efficiency is approaching 100 %. This can be attributed to the strongly suppressed electron-hole recombination in our ultra-thin a-Si hybrid cells.

Regardless of device types (blue, green, or red), the a-Si layer thickness is much thinner than the typical charge diffusion length in a-Si [88, 89] so most photogenerated charges are extracted to the metal contacts through the electron and hole transporting layers. Furthermore the suppressed charge recombination can significantly mitigate the light-induced degradation, which

is a drawback of traditional a-Si solar cells [90-92]. Many previous studies have focused on optimizing p- and n- layer thicknesses to lessen the charge loss in the doped regions without sacrificing an internal electric field [93]. Our devices with undoped a-Si active layer do not suffer from the charge recombination with p- and n- dopants as in the traditional a-Si PV, which is one of major charge loss mechanism in p-i-n a-Si solar cells [93-95].

Because the EQE of our devices directly correlates with the calculated light absorption in a-Si layer, we can estimate the electric current from the simulated optical absorption spectrum in an active layer with good accuracy. As the total number of photons absorbed in the active layer is very similar to the total extracted charges, we can design the electric current performance of the solar cells simply based on the optical calculation before fabricating devices. Based on this understanding, an interesting finding is that we expect to obtain higher photocurrent from the green color cell than the red cell, even though the a-Si layer thickness for the former (11 nm) is much thinner than that of the latter (31 nm).

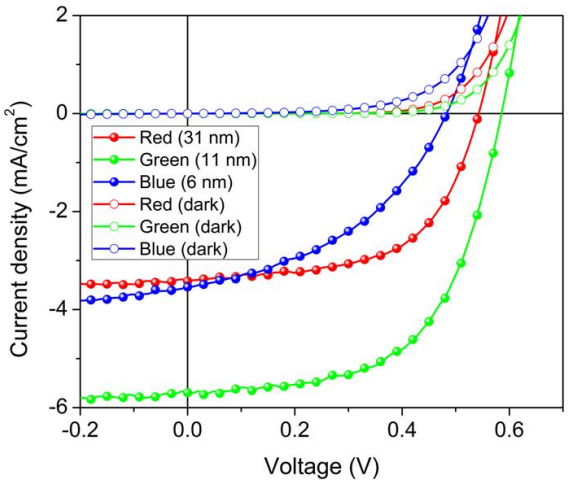

Figure 6.3.9 Current density-voltage characteristics of the hybrid cells under AM1.5 illumination and dark conditions.

To verify this prediction, we measured current density-voltage characteristics under AM1.5 illumination and dark conditions. The device measured has a diameter of 1 mm as in EQE characterization. The current density-voltage curves in **Figure 6.3.9** show the average efficiency performance of multiple devices for each type (red, green, or blue). As we expected from the calculated light absorption in the a-Si layer and EQE spectra previously, the green device has much higher current density (5.69 mA/cm^2) than the red one (3.42 mA/cm^2) with comparable fill factor (58~59 %). The green color device generates almost 2 % power efficiency by only 11 nm of a-Si active layer. This is a remarkable result if comparing with the ~10 % efficiency obtained in traditional a-Si PV with more than twenty folds a-Si thickness [96]. More detail power conversion efficiency factors of the three types of devices are summarized in **Table 6.3.1**.

Table 6.3.1 Summary of power conversion efficiency of colored RGB cells.

	Efficiency (%)	Jsc (mA/cm^2)	Voc (V)	FF (%)
Red device	**1.08**±0.02	**3.42**±0.09	**0.54**±0.01	**59**±0.88
Green device	**1.94**±0.10	**5.69**±0.18	**0.59**±0.01	**58**±1.95
Blue device	**0.73**±0.11	**3.54**±0.23	**0.48**±0.02	**43**±3.11

Most prominently, the blue color device with only 6 nm of a-Si active layer operated well as a solar cell even though the fill factor of the blue device is lower than the other types of devices. We presume that a few nanometer a-Si active layer of the blue device induces more electric charge leaking paths in the device area, thereby reducing shunt resistance of the solar cell compared to the red and green devices that have thicker a-Si active layers.

Experimentally, we confirmed that three types of devices (red, green, and blue) worked well for electric power efficiency, generating short circuit current density as designed in our optical simulation. Other thin-film inorganic materials can potentially borrow this novel concept of our hybrid cells for higher power efficiency, filtering various colors based on appropriate photon management in their active layers.

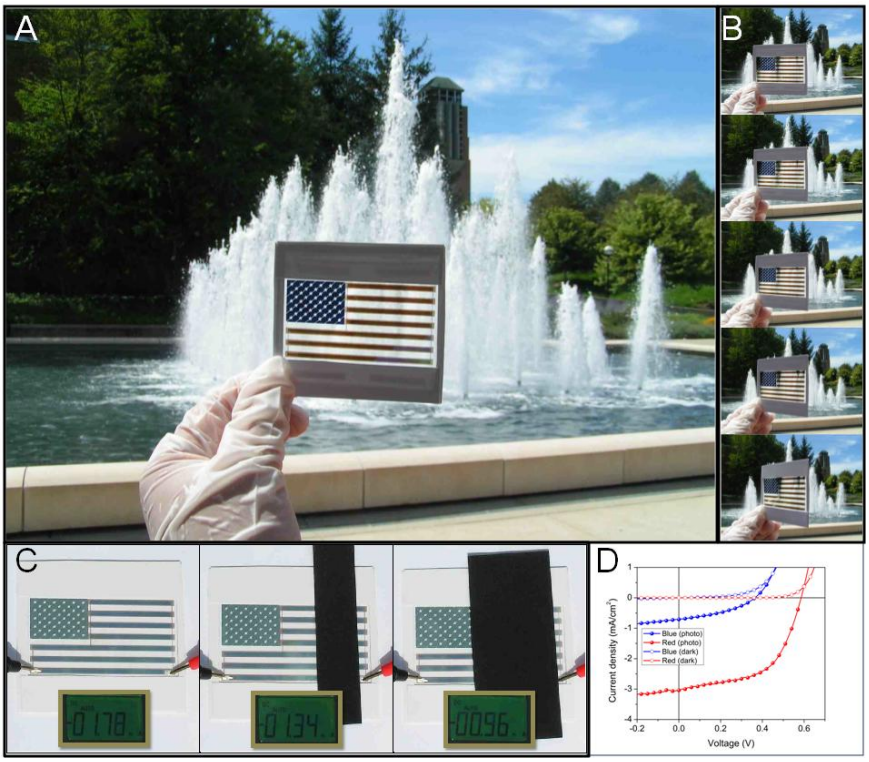

Figure 6.3.10 The demonstration of the electric power-generating national flag of the United States of America (U.S. flag). (a) Photograph of U.S. flag taken at the University of Michigan campus, showing distinct blue (6 nm) and red (31 nm) color patterns. (b) According to angle insensitive property, U.S. flag maintains its colors at oblique angles of incidence up to about 60°, manually controlled. (c) U.S. flag generates electric current as well under outdoor sunlight (less than AM1.5). The electric current level decreases as U.S. flag gets covered more by a piece of black paper. (d) Current density-voltage performances of blue and red colored 1 mm diameter devices under AM1.5 illumination.

As a further demonstration, we fabricated a 3 in × 2.3 in power-generating sample in the form of the national flag of the United States (U.S. flag) shown in **Figure 6.3.10**. The blue and red

regions of the flag use a-Si thickness of 6 nm and 31 nm, respectively, same as in the individual colored samples discussed earlier. In addition, an angle of incidence is changed from normal to 60° in order to verify the angle invariance performance of the power-generating U.S. flag. Indeed, the distinct blue background of the stars and the red stripes in the U.S. flag can maintain their respective colors at oblique angles of incidence as described in **Figure 6.3.10 (b)**.

In terms of electric power performance, the total colored regions (~1.5 in^2) of the U.S. flag generates almost 2 mA electric current under real outdoor sunlight (less than AM1.5) with full light exposure to the flag (**Figure 6.3.10 (c)**). When the flag is partially covered by a piece of black paper, the current level evidently drops by the ratio of the unblocked flag area. We also measured current density-voltage characteristics by 1 mm diameter devices in the same U.S. flag sample and presented in **Figure 6.3.10 (d)**. We note that the other transmission colors can be readily realized by simply tuning the a-Si layer thickness.

6.4 Neutral-Colored Semitransparent a-Si PV

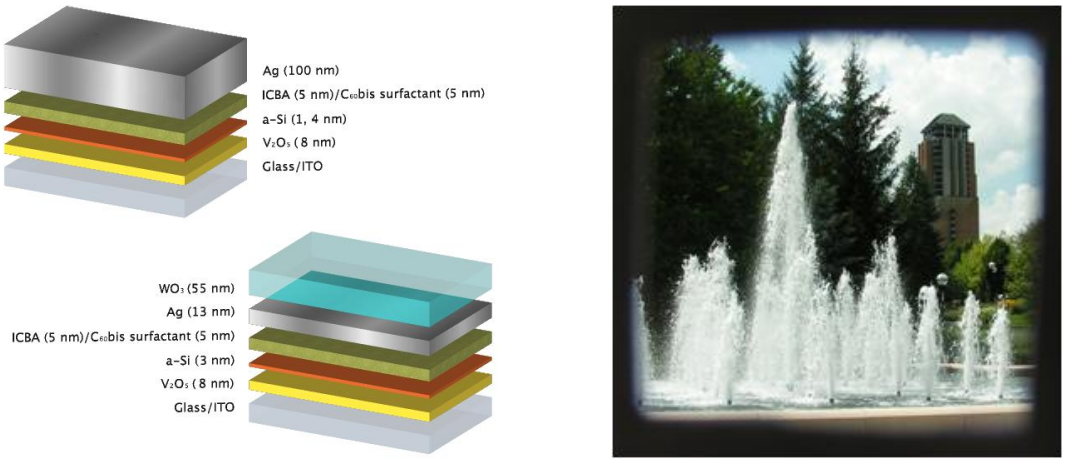

Figure 6.4.1 (a) A device structure of proposed a few nanometer-thick hybrid cells. A cathode comprises thick Ag or Ag (13 nm)-WO_3 (55 nm) with organic electron transport layers, and indium-tin oxide (ITO) with V_2O_5 (8 nm) hole transport layer for an anode. Between the two

electrodes, a few nanometer a-Si is located. (b) Image of the fabricated a-Si (3 nm) hybrid cells with Ag-WO_3 cathode shows obvious transparency (70 % average) enough to see a tower and a fountain through on campus.

The few nanometer-thick a-Si hybrid cells are fabricated on indium-tin oxide (ITO) substrates (**Figure 6.4.1 (a)**). The structures have V_2O_5 for holes transport and indene-C_{60} bisadduct (ICBA) for electrons, which are around 5 nm-thick for each. Followed by ICBA, another 5 nm organic material of bis-adduct fullerene surfactant (C_{60} surfactant) is used to reduce the work function of Ag electrode, offering ohmic contact between Ag and the electron transport layer. The two different thicknesses of a-Si photoactive layers, 1 and 4 nanometers, are used for photovoltaic device study. In addition, as a demonstration, we built a transparent a-Si (3 nm) inorganic/organic hybrid cells by properly designing Ag-WO_3 cathode (**Figure 6.4.1 (a)**) as illustrated in the device picture taken on campus (**Figure 6.4.1 (b)**).

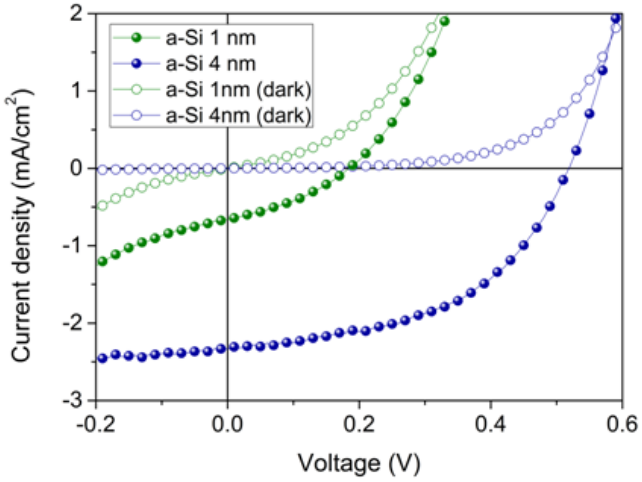

Figure 6.4.2 J-V characteristics of a few nanometer-thick a-Si hybrid cells under AM 1.5 simulated light (solid circle) and dark conditions (open circle). The thicknesses of a-Si are 1 nm and 4 nm with thick Ag cathode.

A single nanometer-thick a-Si hybrid cell performs as a diode responding to AM 1.5 simulated light compared to dark condition (**Figure 6.4.2**). Albeit its reverse current in dark shows less rectifying property, the device provides the short circuit current density (Jsc) and open circuit voltage (Voc) under light illumination, obviously manifesting that the single nanometer cell works as phovoltaics. We compared the performance of a 4 nm-thick hybrid cell in the same figure, which explains a few nanometer thicker a-Si photoactive layer helps the device give better photovoltaic characteristics.

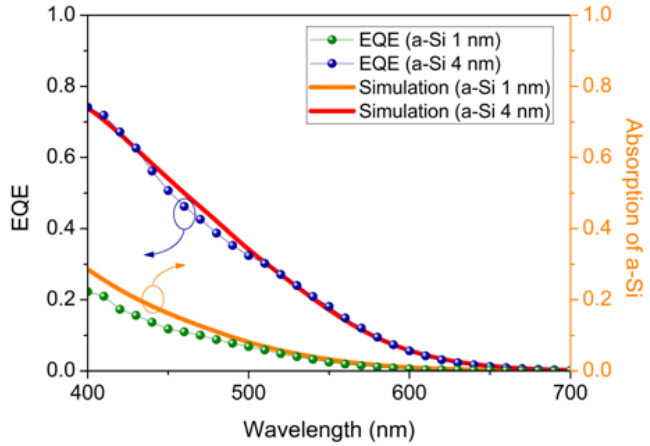

Figure 6.4.3 Calculated a-Si absorption (colored solid lines) and measured EQE (colored solid circles) of 1 and 4 nanometer-thick a-Si hybrid cells with thick Ag cathode.

EQE of the devices was also explored along with the numerically calculated a-Si absorption as shown in **Figure 6.4.3**. The EQE spectrum of 4 nm-thick cell fits very well with the a-Si absorption profile calculation proving that the extremely thin a-Si photoactive layer prevents any possible charge recombination processes. This also implies that all the photogenerated charges are extracted without recombination, which allows the ultra-thin PV devices perform in a designed manner. However, for a single nanometer-thick hybrid cell, we note that there is a slight discrepancy between EQE and a-Si absorption, especially at shorter wavelength region.

We believe that this is because the comparable thickness of a-Si to its surface roughness causes device pinholes as well as light scattering, which will be verified by device transmission and surface morphology measurements.

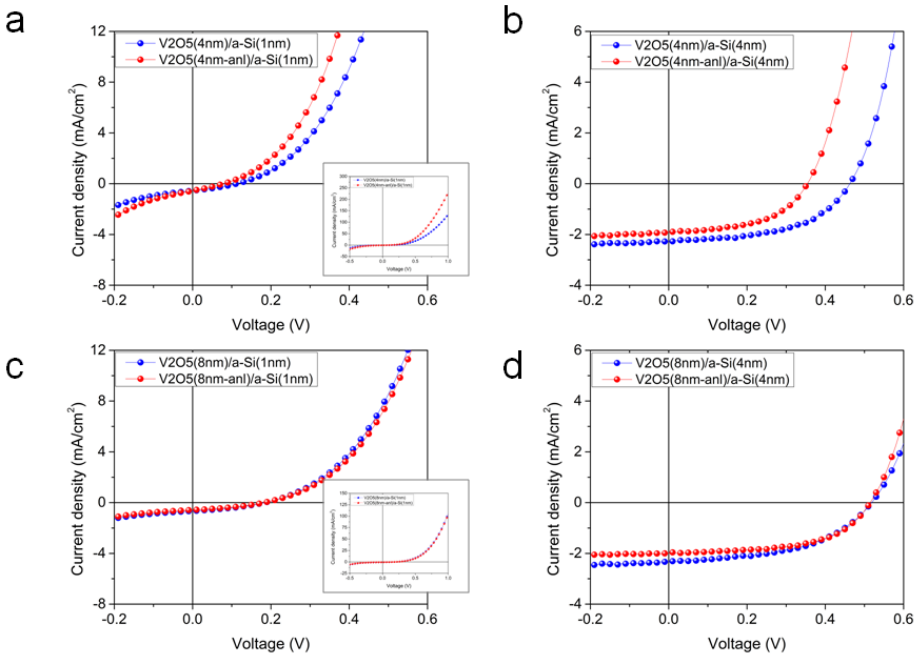

Figure 6.4.4 J-V characteristics of a few nanometer-thick hybrid cells with different properties of the hole transport layer. (a) A single nanometer-thick a-Si photoactive layer incorporates with two different conditions (non-anneal and thermal annealing at 300 ℃) of V_2O_5 (4 nm) in order to allow the hybrid cells to perform as light-responding diodes under AM 1.5 simulated light (inset: J-V curves under wider voltage bias range). The photoactive layer of a-Si (4 nm) is used for further verification of better photovoltaic performance in terms of Jsc and Voc in (b) and (c) A single nanometer-thick a-Si layer with V_2O_5 (8 nm) is studied by varying the hole transport layer (V_2O_5) properties as same as (a) and (b). With the same V_2O_5 properties, a 4 nanometer-thick a-Si is used instead in (d).

Since we utilize V_2O_5 hole transporting property instead of p-doped layer, we investigated further on device performances according to various anode conditions. As depicted in **Figure 6.4.4 (a) – (d)**, two different V_2O_5 thicknesses (4 and 8 nm), with or without 300 ℃ 10-minute thermal annealing process, are explored for J-V characteristics. All the devices are prepared as thermally evaporated V_2O_5 on ITO substrates, some of which are later annealed in a rapid

thermal annealing equipment. In case of 4 nm V_2O_5, the annealing process affects J-V performance in terms of Voc and Jsc, which is observed clearer in 4 nm a-Si devices. Even if the annealing of V_2O_5 still changes the device performance in 8 nm V_2O_5, the variation is comparably smaller than the 4 nm V_2O_5 devices.

We assume that the thermal annealing process changed V_2O_5 property mainly on the surface by nitrogen/oxygen gases but if V_2O_5 is too thin as 4 nm, whole layer property varies causing a big Voc change (**Figure 6.4.4 (b)**). As V_2O_5 thermal annealing is known to reduce its bandgap, inducing phase transition, we observe that V_2O_5 energy band levels play a major role in determining the Voc of the few nanometer-thick a-Si hybrid cells. Moreover, we discovered that the thickness of V_2O_5 is also important for higher Voc of the cells since the thicker V_2O_5 prevents photogenerated electron charges in the a-Si active layer from being lost to the anode (**Figure 6.4.4 (b) and (d)**). Furthermore, the insets of **Figure 6.4.4 (a) and (c)** show J-V curves in wider voltage range, depicting a single nanometer-thick hybrid cells work as diodes regardless of the V_2O_5 variations.

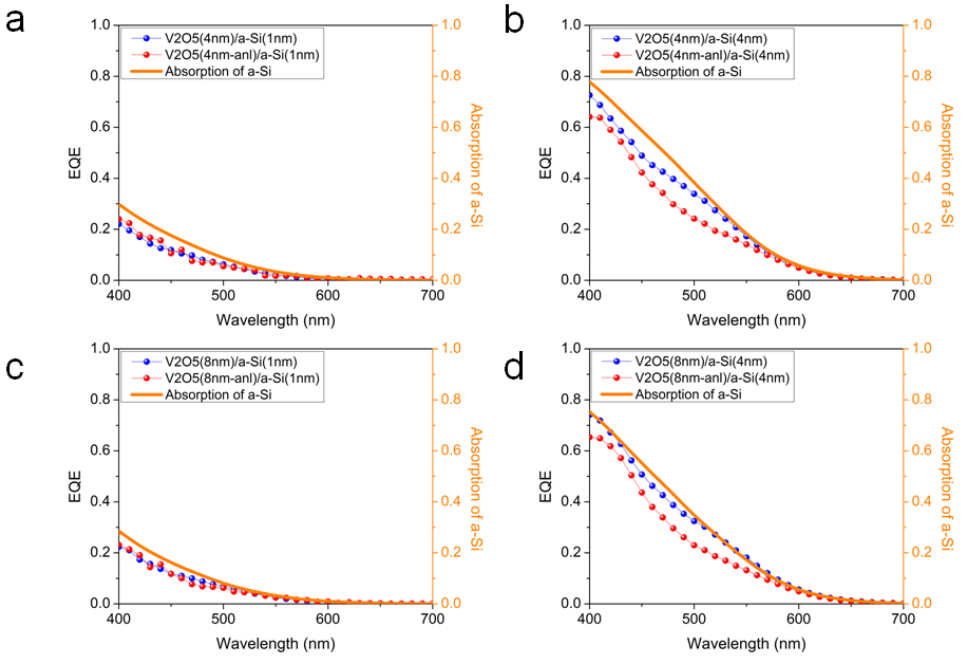

Figure 6.4.5 (a) – (d) Measured EQE spectra and calculated absorption profiles in a few nanometer-thick a-Si layers are investigated by varying hole transport layer (V_2O_5) conditions as same order as in Figure 3.4.4. The experimentally measured EQE spectra (dotted lines) show a good agreement with the numerically calculated a-Si absorption curves (solid lines), especially when photoactive a-Si performs with non-annealed V_2O_5 (8 nm) hole transport layer.

The current density-voltage characteristics are supported by experimentally measured EQE spectra (**Figure 6.4.5 (a) – (d)**). The EQE spectra are from eight different devices same as introduced in **Figure 6.4.4**. The measured EQE curves are compared to the numerically calculated a-Si absorption spectra, which allow us to study how efficiently photogenerated charges are extracted in each case. Since photogenerated electron charges are not effectively blocked by the thinner V_2O_5 to the anode, there is more charge recombination loss in **Figure 6.4.5 (a) and (b)**, compared to the thicker V_2O_5 in **Figure 6.4.5 (c) and (d)**. The thicker a-Si (4 nm) devices show more noticeable difference in **Figure 6.4.5 (b) and (d)**.

However, with V_2O_5 (8 nm without annealing), the measured EQE of the a-Si (4 nm) hybrid cell fits pretty well with a-Si absorption calculation due to the suppressed charge recombination

benefited by a very thin nanometer-thick photoactive layer (**Figure 6.4.5 (d)**). Overall, thermally annealed V_2O_5 is less efficient in extracting photogenerated charges since the EQE spectra reveal larger discrepancy with the numerically simulated a-Si absorption. We also noted that a-Si (1 nm) hybrid cells, regardless of V_2O_5 conditions, show deviations between EQE and a-Si absorption. We attribute this to the comparable V_2O_5 surface roughness to the a-Si photoactive layer thickness, therefore inducing the parasitic pinholes in the devices.

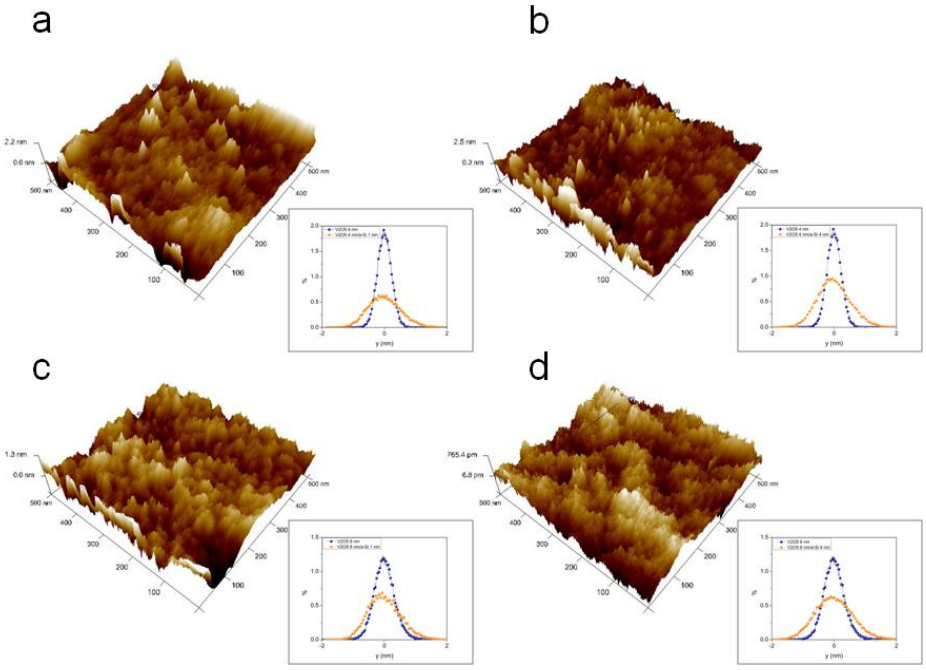

Figure 6.4.6 Surface roughness characterization of a few nanometer a-Si on top of V_2O_5 by atomic force microscopy (AFM). (a) Experimentally measured three-dimensional surface morphology by AFM show the surface roughness of a single nanometer a-Si on the hole transport layer V_2O_5 (4 nm) (inset: root-mean-square (rms) roughness Gaussian distribution profile showing blue dots in V_2O_5 roughness profile, and orange dots for a-Si on V_2O_5). (b) The surface morphology of a-Si (4 nm) instead on the same thickness of V_2O_5 as in (a). (c) – (d) The surface roughness of a few nanometer a-Si (1 and 4 nm) on 8 nm V_2O_5 was characterized in the same manner of (a) – (b).

We analyzed the surface roughness of V_2O_5 (4 and 8 nm) on crystalline silicon substrates and a few nanometer a-Si (1 and 4 nm) deposited on V_2O_5 by employing atomic force microscopy

(AFM). Three-dimensional surface morphology figures by AFM are depicted in **Figure 6.4.6 (a) – (d)**, incorporating the inset information of Gaussian surface profile distribution for each. The V_2O_5 4 nm and 8 nm layers on silicon substrates show the root-mean-square (rms) roughness of 0.28 nm and 0.44 nm, respectively. Once the a-Si is deposited on top of the V_2O_5 layers, the roughness becomes a little bigger as described with red curves in the inset figures, showing the similar rms roughness ranging from 0.58 nm to 0.68 nm. As we anticipated in the previous experimental results, the surface roughness is a lot comparable to 1 nm a-Si, which can cause charge leakage directly via pinholes between anode and cathode. We conclude that, within a few nanometer a-Si thickness range, the surface roughness of hole transport and photoactive layers determines the diode characteristics of the nanometer-thick hybrid cells as analyzed in **Figure 6.4.2**.

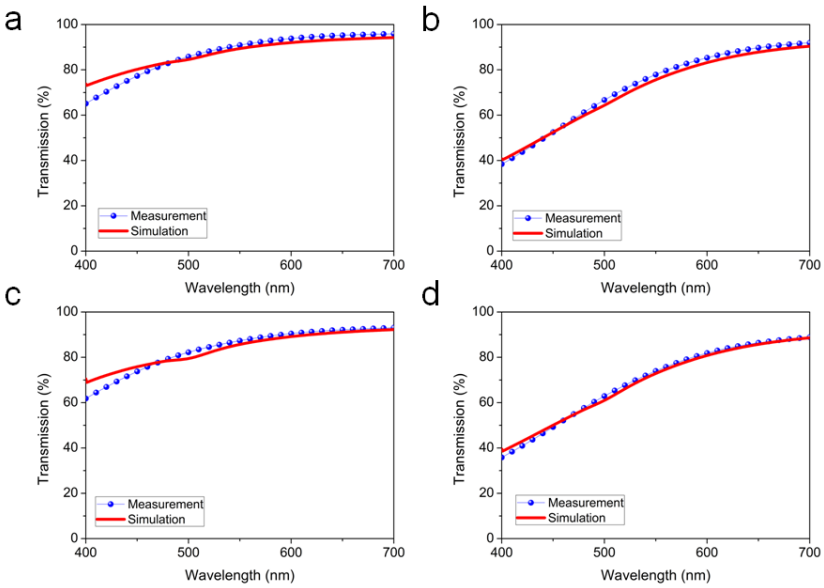

Figure 6.4.7 Numerically simulated and experimentally measured transmission of a few nanometer a-Si on top of V_2O_5. (a) Experimentally measured transmission (dotted line) of a single nanometer a-Si on the hole transport layer V_2O_5 (4 nm) verifies a-Si thickness indirectly by compared with numerically calculated transmission (solid line). (b) The transmission of a-Si (4 nm) instead on the same thickness of V_2O_5 as in (a). (c) – (d) The transmission of a few nanometer a-Si (1 and 4 nm) on 8 nm V_2O_5 was characterized in the same manner of (a) – (b).

In order to verify the thickness of a-Si layer, we performed normal incidence transmission measurements for 1 nm and 4 nm of a-Si films deposited on 4 nm and 8 nm of V_2O_5 layers, each of which is built on top of the fused silica substrate. The measured (blue sphere) and corresponding simulated (red solid lines) transmission spectra of each case are shown in **Figure 6.4.7 (a) – (d)**. The experimental data show great agreement with the simulation results. In the case of 1 nm-thick a-Si film (**Figure 6.4.7 (a) and (c)**), small difference between simulations and measurements is observed, particularly at the shorter wavelength regime, which is attributed to the roughness of 1 nm a-Si surface, thus inducing small scattering loss. This comparable surface roughness to the thickness of a-Si (1 nm) layer was already proved by AFM characterization (**Figure 6.4.6**).

It is noted that the simulated transmission spectra in **Figure 6.4.7** are obtained by using the transfer matrix method and the calculation is carried out based on the refractive indices of a-Si and V_2O_5 measured by a spectroscopic ellipsometer (J. A. Woollam).

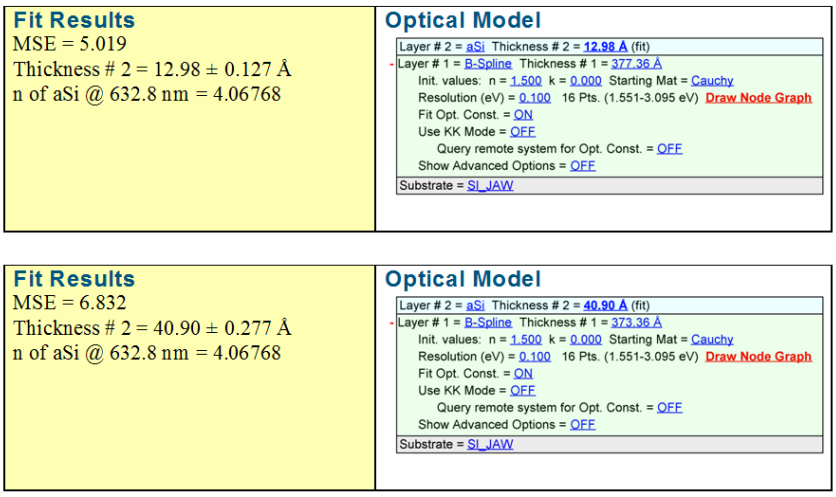

Figure 6.4.8 The confirmation of the ultra-thin a-Si layer thicknesses (1 nm and 4 nm) fitted by using the ellipsometer.

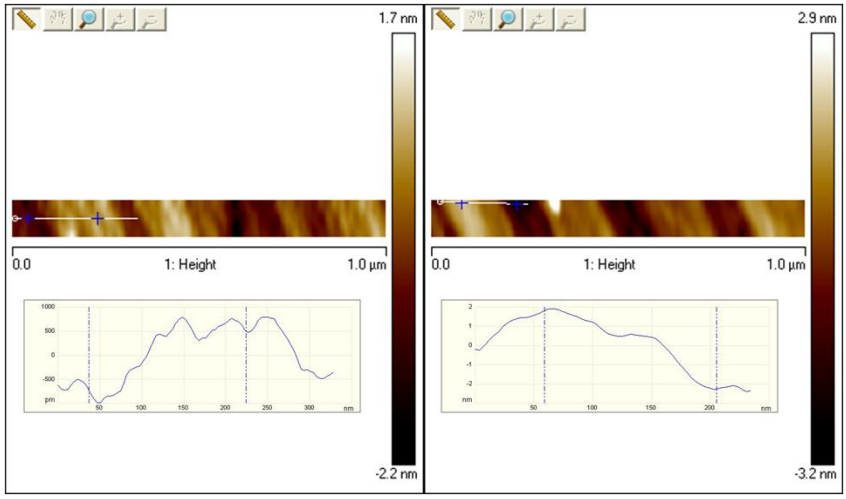

Figure 6.4.9 AFM images of 200 nm-period grating pattern profiles, showing 1 nm thickness.

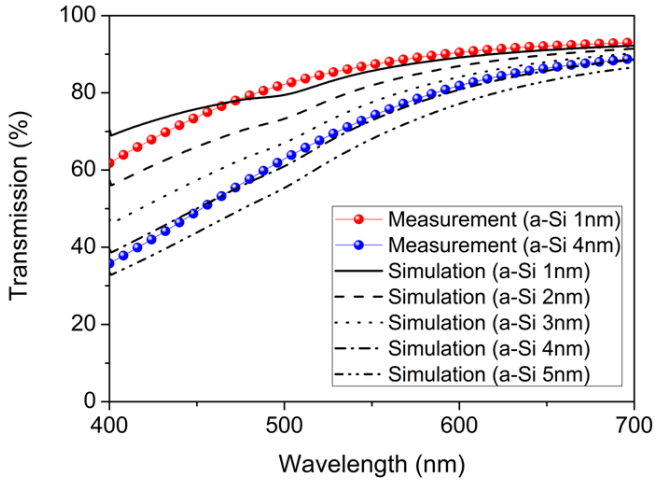

Figure 6.4.10 Simulated and measured transmission spectra of the a-Si layer with the thickness ranging from 1 nm to 5 nm at normal incidence.

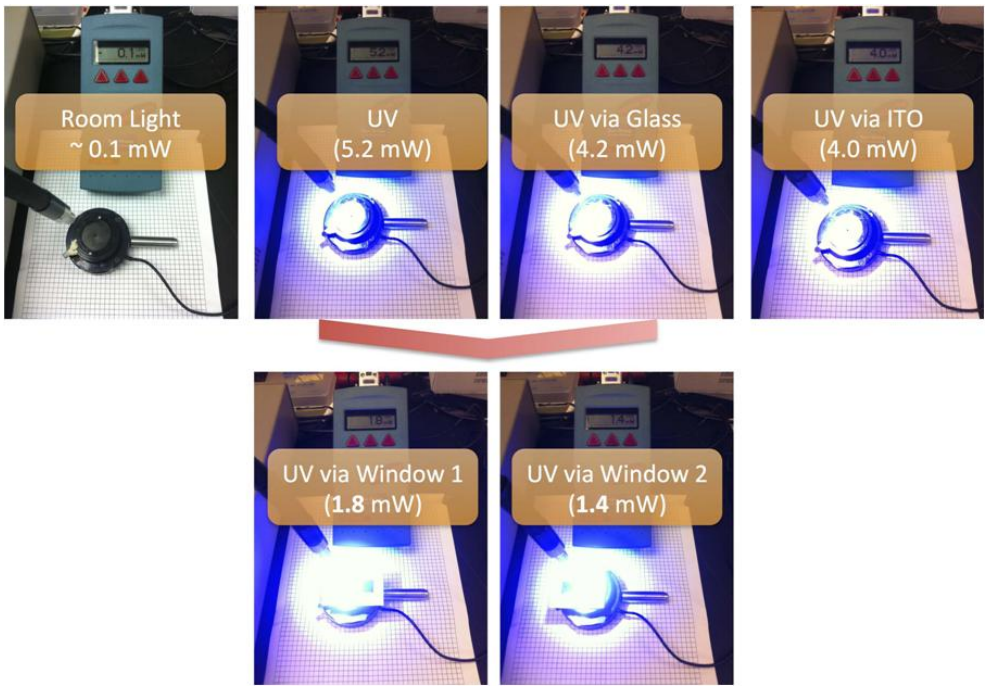

Figure 6.4.11 Intensities of UV light through the fabricated window 1 and 2 are smaller than those of glass and ITO glass, which is attributed to the strong optical absorption of the a-Si material at shorter wavelengths.

We also confirm the thickness of extremely thin a-Si (1 and 4 nm) layers by the ellipsometry measurement (**Figure 6.4.8**) and 200 nm-period grating pattern profiles by AFM (**Figure 6.4.9**). In the simulated transmission spectra of V_2O_5 (8 nm)/a-Si where a-Si thickness ranges from 1 nm to 5 nm (**Figure 6.4.10**), even a few nanometer a-Si absorbs large portion of shorter wavelength light, which will be advantageous to block UV light as demonstrated in **Figure 6.4.11**.

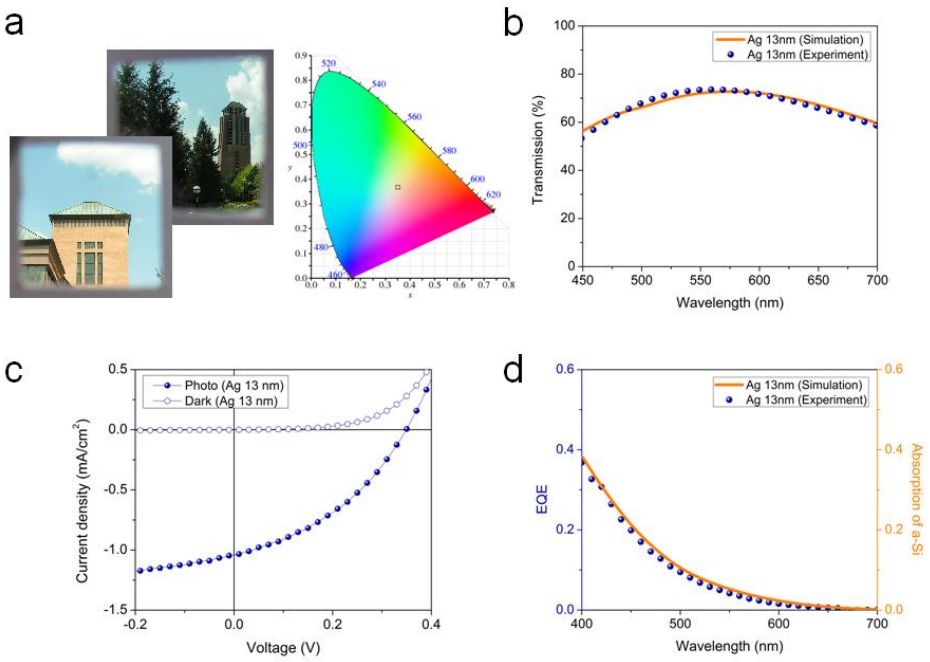

Figure 6.4.12 A few nanometer-thick a-Si hybrid cells for transparent electric power generators. (a) Fabricated hybrid cells with 3 nm a-Si photoactive layers show transparent properties enough to see objects clearly in photos taken on campus along with Figure 3.4.1 (b). The CIE 1931 chromaticity diagram estimates transparency by giving the color coordinate at (0.358, 0.360), close to white light coordinate (0.33, 0.33). (b) Measured transmission (dotted line) fits well with the calculated transmission of the hybrid cells, showing around 70 % average transmission. (c) Current density-voltage characteristics are studied for electric power generating performance under AM 1.5 illumination and dark condition. (d) Measured external quantum efficiency (EQE) spectrum (dotted line) shows a good match with the simulated absorption curve (solid line) in 3 nm-thick a-Si photoactive layer, supporting negligible photogenerated charge recombination in devices.

Benefited by a few nanometer-thick a-Si hybrid cells, we can design fairly transparent solar cell structures by incorporating metal-dielectric transparent cathode instead of conventional thick metal film (**Figure 6.4.12 (a) – (d)**). The 3 nm of a-Si was utilized for a photoactive layer along with the cathode of Ag and WO_3, 13 nm and 55 nm, respectively. The photographs of visibly transparent 3 nm a-Si device are illustrated in Fig. 6a, clearly showing the building through the hybrid cell. Additionally, we calculate the color coordinate (*x*,*y*) under AM 1.5 illumination, which is depicted in the CIE 1931 chromaticity diagram to estimate the transparency perception

of the 3 nm a-Si hybrid cell (**Figure 6.4.12 (a)**). The calculated color coordinate is (0.358, 0.360), demonstrating good transparency that is close to the coordinate representation of the white light (0.33, 0.33). The optical transmission featuring a flat and broad spectrum obtained by the numerical simulation is well matched with the experimentally measured profile as described in **Figure 6.4.12 (b)**. Such a flat and broad transmission characteristics is primarily due to a resonance formed in a cavity consisting of a highly absorptive material (a-Si) with an extremely thin cavity length as well as poor quality factor (Q-factor) arising from the weak reflection at the interfaces (i.e. V_2O_5/a-Si and thin Ag/C_{60} surfactant).

Even with highly transparent property averaging around 70 % transmission, our hybrid cells generate electricity under AM 1.5 simulated light with the suppressed dark current as shown in **Figure 6.4.12 (c)**. The hybrid cells provide around 1.0 mA/cm^2 and 0.35 V, Jsc and Voc, respectively. The electric power-generating performance was verified further by comparing the simulated a-Si absorption spectrum to the measured EQE profile, which presents a great agreement (**Figure 6.4.12 (d)**). This good match provides explicit evidence, indicating that any type of our hybrid device structures with a few nanometer-thick a-Si shows almost negligible photogenerated charge recombination. As a result of the absence of charge recombination, we can eventually eliminate the light-induced degradation issue that conventional a-Si solar cells have struggled for many years. We believe our transparent hybrid solar cell technology has the potential for various applications such as clear windows or modern architectural building components that supply electric power as well.

6.5 Perovskite PV Cells Producing Reflection Colors

The approach discussed in the chapter 6 (i.e., strong resonance effects in ultra-thin highly absorbing media) could be applicable to other PV material system, including the perovskite semiconductor material. But, it is very difficult to attain very smooth and uniform ultra-thin perovskite layer via a solution process at the current stage. To achieve this, a co-evaporation method could be used since the thickness is accurately controlled and the uniformity of the film is much better than solution-processed film under high vacuum condition. Or, it has recently been reported that such an ultra-thin perovskite film can be obtained by a solution extraction method as well, which could be another way to make this colored perovskite PV cells. In this chapter, we will describe how to make the colored ultra-thin perovskite PV devices exploiting the strong resonance effects in the ultra-thin perovskite semiconductor layers.

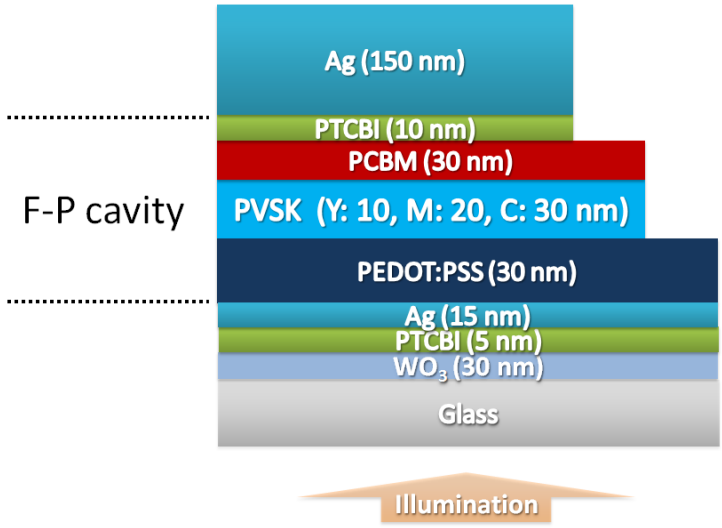

Figure 6.5.1 A schematic representation of the proposed colored ultra-thin perovskite PV device structure based on strong interference effects in ultra-thin semiconductor layers.

Figure 6.5.1 illustrates a schematic diagram of the proposed colored ultra-thin perovskite PV device structures. Instead of the ITO electrode, the dielectric-metal-dielectric (DMD) multilayer electrode is utilized in order to provide somewhat strong reflections from the anode side. In this

design, the F-P cavity is created between the two Ag layers so the effective cavity medium is composed of PEDOT:PSS, perovskite, PCBM, and PTCBI. Due to the relatively small refractive indices of these materials as compared to the inorganic semiconductors like Ge and a-Si, the required F-P cavity medium is thicker than what has been utilized in ultra-thin Ge- or a-Si-based F-P cavity. As discussed in the previous colored ultra-thin a-Si PV cells, the reflective color could be tuned by changing the thickness of the perovskite semiconductor layer. For example, 10, 20, and 30 nm thicknesses are needed for generating the yellow, magenta, and cyan colors, respectively. Although the thickness of the effective F-P cavity medium is fairly thick, the thickness of the perovskite film is much thinner than the wavelength of the incident light. We rely on the strong interference behaviors in the ultra-thin highly absorbing media (i.e., perovskite material) in order to form the F-P cavity resonance at visible frequencies, thus filtering a specific visible band of lights for color generation.

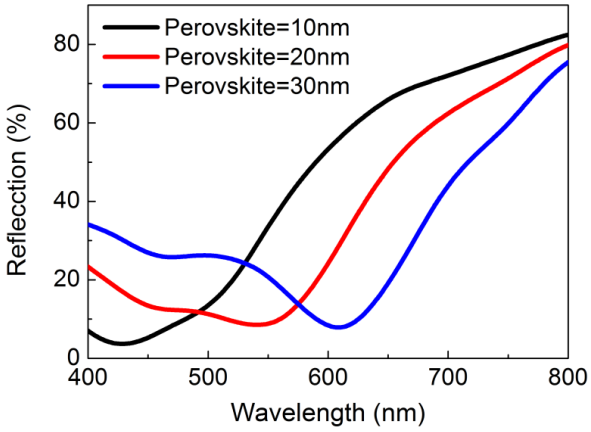

Figure 6.5.2 Calculated reflection spectra of the proposed colored ultra-thin perovskite PV cells at normal incidence.

Figure 6.5.2 exhibits the spectral reflectance curves of the colored ultra-thin perovskite PV cells at normal incidence, which are calculated by the transfer matrix method. The reflection valley

that corresponds to the strong optical absorption, which arises from the strong resonance effects in the ultra-thin perovskite semiconductor layer. The color could be tuned by varying the thickness of the perovskite layer. To create the yellow, magenta, and cyan reflective colors needs 10, 20, and 30 nm of the perovskite layer thickness, respectively. The corresponding resonances are 430, 550, and 610 nm for the yellow, magenta, and cyan colors, respectively.

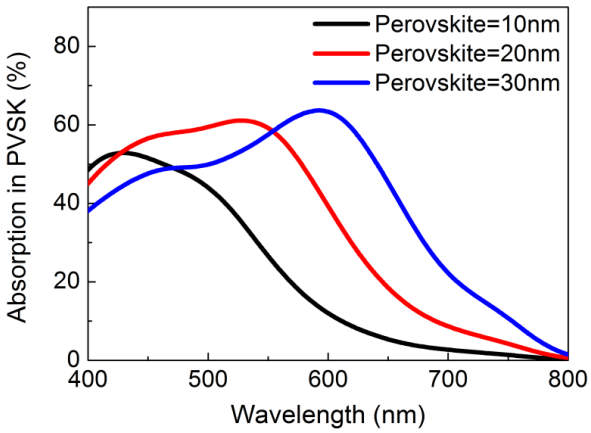

Figure 6.5.3 Calculated optical absorption spectra in the perovskite photoactive layer of the colored ultra-thin perovskite PV devices.

In **Figure 6.5.3**, the calculated absorption profiles in the perovskite layer are described. The peak position of each colored ultra-thin perovskite PV devices matches well with the wavelength of the reflection valley as depicted in **Figure 6.5.2**. The Jsc values of each colored cell are also estimated: Yellow (4.87 mA cm^{-2}), Magenta (8.31 mA cm^{-2}), and Cyan (10.22 mA cm^{-2}). As we observed in the colored ultra-thin a-Si PV devices, it is expected that the measured external quantum efficiency (EQE) spectrum could be in good agreement with the simulated absorption in the photoactive layer since the thickness of the perovskite film used in the device design is much thinner than the charge diffusion length of the semiconductor.

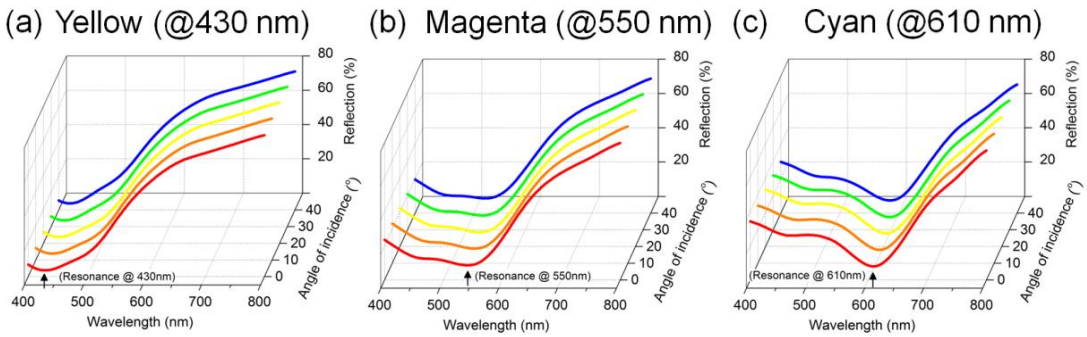

Figure 6.5.4 Calculated angle resolved reflection spectra of the colored perovskite PV cells creating (a) Yellow (430 nm), (b) Magenta (550 nm), and (c) Cyan (610 nm).

From the previous study, it turns out that the dispersion characteristics of the resonance in the ultra-thin semiconductor is relatively flat with respect to the angle of incidence, which is attributed to the negligible propagation phase shift as well as the phase compensation as explained in the chapter 3. It is thus anticipated that the resonance of the colored ultra-thin perovskite PV devices also has angle robustness as can be seen in **Figure 6.5.4**. However, the refractive index of the perovskite material is lower than that of the a-Si or Ge, thus leading to relatively weak angle insensitivity. This is because the cavity associated with the perovskite needs thicker cavity medium, which yields a large change in the propagation phase shift.

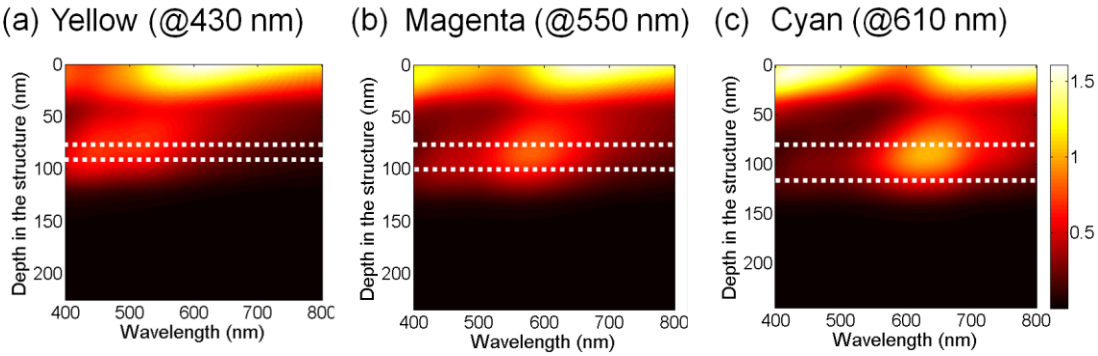

Figure 6.5.5 Normalized optical field intensity distributions of the colored ultra-thin perovskite PV cells with different thickness of the photoactive medium: 10 nm (a), 20 nm (b), and 30 nm (c). The incident light is illuminating from the top side and the perovskite photoactive layer is indicated by two white dotted lines.

Figure 6.5.5 (a) – (c) show normalized intensity profiles of the optical field of the colored ultra-thin perovskite PV devices, each of which has different thickness of the perovskite photoactive layer (Y: 10 nm, M: 20 nm, and C: 30 nm). As can be seen from the figure, the electric field is primarily concentrated in the photoactive layer that is denoted by two white dotted lines. Since the number of the constructive interference is quite many at the resonance wavelength, we have to see the strong field as well. Each resonance wavelength shows good agreement with the position of the reflection valley as shown in **Figure 6.5.2**.

6.6 Conclusion

To sum up, we have described how the concept of the strong resonance effects in the ultra-thin highly absorbing media could be applied to the perovskite material system in order to produce reflective colors and generate the electricity at the same time. The colors could be readily tuned by varying the thickness of the photoactive layer. To fabricate the device, we should note that coating the PEDOT:PSS layer on top of the Ag film is difficult due to the wettability of the Ag surface. The O_2 plasma treatment could be done before coating the PEDOT:PSS film to improve the surface energy of the Ag layer, but the time should be optimized since it could damage the Ag electrode if the time is too long. Otherwise, it is necessary to insert an interfacial layer that can efficiently act as an electron blocking layer (or hole transporting layer) and simultaneously improve the wettability of the Ag surface without sacrificing the function of the Ag electrode. The last thing would be to find another hole transporting layer that can replace the PEDOT:PSS layer and show good energy band alignment.

Chapter 7

Microcavity-Integrated Colored, Semitransparent PV Cells

7.1 Introduction

Although we have achieved the colored semitransparent RGB a-Si PV as discussed in the previous chapter, the purity of the transmission colors is not good. In addition, the power conversion efficiency of the PV cells, in particular blue and red devices, is too low. Here, we will describe how to improve the color purity and simultaneously power conversion efficiency of our previous ultra-thin a-Si PV design by integrating optical microcavity in a cathode. As the design principle is quite general, the approach discussed in this chapter could be applied to other PV material system. To prove this, we will demonstrate how this approach could be applied to the perovskite semiconductor material in order to create colored, see-through perovskite PV cells.

7.2 A-Si PV with Improved Efficiency and Color-Purity

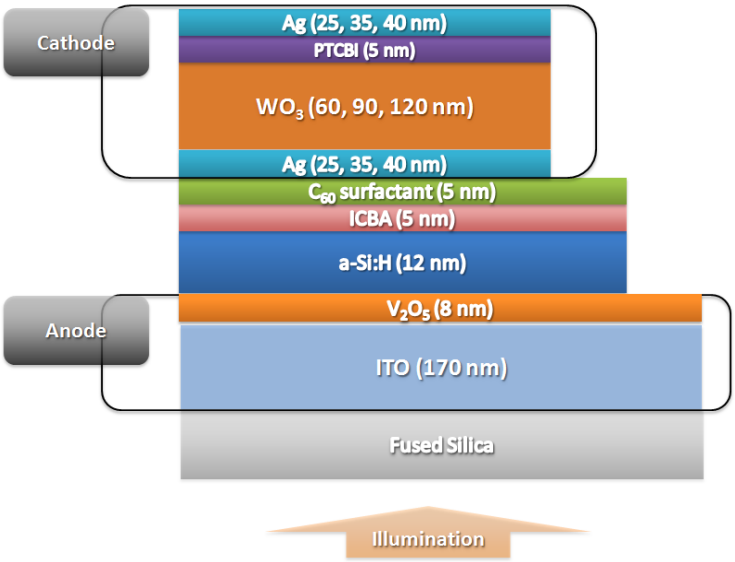

Figure 7.2.1 A schematic representation of the proposed microcavity-integrated ultra-thin a-Si PV with high efficiency and high purity transmission RGB colors.

What we found in the chapter 6.2 is that 20 nm of the a-Si layer leads to the highest Jsc for the reflection CMY colored a-Si PV cells. Similarly, we can also find the photoactive layer thickness showing the highest Jsc for the transmission RGB colored a-Si PV devices, which could be explained in the following figures in more detail. From the numerical simulation, it turns out that the highest Jsc value can be achieved by optimizing thicknesses of the ITO and a-Si layers as 170 and 12 nm, respectively. In the previous designs, we varied the a-Si photoactive layer thickness in order to tune the RGB colors and thus the corresponding power conversion efficiency of each colored cell was different from one another. In this design, however, we will use 12 nm of the a-Si layer that shows the highest Jsc for all the RGB colored PV cells and create the different colors by controlling the F-P cavity embedded in the cathode. Since the optical absorption of the 12 nm-thick a-Si layer is not 100 %, the rest of the incident light can be harvested to produce the transmitted RGB colors. A schematic view of the proposed

microcavity-integrated ultra-thin a-Si PV with high efficiency and high purity transmission RGB colors is shown in **Figure 7.2.1**.

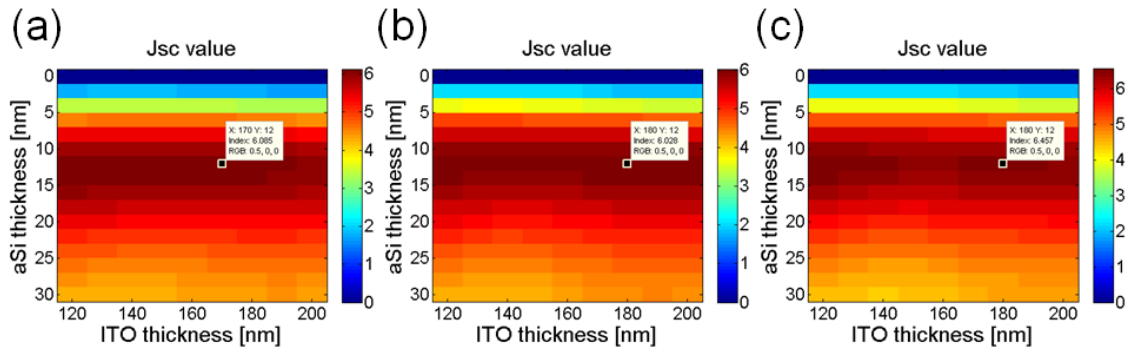

Figure 7.2.2 Calculated contour plots of Jsc values as functions of ITO and a-Si layer thicknesses for blue (a), green (b), and red (c), showing that the highest Jsc can be achieved with 170 nm of ITO and 12 nm of a-Si layer thicknesses for the RGB colors. The Ag thickness in the cathode is 35 nm.

Figure 7.2.2 (a) – (c) presents simulated contour plots of Jsc values as functions of ITO and a-Si layer thicknesses for blue, green, and red, given fixed Ag thickness (35 nm). When the ITO and a-Si thicknesses are 170 and 12 nm, the device exhibits the highest Jsc for the RGB colored PV cells.

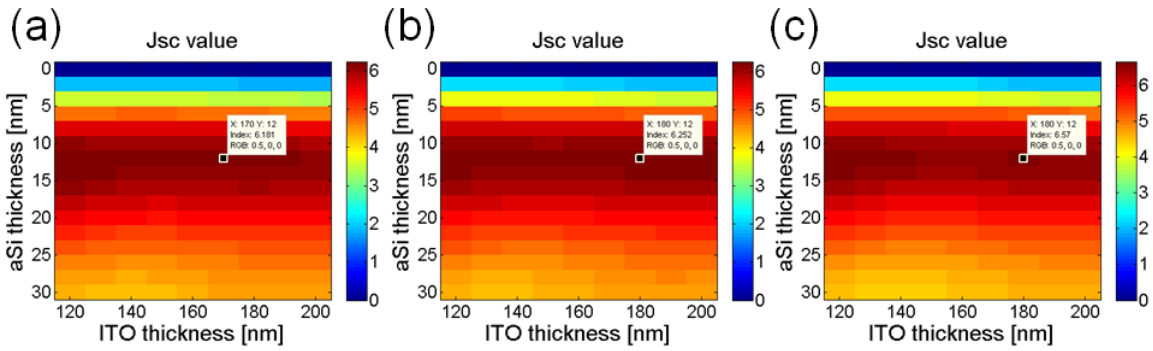

Figure 7.2.3 Calculated contour plots of Jsc values as functions of ITO and a-Si layer thicknesses for blue (a), green (b), and red (c), showing that the highest Jsc can be achieved with 170 nm of ITO and 12 nm of a-Si layer thicknesses for the RGB colors. The Ag thickness in the cathode is 40 nm.

In **Figure 7.2.3 (a) – (c)**, calculated contour plots of Jsc values as functions of ITO and a-Si layer thicknesses for blue, green, and red colors, given fixed Ag thickness (40 nm) are described. As we observed in **Figure 7.2.2**, the highest Jsc values for the RGB colored a-Si PV cells are attained with ITO=170 nm and a-Si=12 nm even though both top and bottom Ag thicknesses of the F-P cavity in the cathode are thicker than a previous case.

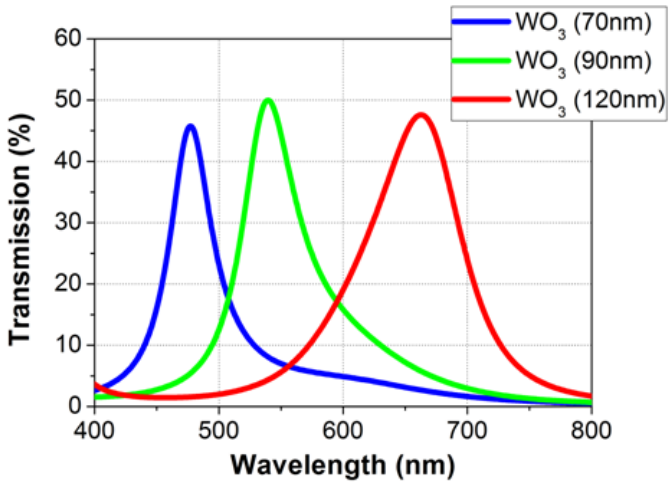

Figure 7.2.4 Calculated RGB transmission spectra at normal incidence with 25 nm of Ag layers in the cathode. The color can be tuned by varying the thickness of WO_3 layer.

Figure 7.2.4 shows simulated RGB transmission spectra of the proposed a-Si PV devices with 25 nm of Ag layers in the cathode at normal incident angle. Varying the thickness of the WO_3 film in the cathode enables the transmitted color to be tuned. 120, 90, and 70 nm of the WO_3 layer in the cathode are used for creating RGB transmission colors and the corresponding resonances are 650, 540, and 480 nm. The transmission spectra of the microcavity-integrated a-Si PV cells show improved color purity as compared to what we obtained in the section of 3.2. It should be noted that the color purity can be improved further by increasing the thicknesses of the Ag layer in the cathode, which will be discussed in the following part.

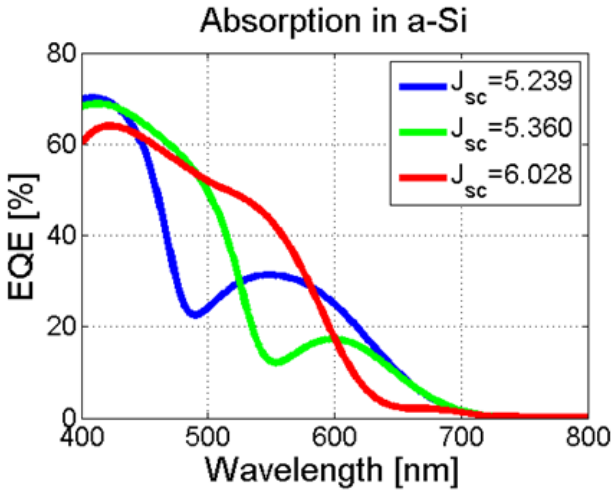

Figure 7.2.5 Calculated absorption spectra in the a-Si layer with 25 nm of Ag layers in the cathode.

Simulated optical absorption spectra in the a-Si photoactive layer, which are proportional to the Jsc, with 25 nm of the Ag layers are shown in **Figure 7.2.5**. Since there is a transmitted light at the resonance, which cannot be harvested by the PV cells, it is clear to see that there is a dip in the optical absorption spectra in the a-Si layer at 650, 540, and 480 nm for RGB colors, respectively. As discussed previously, the photoactive layer thickness (12 nm) is much thinner than the diffusion length of the a-Si material, which leads to almost 100 % of internal quantum efficiency (IQE). This means that the measured EQE spectra would be nearly same with the simulated optical absorption profiles in the a-Si photoactive layer (i.e., EQE = IQE * Absorption in the active layer). Using the **Equation 7.2.1**, we can estimate how high Jsc can be obtained from the microcavity-integrated ultra-thin a-Si PV cells with 25 nm of the Ag films in the cathode.

$$J_{SC} = \int_{300nm}^{800nm} \frac{e\lambda}{hc} QE(\lambda) I_{AM1.5}(\lambda) d\lambda \qquad (7.2.1)$$

Calculated Jsc values of RGB colored PV devices are 6.028, 5.360, and 5.239 mA cm^{-2}, respectively. It is noteworthy to mention that the red device shows the highest Jsc vale among the three samples, which can be explained by the following reason. Due to the band gap of the a-Si material at visible frequency (1.6 eV), the a-Si more strongly absorbs shorter wavelengths than longer wavelength lights. When creating the resonance at the shorter wavelength ranges (i.e., blue device), which the absorption of the a-Si material is fairly significant, the shorter wavelength lights cannot be utilized to generate electric power instead producing the transmitted resonance (i.e., transmission color). In contrary, the a-Si material can absorb the shorter wavelengths without any disturbance, which can be harvested for electric power generation when the resonance is formed at longer wavelengths (i.e., red device). In this reason, the blue colored PV cell shows the lowest Jsc than the green and red PV devices.

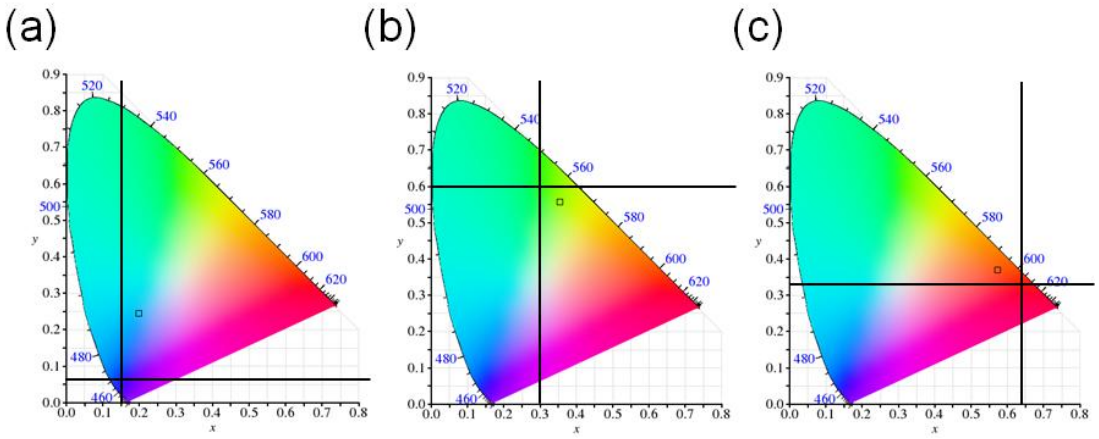

Figure 7.2.6 The representation of the color coordinates calculated from the transmission spectra (Figure 7.2.4) described on the CIE 1931 chromaticity diagram. The crossing point of the two black solid lines indicates the standard RGB points for LCD. The Ag film thickness in the cathode is 25 nm.

In order to investigate how the chromaticity of the proposed microcavity-integrated ultra-thin colored a-Si PV devices is enhanced, we perform a numerical simulation to estimate the color

coordinates that are calculated from the transmission spectra shown in **Figure 7.2.4** and its representation is depicted on the CIE 1931 chromaticity diagram as exhibited in **Figure 7.2.6**. The crossing point of the two black solid lines denotes the standard RGB points for LCD. In this design, the Ag thickness in the cathode part is 25 nm that is still not too thick to provide high reflections (i.e., low Q-factor resonance), thus resulting in somewhat broad profiles. The color purity can be further improved by simply increasing the Ag thicknesses to be demonstrated in the following section.

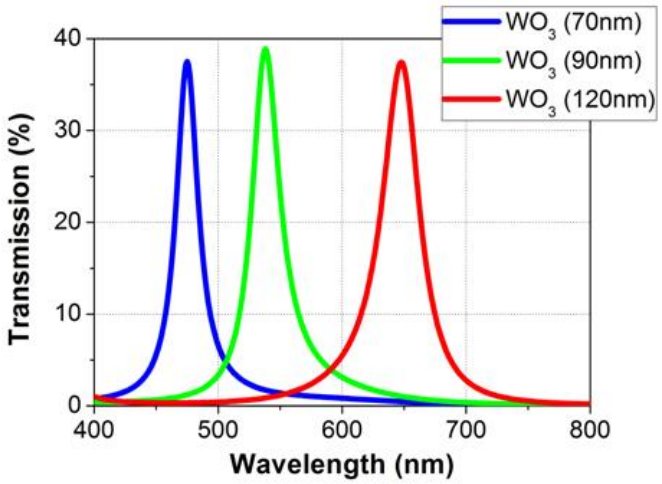

Figure 7.2.7 Calculated RGB transmission spectra at normal incidence with 35 nm of Ag layers in the cathode.

Figure 7.2.7 presents calculated transmittances of the proposed microcavity-integrated ultra-thin colorful a-Si PV cells with 35 nm of the Ag layers in the cathode at normal incidence. Likewise, the transmission colors can be tunable by changing the thickness of the WO_3 layer in the cathode. In order to produce RGB transmitted colors, 120, 90, and 70 nm of the WO_3 film in the cathode side are utilized and the corresponding resonances are 650, 540, and 480 nm, respectively. As is seen from the figure, the transmission spectra have narrow bandwidth and low background noise level as compared to what we have seen in **Figure 7.2.4** obtained with 25 nm of the Ag layers. It

is therefore expected that the color purity will also be improved to some extent, which will be examined in more detail.

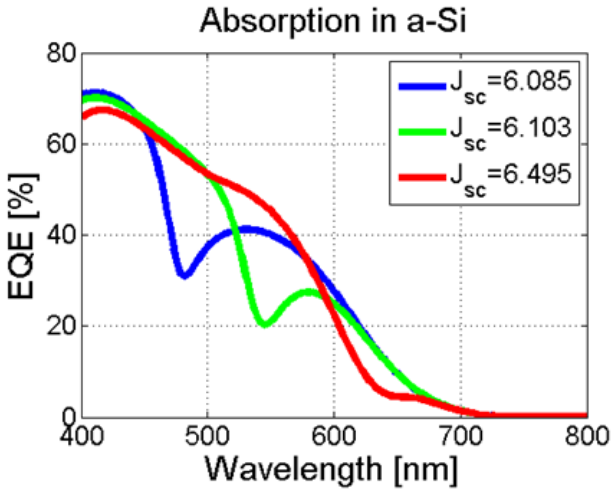

Figure 7.2.8 Calculated absorption spectra in the a-Si layer with 35 nm of Ag layers in the cathode.

Figure 7.2.8 shows calculated optical absorption profiles in the a-Si film with 35 nm of the Ag layers in the cathode side. As we mentioned earlier, we are producing the transmission resonance (i.e., colors) whose wavelengths cannot be harvested by the PV devices to generate electric power. In this regard, we can also have the absorption valley in the a-Si photoactive layer. Jsc values of each colored samples calculated from the optical absorption profiles in the a-Si layer described in **Figure 7.2.8** are 6.495, 6.103, and 6.085 mA cm^{-2} for the RGB colored cells, respectively, which show higher Jsc than the previous structure with 25 nm of the Ag layers. This is because of the thicker Ag film in the cathode that can provide stronger reflections so that the a-Si photoactive layer can absorb a large proportion of the reflected light. The interesting thing I should mention here is that increasing the Ag film thickness in a cathode allows both the color purity and the power conversion efficiency of the PV cells to be enhanced simultaneously. Since the resonance in the transmission spectrum is sharp with the narrow bandwidth, a wide

range of incident light energy can be absorbed by the photoactive layer, thus leading to the high Jsc (i.e., high power conversion efficiency).

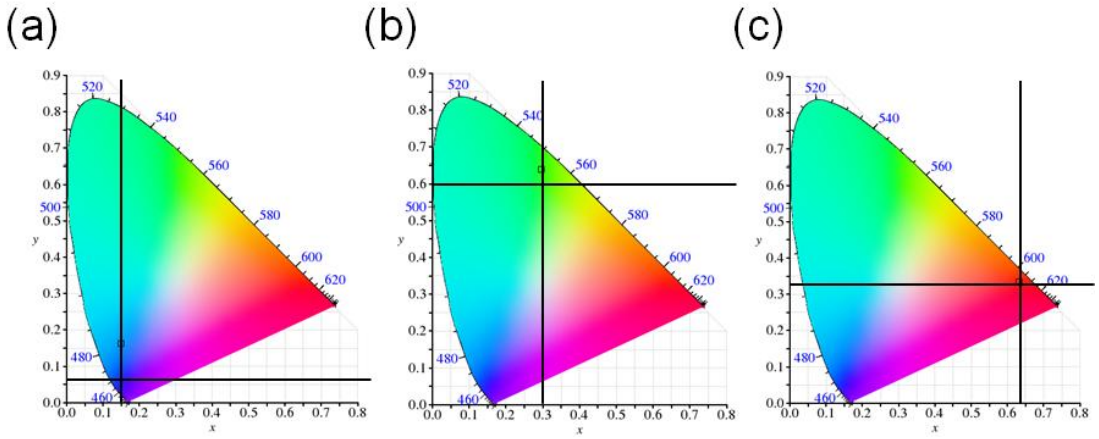

Figure 7.2.9 The representation of the color coordinates calculated from the transmission spectra (Figure 7.2.7) described on the CIE 1931 chromaticity diagram. The crossing point of the two black solid lines indicates the standard RGB points for LCD. The thickness of the Ag layer inside the cathode is 35 nm.

To study an influence of the Ag layer thickness on the color purity of the proposed microcavity-integrated ultra-thin colored a-Si PV devices, the color coordinates calculated from the transmittances exhibited in **Figure 7.2.7** and its color description is demonstrated on the CIE 1931 chromaticity diagram as displayed in **Figure 7.2.9**. It is obvious that the color coordinates are pretty close to the standard RGB points of the LCD (i.e., crossing point of the two black solid lines), showing greatly improved chromaticity.

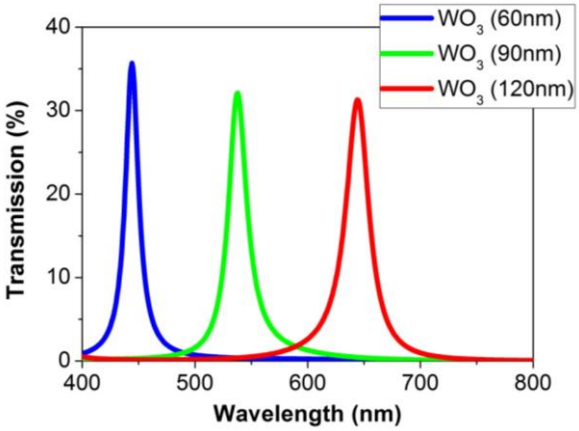

Figure 7.2.10 Calculated RGB transmission spectra at normal incidence with 40 nm of Ag layers in the cathode.

In **Figure 7.2.10**, simulated transmittance profiles of the proposed microcavity-integrated ultra-thin colorful a-Si PV cells with 40 nm of the Ag layers in the cathode at normal incidence are illustrated. The transmission colors can also be tuned by varying the thickness of the WO_3 layer in the cathode side. For generating transmission RGB colors, 120, 90, and 60 nm of the WO_3 film are employed and the corresponding resonances are 650, 540, and 450 nm, respectively. Although the transmission efficiency of each colored sample with 40 nm-thick Ag layers is slightly reduced, the background light leakage loss is remarkably diminished and the as compared to that attained with 25 nm-thick Ag layers (**Figure 7.2.4**), implying that the color purity is significantly improved.

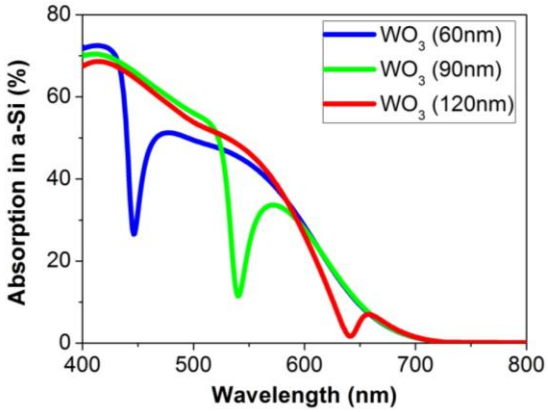

Figure 7.2.11 Calculated absorption spectra in the a-Si layer with 40 nm of Ag layers in the cathode.

Figure 7.2.11 presents simulated spectral optical absorption responses in the a-Si photoactive layer with 40 nm of the Ag layers in the cathode part, along with the calculated Jsc values of each colored PV cell shown in the inset of the image. As we have observed in the simulated optical absorption profiles in the a-Si layer with 25 and 35 nm-thick Ag layers, there are also optical absorption dips at 650, 540, and 450 nm for the RGB colored PV cells, respectively. The reflection of 40 nm-thick Ag films is higher than that of 25 and 35 nm-thick Ag surfaces, therefore giving rise to higher Jsc values.

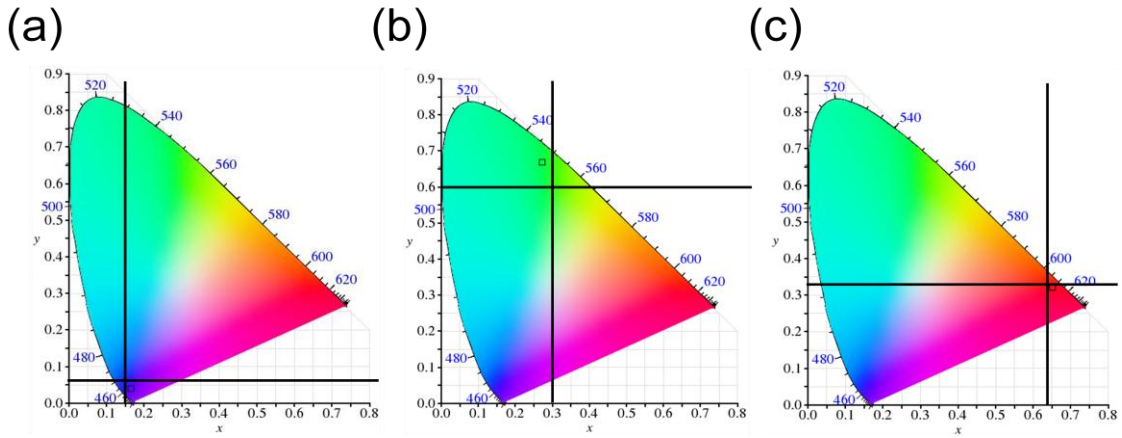

Figure 7.2.12 The representation of the color coordinates calculated from the transmission spectra (Figure 7.2.10) described on the CIE 1931 chromaticity diagram. The crossing point of

the two black solid lines indicates the standard RGB points for LCD. The Ag layer thickness in the cathode is 40 nm.

To examine the color purity of the proposed microcavity-integrated ultra-thin colored a-Si PV cells, the color coordinates obtained from the transmittance profiles shown in **Figure 7.2.10** and the corresponding representation on the CIE 1931 chromaticity diagram is described in **Figure 7.2.12**. It is apparent that the color coordinates are closer to the standard RGB points of the LCD (i.e., crossing point of the two black solid lines) than those with 25 and 25 nm of the Ag layers. It is interesting to note that the calculated color coordinates for the green and red colors are beyond the standard RGB points of the LCD, indicating much enhanced chromaticity of our design. We also note that our proposed structures with 40 nm-thick Ag layers in the cathode show markedly improved color purity as well as higher power conversion efficiency as compared to the structure demonstrated in the chapter 6.3. **Table 7.2.1** summarizes how much Jsc improves in comparison to the previous design.

Table 7.2.1 Summary of Jsc values for the three RGB colored ultra-thin a-Si PV cells.

Color	J_{sc} (mA/cm^2)	J_{sc} (mA/cm^2)	Improvement (%)
Blue	3.54	6.348	~79
Green	5.69	6.351	~12
red	3.42	6.639	~94

7.3 Perovskite PV Cells Employing an Optical Cavity

Recently, perovskite semiconductors have emerged as a highly attractive photovoltaic (PV) material due to their ability to be fabricated via solution process at low temperatures and with low cost, offering clear advantages over the conventional inorganic PV platforms. In addition, their properties are similar to the inorganic materials, thus being able to achieve high performances. Particularly, considerable attention has been given to the organolead halide perovskite material $CH_3NH_3PbI_{3-x}Cl_x$ that shows strong optical absorption characteristics over a wide range of visible spectrum, and high power conversion efficiency has been achieved even in a simple planar device structure. The thickness of the semiconducting perovskite films used in previous reports is typically a few hundred nanometers so that the majority of the visible lights can be fully absorbed by the photoactive layer for generating large amounts of electricity [97-107]. However such a thick photoactive layer always leads to a black appearance that is not visually attractive, and only suitable for a rooftop installation with limited area, especially for modern high-rise building, while a large number of building envelopes, such as facades, skylights, walls, and windows, cannot be efficiently used for light-harvesting. In order to achieve a semitransparent characteristic, the semiconductor layer thickness has to be greatly reduced. However, the resulting color of a thinner perovskite film has a dark brown color with a reddish tint, very limited in terms of producing visually appealing PV panels [108].

In PV applications, aesthetic features of PV cells have attracted significant interest due to increasing needs for building-integrated PV (BIPV) that can be harmoniously integrated with the building envelopes. Driven by these strong demands, an organic PV device structure integrated with plasmonic color filters was developed to create desired reflective colors and simultaneously generate the electric power [16]. However the resulting PV cells can produce the colors only at a certain angle and also work for a specific polarization, both of which are attributed to the

inherent property of the surface plasmon resonance. To address these challenges, amorphous silicon (a-Si) based hybrid PV cells exploiting strong interference effects in an ultra-thin a-Si active layer and able to create a wide range of transmission and reflection colors have recently been demonstrated [51, 52]. In particular, the incident angle and polarization insensitive performances have been achieved by zeroing the optical phases of propagation and reflections. In this configuration, the a-Si layer functions as an optical cavity medium as well as photoactive layer, and therefore, the thickness of the a-Si film was limited up to 31 nm so as to make an optical resonance at visible frequency. However, the power conversion efficiency is limited by the ultra-thin thickness of the photoactive layer and achieving a very thin and smooth a-Si layer could be challenging. In fabrication, plasma-enhanced chemical vapor deposition (PECVD) process needs to be used to deposit a-Si. Therefore, a new scheme that can create aesthetic functionalities and PV performance enhancements with solution processability is strongly desirable for large area decorated PV application.

In this chapter, I demonstrate colored and semitransparent perovskite PV cells by adopting an optical microcavity configuration where two optically thin metallic layers separated by a dielectric film are employed as a cathode. Simply altering the thickness of the dielectric layer inside such a composite cathode structure enables the resonance transmission of certain wavelength of visible lights (e.g., transmitting red, green, and blue (RGB) colors), without impacting the charge collections by the electrode. In this proposed device structures the non-transmitted portion of the incident light is reflected back to the perovskite material and leads to a strong optical field in the photoactive layer at these complementary spectral regions that improve the photocurrent generation. I also show that the majority of the incident photons absorbed by the perovskite photoactive layer are effectively collected by the electrode due to the thin perovskite

film thickness (~80 nm) that is much shorter than a charge diffusion length in the perovskite material, thus leading to highly suppressed charge carrier recombination. The presented scheme offers an appealing path towards decorative BIPV and energy-efficient e-media.

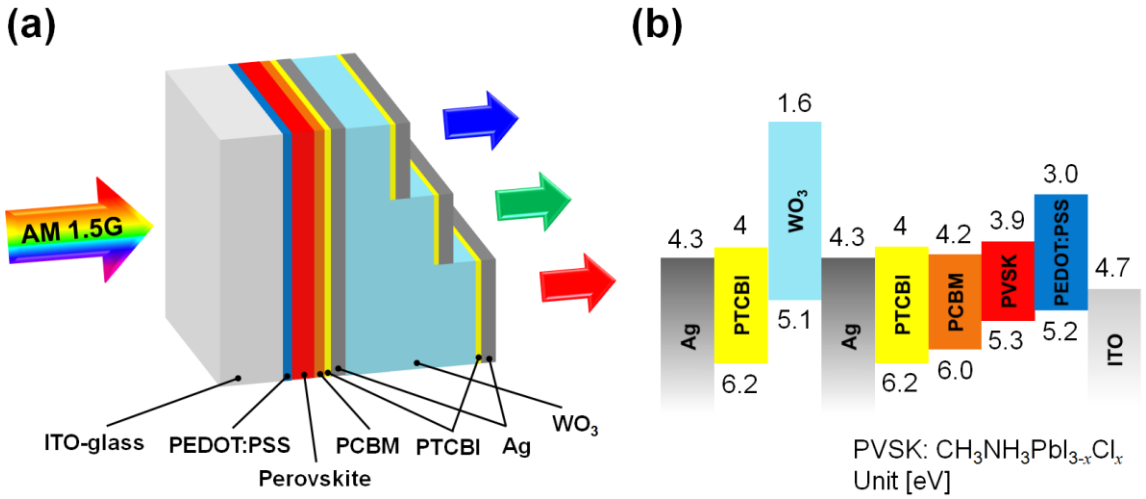

Figure 7.3.1 (a) A schematic view of the proposed colored, semitransparent perovskite PV device employing a microcavity consisting of a dielectric medium sandwiched by optically thin metallic layers in the cathode side. The desired transmission RGB colors can be tuned by simply altering the thickness of the dielectric layer in the microcavity. Each layer's thickness is as follows: PEDOT:PSS=50 nm, Perovskite=80 nm, PCBM=60 nm, Ag=20 nm, PTCBI=8 nm, WO_3=65 (Blue), 85 (Green), 115 nm (Red). (b) Energy level diagram of each layer in the proposed device structure. The energy level is relative to the vacuum level. PVSK represents $CH_3NH_3PbI_{3-x}Cl_x$ and the unit is electron volt (eV).

Figure 7.3.1 (a) presents a schematic diagram of the proposed colored perovskite PV device structure: glass/ITO/poly(3,4-ethylenedioxythiophene):poly(styrenesulfonate) (PEDOT:PSS)/$CH_3NH_3PbI_{3-x}Cl_x$/phenyl-C_{61}-butyric acid methyl ester (PCBM)/perylenetetracarboxylic bis-benzimidazole (PTCBI)/Ag/tungsten trioxide (WO_3)/PTCBI/Ag. The details of a device fabrication are as follows. ITO coated glasses (Rs=8-12 Ω/square, Delta Technologies) were cleaned with acetone and 2-propanol for 10 minutes successively under sonication, followed by further cleaning with oxygen plasma treatment for 3

minutes. PEDOT:PSS (CLEVIOS™ AI 4083) filtered with 0.45 m NY filter were spun on ITO coated glasses at 4000 rpm for 60 seconds and annealed at 120 ℃ for 15 minutes. After the substrates were transferred to N_2 glovebox, 20wt% solution of methylammonium iodide and lead chloride (3:1 molar ratio in DMF) was spun on PEDOT:PSS at 6000 rpm for 45 seconds, followed by annealing at 80 ℃ for 3 hours. Afterward, PCBM was coated by spin coating at 800 rpm for 30 seconds. PTCBI/Ag/WO_3/PTCBI/Ag was deposited successively by a thermal evaporation with shadow masks, making the device area of 0.785 mm^2 (a circular area with the diameter of 1mm).

Here, PEDOT:PSS, $CH_3NH_3PbI_{3-x}Cl_x$ and PCBM correspond to p-, i- and n- layers, respectively, and a planar p-i-n structure is constructed by layer-by-layer deposition. The thickness of the perovskite layer is 80 nm, allowing some portions of incident light to pass through to reach the microcavity cathode, which will be utilized for creating transmitted R, G, B colors. Ag/WO_3/Ag, a metal-dielectric-metal (MDM) multilayer structure, is utilized not only as a semitransparent electrode but also functions as a Fabry-Perot optical cavity to transmit a certain portion of the incident solar spectrum tuned easily by the thickness of the WO_3 layer. It should be noted that each Ag layer is preceded by a very thin organic material, PTCBI, to promote a smooth surface of an optically thin Ag film that minimizes the light scattering loss. In addition to the smooth thin Ag film formation, the PTCBI layer, in particular interfaced with the PCBM, functions as an efficient hole blocking layer due to good energy band alignment as shown in **Figure 7.3.1 (b)**.

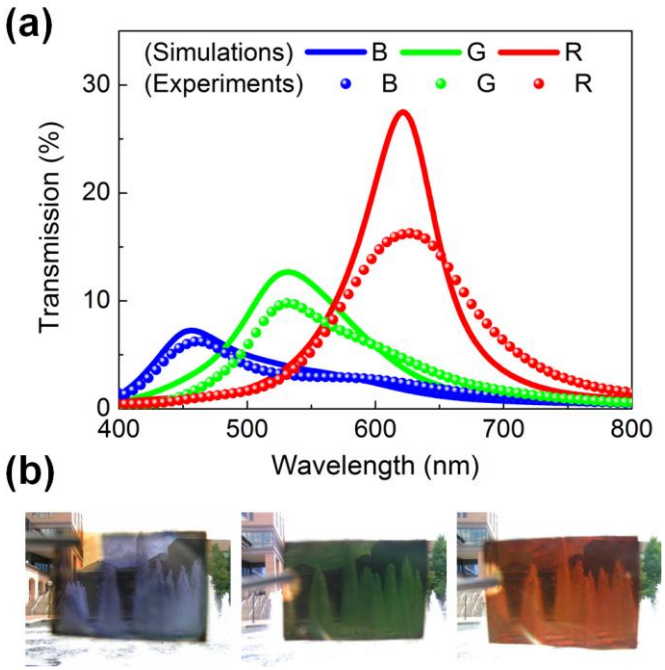

Figure 7.3.2 (a) Simulated and measured spectral transmittance curves of the proposed colorful, see-through perovskite PV devices at normal incidence. Increasing the thickness of the WO_3 layer in the microcavity cathode allows the resonance (i.e., transmission peak) to be shifted toward the longer wavelengths. The resonances at 630 (Red), 540 (Green), and 450 nm (Blue) are attained by 115, 85, and 65 nm of the WO_3 layer thicknesses, respectively. As the wavelength increases, the difference between the simulated and measured transmission spectra becomes large. Due to the negligible absorption of the perovskite photoactive layer at longer wavelengths, the red colored PV cell has the sharpest resonance behavior that can be strongly weakened by the surface roughness. (b) Optical photographs of fabricated colored PV devices. The background image can be clearly seen through our fabricated samples with RGB colors.

In **Figure 7.3.2 (a)**, the simulated (solid curves) and measured (dotted curves) spectral transmittance curves of the RGB colored perovskite PV devices at normal incidence are presented. 115, 85, and 65 nm of the WO_3 film thickness are used in order to produce RGB transmission colors, respectively, while the rest of layers' thicknesses remain the same for all colored devices as described in the caption of **Figure 7.3.1 (a)**. The corresponding Fabry-Perot resonances in the transmittance are 630, 540, and 450 nm, respectively. A transfer matrix method-based optical simulation was carried out based on refractive indices of all the materials

measured by using a spectroscopic ellipsometer (M-2000, J. A. Woollam), which is given in **Figure 7.3.3**.

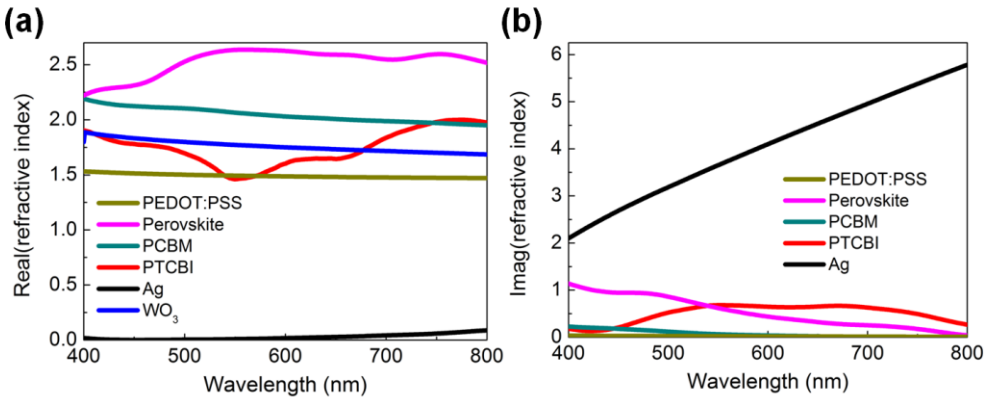

Figure 7.3.3 The real (a) and imaginary (b) part of refractive indices of PEDOT:PSS, perovskite, PCBM, PTCBI, Ag, and WO_3.

Each resonant wavelength in the measured transmittance spectra was in good agreement with that in the simulated results. On the other hands, bandwidth and peak values of the simulated transmittances were slightly higher than those of measured ones. These discrepancies between the simulated and measured profiles get large as the wavelength increases, which is attributed to the fact that the red colored cell has the sharpest resonance among the three colored devices due to relatively small optical absorptions of the perovskite material at longer wavelengths (See the wavelength-dependent imaginary part of the refractive index of the perovskite material in **Figure 7.3.3**). Such a sharp resonance effect (i.e., strong optical interference) can be strongly influenced by the roughness in thin films that cause the scattering and graded refractive index effect, thus rendering the resonance broad with lower efficiency. Note that our colored devices show a low transmission at around 780 nm that corresponds to the band gap of the perovskite material, which is distinctly different from what has been observed from the previously reported semitransparent perovskite solar cells. Due to the low absorption coefficient of the perovkiste material at 780 nm,

the transmission of the previous demonstration is always high, showing reddish transmitted colors. In our case, however, strong optical interference behaviors in the MDM multilayer structure allows incident light at off-resonance wavelengths to be destructively interfered, thus leading to strong reflections. We also note that a part of the photons in the blue spectral region of AM1.5 is transmitted, which cannot be harvested by the blue colored cell. This is responsible for the lowest short-circuit current density (Jsc) among the three colored devices, which will be validated by measuring a current density-voltage (J-V) characteristics later. On the other hand, the highest Jsc can be achieved by the red colored device since most incident solar light energy, in particular shorter wavelengths where the optical absorption of the perovskite material is fairly large, can contribute to electric power generation without much disturbance. **Figure 7.3.2 (b)** exhibits optical images of the fabricated devices, showing that a background water fountain can be seen through the fabricated colored cells with distinctive RGB colors. Note that the different colors can be readily tuned by altering the thickness of the optical spacer layer (i.e., WO_3) in the MDM while keeping the other layers the same (including perovskite semiconductor), therefore the proposed approach can be easily scaled to large areas.

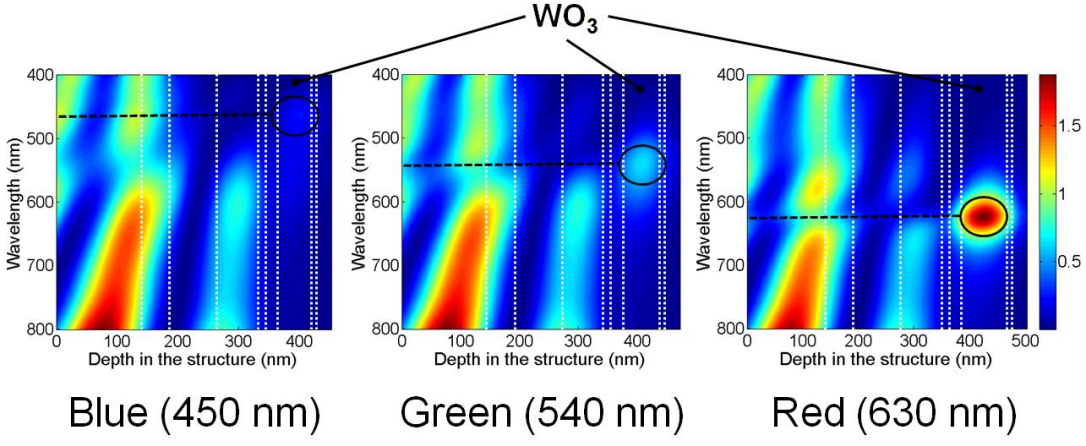

Figure 7.3.4 Normalized optical field intensity profiles of the colored PV cells with different thickness of the WO_3 medium: 65 nm (left), 85 nm (medium), and 115 nm (right). The incident light is coming from the left-hand side and the boundary of each medium is indicated by white

dotted lines. The position where the optical field is highly concentrated in the WO_3 layer corresponds to the resonance wavelength that is in good agreement with the transmission peak as shown in Figure 7.3.2 (a).

Figure 7.3.4 depicts normalized intensity distributions of the optical field of the RGB colored PV devices, each of which has different thickness of the optical spacer layer WO_3 (R: 115 nm, G: 85 nm, and B: 65 nm). In all three structures there is strong optical field intensity in the WO_3 layer inside the MDM structure, and the wavelength showing high optical field concentration in the optical spacer layer matches well with the peak position of the spectral transmittance as exhibited in **Figure 7.3.2 (a)**, indicating a strong Fabry-Perot resonance behavior for the three colored cells. We also note that the blue colored cell shows a lower magnitude of the optical field intensity in the MDM structure since the majority of shorter wavelengths are harvested by the perovskite photoactive layer.

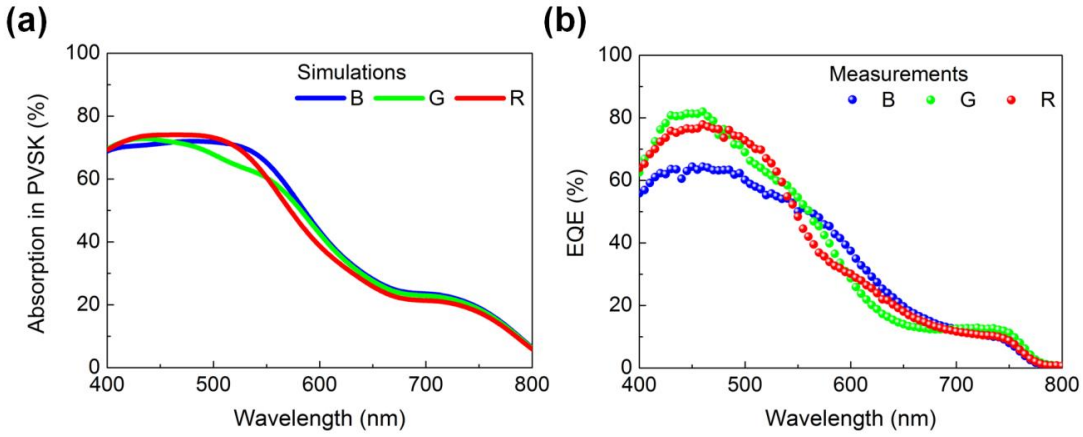

Figure 7.3.5 (a) Simulated optical absorption spectra in the perovskite photoactive layer for three RGB individual colored PV cells. (b) The corresponding measured external quantum efficiency (EQE) profiles exhibiting relatively good agreement with the simulated results. This leads to insignificant charge carrier recombination implying that converting the absorbed photons into photogenerated charges with high efficiency is achieved.

The optical resonance in the MDM structure could affect the total optical interference inside the devices; hence, the light absorption at the perovskite layer is influenced as well. To elucidate how much the light absorption at the perovskite layer is changed by the optical interference effects, we focus on the absorption spectra of the photoactive layer and the corresponding photocurrent. As the photoactive layer thickness is the same and the thin Ag layer in the cathode results in a weak reflection, it is thus expected to have the similar optical absorption characteristics for the three colored devices despite the different resonance wavelength. Simulated absorption spectra in the photoactive layer of the colored solar cells are shown in **Figure 7.3.5 (a)**, which match well with measured external quantum efficiency (EQE) spectra depicted in **Figure 7.3.5 (b)**. This good agreement indicates that there is negligible charge carrier recombination, and that a conversion of the absorbed photons into photogenerated charges collected by the electrode with nearly 100% efficiency. This can be explained by the fact that a typical diffusion length of the perovskite material is much longer than the thickness of the perovskite layer used in our colored cell design [109, 110]. From the measured EQE spectra, it is clear that the blue colored cell has the relatively lower EQE profiles at a blue spectral range as compared to the green and red cell devices because the resonance in the spectral transmittance at 450 nm is created for transmitting the blue color, which cannot be utilized for electric power generation, while the EQE spectrum of the red colored device is lower than that of both the blue and green colored cells at around 600 nm.

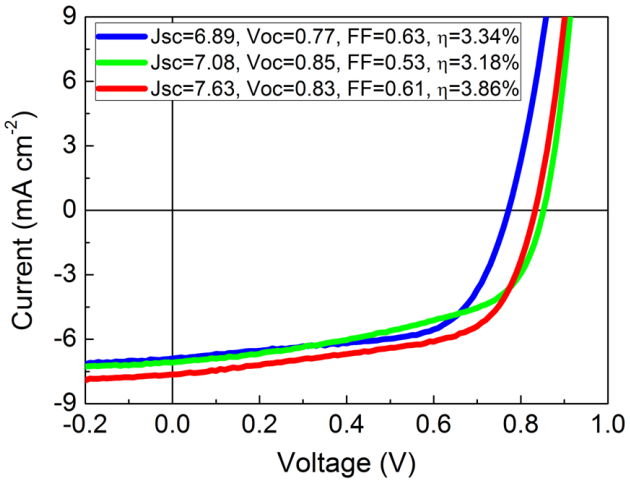

Figure 7.3.6 Measured current density vs. voltage (J–V) characteristics of the colored semitransparent perovskite PV cell devices under a simulated AM1.5 solar spectrum illumination (100 mW cm^{-2}). The electrical performances, including Jsc, Voc, and FF, of RGB colored PV devices are given in the inset.

Finally we show the electrical characteristics of the microcavity-embedded perovskite PV devices. The current – voltage (J-V) measurements of the colored PV cells under simulated AM 1.5 sunlight illumination are shown in **Figure 7.3.6**. The electrical performances of each colored PV cells are also summarized in the inset. As we expected, the blue colored device shows a lower Jsc value (6.89 mA cm^{-2}) than the green (7.14 mA cm^{-2}) and red cells (7.63 mA cm^{-2}). This is attributed to the fact that creating the transmitted resonance at the short wavelength region that corresponds to strong absorption range of the perovskite absorption causes the short wavelengths of the incident solar spectrum not to be fully harvested by the solar cell devices, thus leading to lower Jsc value for the blue colored device. The red colored cell shows Jsc of 7.63 mA cm^{-2}, an open-circuit voltage (Voc) of 0.812 V and a fill factor (FF) of 66%, yielding a power conversion efficiency of 3.83%. In such a colored device configuration, Jsc is limited due to the requirement of transmitting a specific color. However, Voc and FF could be improved by the optimization of the interface and device fabrication as for the case of conventional perovskite PV cells. We

believe the design strategy described here could bring the PV cells into architectures with a wide variety of appealing design features, thus opening the potential for decorative BIPV.

7.4 Comparison of Microcavity-Integrated PV Cells and PV Devices with External Color Filters

One would ask what the advantage of the microcavity-integrated colored semitransparent PV devices over the PV cells with external color filters (either absorptive or dichroic filter) is. The following table summarizes the performance of each color filter.

Table 7.4.1 Summary of the performance of absorptive, dichroic, and microcavity color filters.

Performance	Absorptive	Dichroic	Microcavity
Efficiency	Poor (< 45%)	Good (> 80%)	Good (> 80%)
Fabrication	Simple	Difficult (> 20 layers)	Simple (~4 layers)
Integration	Difficult	Difficult	Easy
Angle tolerance	Good	Poor	Good
Heat tolerance	Poor	Good	Good
Thickness	Thick	Thick (> 2mm)	Thin (< 200 nm)
Cost	Cheap	Expensive	Cheap
Light recycling	Impossible	Possible	Possible
Lifetime	Short	Long	Long

As described in the **Table 7.4.1**, the absorptive type color filter is very cheap and simple to make. However, the transmission efficiency of the color filter is less than 45% and it is thus expected that the transmission efficiency of the PV cell combined with this type of the color filter would

be very low. In addition, a certain wavelength is transmitted to create a color while the rest of the wavelengths are absorbed so that the photoactive layer can harvest just a single path of incident light (i.e., no reflections), thus leading to much reduced power conversion efficiency. Definitely, these issues could be addressed by incorporating the dichroic color filter (interference filter) instead. The dichroic color filter can transmit the desired wavelength range and reflect the complementary spectrum that will be potentially harvested by the PV cell again. However, the dichroic color filter consists of multiple layers (typically more than 20 layers) and shows a dramatic resonance shift at the oblique angle of incidence. Additionally, the dichroic color filter is pretty expensive and its thickness is too thick that causes the integration to be difficult. On the contrary, the microcavity color filter comprising metal-insulator-metal, which is a very simple geometry, and the angle dependent property could be significantly improved by putting the phase compensating layer on top of the microcavity [111]. Due to its ultra-thin thickness less than 200 nm, it is very easy to be directly integrated with the PV cells.

7.5 Conclusion

In conclusion, we have demonstrated a microcavity-embedded photonic color filtering scheme integrated with a-Si and perovskite PV cells capable of transmitting distinctive colored lights. The colors can be readily tuned by varying the thickness of the optical spacer inside the composite cathode. Therefore the design principle is applicable to the entire visible wavelength range and the devices can simultaneously generate electric power with up to ~4% of power conversion efficiency. It has also been shown that greatly suppressed electron-hole recombination is enabled by the ultra-thin photoactive layer thickness as compared to the charge

diffusion length of the a-Si and perovskite material. This technique open the door to a number of applications, such as energy-efficient colored display systems and decorative solar panels that can be harmoniously integrated with the interior and exterior of the buildings.

Chapter 8

Flexible, ITO-Free Perovskite PV Creating Reflective Colors

8.1 Introduction

In a previous chapter, we have demonstrated that the colored, semitransparent a-Si and perovskite PV by adopting an optical microcavity configuration in a cathode. Herein, we will point out the problems of above designs when employing a similar approach to create the reflective colored perovskite PV in terms of the color purity and then provide a solution in order to produce the distinctive CMY reflective colors.

8.2 Design Principle and Results

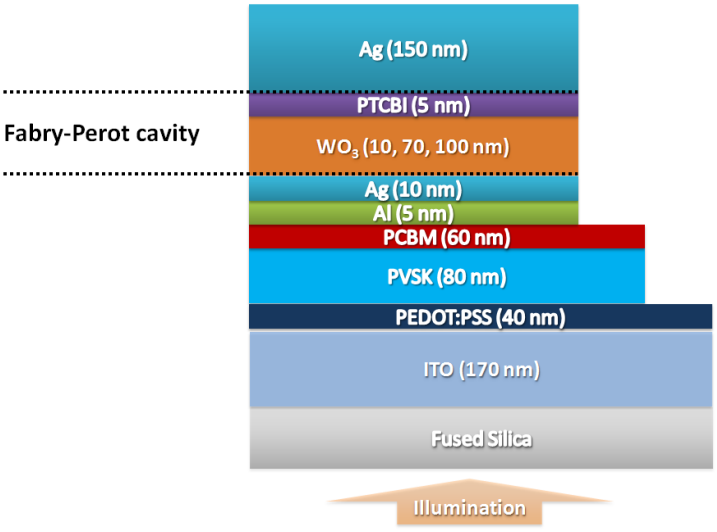

Figure 8.2.1 A schematic diagram of the proposed perovskite PV producing the reflective CMY colors by incorporating the F-P cavity.

A schematic representation of the proposed perovskite PV creating the reflective CMY colors is depicted in **Figure 8.2.1**. By simply making the topmost Ag layer optically thick (i.e., no transmitted light) in the structure shown in **Figure 8.2.1**, we can produce reflective CMY colors instead of transmissive RGB colors.

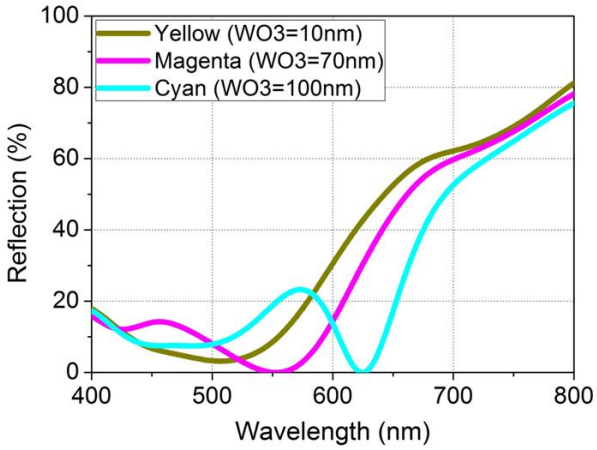

Figure 8.2.2 Simulated spectral reflectance curves of the reflective CMY colored cells. The color can be tuned by changing the thickness of WO_3 layer.

In **Figure 8.2.2**, calculated reflection spectra of the CMY colored devices at normal incidence are present. Varying the thickness of the WO_3 layer enables the reflective color to be tuned from yellow to magenta and then cyan. 100, 70, and 10 nm of the WO_3 layer thicknesses are utilized in order to create reflective CMY colors, respectively. We can see that there is an additional reflection valley at 450 nm for the three CMY colored devices, which is attributed to the fact that another F-P cavity is formed between ITO, and Al and bottom Ag layer. The effective cavity medium would be the sum of PEDOT:PSS, perovskite, and PCBM layers. This additional F-P

cavity results in one more dip in the reflection spectrum, which is located at 450 nm. This will be confirmed by investigating the intensity of the electric field distributions at 450 nm later.

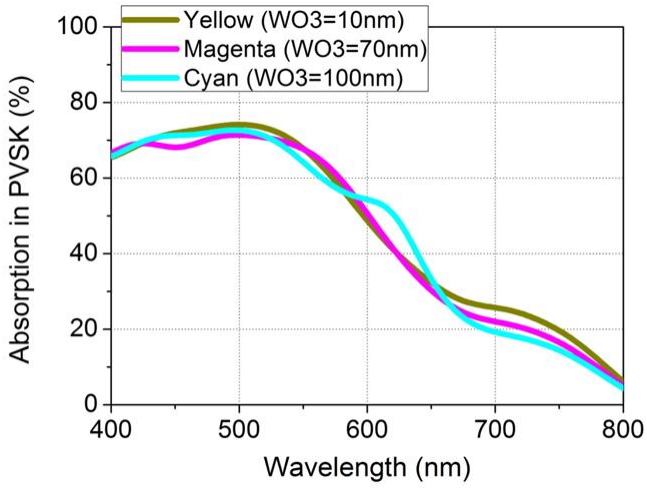

Figure 8.2.3 Simulated absorption profiles in the perovskite film of the reflective CMY colored cells.

Figure 8.2.3 presents simulated absorption spectra in the perovskite layer of the proposed reflective CMY colored devices. There is not a big difference between the yellow and magenta devices as is seen from the **Figure 8.2.3**. Due to the strong optical absorption of the perovskite film at shorter wavelengths, it is hard to see the F-P resonance in the absorption spectra in both yellow and magenta cells. For the cyan colored cell, it is obvious that there is an absorption peak at 620 nm that corresponds to the F-P resonance resulting from the F-P cavity in the cathode.

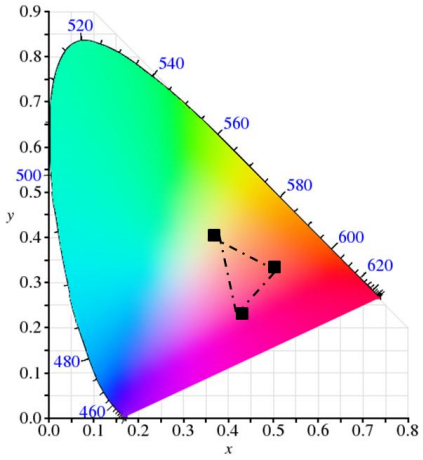

Figure 8.2.4 The illustration of the color coordinates obtained from the reflection spectra (Figure 8.2.2) depicted on the CIE 1931 chromaticity diagram.

In order to explore the chromaticity of the proposed CMY colored perovskite PV, the color coordinates are calculated from the reflection spectra in **Figure 8.2.2** and then illustrated on the CIE 1931 chromaticity diagram in **Figure 8.2.4**. However, a size of the triangle consisting of the calculated basic CMY colors is too small and the calculated colors for the yellow and cyan are not basic yellow and cyan colors, which will be addressed by employing a different geometry.

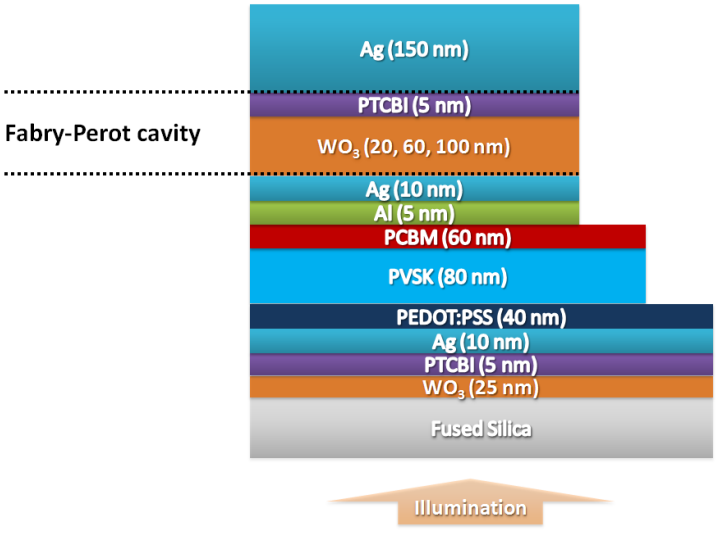

Figure 8.2.5 A schematic representation of the proposed ITO-free perovskite PV producing the reflective CMY colors.

ITO has been widely utilized as a transparent electrode since it can offer a high transparency (> 95%) and a low resistivity over a broad range of visible wavelengths. However ITO suffers from a scarcity of indium and a low mechanical flexibility. Additionally, more importantly, a high temperature (> 300℃) annealing process is needed to attain such characteristics, thus limiting the application to the flexible or organic based optoelectronic devices. In **Figure 8.2.5**, a schematic diagram of the proposed ITO-free reflective colored perovskite PV is exhibited. In this design, ITO anode is replaced by a multilayer electrode (i.e., DMD structure) so that our concept can be applied to the plastic substrate, potentially achieving the flexible PV devices.

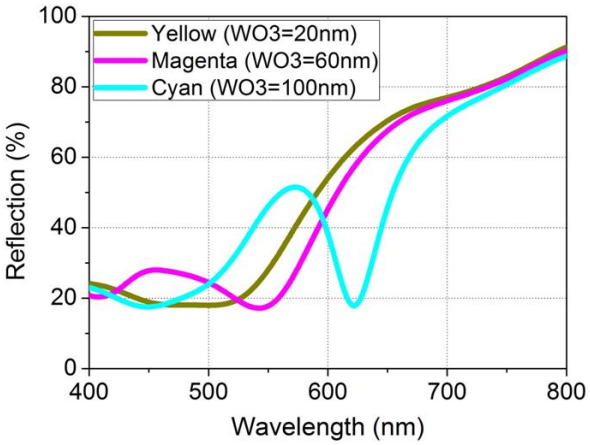

Figure 8.2.6 Simulated spectral reflectance curves of the ITO-free reflective CMY colored cells. The color can be tuned by changing the thickness of WO_3 layer.

Figure 8.2.6 displays calculated reflection spectra of the CMY colored perovskite PV devices at normal incident angle. The CMY reflection colors can be varied by modifying the thickness of the WO_3 layer. 100, 60, and 20 nm of the WO_3 layer thicknesses are used to produce reflective CMY colors, respectively.

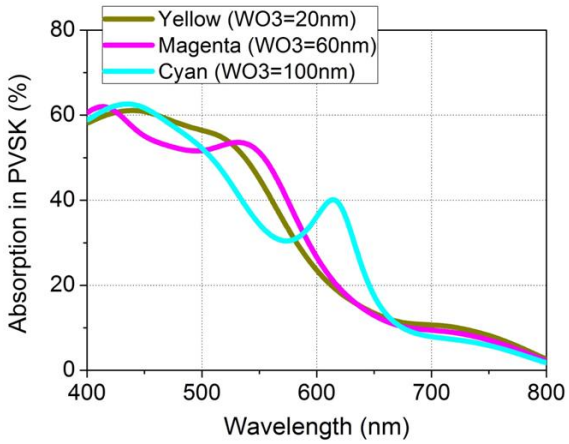

Figure 8.2.7 Simulated absorption profiles in the perovskite film of the ITO-free reflective CMY colored cells.

Calculated absorption spectra in the perovskite layer of ITO-free reflective colored perovskite PV are depicted in **Figure 8.2.7**. Unlike **Figure 8.2.3**, the resonance behavior gets significant so that the absorption peak at each resonance wavelength for CMY colors can be observed. This can be explained by the following reason. Since the reflection of the DMD electrode surface is higher than that of the ITO electrode, an amount of the incident light to be absorbed by the perovskite film is smaller for ITO-free colored cells. Thus the optical absorption in the perovskite layer is generally lower than that observed in **Figure 8.2.3**. Because of this lower absorption, the resonance effect can become more conspicuous as compared to what has been observed in **Figure 8.2.3**.

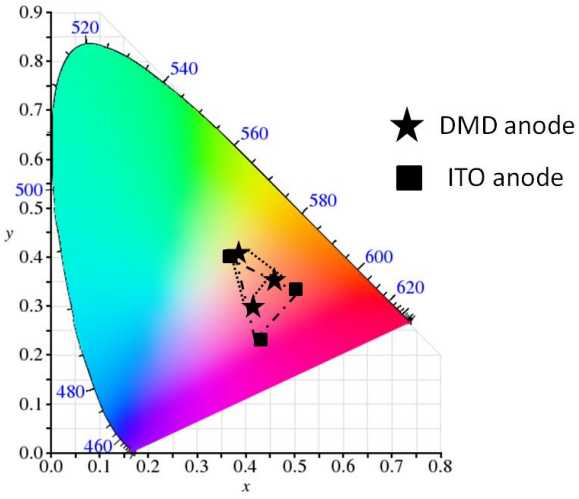

Figure 8.2.8 The description of the color coordinates obtained from the reflection spectra (Figure 8.2.6) illustrated on the CIE 1931 chromaticity diagram.

To investigate the color purity of the proposed ITO-free CMY colored perovskite PV cells, the color coordinates are calculated from the spectral reflectance curves shown in **Figure 8.2.6** and then described on the CIE 1931 chromaticity diagram in **Figure 8.2.8**. However, a triangle that is composed of the calculated CMY colors for ITO-free design is much smaller than the triangle for previous structure (**Figure 8.2.1**) even though we have observed more distinct resonance behavior. This is because an effect of another F-P cavity forming between Ag in anode and bottom Ag in the cathode on the reflection spectra is also getting significant since the reflection of the DMD multilayer electrode surface is higher than that of the ITO surface as mentioned earlier, which can degrade the color purity of the structure.

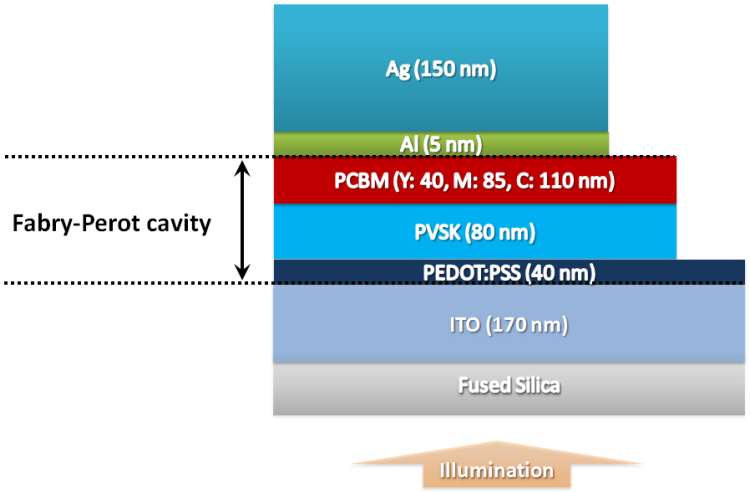

Figure 8.2.9 A schematic description of the proposed reflection colored perovskite PV based on F-P cavity geometry.

It is demonstrated that the proposed structures discussed in **Figure 8.2.1** and **Figure 8.2.5** show poor color purity resulting from the two different F-P cavity resonances. To address this issue, we propose a different geometry by removing the F-P cavity in the cathode side so that we can rely on only one F-P resonance as shown in **Figure 8.2.9**.

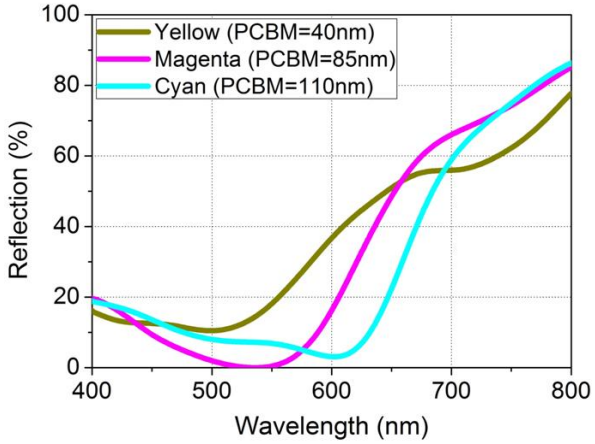

Figure 8.2.10 Simulated CMY reflection profiles of the perovskite cells. The color can be tuned by changing the thickness of PCBM layer.

In **Figure 8.2.10**, simulated reflection profiles of the CMY colored perovskite PV cells at normal incident angle are depicted. The CMY reflection colors can be varied by modifying the thickness of the PCBM layer. 110, 85, and 40 nm of the PCBM layer thicknesses are used to produce reflective CMY colors, respectively. Although only one resonance (i.e., reflection valley) is created, one concern still to be resolved is that the reflection spectra have somewhat broad profiles mainly due to the weak reflection of the ITO anode surface. This can be addressed by replacing the ITO electrode with the multilayer electrode in the following section.

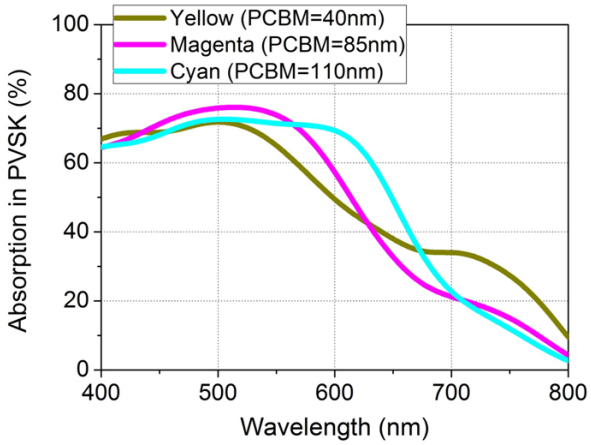

Figure 8.2.11 Simulated absorption spectra in the perovskite layer of the reflective CMY colored cells.

Calculated optical absorption spectra in the perovskite film of the proposed CMY colored PV cells are exhibited in **Figure 8.2.11**. Even though the absorption spectra have fairly broad profiles for the CMY colored cells, it is clear to see that the resonance of each colored perovskite PV device. In particular, the yellow colored PV cell has additional peak at around 730 nm in the optical absorption spectrum, which would be arising from the fundamental F-P cavity mode. This will be verified by examining the electric field distributions later.

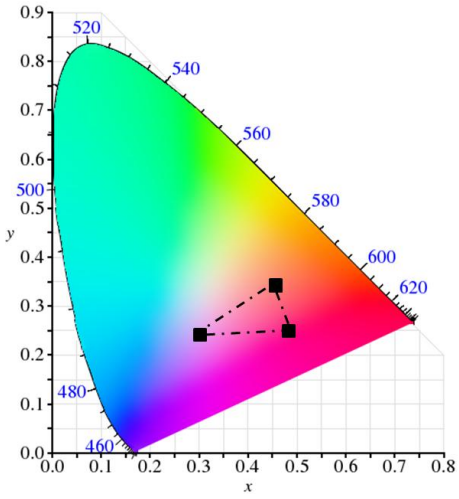

Figure 8.2.12 The description of the color coordinates calculated from the reflection spectra (Figure 8.2.10) illustrated on the CIE 1931 chromaticity diagram.

In **Figure 8.2.12**, the color coordinates calculated from the spectral reflectance curves in **Figure 8.2.10** are depicted on the CIE 1931 chromaticity diagram to evaluate the purity of the color created from the reflective CMY colored perovskite PV cells. However, a triangle comprising the calculated CMY colors is too small and the calculated colors for the yellow and cyan are not basic yellow and cyan colors. This is primarily because of the broad reflection spectrum, which will be improved by replacing the ITO anode with the DMD multilayer electrode in the following part.

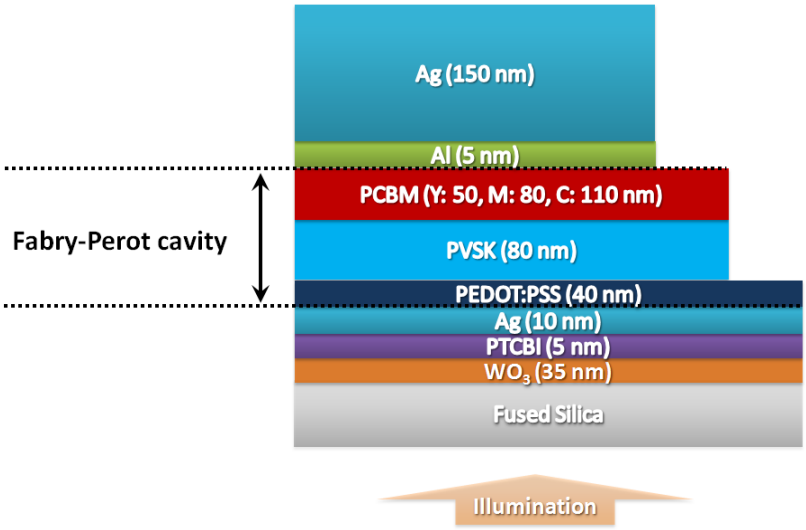

Figure 8.2.13 A schematic view of the proposed ITO-free reflection colored perovskite PV based on F-P cavity geometry.

The F-P cavity resonance gets sharp that leads to great purity of the colors as the reflection of each surface increases. As we mentioned earlier, the DMD electrode surface's reflection is higher than that the ITO surface's reflection. Replacing the ITO anode with the DMD electrode allows the color purity to be enhanced to some extent and a schematic diagram of the ITO-free high purity reflective colored perovskite PV cells is depicted in **Figure 8.2.13**. Additionally, the glass substrate can be replaced by any plastic flexible substrate since high temperature annealing process is not required for the DMD electrode.

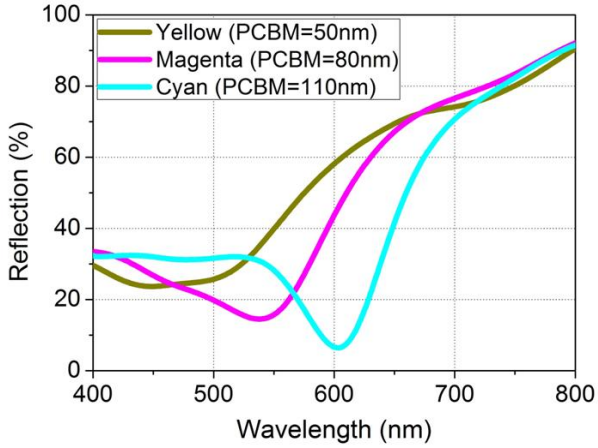

Figure 8.2.14 Simulated CMY reflection profiles of the ITO-free perovskite cells. The color can be tuned by changing the thickness of PCBM layer.

Figure 8.2.14 presents simulated optical absorption profiles in the perovskite layer of the proposed ITO-free CMY colored perovskite PV cells. It is apparent that the reflection spectra have narrow bandwidths as compared to what we have seen in the previous part shown in **Figure 8.2.10**. It is thus expected that the chromaticity of the reflective CMY colors produced from this design would be better than any other structures discussed in the previous sections, which will be described in **Figure 8.2.16** in more detail.

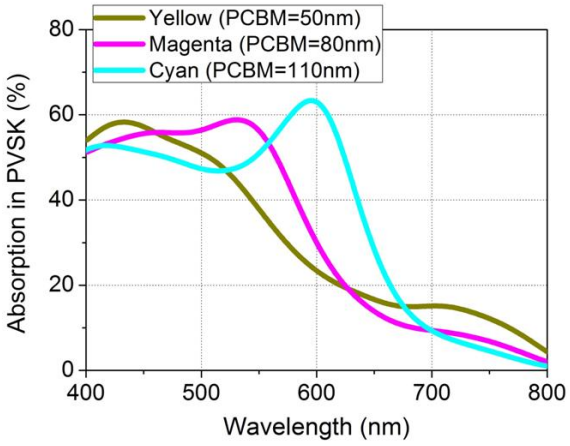

Figure 8.2.15 Simulated absorption spectra in the perovskite layer of the ITO-free reflective CMY colored cells.

Figure 8.2.15 presents simulated optical absorption spectra in the perovskite film of the proposed ITO-free CMY colored PV cells. It is highly obvious to see the distinct resonance behaviors for the three colored perovskite PV devices. To create the reflective CMY colors, 110, 80, and 50 nm of PCBM layer thicknesses are used and the corresponding resonance positions are 600, 550, and 440 nm, respectively. It should be noted that there is a trade-off between the color purity and the power conversion efficiency of the PV cells. The optical absorption in the perovskite layer of the ITO-free PV structures, which is directly proportional to the Jsc, is always weak as compared to that of the ITO-based PV device structures, implying that the power conversion efficiency of the ITO-free PV is lower whereas showing the improved color purity.

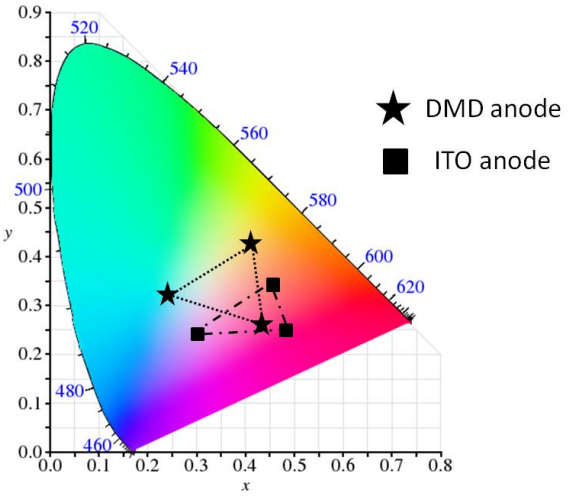

Figure 8.2.16 The representation of the color coordinates calculated from the spectral reflectance curves (Figure 3.8.14) depicted on the CIE 1931 chromaticity diagram.

In **Figure 8.2.16**, the color coordinates calculated from the reflection profiles exhibited in **Figure 8.2.14** are described on the CIE 1931 chromaticity diagram to estimate the chromaticity of the reflective CMY colors. It is clear that a size of the triangle obtained from the DMD electrode-

based PV structure is larger than that of the ITO anode-based PV structure. In addition, the reflective colors created from the DMD electrode-based PV structure correspond to the basic CMY colors while the yellow and cyan colors of the ITO anode-based structure is not matched with the basic colors, thus showing greatly improved color purity.

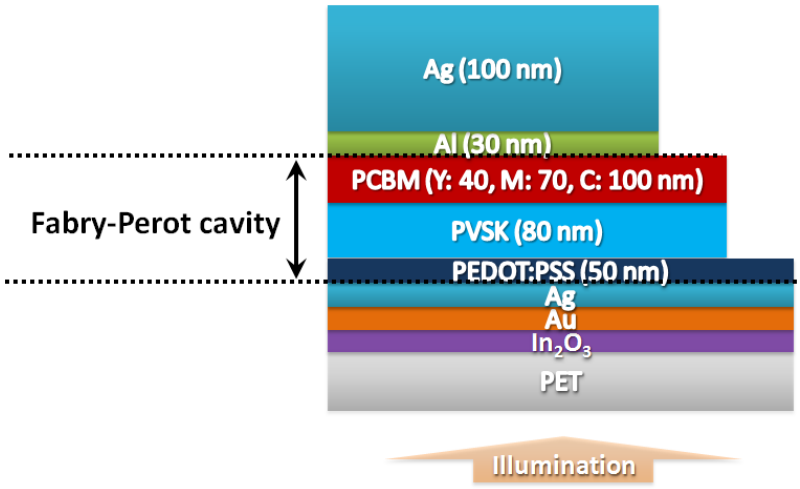

Figure 8.2.17 A schematic view of the proposed flexible, ITO-free perovskite PV creating distinctive reflective CMY colors. Modifying the thickness of the PCBM layer enables the reflective colors to be tuned.

When the DMD electrode is involved, the high temperature annealing step is not needed so that the colored perovskite PV cells can be built on the flexible substrate. We will use a PET film with In_2O_3, Au, and Ag deposited on top of the PET film (PF-65IN-1502, Delta technologies) as a substrate. This substrate shows more than 74 % of average transmittance at visible frequencies and 10 ohm/sq of a sheet resistance. **Figure 8.2.17** depicts a schematic representation of the proposed flexible, ITO-free colored perovskite PV cells to be fabricated in the near future.

8.3 Conclusion

We have presented a design of the flexible, ITO-free perovskite PV cells creating reflective colors. Firstly, the perovskite PV devices are integrated with the microcavity cathode but the color purity is too poor due to the two F-P resonances at different wavelengths. To improve the color purity, we have removed the microcavity-based cathode and created a F-P cavity between the multilayer DMD electrode and the thick metallic cathode.

Chapter 9

Extraordinary Optical Absorption (EOA) Behaviors in Ultra-Thin Semiconductor Films

9.1 Introduction

Generally, people have been thinking that the PV device with thicker photoactive layer always show higher Jsc value and therefore higher power conversion efficiency. As presented in the previous sections, however, the green colored a-Si PV cell shows higher power conversion efficiency, in particular Jsc, than the red PV devices that have thicker a-Si layer. Similarly, for the reflective CMY colored a-Si PV cells, the yellow and magenta devices exhibit higher Jsc than the cyan colored a-Si PV cell although the cyan device has the thickest a-Si layer among them. Considering Voc and FF of each colored cell are similar to one another whereas each device shows different Jsc with creating a resonance at different wavelength, there would be something interesting to investigate further in terms of the optical performance of the ultra-thin a-Si PV. In this chapter, I will discuss an extraordinary optical absorption effect in the ultra-thin a-Si PV in more detail.

9.2 EOA Effects in Ultra-Thin a-Si PV Cells

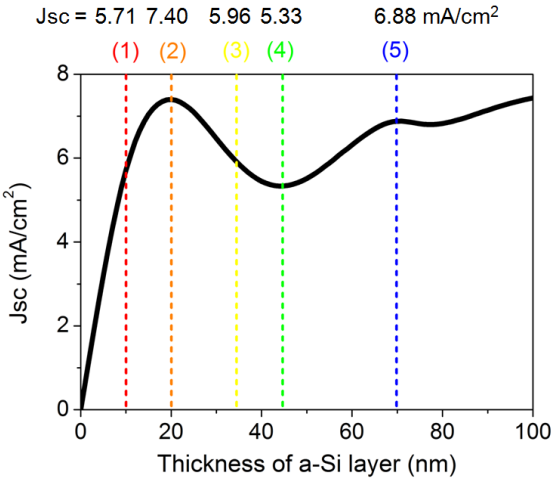

Figure 9.2.1 Calculated Jsc as a function of the thickness of a-Si layer.

Figure 9.2.1 presents calculated Jsc values as a function of the a-Si layer thickness from 0 to 100 nm. A schematic diagram under investigation is the same as shown in **Figure 6.2.1**. (i.e., reflective colored ultra-thin a-Si PV) Interestingly, the PV cell with 20 nm of the a-Si photoactive layer shows the highest Jsc value (7.4 mA/cm^2) than the PV cells with 34, 44, and even 70 nm thicknesses of the a-Si layer.

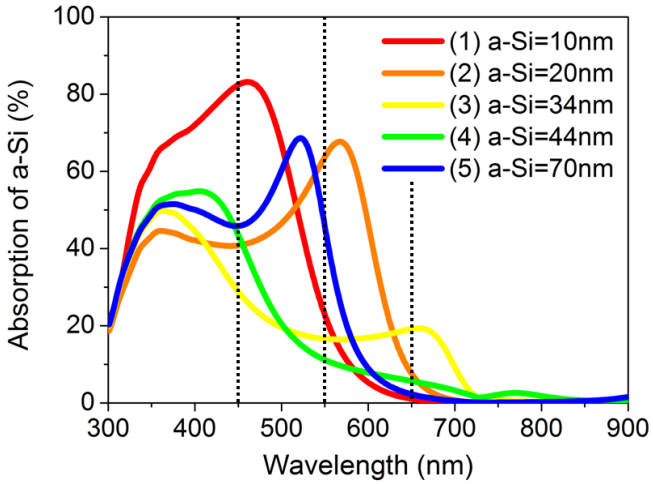

Figure 9.2.2 Calculated absorption spectra in the a-Si layer with several different thicknesses.

Simulated absorption spectra in the a-Si photoactive layer with different thicknesses are described in **Figure 9.2.2**. By increasing the a-Si thickness, the F-P cavity resonance mode is red-shifted (i.e., toward the longer wavelengths). For example, 10, 20, 34, 44 nm of the a-Si PV cells have the fundamental F-P resonance at 460, 560, 655, 760 nm, respectively. For the PV device with 70 nm of the a-Si layer, the fundamental F-P resonance is at around 900 nm and the second-order F-P mode is at 535 nm. It is seen that there is an additional absorption peak located at 350 nm that is attributed to the intrinsic absorption property of the a-Si material. As we explained earlier, the material absorption is proportional to both the *n* and *k* values of the material. **Figure 9.2.3** displays the *n*, *k*, and their product of the a-Si material measured by a spectroscopic ellipsometer (M-2000, J. A. Woollam). As is seen from the figure, it is clear to see the peak at 350 nm when multiplying the *n* and *k* of the a-Si material, which can lead to strong optical absorption at 350 nm.

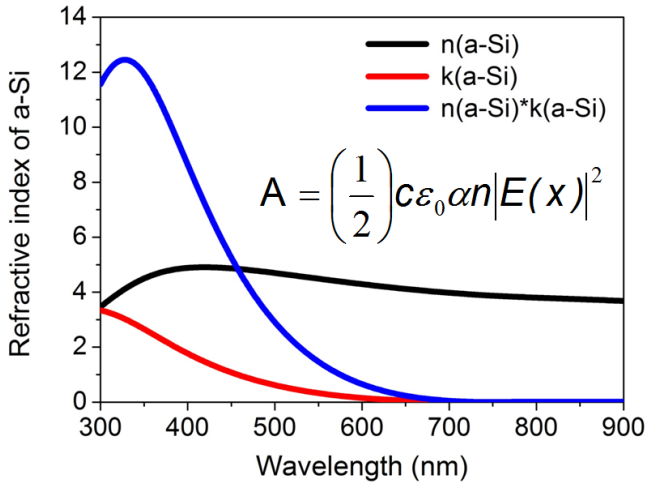

Figure 9.2.3 Complex refractive index of the a-Si material measured by a spectroscopic ellipsometer (M-2000, J. A. Woollam).

Jsc can be calculated by the following equation (**Equation 9.2.1**).

$$J_{SC} = \int_{300nm}^{800nm} \frac{e\lambda}{hc} QE(\lambda) I_{AM1.5}(\lambda) d\lambda \quad (9.2.1)$$

where *e*, *h*, λ and *c* are elementary charge, Plank constant, wavelength, and speed of light, respectively. $I_{AM1.5}(\lambda)$ is AM 1.5G solar radiation spectrum. We assume that $QE(\lambda)$ is equal to the optical absorption spectrum in the a-Si layer (i.e., internal quantum efficiency is 100 %). Since we have used the a-Si photoactive layer whose thickness is much thinner than a carrier diffusion length of the a-Si material, 100 % of internal quantum efficiency would be good approximation. When calculating the Jsc, the AM 1.5G solar spectrum also needs to be considered, which has the highest intensity between 450 and 550 nm as is seen in **Figure 9.2.4**.

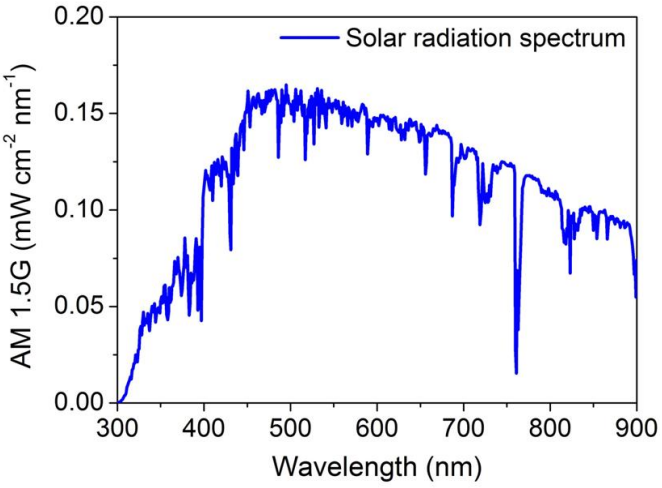

Figure 9.2.4 A solar radiation spectrum (AM 1.5G).

The optical absorption in the a-Si layer at each wavelength range is summarized in **Table 9.2.1**. According to the **Equation 9.2.1**, Jsc would be higher when having the strong absorption in the a-Si layer at longer wavelengths since Jsc is proportional to the wavelength. In addition, AM 1.5G solar radiation spectrum has very small intensity between 300 and 450 nm whereas its intensity continuously decreases from 450 nm. For instance, the absorption spectrum in the a-Si

layer with 10 nm thickness has the highest absorption between 300 and 450 nm but the AM 1.5G intensity is very low at these wavelength ranges. Additionally, 10 nm thick a-Si PV shows the lowest optical absorption between 550 and 650 nm, thus resulting in lower Jsc. However, the optical absorption profile in the a-Si layer with 20 nm thickness has the lowest absorption between 300 and 450 nm, which are not important regions since the AM 1.5G solar radiation intensity is pretty low at these regimes. Also, 20 nm thick a-Si PV cell exhibits intermediate absorptions between 450 and 550 nm and the highest absorptions at longer wavelength ranges from 550 to 650 nm, which lead to the highest Jsc.

Table 9.2.1 Summary of the optical absorption in the a-Si layer as a function of the a-Si thickness at each wavelength range.

Absorption	**a-Si layer thickness (nm)**				
λ range (nm)	10	20	34	44	70
300 – 450	highest	lowest	low	high	medium
450 – 550	high	medium	low	lowest	highest
550 – 650	lowest	highest	high	low	medium
Total	low	highest	medium	lowest	high

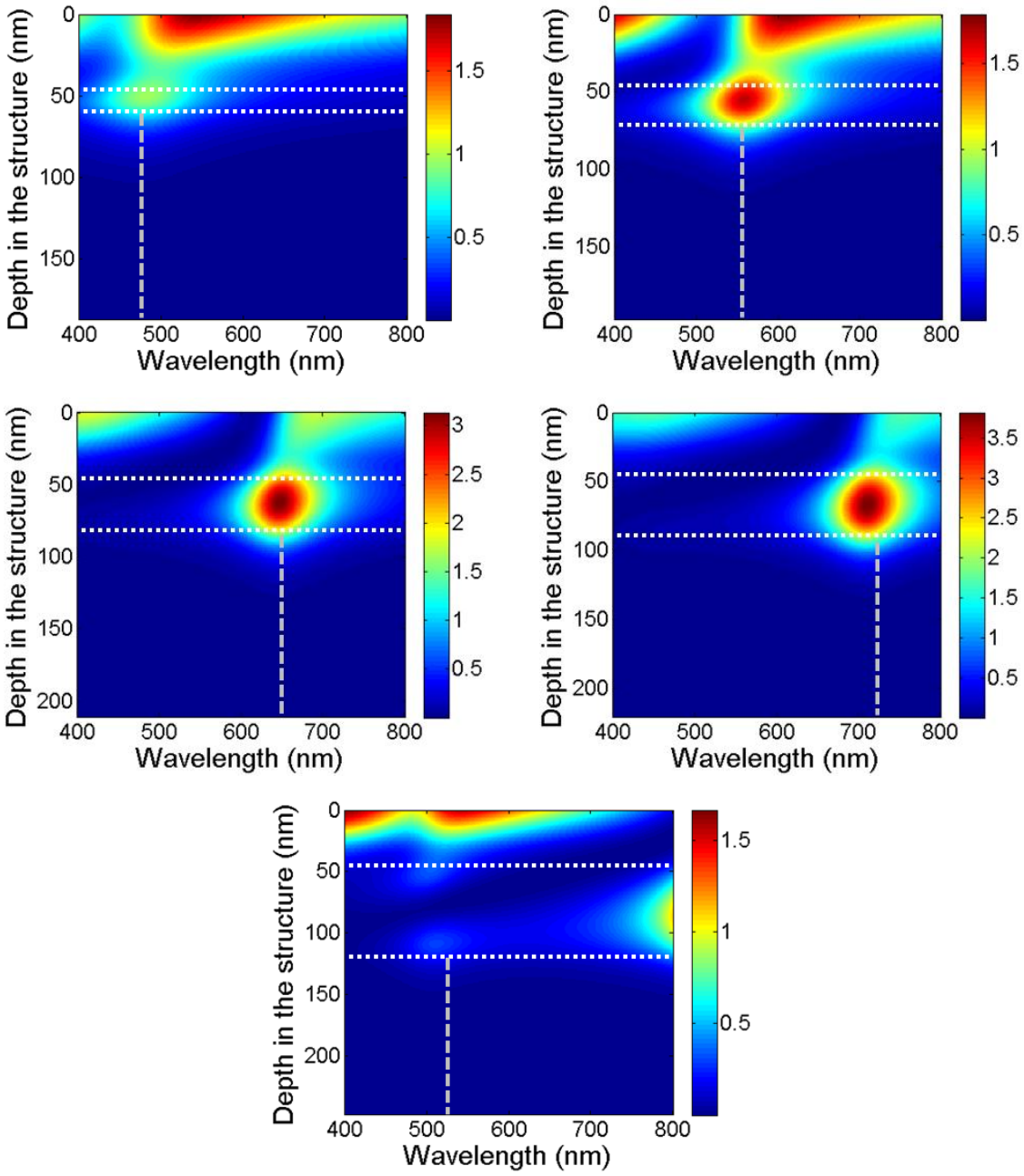

Figure 9.2.5 Electric field distributions for reflective colored ultra-thin a-Si solar cells with 10 (a), 20 (b), 34 (c), 44 (d), 70 nm (e) of the a-Si photoactive layer. The corresponding fundamental F-P resonances are 470, 565, 660, 745, and 520 nm (second-order F-P mode).

Figure 9.2.5 (a) presents normalized intensity of electric field distributions of the colored a-Si PV cell that has 10 nm of the photoactive layer. The corresponding resonance wavelength of this cell is 470 nm from the calculation. The region between two white dotted lines indicates the a-Si

photoactive layer and green dashed line represents the position of the resonance. As can be seen from the figure, the electric field is primarily concentrated in the a-Si layer at around 470 nm, thus validating the F-P resonance mode occurring in the ultra-thin a-Si layer. Likewise, **Figure 9.2.5 (b) – (e)** exhibit that the wavelength position where the highest intensity of electric field distributions exist in the ultra-thin a-Si layer matches well with the calculated F-P cavity resonance. It is noted that the field intensity gets higher and narrower as the a-Si layer thickness increase, which is attributed to the fact that the a-Si material has the insignificant absorption loss as the wavelength increases due to its band gap.

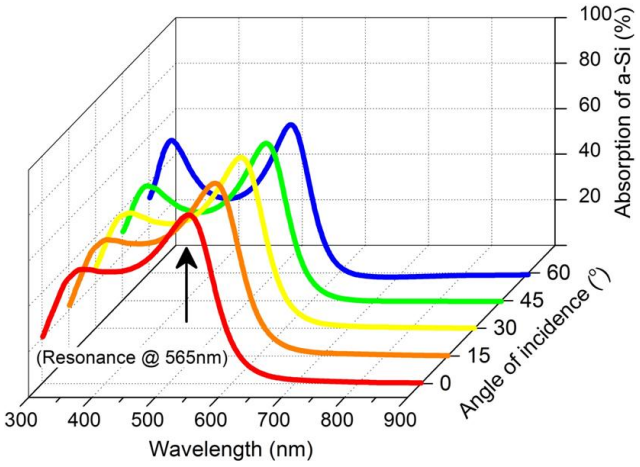

Figure 9.2.6 Calculated angle resolved absorption spectra in a-Si layer with the resonance of 565 nm for TE polarization.

As we discussed previously, the propagation phase shift through the ultra-thin semiconductor layer is almost negligible and the non-trivial reflection phase shifts compensate the propagation phase shift, thus resulting in angle invariant as well as polarization-independent performances that are highly desired for solar cell applications.

Figure 9.2.6 shows simulated angle resolved absorption spectra in the a-Si layer with the resonance of 565 nm for TE polarization. It is clear that the absorption profile with the distinct resonance (i.e., absorption peak at 565 nm) is invariant with respect to the angle of incidence up to ±60°. This implies that the Jsc would be not changed even at the large incident angle as the absorption in the a-Si photoactive layer is proportional to the Jsc, which will be confirmed by the experiment later.

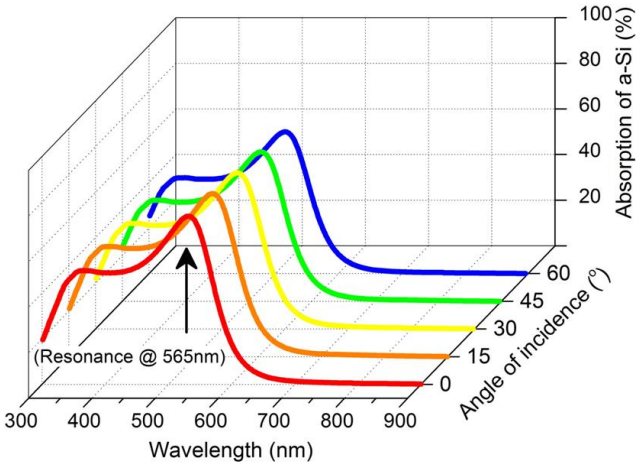

Figure 9.2.7 Calculated angle resolved absorption spectra in a-Si layer with the resonance of 565 nm for TM polarization.

In **Figure 9.2.7**, simulated angle resolved absorption profiles in the a-Si layer with the resonance of 565 nm for TM polarization are shown. As we observed in **Figure 9.2.6**, there is a negligible change in the absorption spectra as the incidence angle increases. These confirm both the polarization-independent and angle-insensitive properties of our ultra-thin colored a-Si PV cells.

9.3 Conclusion

In summary, we have investigated the extraordinary optical absorption effect in the ultra-thin a-Si film. The a-Si PV device with 20 nm thickness of the photoactive layer shows higher Jsc than the devices that have more than three times thicker active layer like 70 nm. In addition, the optical absorption spectrum in the photoactive layer, which is directly proportional to the Jsc of the PV device, is insensitive to the angle of incidence and polarization state of incident light due to the negligible propagation phase shift as well as the phase compensation as discussed in previous chapters. Such polarization- and angle-insensitive performances are highly beneficial to the PV applications since the unpolarized sunlight is incident upon the PV cells from wide angles.

Chapter 10

Wide-Angle, Ultra-Thin Broadband Visible Absorbers Exploiting Multi-Cavity Resonances

10.1 Introduction

The light absorption properties in plasmonic nanostructures and metamaterials have attracted substantial attention for their potential in a wide variety of areas such as color filters, photodetectors, photovoltaics, sensors, bolometers, optical lithography, and thermal emitters. Diverse approaches have been proposed and studied to achieve the enhanced absorption in multilayer architectures, and metal grating nanostructures. Most of the previous works on light absorbers, however, rely on the surface plasmon resonance (SPR) at the interface between metal and dielectric, which results in the absorption within a narrow wavelength region. This limits many applications, including photovoltaics and thermal emitters that require a large absorption over a wide range of wavelengths. In addition to the narrow band absorption, such property depends strongly on not only an angle of incidence but also a polarization state of incident light, consequently restricting their potential within narrow limits. An enormous amount of effort has been dedicated to improving the angle-dependent performance by employing a magnetic resonance or a localized surface plasmon resonance (LSPR), particularly in structures consisting of metal-insulator-metal. To overcome the polarization-dependent property, two dimensional

patterns, such as square patch, nanodisk, circular hole array, crossed trapezoid array, are utilized. Even though angle- and polarization-dependent characteristics can be improved, the vast majority of designed structures involve complicated and costly fabrication, making them difficult for the applications over a large area.

In this chapter, we propose and experimentally demonstrate an ultrathin (< 150 nm) broadband absorber capable of absorbing the light from 400 nm to 650 nm. The proposed structure comprises two stacks of highly absorbing material and metal showing 85 % absorption at a resonance. Additionally, our device exhibits the high performance of the absorption that is insensitive to the angle of incidence up to ±70° as well as the incident light polarization. The fundamentals of this work, which rely on strong interference effects in highly absorbing materials, is completely different from the mechanisms described in plasmonic related works. Besides of these features, only deposition is necessary to fabricate our designed absorber, providing a powerful scheme for attaining high efficient absorbing device with relatively simple and cost-effective means for large scale that are distinctly different from those observed in previous reports, involving expensive fabrication techniques, such as e-beam lithography. We also investigate the influence of the metal and absorbing materials on the absorption behavior of the device. The strategy discussed here could have the potential for many applications, such as metamaterials, thermal emitters, and photovoltaics.

10.2 Design Principle and Results

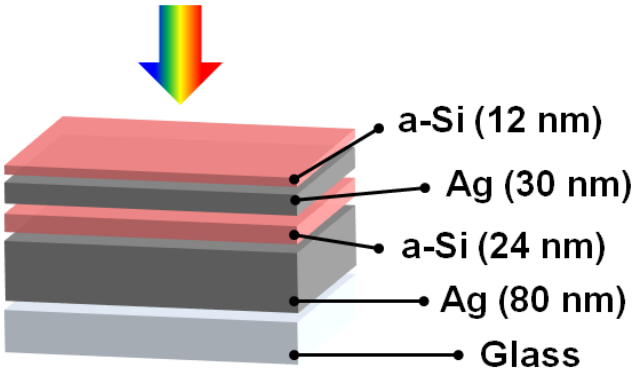

Figure 10.2.1 A schematic diagram of the proposed broadband visible absorber with improved viewing angle employing multi-cavity resonances in ultra-thin highly absorbing materials.

Figure 10.2.1 depicts a schematic view of the proposed wide-angle broadband visible absorber exploiting strong interference behaviors in ultra-thin semiconductor layers. Ag is chosen since it has the lowest absorption loss at visible frequency and a-Si is utilized as a semiconductor material.

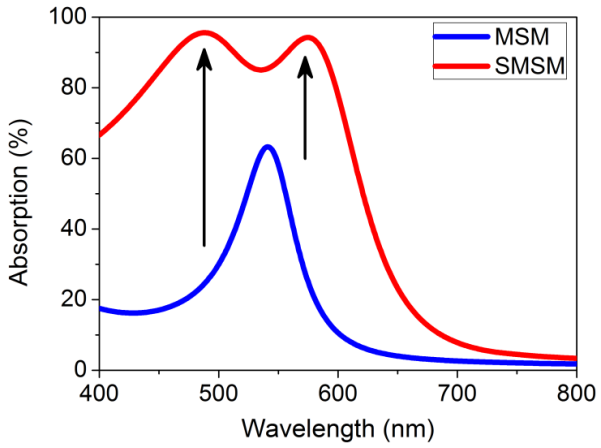

Figure 10.2.2 Simulated absorption spectra obtained from metal-semiconductor-metal (MSM) and semiconductor-metal-semiconductor-metal (SMSM) configurations.

In **Figure 10.2.2**, the simulated absorption profiles are described from metal-semiconductor-metal (MSM) and semiconductor-metal-semiconductor-metal (SMSM) geometries. It is obvious that the spectral response of SMSM structure is much wider and higher than that of MSM

structure. For MSM case, there is only one peak (@ 545 nm) that is arising from the F-P resonance in an ultra-thin semiconductor layer. Making two resonances at different wavelength (@ 490 and 575 nm) in the two a-Si cavity layers allows the absorption to be significantly increased. This is enabled by putting additional semiconductor layer on top of the MSM structure, which creates another resonance at 490 nm. We note that the resonance of the middle cavity (a-Si=24 nm) is somewhat sharper than that of the top cavity (a-Si=12 nm), which is attributed to strong reflections from both top and bottom metal-semiconductor interfaces as compared to the reflection at air-semiconductor interface.

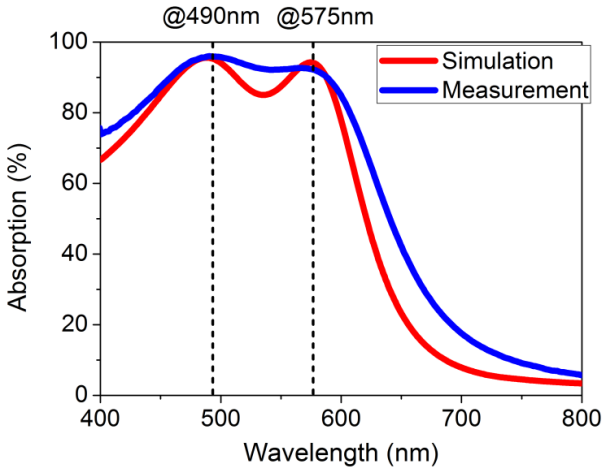

Figure 10.2.3 Simulated (red) and measured (blue) absorption spectra of the proposed ultra-thin broadband visible absorber at normal incident angle.

The simulation is carried out by using a transfer matrix method and the experimental spectra of the reflectance are measured by using a film thickness measurement instrument (Filmetrics F20-EXR) integrated with a spectrometer and a white light source unit, and the absorption profiles are obtained from 1 – R relation as illustrated in **Figure 10.2.3** that shows good match with the simulated profiles. It is important to note that only deposition method (i.e. thermal evaporation for Ag and PECVD for a-Si) is involved since our design simply consists of four layers without

any pattern, which can be easily scalable to large area. As can be seen from the figure, 95.6 (96.1) % and 94.3 (92.3) % of nearly perfect absorptions are obtained at 490 nm and 575 nm, respectively, from the simulation (experiment). Non-even surface of actual films induces the light scattering, leading to a relatively broader profile from the measured spectrum. Such a broadband absorption property with fairly high efficiency (> 90 %) is greatly desired in numerous applications, in particular PV. It is noteworthy to mention that tandem-mimicking ultra-thin a-Si PV could be realized by inserting interfacial layers discussed in the previous reports. Due to the nature of the resonance, the top PV cell (a-Si=12 nm, resonance @ 490 nm) primarily harvests the shorter wavelengths (i.e., blue ranges), whereas the middle PV cell (a-Si=24 nm, resonance @ 575 nm) strongly absorbs the green spectral regions, thus spanning a wide range of visible wavelengths toward high power conversion efficiency. Note that it is difficult for the a-Si material to absorb the wavelengths beyond 680 nm due to its band gap.

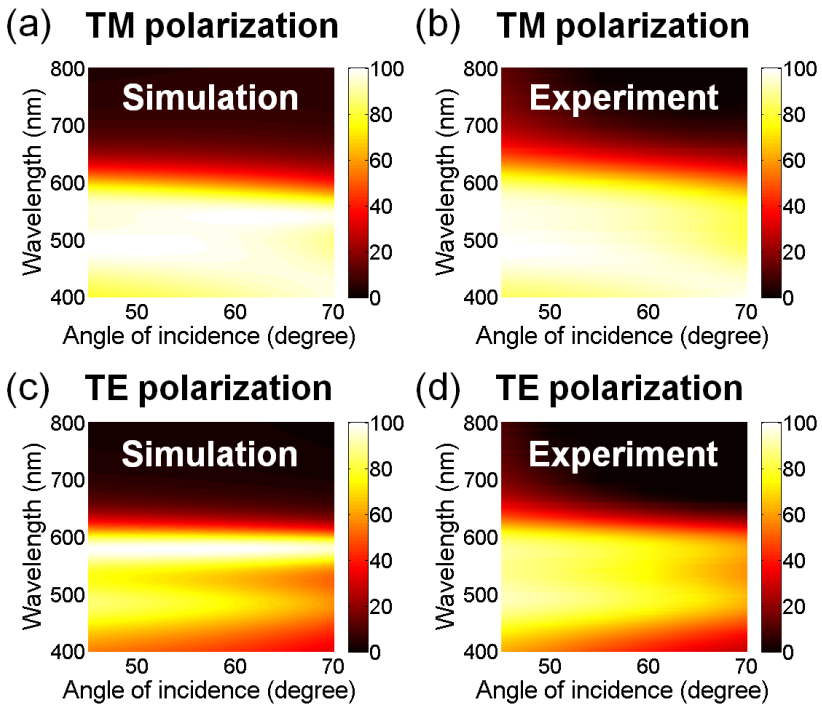

Figure 10.2.4 Simulated and measured angle resolved absorption spectra for TM (a), (b) and TE (c), (d) polarizations.

The simulated and measured angular dependences for TM and TE polarizations are shown in **Figure 10.2.4 (a) – (d)**, respectively. The angle resolved absorption spectra of the fabricated device is measured by a spectroscopic ellipsometer (M-2000, J. A. Woollam) at the angle of incidence ranging from 45° to 70° exhibiting good agreement with the simulation. Highly efficient absorption characteristic encompassing the wavelengths from 400 nm to 650 nm is accomplished over a wide range of incident angles up to ±70°. The angle insensitive characteristics could be explained by the fact that the phase shift accumulated during the propagation through the ultra-thin a-Si layer is nearly negligible since the a-Si film thickness is very thin as compared to the wavelength of incident light. Such angle robust property is crucial functionality for a variety of applications, such as PV, photodetectors, and thermal emitters.

10.3 Conclusion

In summary, we have shown a wide-angle, polarization-independent ultra-thin broadband absorber in the visible range. The designed structure is simply composed of four layers and any complex fabrication process (e.g. lithography and etching) is not required to fabricate the device. Putting additional absorbing layer with proper thickness on top of metal-semiconductor-metal architecture enables the absorption property to be significantly enhanced. The absorption peak of 95 % is achieved at a resonance and our device retains its strong absorption performance over a large angular range (±70°) under both TE- and TM-polarized light illumination. These features are desirable for various applications such as photovoltaics, thermal emitters, photodetectors, and metamaterials.

Chapter 11

Design of Electrodes for Visible-Blind UV Photodetectors

11.1 Introduction

Ultraviolet (UV) photodetectors (PDs) have been widely used as essential elements for a variety of applications, such as fire flame detection, space communication, health care, missile tracking, and pharmaceutical sunscreen product testing, depending on the UV region. For example, both an oil spill detection in the sea and a pharmaceutical sunscreen testing need to detect the wavelength ranging from 200 nm to 400 nm, while it is necessary to detect the wavelength region between 10 nm and 280 nm for the detection of fire flame and tracking of missiles. It is very difficult for a typical low band gap semiconductor like Ge and Si to achieve the high responsivity since these materials can also detect the visible light. Some researchers propose to utilize a large band gap semiconductor such as TiO_2 but the optical absorption is still limited. Thus, there is a strong need to integrate a new functionality that efficiently blocks the visible light. In this chapter, we will show a design of transparent electrodes, which could be potentially used for visible-blind UV PDs.

11.2 Design Principle and Results

First, we will show the electrode design that can transmit the range from 300 nm to 400 nm using multilayer structure.

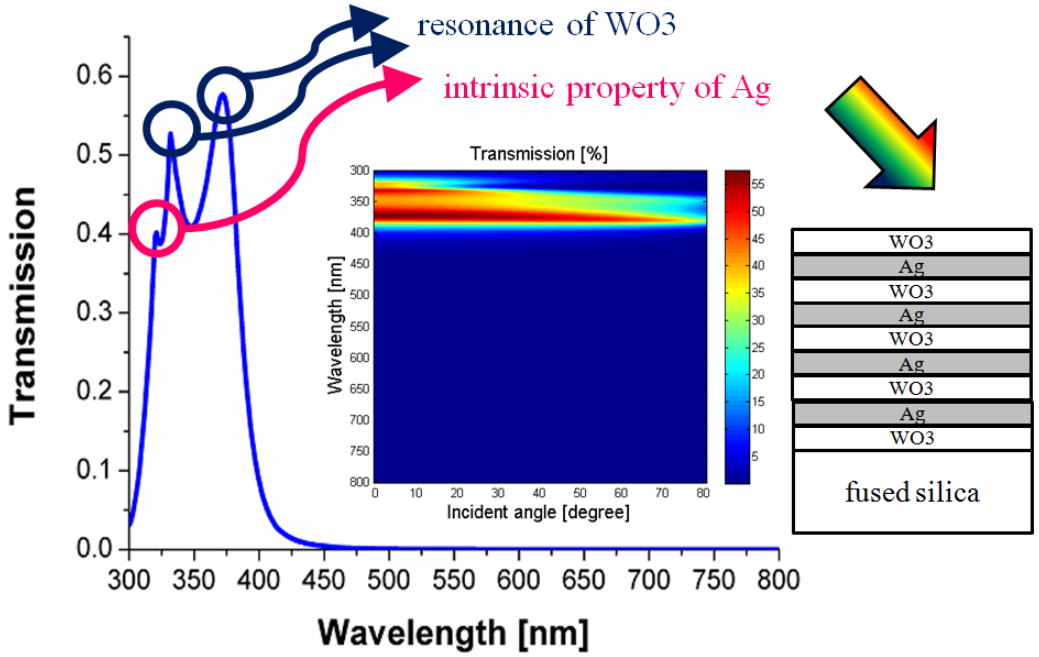

Figure 11.2.1 A schematic diagram of the proposed visible-blind UV PD electrode consisting of an alternating sequence of WO_3 and Ag. The thickness of both WO_3 and Ag materials are 30 nm. The simulated transmission spectrum at normal incidence and the corresponding dispersion curve are plotted.

Figure 11.2.1 shows the proposed device structure comprising multilayer of WO_3 and Ag, each of which has 30 nm of thickness along with the transmission spectrum at normal incidence calculated by transfer matrix method and the corresponding angle resolved transmission spectrum. In the simulation, n=2 is used for WO_3 and refractive index of Ag is obtained from Palik. So the transmission efficiency could be lower when considering the absorption of the WO_3 material at UV frequencies, which could be resolved by choosing a relatively transparent material such as MgF_2. As can be seen in the figure, there are three peaks at 321 nm, 330 nm, and 385 nm in the transmission spectrum. The peak at 321 nm is resulting from the interband

transition of the Ag layer. And both 330 nm and 385 nm transmission peaks are due to the resonance in WO_3 layers. Basically, there are 5 cavities and each of them could have the resonance, which will be evaluated in the next section.

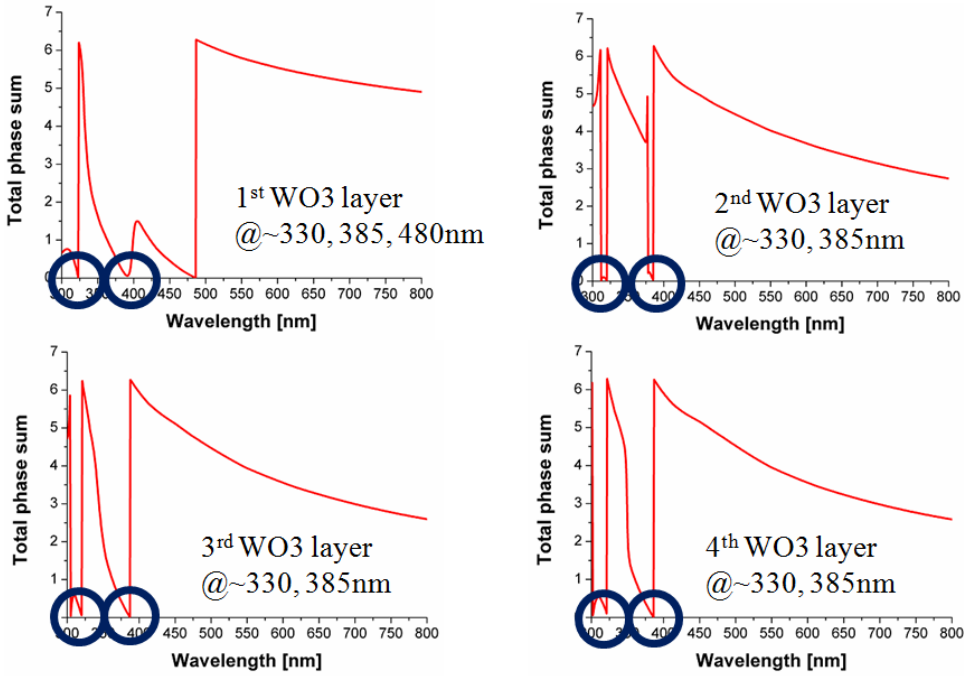

Figure 11.2.2 Calculated sum of the total phase shift, including two phase shifts occurring upon the reflection at the top and bottom interfaces and propagation phase shift through the WO_3 medium.

In **Figure 11.2.2**, the sum of the total phase shift is calculated in order to see how the resonance in each WO_3 cavity medium is related to the peak position in the transmission spectrum. When the sum of the propagation phase shift and the two reflection phase shifts is equal to $2m\pi$, the resonance occurs. The zero value of the total phase shift in the figure indicates where the resonance appears. It is clear to see that each WO_3 cavity has two resonances at 330 nm and 385 nm, which overlaps with one another, thus boosting up the transmission efficiency at these wavelengths. We note that the effect of the resonance in the 2^{nd}, 3^{rd}, and 4^{th} WO_3 cavity on the overall transmission profile is dominant as these cavities are sandwiched by two Ag mirrors. We

also note that the transmission efficiency could be further increased by reducing the thickness of the Ag layer. **Figure 11.2.3** exhibits a schematic diagram of the visible-blind UV a-Si PD design with the proposed electrode. Since the multilayer-based anode is transparent at UV frequencies, the light could be illuminating from the bottom. The same interfacial layers (V_2O_5 and ICBA) are used as shown in the colored a-Si PV cells and cathode is completed by Alq_3, LiF, and Al electrode.

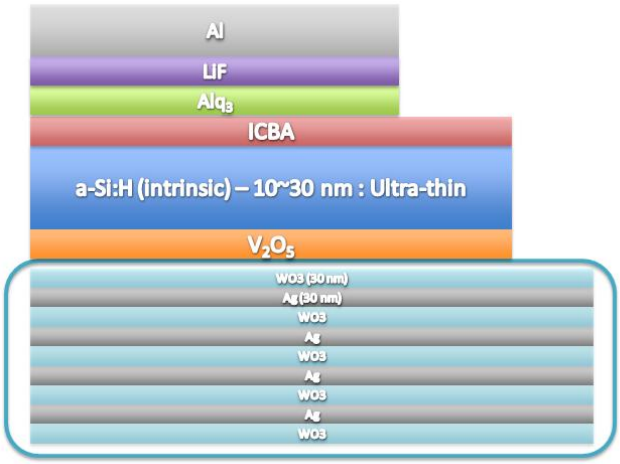

Figure 11.2.3 A possible device representation of the UV a-Si-based PD device structure with the proposed visible-blind electrode.

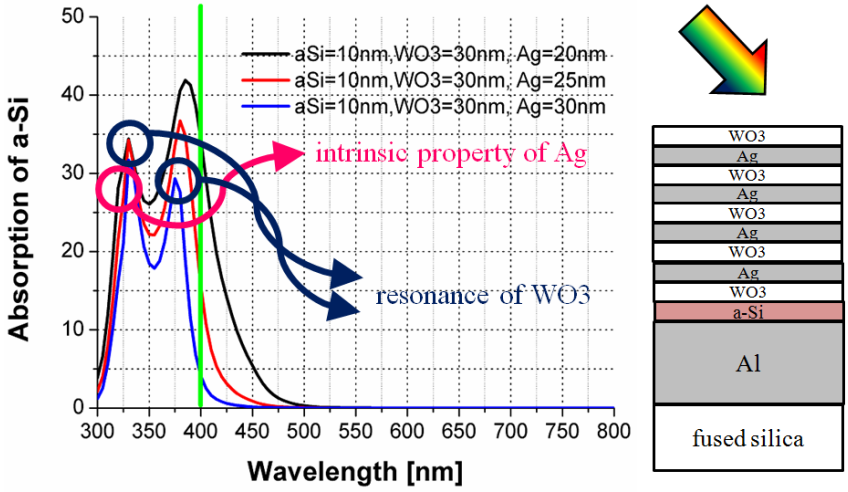

Figure 11.2.4 Calculated optical absorption in the a-Si layer, which shows good agreement of the transmission spectrum described in Figure 9.2.1.

Figure 11.2.4 presents the simulated absorption spectrum in the photoactive layer. As the Ag layer thickness inside the anode decreases, the transmission efficiency of the anode could be enhanced, thus resulting in a higher absorption in the a-Si intrinsic layer. These types of the UV PDs could be used for the detection of the oil spills in the sea and the sunscreen testing.

Next, we will explore different electrode design for the detection of deeper UV range of wavelength. Due to the plasma frequency of aluminum (Al), Al is better candidate than Ag from the absorption point of view for UV-related applications.

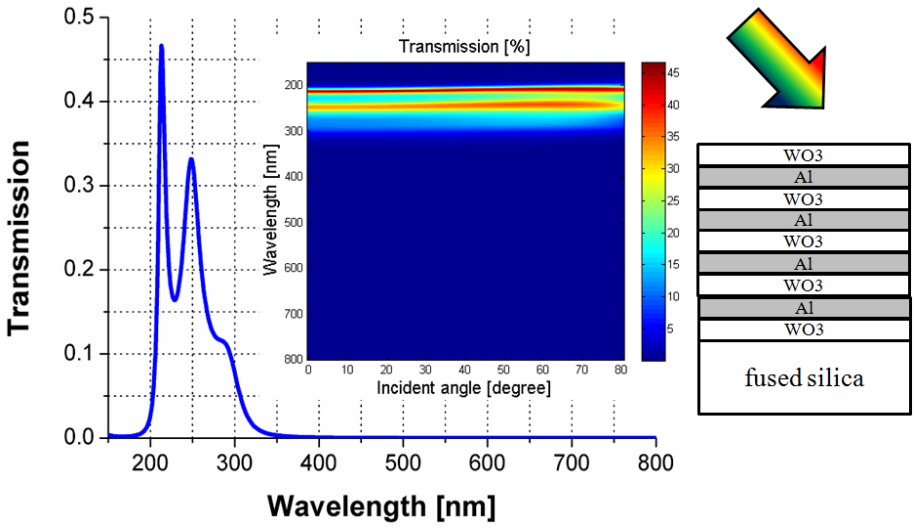

Figure 11.2.5 A schematic representation of the proposed visible-blind deep UV PD electrode that consists of an alternating sequence of WO_3 and Al. The calculated transmission spectrum at normal incidence and the angle resolved transmission spectrum are shown.

Figure 11.2.5 depicts the proposed device architecture that consists of an alternating sequence of WO_3 and Al, plotted together with the calculated transmission spectrum at normal incidence and the angle resolved transmission spectrum. In the simulation, n=2 is used for WO_3 and refractive index of Al is obtained from Palik. It is thus expected that the transmission efficiency could be significantly reduced when taking into the absorption loss of the WO_3 material at such a deep UV region account. Therefore, it is necessary to find a proper dielectric material whose absorptions are not large at the wavelength between 200 nm and 300 nm. Two distinct peaks at 213 nm and 248 nm are observed and there is a weak peak at 290 nm in the transmission spectrum, all of which are attributed to the existence of the resonance in each WO_3 cavity medium.

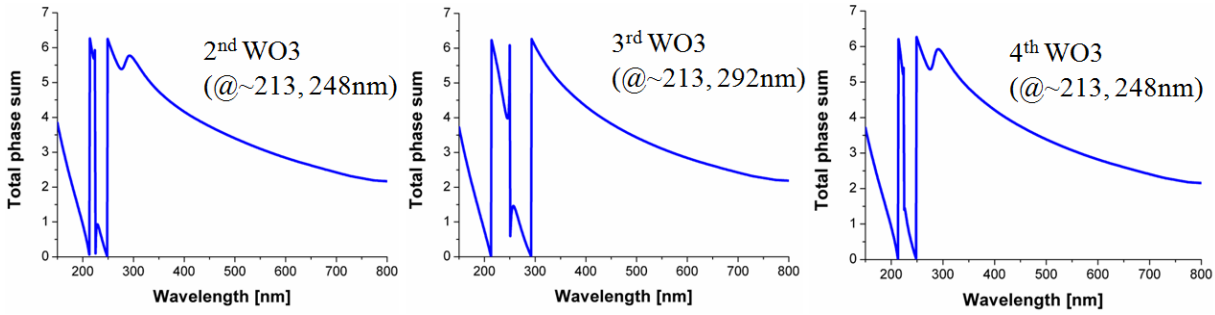

Figure 11.2.6 Calculated sum of the net phase change, including two reflection phase changes and propagation phase change.

Figure 11.2.6 describes the calculated sum of the total phase shift in order to explore how the peak position in the transmittance (**Figure 11.2.5**) is associated with the resonance wavelength in each WO_3 cavity. As explained above, the point where the total phase shift drops to zero corresponds to the resonance. It is obvious that the 2nd, 3rd, and 4th WO_3 cavities have the common resonance at 213 nm, thereby leading to the highest transmission efficiency (~47%) as

compared to other resonances. Both 2nd and 4th cavities have another resonance at 248 nm so another strong transmission peak appears at 248 nm in the spectrum. The weak transmission peak at 290 nm arises from the resonance that only exists in the 3rd WO_3 cavity. Also, the transmission efficiency could be improved by decreasing the thickness of the Al layers. Such a visible-blind deep UV PD electrode design could be used for the fire flame detection and tracking missile.

11.3 Conclusion

In conclusion, we have described possible designs of the multilayer-based transparent electrodes for the visible-blind UV PDs. At this stage, the number of layers, materials, and thicknesses are not optimized yet. After finding proper materials, particularly highly transparent dielectric films in the UV wavelength region of interest, both the thickness and the number of layers required for the electrode to achieve the functionality that efficiently blocks visible and IR band of lights and simultaneously transmits UV light of interest depending on the applications should be optimized.

Chapter 12

Summary and Future Works

The vast majority of the works in this dissertation are based on the strong interference effects in the ultra-thin highly absorbing materials. In chapter 2, we have thoroughly analyzed how such highly absorbing medium-based optical cavity is different from the traditional F-P optical cavity. We have explored which condition is needed in order to form a resonance in an ultra-thin lossy material and have also studied the phase cancellation, which is required for achieving the angle invariant property. Utilizing the concept, we have demonstrated the high-color-purity structural color filters creating both transmissive and reflective colors with much improved viewing, and suggested the one-step fabricated color filters for patterning the individual colors by pixel units in chapter 3. We have expanded our approach to the PV cells and successfully reported colored, ses-through ultra-thin PV devices in chapter 6. Wide-angle structural color filters employing either the plasmonic perfect absorptions or the photonic crystals have been proposed and experimentally demonstrated in chapter 4 and 5, respectively. We have also presented microcavity-integrated high efficiency colored semitransparent a-Si and perovskite PV cells in chapter 7. We have described a design principle of how to accomplish flexible, ITO-free perovskite PV creating distinctive reflective colors in chapter 8. We have exhibited several possible designs, their issues to be addressed, and then provide solutions. In chapter 9, we have demonstrated extraordinary optical absorption behaviors in ultra-thin a-Si PV devices. We have explored the effect of the resonance depending on the thickness of the photoactive layer on the

electrical performance (short-circuit current density) of the PV cells. We have also investigated angular dependences of the optical absorptions in the photoactive layer of the ultra-thin a-Si PV. We have reported wide-angle, ultra-thin broadband visible absorbers exploiting multi-cavity resonances in chapter 10. We have demonstrated how the optical absorptions could be significantly boosted up by employing another cavity at different resonance wavelength, which could be useful for PV applications. We have also proposed the potential of tandem-mimicking ultra-thin a-Si PV device architectures based on such broadband visible absorber designs. In chapter 11, we have described possible designs of a transparent electrode for visible-blind ultra-violet (UV) photodetectors. We have examined how the peaks in the transmission spectrum are associated with the resonance of each cavity in the multilayer-based electrode design.

We will suggest some potential future works based on strong interference effects in ultra-thin lossy media.

12.1 Polarization-Independent, Angle-Insensitive Nearly Perfect Broadband Absorbers

Although a broad band of the visible wavelengths is absorbed by multiple resonances in ultra-thin highly absorbing media as shown in a chapter 10, it is still difficult to absorb the lights from 650 to 800 nm due to the band gap of the a-Si material. Here, we will propose a different geometry with lossy metallic layers in order to achieve nearly perfect broadband visible absorbers.

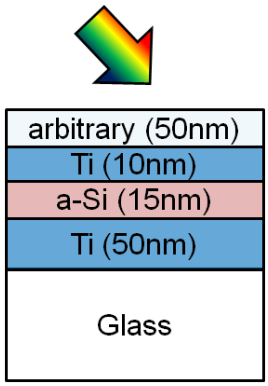

Figure 12.1.1 A schematic view of the proposed polarization-independent, angle-insensitive nearly perfect broadband absorber operating at visible frequencies.

Figure 12.1.1 presents a schematic diagram of the suggested polarization-independent, angle-insensitive nearly perfect broadband visible absorber consisting of the a-Si layer sandwiched by two titanium (Ti) layers and we put an arbitrary layer atop the structure as an AR coating. Since Ti has higher optical absorptions in visible wavelength ranges than other metals such as Ag, Au, and Al, the resonance created by Ti-based F-P cavity would have much broader profiles (i.e., poor Q-factor) than the resonance demonstrated in the chapter 10.

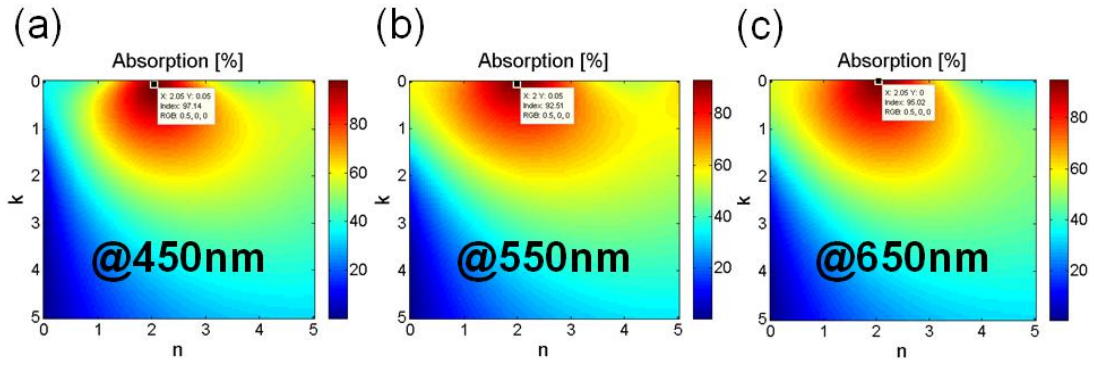

Figure 12.1.2 Calculated contour plots of the optical absorption as a function of a complex index of refraction (real (*n*) and imaginary (*k*) parts) of the 50 nm-thick AR layer at 450 (a), 550 (b), and 650 nm (c), respectively. Color maps denote the intensity values of the optical absorption.

In **Figure 12.1.2 (a) – (c)**, the calculated absorptions as functions of real (*n*) and imaginary (*k*) parts of the refractive index of an anti-reflection (AR) layer with a given thickness (50 nm) at

450, 550, and 650 nm are shown. It is clear that the optical absorption value is higher than 95 % in the wavelength regions from 450 to 650 nm when *n* and *k* are equal to 2.05 and 0.05, respectively. It is noted that the small (or large) thickness of the AR layer could be used with the large (or small) *n* value of the AR film. Because the optical constant of Si_3N_4 is highly close to the optimized optical constant to be needed for achieving the AR effect (i.e., *n*=2), we select Si_3N_4 as the AR coating layer. We also note that any other material with the refractive index of 2 such as WO_3, MoO_3, and Ta_2O_5 etc. can be used for the AR layer as well.

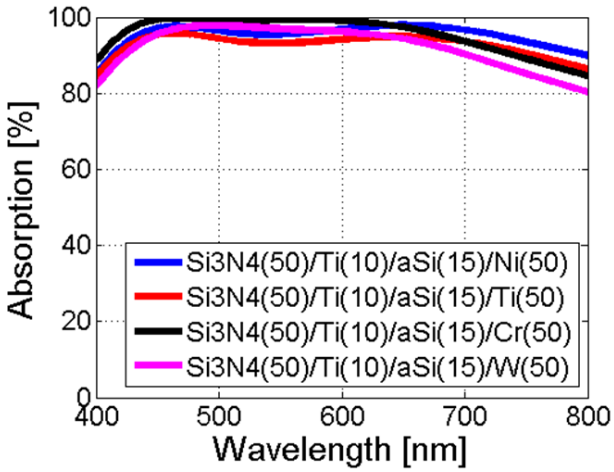

Figure 12.1.3 Simulated optical absorption spectra at normal incidence obtained from several structures with the different metallic substrates.

Figure 12.1.3 depicts calculated optical absorption profiles at normal incidence attained from the proposed device structures with the different metallic substrates, such as chromium (Cr), tungsten (W), and nickel (Ni). It is demonstrated that the nearly 100 % of optical absorptions across whole visible wavelengths are achieved.

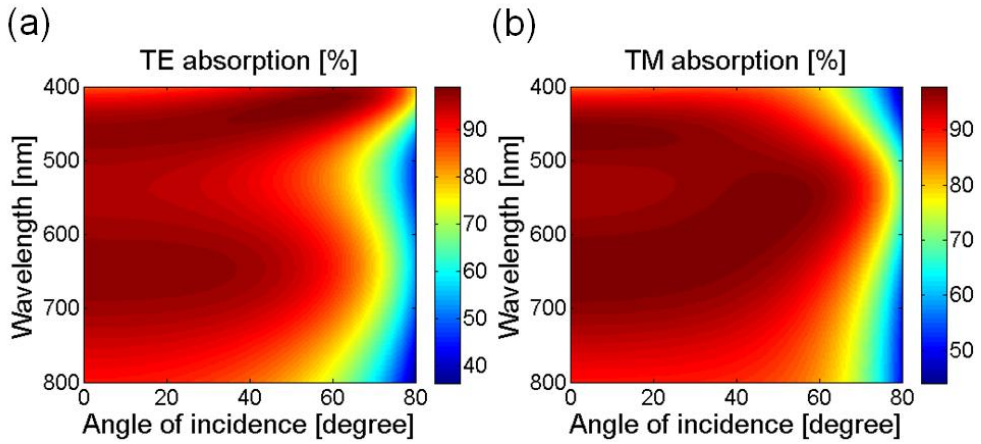

Figure 12.1.4 Simulated angle resolved absorption spectra of the proposed broadband visible absorber for TE (a) and TM polarizations (b).

Calculated angular behaviors of the proposed nearly perfect broadband visible absorber for TE and TM polarization are displayed in **Figure 12.1.4 (a) – (b)**, respectively. The numerical simulation is carried out by using the transfer matrix method with a white plane light wave at an angle of incidence from 0° to ±80°. Regardless of the polarization state of the incident light, a wide range of visible wavelength lights can be absorbed by the proposed structure up to ±70°. Such angle-insensitive and polarization-independent characteristics have tremendous potentials for applications in the areas of PV, thermal emitter, bolometers, and photodetectors.

12.2 Wire Grid Polarizers with Low Reflections

Many researchers in the field of the display have been trying to develop very efficient wire grid polarizer in order to replace the conventional absorption typed sheet polarizer. However, when they apply the wire grid polarizer to the display, the light will gets strongly reflected from the surface of the wire grid polarizer, which could interfere with the original information from the backside. Therefore, there is a critical need to develop the wire grid polarizer that can efficiently

transmit TM polarization and strongly absorb TE polarization at the same time. In this chapter, we will present how to achieve this functionality exploiting the strong resonance behaviors in the ultra-thin highly absorbing media on a metallic substrate.

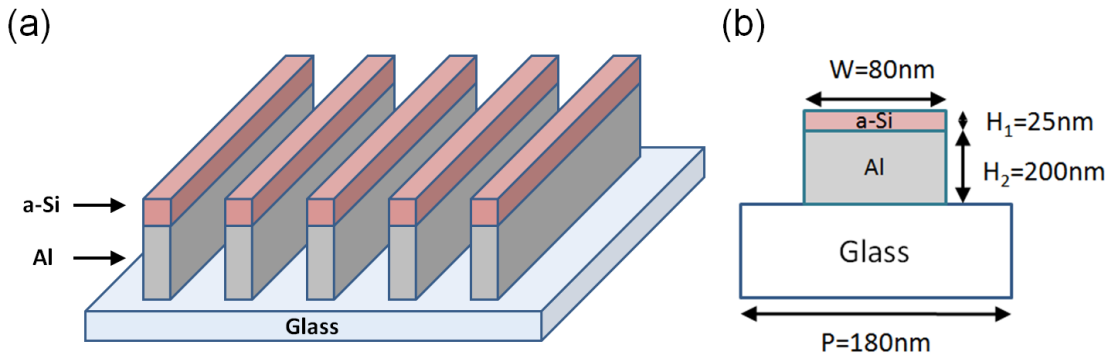

Figure 12.2.1 (a) A bird's-eye view of the proposed wire grid polarizer with low reflections comprising an ultra-thin a-Si film on top of the Al gratings on a glass substrate. (b) A cross-sectional view of the device. The period and width of the gratings is 180 nm and 80 nm, respectively. The thicknesses of a-Si and Al layers are 25 nm and 200 nm, respectively. Note that the period of the grating should be smaller than the half wavelength of interest, which is a necessary condition for working as a wire grid polarizer.

Figure 12.2.1 shows the schematic diagram of the proposed wire grid polarizer with low TE reflections. The structure is 1D patterned so that it could respond to only one polarization. When the light with the electric field that is parallel to the grating direction (i.e., TE polarization) is incident upon the structure, the electrons could move freely along the direction of the metallic layer, it will behave like typical metals so the light will get reflected from the surface of the metallic wires. Of course, they would be some absorption loss due to the joule heating of the metal. On the contrary, electromagnetic waves with the electric field that is perpendicular to the grating direction (i.e., TM polarization), it is difficult for the electrons to move freely along the wires due to the narrow linewidth of the metallic gratings. Thus, a vast majority of incident light wave will pass through the metal grating structure with experiencing negligible loss of the metal.

This is a typical behavior of the wire grid polarizer, saying that the TE-polarized light will get highly reflected whereas the TM-polarized light will be transmitted.

The working principle is based on the strong interference effects in the ultra-thin a-Si layer on top of the Al metallic substrate in order to create a strong resonance (i.e., absorption peak) at visible frequencies. Creating a resonance that corresponds to the absorption peak (i.e., reflection velley) at the resonance wavelength allows the reflections at a certain wavelength to be highly reduced, which can be observed in the calculated reflection spectrum as shown in **Figure 12.2.2**.

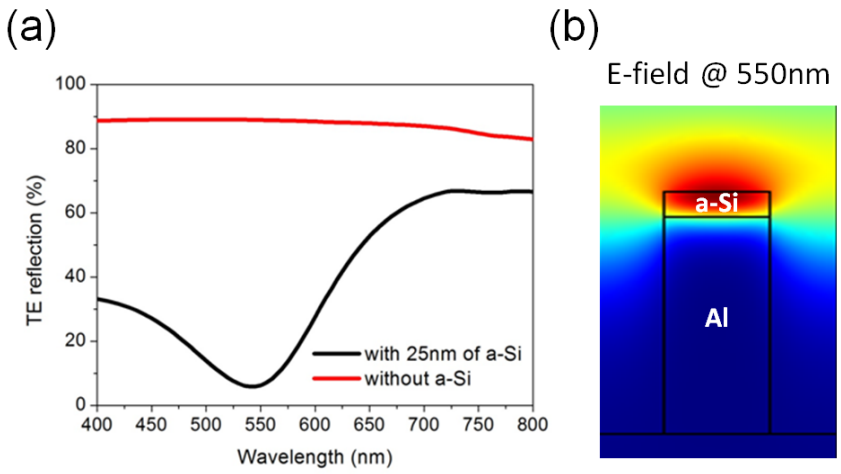

Figure 12.2.2 (a) Calculated spectral reflectance curves of the wire grid polarizer with (black) and without (red) 25 nm of the a-Si film on top of the Al gratings under the TE-polarized light illumination. (b) Electric field profile at 550 nm (resonance) showing that the field is primarily concentrated in the a-Si layer.

In **Figure 12.2.2 (a)**, the calculated reflection spectra of the Al gratings with (black solid line) and without (red solid line) 25 nm of the a-Si layer on top of the metallic gratings for TE polarization are exhibited. As can be seen in the figure, the TE reflection at 550 nm (~5 %) is significantly reduced as compared to the TE reflection (~90 %) of the general wire grid polarizer. As explained above, we basically create a F-P resonance in the ultra-thin a-Si film. Increasing

the thickness of the a-Si layer leads to the red-shifted resonance. **Figure 12.2.2 (b)** describes the electric field distribution at 550 nm, exhibiting that the field is mainly concentrated into the ultra-thin a-Si layer that indicates the fundamental mode of the F-P resonance. Even though we have achieved the reduced reflections at a certain wavelength, the reflections at off-resonance wavelengths are still pretty high, which needs to be further mitigated by some other mean. To address this, the a-Si material could be replaced by a low band gap semiconductor, such as Ge, so that a wide range of wavelengths could be strongly absorbed by the ultra-thin semiconductor. This basically implies that we are making the poor cavity system (i.e., poor Q-factor) by introducing more loss in the cavity.

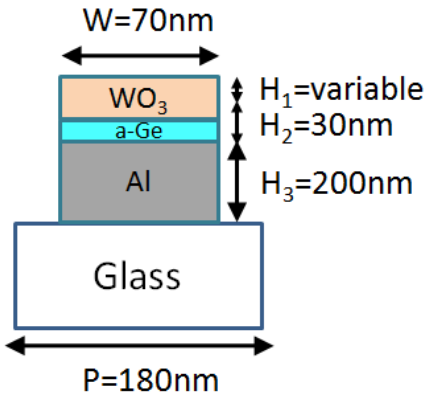

Figure 12.2.3 A schematic view of the proposed wire grid polarizer with highly suppressed TE reflections. The a-Si layer in the previous design as exhibited in Figure 12.2.1 is replaced by the Ge semiconductor and then another optically transparent dielectric, WO_3, is introduced for anti-reflection (AR) coating of the Ge layer. The period and the width of the gratings are 180 nm and 70 nm, respectively. Ge layer thickness is 30 nm and the top WO_3 film thickness is found to be 50~60 nm.

Figure 12.2.3 depicts the schematic diagram of the proposed wire grid polarizer that can highly suppress the TE reflections over the wide range of wavelengths. The device structure consists of three patterned layers (WO_3/Ge/Al) on the glass substrate. As the Ge (0.66 eV) has a lower band gap than the a-Si (1.7 eV), it could strongly absorb a broad range of visible lights, thus giving

rise to the reduced TE reflections over the wide range of visible wavelengths as is seen from **Figure 12.2.4**.

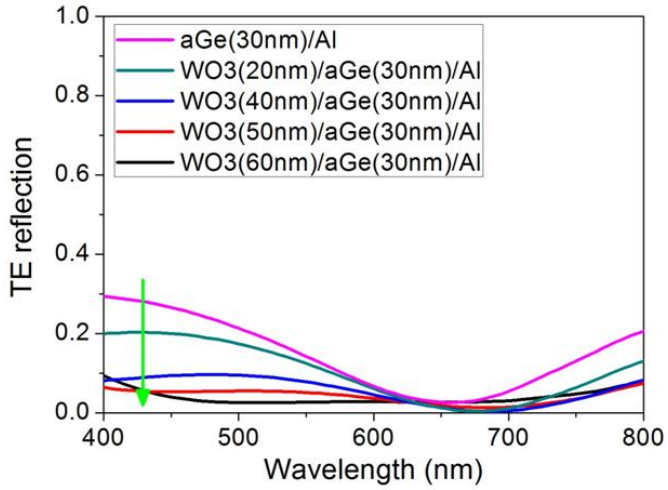

Figure 12.2.4 Calculated reflection spectra of the proposed low reflective wire grid polarizer with and without different thickness of the top WO_3 AR layer for TE polarization.

Figure 12.2.4 illustrates the calculated spectral reflection curves of the proposed wire grid polarizer with highly suppressed TE reflections with and without several thicknesses of the top WO_3 AR layer. Employing the low band gap semiconductor (magenta solid line) results in a fairly broad resonance at visible frequencies, which already demonstrate the highly reduced reflections as compared to what has been observed with the a-Si material as described in **Figure 12.2.1**. However, the reflections at shorter wavelengths are still 30 % that results from the large index contrast between air and Ge. In order to further mitigate the reflections, a low index material (WO_3) is introduced atop the structure. With the proper thickness of the WO_3 layer, the TE reflections could be less than around 10 % across the whole visible wavelength range. It should be noted that both the thicknesses of the Ge and WO_3 layers are not yet optimized so it would be possible to further reduce the TE reflection efficiently with the optimized parameters.

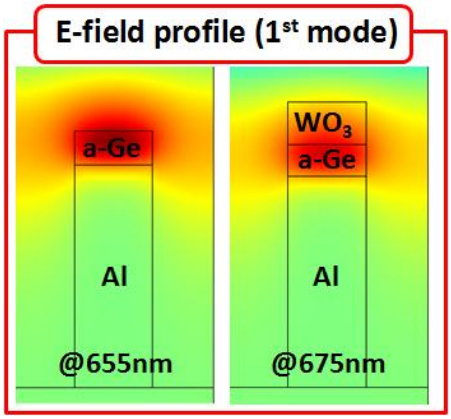

Figure 12.2.5 Electric field distribution at a resonance wavelength demonstrating that the field is largely concentrated in the Ge layer.

In **Figure 12.2.5**, the intensity distributions of the electric field at the resonance with and without the top WO_3 AR layer are shown. Regardless of the presence of the AR layer, the field is chiefly concentrated in the ultra-thin Ge film, suggesting that the first F-P resonance mode.

Bibliography

[1] J. A. Stratton, Electromagnetic Theory (McGraw-Hill, 1941).

[2] A. W. Snyder and J. D. Love, Optical Waveguide Theory (Chapman & Hall, 1983).

[3] K. J. Vahala, Nature **424**, 839–846 (2003).

[4] V. S. Ilchenko and A. B. Matsko, IEEE J. Sel. Top. Quantum Electron. **12**, 15-32 (2006).

[5] M. A. Kats, R. Blanchard, P. Genevet, and F. Capasso, Nature Mater. **12**, 20-24 (2013).

[6] M. A. Kats, S. J. Byrnes, R. Blanchard, M. Kolle, P. Genevet, J. Aizenberg, and F. Capasso, Appl. Phys. Lett. **103**, 101104 (2013).

[7] M. A. Kats, D. Sharma, J. Lin, P. Genevet, R. Blanchard, Z. Yang, M. M. Qazilbash, D. N. Basov, S. Ramanathan, and F. Capasso, Appl. Phys. Lett. **101**, 221101 (2012).

[8] R. W. Sabnis, Displays **20**, 119-129 (1999).

[9] Y. Kanamori, M. Shimono, and K. Hane, IEEE Photon. Technol. Lett. **18**, 2126-2128 (2008).

[10] Y.-T. Yoon, H.-S. Lee, S.-S. Lee, S. H. Kim, J.-D. Park, and K.-D. Lee, Opt. Express **16**, 2374-2380 (2008).

[11] T. Xu, Y.-K. Wu, X. Luo, and L. J. Guo, Nat. Commun. **1**, 59 (2010).

[12] K. Diest, J. A. Dionne, M. Spain, and H. A. Atwater, Nano Lett. **9**, 2579-2583 (2009).

[13] C.-H. Park, Y.-T. Yoon, and S.-S. Lee, Opt. Express **20**, 23769–23777 (2012).

[14] T. Xu, H. Shi, Y.-K. Wu, A. F. Kaplan, J. G. Ok, and L. J. Guo, Small **7**, 3128-3136 (2011).

[15] Y. S. Do, J. H. Park, B. Y. Hwang, S.-M. Lee, B.-K. Ju, and K. C. Choi, Adv. Opt. Mater. **1**, 133-138 (2013).

[16] H. J. Park, T. Xu, J. Y. Lee, A. Ledbetter, and L. J. Guo, ACS Nano **5**, 7055-7060 (2011).

[17] A. F. Kaplan, T. Xu, and L. J. Guo, Appl. Phys. Lett. **99**, 143111 (2011).

[18] Y.-K. R. Wu, A. E. Hollowell, C. Zhang, and L. J. Guo, Sci. Rep. **3**, 1194; DOI:10.1038/srep01194 (2013).

[19] P. G. Etchegoin, E. C. Le Ru, and M. Meyer, J. Chem. Phys. **125**, 164705 (2006).

[20] M. El Kurdi, S. David, X. Checoury, G. Fishman, P. Boucaud, O. Kermarrec, D. Bensahel, and B. Ghyselen, Opt. Commun. **281**, 846-850 (2008).

[21] K.-T. Lee, S. Seo, J. Y. Lee, and L. J. Guo, Adv. Mater. **26**, 6324-6328 (2014).

[22] K.-T. Lee, S. Seo, J. Y. Lee, and L. J. Guo, Applied Physics Letters **104**, 231112 (2014).

[23] K.-T. Lee, S. Seo, J. Y. Lee, and L. J. Guo, Conference on Lasers and Electro-Optics (CLEO): 2014, San Jose, CA, USA, June 8-13, (2014).

[24] K.-T. Lee, S. Seo, J. Y. Lee, and L. J. Guo, IEEE Photonics Conference 2013, Bellevue, WA, USA, Sep. 8-12, (2013).

[25] L. A. A. Pettersson, L. S. Roman, and O. Inganas, J. Appl. Phys. **86**, 487 (1999).

[26] P. Biagioni, J.-S. Huang, and B. Hecht, Rep. Prog. Phys. **75**, 024402 (2012).

[27] S. O'Brien, D. McPeake, S. A. Ramakrishna, and J. B. Pendry, Phys. Rev. B **69**, 241101 (2004).

[28] H. Kim, J. Park, and B. Lee, Fourier Modal Method and Its Applications in Computational Nanophotonics (Taylor & Francis, CRC Press Inc, 2012).

[29] C.-C. Lee, S.-H. Chen, and C.-C. Jaing, Appl. Opt. **35**, 5698-5703 (1996).

[30] K.-T. Lee and L. J. Guo, (in preparation).

[31] A. S. Roberts, A. Pors, O. Albrektsen, and S. I. Bozhevolnyi, Nano Lett. **14**, 783-787 (2014).

[32] H.-S. Lee, Y.-T. Yoon, S.-S. Lee, S.-H. Kim, and K.-D. Lee, Opt. Express **15**, 15457-15463 (2007).

[33] D. Inoue, A. Miura, T. Nomura, H. Fujikawa, K. Sato, N. Ikeda, D. Tsuya, Y. Sugimoto, and Y. Koide, Appl. Phys. Lett. **98**, 093113 (2011).

[34] S. Yokogawa, S. P. Burgos, and H. A. Atwater, Nano Lett. **12**, 4349-4354 (2012).

[35] D. Chung, C. Shin, B. Song, M. Jung, Y. Yun, S. H. Nam, C. Noh, J. Kim, and S. Lee, Appl. Phys. Lett. **101**, 221120 (2012).

[36] E.-H. Cho, H.-S. Kim, J.-S. Sohn, C.-Y. Moon, N.-C. Park, and Y.-P. Park, Opt. Express **18**, 27712-27722 (2010).

[37] H. Kim, J. Ge, J. Kim, S.-e. Choi, H. Lee, H. Lee, W. Park, Y. Yin, and S. Kwon, Nat. Photon. **3**, 534-540 (2009).

[38] C.-H. Park, Y.-T. Yoon, V. R. Shrestha, C.-S. Park, S.-S. Lee, and E.-S. Kim. Opt. Express **21**, 28783-28793 (2013).

[39] B. Ai, Y. Yu, H. Möhwald, and G. Zhang, Adv. Opt. Mater. **1**, 724-731 (2013).

[40] G. Si, Y. Zhao, J. Lv, M. Lu, F. Wang, H. Liu, N. Xiang, T. J. Huang, A. J. Danner, J. Teng, and Y. J. Liu, Nanoscale **5**, 6243 (2013).

[41] K. Seo, M. Wober, P. Steinvurzel, E. Schonbrun, Y. Dan, T. Ellenbogen, and K. B. Crozier, Nano Lett. **11**, 1851-1856 (2011).

[42] E. N. Economou, Phys. Rev. **182**, 539-554 (1969).

[43] J. Chen, G. A. Smolyakov, S. R. J. Brueck, and K. J. Malloy, Opt. Express **16**, 14902-14909 (2008).

[44] J. A. Dionne, L. A. Sweatlock, H. A. Atwater, and A. Polman, Phys. Rev. B **72**, 075405 (2005).

[45] R. Zia, M. D. Selker, and M. L. Brongersma, Phys. Rev. B **71**, 165431 (2005).

[46] H. Shin, M. F. Yanik, S. Fan, R. Zia, and M. L. Brongersma, Appl. Phys. Lett. **84**, 4421 (2004).

[47] A. Yariv, Electron. Lett. **36**, 321-322 (2000).

[48] E. Almpanis and N. Papanikolaou, J. Appl. Phys. **114**, 083106 (2013).

[49] T. V. Teperik, F. J. Garcia De Abajo, A. G. Borisov, M. Abdelsalam, P. N. Bartlett, Y. Sugawara, and J. J. Baumberg, Nat. Photon. **2**, 299-301 (2008).

[50] J. Yoon, K. H. Seol, S. H. Song, and R. Magnusson, Opt. Express **18**, 25702-25711 (2010).

[51] K.-T. Lee, J. Y. Lee, S. Seo, and L. J. Guo, Light Sci. Appl. **3**, e215; DOI:10.1038/lsa.2014.96 (2014).

[52] J. Y. Lee, K.-T. Lee, S. Seo, and L. J. Guo, Sci. Rep. **4**, 4192, doi:10.1038/srep04192 (2014).

[53] C. Zhang, D. Zhao, D. Gu, H. Kim, T. Ling, Y.-K. R Wu, and L. J. Guo, Adv. Mater. **26**, 5696-5701 (2014).

[54] F.-J. Ko and H.-P. D. Shieh, Appl. Opt. **39**, 1159–1163 (2000).

[55] P. B. Catrysse, W. Suh, S. Fan, and M. Peeters, Opt. Lett. **29**, 974–976 (2004).

[56] K. Chung, S. Yu, C.-J. Heo, J. W. Shim, S.-M. Yang, M. G. Han, H.-S. Lee, Y. Jin, S. Y. Lee, N. Park, and J. H. Shin, Adv. Mater. **24**, 2375–2379 (2012).

[57] K. Chung and J. H. Shin, J. Opt. Soc. Am. A **30**, 962-968 (2013).

[58] J.-G. Park, S.-H. Kim, S. Magkiriadou, T. M. Choi, Y.-S. Kim, and V. N. Manoharan, Angew. Chem. Int. Ed. **53**, 2899–2903 (2014).

[59] D. Banerjee and M. Zhang, J. Mod. Optic. **57**, 1180-1188 (2010).

[60] G.B. Smith, A. Gentle, P. D. Swift, A. Earp, and N. Mronga, Sol. Energ. Mat. Sol. C. **79**, 179–197 (2003).

[61] S. Magkiriadou, J.-G. Park, Y.-S. Kim, and V. N. Manoharan, Phys. Rev. E **90**, 062302 (2014).

[62] D. Banerjee and M. Zhang, J. Mod. Opt. **57**, 1180-1188 (2010).

[63] P. Yeh, A. Yariv, and C.-S. Hong, J. Opt. Soc. Am. **67**, 423-438 (1977).

[64] J. N. Winn, Y. Fink, S. Fan, and J. D. Joannopoulos, Opt. Lett. **23**, 1573-1575 (1998).

[65] Y. Fink, J. N. Winn, S. Fan, C. Chen, J. Michel, J. D. Joannopoulos, and E. L. Thomas, Science **282**, 1679 (1998).

[66] C.-C. Lee, S.-H. Chen, and C.-C. Jaing, Appl. Opt. **35**, 5698-5703 (1996).

[67] H. Kostlin and G. Frank, Thin Solid Films **89**, 287-293 (1982).

[68] H. A. Macleod, Thin-Film Optical Filters (CRC Press, Boca Raton, 2010), chap. 3.

[69] Grossiord N, Kroon JM, Andriessen R, Blom PWM. Org. Electron. **13,** 432-456 (2012).

[70] Myong SY, Kim SS, Lim KS. J. Appl. Phys. **95**, 1525-1530 (2004).

[71] Soderstrom T, Haug FJ, Niquille X, Ballif C. Prog Photovolt Res Appl **17**, 165-176 (2009).

[72] Shah AV, Schade H, Vanecek M, Meier J, Vallat-Sauvain E, et al. Prog Photovolt Res Appl **12**, 113-142 (2004).

[73] M. Fukuda, K.-T. Lee, J. Y. Lee, and L. J. Guo, IEEE J. of Photovoltaics **4**, 1337-1342 (2014).

[74] J. Y. Lee, K.-T. Lee, S. Seo, and L. J. Guo, Conference on Lasers and Electro-Optics (CLEO): 2014, San Jose, CA, USA, June 8-13 (2014).

[75] K.-T. Lee, J. Y. Lee, S. Seo, and L. J. Guo, Conference on Lasers and Electro-Optics (CLEO): 2014, San Jose, CA, USA, June 8-13 (2014).

[76] J. Y. Lee, K.-T. Lee, S. Seo, and L. J. Guo, 40th IEEE Photovoltaic Specialists Conference (PVSC), Denvor, CO, USA, June 8-13 (2014).

[77] J. Y. Lee, K.-T. Lee, S. Seo, H. J. Park, and L. J. Guo, 2013 Renewable Energy and the Environment meeting, Tucson, AZ, USA, Nov. 04-07 (2013).

[78] Meyer, J., Zilberber, K., Riedl, T. and Kahn, A., J. Appl. Phys. **110**, 033710 (2011).

[79] Eisler CN, Kosten ED, Warmann EC, and Atwater HA., Proceeding of the SPIE Solar Energy + Technology, **8821**, 25 – 29 August 2013; San Diego, CA, USA (2013).

[80] Escarra MD, Darbe S, Warmann EC, Atwater HA., Proceedings of the 39th IEEE Photovoltaic Specialists Conference; 16 – 21 June 2013; Tampa, FL, USA (2013).

[81] Stefancich M, Zayan A, Chiesa M, Rampino S, Roncati D, et al., Opt. Express **20**, 9004-9018 (2012).

[82] Mitchell B, Peharz G, Siefer G, Peters M, Gandy T, et al., Prog Photovolt: Res Appl **19**, 61-72 (2011).

[83] Jin, H. et al., Adv. Mater. **24**, 2572-2577 (2012).

[84] Guo, X. et al., J. Mater. Chem. **22**, 17176-17182 (2012).

[85] Logeeswaran, VJ. et al., Nano Lett. **9**, 178-182 (2009).

[86] He, Y., Chen, H.-Y., Hou, J. and Li, Y., J. Am. Chem. Soc. **132**, 1377-1382 (2010).

[87] O'Malley, K. M., Li, C.-Z., Yip, H.-L. and Jen, A. K.-Y., Adv. Energy Mater. **2**, 82-86 (2012).

[88] Goerlitzer, M. et al., J. Appl. Phys. **80**, 5111-5115 (1996).

[89] Schiff, E. A., Sol. Energy Mater. Sol. Cells **78**, 567-595 (2003).

[90] Deng, X. and Schiff, E. A., Handbook of Photovoltaic Science and Engineering (Chap. 12) [Luque, A. and Hegedus, S. (ed.)] [505-566] (John Wiley and Sons, Chichester, 2003).

[91] Staebler, D. L. and Wronski, C. R., Appl. Phys. Lett. **31**, 292 (1977).

[92] Branz, H. M. et al., Phys. Rev. B **59**, 5498-5512 (1999).

[93] Deceglie, M. G., Ferry, V. E., Alivisatos, A. P. and Atwater, H. A., Nano Lett. **12**, 2894-2900 (2012).

[94] Carlson, D. E. and Wronski, C. R., Appl. Phys. Lett. **28**, 671 (1976).

[95] Shah, A. V. et al., Prog. Photovolt. Res. Appl. **12**, 113-142 (2004).

[96] Benagli, S. et al., 24th European Photovoltaic Solar Energy Conference (2009).

[97] M. Liu, M. B. Johnston, and H. J. Snaith, Nature **501**, 395-398 (2013).

[98] M. A. Green, A. Ho-Baillie, and H. J. Snaith, Nature Photon. **8**, 506-514 (2014).

[99] J. M. Ball, M. M. Lee, A. Hey, and H. J. Snaith, Energy Environ. Sci. **6**, 1739 (2013).

[100] C. Wehrenfennig, M. Liu, H. J. Snaith, M. B. Johnston, and L. M. Herz, Energy Environ. Sci. **7**, 2269 (2014).

[101] G. E. Eperon, V. M. Burlakov, P. Docampo, A. Goriely, and H. J. Snaith, Adv. Funct. Mater. **24**, 151-157 (2014).

[102] B. Cai, Y. Xing, Z. Yang, W.-H. Zhang, and J. Qiu, Energy Environ. Sci. **6**, 1480-1485 (2013).

[103] P. Qin, S. Tanaka, S. Ito, N. Tetreault, K. Manabe, H. Nishino, M. K. Nazeeruddin, and M. Grätzel, Nat. Commun. **5**, 3834 (2014).

[104] H. Zhou, Q. Chen, G. Li, S. Luo, T.-b. Song, H.-S. Duan, Z. Hong, J. You, Y. Liu, and Y. Yang, Science **345**, 542-546 (2014).

[105] H. Yu, F. Wang, F. Xie, W. Li, J. Chen, and N. Zhao, Adv. Funct. Mater. **24**, 7102-7108 (2014).

[106] E. Edri, S. Kirmayer, S. Mukhopadhyay, K. Gartsman, G. Hodes, and D. Cahen, Nat. Commun. **5**, 3461 (2014).

[107] A. T. Barrows, A. J. Pearson, C. K. Kwak, A. D. F. Dunbar, A. R. Buckleya, and D. G. Lidzey, Energy Environ. Sci. **7**, 2944-2950 (2014).

[108] G. E. Eperon, V. M. Burlakov, A. Goriely, and H. J. Snaith, ACS Nano **8**, 591-598 (2014).

[109] S. D. Stranks, G. E. Eperon, G. Grancini, C. Menelaou, M. J. P. Alcocer, T. Leijtens, L. M. Herz, A. Petrozza, and H. J. Snaith, Science **342**, 341-344 (2013).

[110] G. Xing, N. Mathews, S. Sun, S. S. Lim, Y. M. Lam, M. Grätzel, S. Mhaisalkar, and T. C. Sum, Science **342**, 344-347 (2013).

[111] C.-S. Park, V. R. Shrestha, S.-S. Lee, E.-S. Kim, and D.-Y. Choi, Sci. Rep. **5**, 8467, doi: 10.1038/srep08467 (2015).